DISSERTATION

# CYTOTOXICITY, GENOTOXICITY AND DNA DOUBLE-STRAND BREAK REPAIR MECHANISMS ACROSS THE FULL CARBON-ION BEAM RANGE

Submitted by

Dylan Buglewicz

Department of Environmental and Radiological Health Sciences

In partial fulfillment of the requirements

For the Degree of Doctor of Philosophy

Colorado State University

Fort Collins, Colorado

Summer 2021

Doctoral Committee:

Advisor: Takamitsu Kato

Marie Legare
Aaron Sholders
Del Leary

ABSTRACT

CYTOTOXICITY, GENOTOXICITY AND DNA DOUBLE-STRAND BREAK REPAIR MECHANISMS ACROSS THE FULL CARBON-ION BEAM RANGE

Background: The ability for the high-linear energy transfer (high-LET) carbon-ion beam used in carbon-ion radiotherapy (CIRT) to effectively treat tumors that are located near at-risk organs, such as in the head and neck, as well as tumors that have demonstrated to be low-LET proton and photon radioresistant has enhanced international interest in the wide-spread use and development of CIRT. The success of CIRT is attributed to its excellent physical dose-depth distribution and deposition around the carbon-ion Bragg peak as well as its high-LET components, such as an enhanced relative biological effectiveness (RBE) and DNA double-strand break (DSB) distribution as well as a lower oxygen enhancement ratio (OER), that allows for the treatment of radioresistant tumors to conventional low-LET radiotherapy methods.

CIRT utilizes ionizing radiation to induce DNA damage, the most consequential of which being DSBs, to effectively "kill" the tumor cells within its targeted region. Low-LET ionizing radiations, such as photon and proton beams, are sparsely ionizing and results in DSBs that are randomly distributed within the cell. On the other hand, high-LET ionizing radiations, such as carbon-ion or iron-ion beams, are densely ionizing, meaning they distribute their energy in very dense tracks of ionizations along their path as the beam traverses through the cells. This results in close localizations of DSBs that are very difficult for the cell to repair. Although, the carbon-ion beam is composed of a mixed field of radiation qualities (low- and high-LET), as the LET increases as it approaches the carbon-ion Bragg peak and the LET reaches its maximum value.

Following the carbon-ion Bragg peak there is a drastic decrease in the deposited dosage and LET value. However, nuclear reactions that occur along the carbon-ion beam's path results in nuclear fragmentation ions that travel in nearly the same direction with nearly the same velocity that can carry energy much further distances past the carbon-ion Bragg peak depth.

Ionizing radiation can induce DNA damage either by indirect or direct action. Indirect action occurs through the production of reactive oxygen species (ROS) via the radiolysis of water, with hydroxyl radical ions being the most consequential. Direct action occurs via the direct ionization of secondary molecules to induce the DNA damage. Low-LET radiation induced DNA damage is known to be mostly contributed to the indirect action of ionizing radiation. On the other hand, high-LET radiation induced DNA damage is known to be mostly through the direct action of ionizing radiation. Although, the radiolysis of water with high-LET radiation results in higher radical concentrations within its dense ionization tracks. This leads to more radial-radical reactions and results in the formation of more bimolecular products, such as hydrogen peroxide ($H_2O_2$) and molecular oxygen ($O_2$). This presents a unique opportunity to enhance the indirect action contribution of high-LET radiation, further increasing the DNA damage it induces by exploiting this increase in the bimolecular products.

As DSBs are known to be the main actor behind radiation-induced cell death, the faithful repair of the radiation-induced DSBs is essential to the cell's survival. In mammalian cells, the main DSB repair pathways are non-homologous end joining (NHEJ) and homologous recombination (HR). While NHEJ has been identified as the main DSB repair pathway for low-LET radiation, the debate behind which of the DSB repair pathways are most important for high-LET radiation-induced DSBs is still ongoing. Studies on how the HR and NHEJ pathways contribute to the repair of carbon-ion radiation induced DSBs are essential in our understanding

of the responses of cancers to this type of radiotherapy as well as important for developing molecularly targeted radiosensitizing therapies to incorporate during treatment to enhance the effectiveness of CIRT to eradicate the target tumor cells.

Purpose: This present study was designed to investigate the biological effects at different depths within the full carbon-ion beam range in a single biological system as well as introducing methods to enhance the cell killing ability of the high-LET carbon-ion beam. Specifically, we investigated the DSB distribution throughout the full carbon-ion beam range, how the DSB repair pathway choice may change at different depths within the full carbon-ion beam range as well as introducing a method for enhancing its cell killing ability through exploiting the bimolecular products increased following the high-LET radiolysis of water.

As the international interest for CIRT continues to grow, it is important to not only identify the accuracy in which the carbon-ion beam deposits its dosages but also enhance the efficiency in which it can induce cell death. Doing so will provide fundamental knowledge into its depth-dose distribution to aid in more accurately targeting the tumor tissue while minimizing the damage to the surrounding healthy tissues, thereby reducing potential unwanted adverse effects as well as increasing its ability to eradicate the tumor. Collectively, this will help provide essential evidence into the benefits of this type of therapy to further outweigh its high cost and aid in the wide-spread development of CIRT facilities.

Methods: Utilizing our novel method of horizontal irradiation of Chinese hamster ovary (CHO) cell line in a large (T-175) cell culture flask allowed for the incorporation of the full monoenergetic and spread-out Bragg peak 290 MeV/n carbon-ion beam ranges in a single biological system. This method of irradiation made it possible to address changes in the survival fractions via the cell survival assay as well as the DSB distribution using γ-H2AX as a surrogate

marker for DSBs via the γ-H2AX assay at increasing depths within the full monoenergetic carbon-ion beam range. Visualization of the γ-H2AX foci allowed for us to not only observe how the DSB distribution increased as the carbon-ion beam approaches the Bragg peak but also allowed for us to differentiate between the high-LET regions within the carbon-ion beam range as these regions demonstrated the high-LET characteristic track structures. Furthermore, we were able to differentiate between the high-LET characteristic track structures induced by the lighter- or heavier-fragmentation ions within the post-Bragg peak regions.

This method of irradiation was also used to identify the most important DSB repair pathways at different depths within the full carbon-ion SOBP beam range. We accomplished this by addressing the differences in survival fractions of several cell lines via the cell survival assay and compared the radiosensitivity between DSB repair mutant cell lines, V3 and 51D1, which are deficient in NHEJ and HR, respectively, at each depth within the full carbon-ion SOBP beam range.

In addition, in an *in-vitro* study, we also addressed whether the addition of the transition metals, $Cu^{2+}$ or $Co^{2+}$, in solution with DNA increased the indirect action contribution of DNA damage with high-LET radiation to exploit the increase in the bimolecular product formation of $H_2O_2$. The reasoning behind this is due to the reaction of $H_2O_2$ with a transition metal, such as $Cu^{2+}$, it should produce higher levels of the more damaging hydroxyl radical ions through the Fenton-type reaction. We addressed the increase in DNA damage by irradiating DNA in solution with $Cu^{2+}$ or $Co^{2+}$ with ionizing radiation sources increasing in their LET values, such as X-ray, carbon-ion or iron-ion beams, respectively, as well as with increasing chemical concentrations of DNA damaging agents, such as $H_2O_2$ and the radiomimetic chemical bleomycin. DNA damage was then assessed by gel electrophoresis followed by band intensity analysis.

Results: Following monoenergetic 290 MeV/n carbon-ion beam irradiation, the depth with the lowest survival fraction via the cell survival assay was identified at the depth of 140 mm, regardless of initial treatment dosage, which we defined as our biological Bragg peak depth. We also observed that the number, cluster size and intensity of the γ-H2AX foci increased the closer the beam approached to its peak depth at 142 mm, with a significant increase being within the depths from 140 – 142 mm. Thus, we defined this range as our biological foci Bragg peak range (FBPR). Results of this experiment also demonstrated that the high-LET characteristic track structures were apparent between 115 mm to our last evaluated depth at 155 mm, with a peak number of tracks/cell at 140 mm. However, the density of the tracks within each track positive cell increased to a peak at 142 mm. In the post-FBPR (143 – 155 mm), there were clear differences in the track structures of the track positive cells within the same depths. This allowed us to differentiate the track structures that were possibly the result of the lighter- or heavier-fragmentation ions by the track structure density.

Following 290 MeV/n carbon-ion SOBP beam irradiation, we observed the lowest survival fractions within the depths of 8.0 – 14.0 cm, thus we defined this range as the biological SOBP. Our results also demonstrated that both NHEJ- and HR-deficient cells (V3 and 51D1, respectively) portrayed an increase in radiosensitivity as compared to wild type cells (CHO 10B2) throughout the full carbon-ion SOBP beam range. In addition, NHEJ-deficient cell line, V3, had the highest sensitization enhancement ratio throughout the SOBP. Although, V3 cells also demonstrated the greatest increase in radiosensitivity in the depths from beam entrance up to the proximal depth of the SOBP and demonstrated a dose-dependent increase in survival fractions throughout the SOBP. On the other hand, HR-deficient cell line, 51D1, had the greatest ratio of the survival fraction at entrance depth to the lowest survival fraction within each of the

SOBP regions (proximal, mid, and distal), meaning the sensitization effect for this cell line was higher within the SOBP in respect to the surrounding regions.

The addition of the transition metals, $Cu^{2+}$ and $Co^{2+}$, in solution with DNA demonstrated an increase in both DSBs and single-strand breaks (SSBs) under all irradiation conditions and chemical treatments. DNA in solution with the metals demonstrated the most DNA damage when treated with $H_2O_2$ followed by irradiation with low-LET (X-ray), high-LET carbon-ion and high-LET iron-ion, respectively, and demonstrated the least damage when in solution with bleomycin. $Cu^{2+}$ was also observed to induce greater DNA damage than $Co^{2+}$ under all experimental conditions.

Conclusions: Comparison of the γ-H2AX foci results with the cell survival results following monoenergetic carbon-ion beam irradiation suggests that cell death from high-LET radiation is more correlated with the density of the DSBs within the track structures rather than only their presence. In addition, investigation into the post-Bragg peak track structures suggests that the lighter fragmentation ions can travel further distances then the heavier ions. Cell survival results utilizing DSB repair mutant cell lines, V3 and 51D1, suggest that the most beneficial pathway to inhibit in order to enhance the cell killing effect of CIRT in the targeted cells within the SOBP pathway while limiting the damage to the surrounding cells is the HR DSB repair pathway. Metals in solution with DNA demonstrated to cause more DNA damage than DNA in solution alone and was observed to be LET dependent for SSB formation but inversely dependent for DSB formation. In addition, these results suggest that treatment with $Cu^{2+}$ would be more effective than $Co^{2+}$ at increasing the indirect action of DNA damage with high-LET radiation.

Future Directions: Utilizing the results obtained in this study will provide fundamental insight to build upon in future studies to help further identify not only the most important DSB repair pathway involved in repairing the carbon-ion radiation-induced DSBs in human cell lines but also identify the specific factors within each pathway that may be most essential to inhibit. In addition, we will further investigate the post-Bragg peak carbon-ion nuclear fragmentations by examining the extent of their mutational capabilities.

# ACKNOWLEDGEMENTS

I would like to thank my advisor Dr. Takamitsu Kato whose kindness and guidance has had a tremendous impact on my development as a researcher and as a person. His genuine passion for research as well as providing me with the opportunity to travel across the world has heightened my desire to further pursue research as a profession. Dr. Kato goes far beyond expectations as an advisor and our time together has led me to consider him as a dear friend.

I would also like to thank my committee members Dr. Aaron Sholders, Dr. Marie Legare and Dr. Del Leary. Dr. Sholders is not only a great professor but a great person as well who has always been there for me. Ever since my time during my undergraduate studies he has been one of my favorite professors and it has been a true blessing to be able to get to know him even more over these past years. Dr. Legare is one of the kindness and caring individuals I have ever met. No matter the situation she always has made the time to help. Her support has helped me through some of the toughest times during my PhD and I wish the best for her in all her future endeavors. Dr. Leary has gone far above and beyond in helping me with designing my experiments. This work would not have been possible without his help and words cannot express my appreciation towards him. I look forward to our continued collaboration throughout my future research.

I would like to also thank everyone who made this research possible. I would like to thank JAXA for funding my travels and research in Japan. A special thank you to Dr. Fujimori at NIRS for allowing us to use his laboratory while in Japan and always being more than willing to lend a helping hand.

TABLE OF CONTENTS

LIST OF TABLES

LIST OF FIGURES

# CHAPTER ONE

# BACKGROUND

## 1.1 Introduction

Cancer has become the leading cause of death in high income countries, such as the United States and remains the second leading cause of death globally behind cardiovascular disease (CVD) [1, 2]. Although, over the past 4 decades the risk for death with CVD has declined more steeply than with cancer. It has been predicted that if this trend continues that cancer will overcome CVD to become the leading cause of death worldwide in the following years [3]. While improvements in earlier detection of many cancer types has greatly improved our ability to reduce cancer mortality, further advancements in cancer therapies are needed to more effectively treat cancer patients.

The three main cancer treatment modalities are surgery, chemotherapy and radiotherapy [4]. With the varying types, sizes, and location of differing cancers, each modality may best be used alone or in conjunction with the others [5]. Of these, radiotherapy has become one of the most effective treatment modalities utilized for a wide variety of cancer types. Technological advancements in ionizing radiation over the past few decades has also greatly reduced the cost of undergoing radiotherapy and has improved the accuracy at which the dose can be distributed to the tumor. This has allowed for a more precise deposition of dose into the target tumor, while reducing damage in the normal surrounding tissue [6].

## 1.2 Three Main Cancer Treatment Modalities

The first main cancer treatment modality is surgery. It is the most direct approach for removing a clearly localized tumor, to diagnose a cancer type, or can even be used to address the extent of which the cancer has spread [7]. However, this modality has several negative factors associated with it as it is a highly invasive form of treatment and is typically the less preferred option when dealing with tumors close in proximity to delicate organs, such as the brain. In addition, surgery may also result in permanent disfigurement of the patient as well as be dangerous to elderly patients, as the recovery time may be too strenuous for these individuals. Furthermore, treating cancers with surgery alone has a high risk of recurrence and tumor cells may also invade into other tissues [5].

Chemotherapy is another commonly used cancer treatment modality. This utilizes a wide range of cytotoxic drugs to stop or slow the growth of cancerous cells. However, they also inevitably cause damages to the normal healthy tissue surrounding the tumor creating a wide range of unwanted side-effects. This is because these chemotherapeutic agents target cells with high levels of proliferation and regeneration. Thus, both tumor cells and non-tumor rapidly proliferating cells can be affected by such agents which results in a high level of toxicity [8, 9].

One such side-effect of chemotherapy involves inflammation, as it is a key factor behind gastrointestinal toxicity of chemotherapy with the most common gastrointestinal abnormality being chronic liver damage [10]. Different chemotherapeutic agents are known to activate a diverse range of pro-inflammatory pathways which result in distinct histopathological changes in the small intestine and colonic mucosa [11]. In addition, results from an examination of the side-effects in 99 chemotherapy patients demonstrated that 54% of the patients endured 15 of the most severe symptoms involving non-physical side-effects and a majority of the patients suffered

from the major physical side-effects, such as vomiting, nausea and hair loss [12]. Cardiac side-effects of chemotherapies are another major area of concern as cardiovascular and/or coronary artery disease may arise following this type of treatment, particularly in older patients [13, 14]. Therefore, the use of chemotherapy must rely on weighing the benefits of the anti-tumor effects vs the harmful side-effects of this type of treatment modality.

The third cancer treatment modality is Radiotherapy which is the most notable and expanding modality available today. When it comes to cancer treatment at least 50% of all cancer patients undergo some form of radiation therapy and it contributes towards 40% of the curative treatments for cancer [15, 16]. This modality has also been very successfully used for treating solid cancers that would otherwise be difficult to remove via an invasive surgical procedure that may not fully eradicate malignant tumors, such as in the head and neck [17, 18].

The most important physical quantity in radiotherapy is the dose that is deposited into the tissue, defined by the term absorbed dose. The absorbed dose is measured in terms of Gray units (Gy), as the mean energy deposited by ionizing radiation in a mass element [19]. The fundamental principle behind radiotherapy is to deliver a precise dose of radiation, to the target tumor tissue while minimizing the radiation dosage/damage to the surrounding healthy tissue, thus limiting potential unwanted side-effects [20]. This principle plays an important role when treating bone tumors, particularly chordomas, as they are highly responsive to carbon-ion radiotherapy and allows for the maximum preservation of the adjacent organs as well as their functions, which would be very difficult to accomplish via an invasive surgery. Radiotherapy can also be used either before surgery (neoadjuvant therapy) to shrink the tumor, or it can be utilized after surgery (adjuvant therapy) to destroy any remaining tumor cells [15].

The disadvantage to radiotherapy is that it selectively targets tumors which means it may not be capable to treat cancers that have spread to many places within the body, i.e., metastasized. In addition, a possible rare long-term complication from treatment with either chemotherapy or radiation involves a possible therapy-induced secondary malignancy [21]. This is a serious concern in adult patients being treated for Hodgkin's lymphoma as they have the highest reported risk of developing these secondary cancers [10, 22].

### 1.3 General Radiobiology

The main goal behind radiotherapy is to deprive cancer cells of their reproductive potential, i.e. stopping their ability to divide and grow [23]. X-rays and particle beams, such as carbon-ion or iron-ion beams, are a form of ionizing radiation meaning they have enough energy to detach electrons, i.e. ionize the atomic structure of the substances they pass through [24]. Radiotherapy utilizes this ionizing radiation (IR) to induce all known types of DNA (Deoxyribonucleic acid molecule) lesions including single-stranded DNA breaks (SSBs), double-stranded DNA breaks (DSBs), chemically altered base lesions, interstrand crosslinks, intrastrand crosslinks, or their combinations [25-27]. Base lesions and SSBs are repaired with the base excision repair (BER) pathway that is known to be a fast and simple repair process. On the other hand, DSBs are repaired by multiple different repair pathways, including homologous recombination (HR), nonhomologous end-joining (NHEJ), microhomology-mediated end-joining (MMEJ) which is also known as alternative non-homologous end-joining (alt-NHEJ), and single-strand annealing (SSA). However, it has been suggested that the SSA and MMEJ pathways in mammalian cells are a backup to the NHEJ process [28]. Moreover, both NHEJ and MMEJ DSB repair pathways are error prone and typically lead to a limited loss of genetic information which results in short deletions at the DSB site that can induce genetic mutations [29].

Among these DNA damages, DSBs are considered the major actor responsible for radiation-induced cell death [30]. A DSB occurs when there is a break in the phosphodiester backbone of both strands of the DNA that are separated by around 10 base pairs or less [31]. Moreover, the yield of DSBs is known to increase linearly with the radiation dose [32]. A DSB can either be one-ended or two-ended. Two-ended DSBs typically form when both strands of linear double-strand DNA (dsDNA) are broken simultaneously or as previously mentioned, when two SSBs form within immediate proximity to each other. When the DSB is created by two SSBs that are in close proximity to each other, the broken end contains a short stretch of overhanging single-strand DNA (ssDNA). Depending on the mechanism of DSB formation, the DNA ends can be either chemically "clean" or "dirty." The clean DNA breaks, apart from the broken phosphodiester backbone, contain normal DNA chemistry. On the other hand, the dirty DNA ends contain additional adducts including anything from a small chemical group to covalently attached proteins [33]. This is important as ionizing radiation-induced DSBs are typically considered to be dirty DNA breaks [34].

Radiosensitivity is governed by the amount of DNA damage resulting from exposure and the cells abilities to repair the DNA damage is a key aspect of radiation-induced genetic damage. Therefore, it is important to not only predict the level of DSBs which arise following a given IR dose, but also to understand their repair mechanisms. In mammalian cells, induction of DSBs initiates the DNA damage response (DDR) pathway involving damage recognition, information transfer, cell cycle regulation via checkpoints and the inactivation of appropriate repair systems [35, 36]. The two main DSB repair pathways in mammalian cells following ionizing radiation are known to be non-homologous end joining (NHEJ) and homologous recombination (HR), the latter of which is only active in S and G2-phases of the cell cycle [37]. Although, while HR

provides for greater repair fidelity than NHEJ, NHEJ is the major pathway to repair prompt DSBs throughout all phases of the cell cycle [38]. Each of these pathways is discussed in further detail in the following sections.

When radiation-induced DNA damage is extensive and cell-cycle check-point functions are impaired, as often found in tumor cells, unrepaired or improperly repaired DSBs can pass through these check points and can result in significant chromosomal aberrations during the mitotic phase of the cell cycle [39, 40]. As a result, cells possessing DNA damage can be effectively observed by chromosomal aberrations as an indicator of radiation exposure, as these correlate well with radiation-induced cell death [41]. However, it is important for the radiation damage to be extensive enough to effectively kill the cells. This is because if the DSBs are improperly repaired, they may lead to genomic instability leading to cancer [42]. Thus, is it also important to address the actual extent of the DNA damage for a more valid indicator of the radiation exposure.

As DNA damage is a critically component of radiation, proper DNA repair is important for the cell's survival. Cancer cells are often defective in certain aspects of DNA repair, but these cells can possess backup pathways for accomplishing the DNA repair. Although, cancer cells are not as efficient at repairing the DNA damage, even with these backup pathways, resulting in their cell death [6]. In contrast to rapidly proliferating cancer cells, normal cells do not proliferate as quickly, which allows them to repair the damage before their replication.

This is important as radiotherapy does not kill cancer cells right away. It may take hours or even weeks of treatment before cancer cells begin to die. It may also take weeks to months for all the cancer cells in a tumor to be effectively killed off following treatment [15]. Radiation-induced cell death is mainly through apoptosis (programmed cell death) or mitotic catastrophe,

also known as mitotic cell death [43]. Mitotic catastrophe is a type of cell death that occurs during or after aberrant mitosis caused by the missegregation of chromosomes. This results in the formation of giant cells possessing multiple nuclei, otherwise known as micronuclei [44]. For solid tumors, which radiotherapy is highly effective in treating, cell death occurs predominantly resulting from aberrant mitotic events resulting in mitotic catastrophe [45].

### 1.3.1 The R's of Radiobiology

The success or failure of radiotherapy is in part determined by the R's of radiobiology. These include the repair of DNA damage, redistribution (reassortment) of cells in the cell cycle, repopulation, reoxygenation of hypoxic tumor areas, and the intrinsic radiosensitivity of the cells. For these reasons, radiations are typically given in multiple low dose fractions to aid in the sensitization of the tumor cells while helping to minimize the damage to the surrounding normal healthy cells. In the fractionated dose delivery approach, the total dose of the radiation is divided into several daily doses. In conventional fractionation radiotherapy, this involves delivering multiple dosages of around 1.8 – 2.0 Gy per fraction. The dose and number of fractions per day is adjusted as required for the tumor volume and/or location [46].

Repair is one of the primary reasons to fractionate radiotherapy. This is because there are three main types of damage that ionizing radiation can cause to cells. These involve lethal damage (LD), irreversible and irreparable which inevitably results in cells death; potentially lethal damage (PLD), this can be modified by post irradiation environmental conditions; and sublethal damage (SLD) where under normal circumstances the damage can be repaired unless additional sublethal damage is added [47]. The cell killing ability of ionizing radiation revolves around the ability for it to cause unrepairable lesions involving DSBs. However, most of the radiation-induced DNA damage is sublethal and is repaired at lower dosages. On the other hand,

higher dosages result in accumulation of SLD which also contributes to lethality. Repair of the SLD between radiation fractions is exploited in radiotherapy. This is because the ability to repair radiation damage often differs between the normal tissue and tumor tissue. In addition, fractionation allows for the repair in slowly proliferating, late-responding tissues at the expense of tumors that are less able to repair the SLD [46].

Redistribution is important to sensitize the tumor cells by allowing for cell-cycle progression into radiotherapy-sensitive phases. Radiosensitivity of cells varies considerably as they pass through the cell cycle with S-phase being the most resistant and late G2/M phases being the most sensitive to ionizing radiation [48]. Because of the cell cycle progression of surviving cells between the radiation fractions, dose fractionation allows for the reassortment of the S-phase radioresistant tumor cells into the more sensitive phases of the cell cycle. In addition, this allows for a therapeutic benefit for the slowly cycling normal healthy cells [49].

Repopulation of tumor cells tends to contribute largely for the failure of conventional fractionated radiation therapy. The reasoning behind this is postulated to be the result of tumors having an accelerated repopulation creating a situation in which the regrowth rate of the tumor following radiation treatment with a sublethal radiation dose exceeds the growth rate of the untreated tumor [50, 51].

Reoxygenation between dose fractions helps to improve the efficacy of radiation treatment by increasing the tumor radiosensitivity. Oxygen is known to be one of the most potent modifiers of radiation sensitivity [52]. In addition, hypoxic tumor cells have been shown to be 2 – 3 times more resistant to radiation [53]. In this situation, fractionation helps the efficiency of radiotherapy as it allows for the cells that were resistant, because they were hypoxic, to be reoxygenated, therefore, allowing them to be more sensitive at the time of the subsequent dose.

### 1.3.2 The Bystander Effect

Ionizing radiation-induced DNA damage is not only associated with the directly exposed cells but can also cause damage in the neighboring non-irradiated cells. This is known as the radiation-induced bystander effect (RIBE) (Figure 1.1) [54]. This happens as the ionizing radiation exposed living cells, dead cells and dying cells can release several complex reactive signaling factors into the surrounding microenvironment that can affect the bystander (neighboring) cells, such as reactive oxygen species (ROS), transforming growth factor β1(TGF-β1), interleukin-8 (IL-8) and nitric oxide (NO) [55, 56]. These signaling factors can also be introduced to the bystander cells through gap junctional intercellular communication (GJIC). These gap junctional channels are known to play an essential role in the RIBE by modulating the release of the radiation-induced signaling factors [57].

These signaling factors are important as they can go on to stimulate a series of responses in the neighboring cellular organelles including the endoplasmic reticulum and mitochondria which release calcium-ions and cytochrome-c, respectively, which further triggers DNA damage and repair in the bystander cells [58]. The fate of the DNA damage repair to the bystander cells can result in either their survival, genomic instability or cell death. Furthermore, it has been demonstrated that not only the DNA repair capacity, but also the linear energy transfer (LET) of radiation has been involved in the DNA damage induced in both irradiated and non-irradiated bystander cells [58].

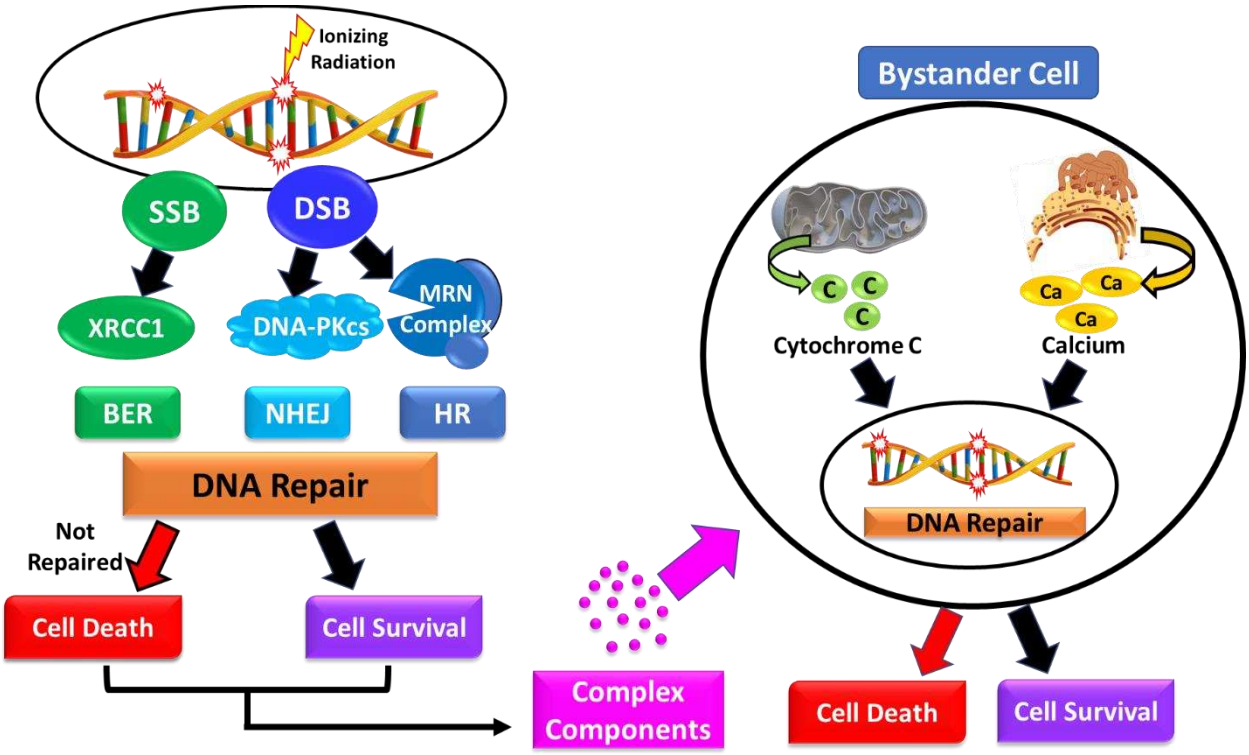


**Figure 1.1. Schematic representation of the radiation-induced bystander effect (RIBE).** Both living, dead and dying cells can release complex reactive factors into the surrounding microenvironment that can affect the bystander cells. These signaling factors can stimulated responses of these bystander cells in their cellular organelles, including their mitochondria and endoplasmic reticulum which release cytochrome c and calcium-ions, respectively. This further triggers DNA damage and repair. The ultimate fate of the bystander cells may be cell survival, death or genomic instability.

## 1.4 Linear Energy Transfer (LET) and Radiation Quality

Linear energy transfer (LET) involves the rate at which a charged particle deposits its energy along its path, and is equivalent to the energy loss *dE/dx* which is usually measured in keV/μm [59]. The LET of a particle is primarily determined by its charge and its speed. This rate is also known to increase as the mass of the particle increases [60]. Thus, the ionizing radiation quality can be classified as either low-LET (sparsely ionizing) or high-LET (densely ionizing). Protons and photons (X- or gamma-rays) are clinically considered as low-LET radiations, while carbon-ions and Fe-ions are considered as high-LET radiations [61].

Low-LET photons have a broad distribution of dose within the tissue peaking relatively near the surface. In contrast, heavier charged particles, such as carbon-ions, can be either lower-

or higher-LET, depending on their speed as they traverse through the medium. For these charged particle radiations, the entrance regions in the tissue will have lower LET values due to their high speeds, with increasing LET values at lower kinetic energies as the particles come to rest in the deeper regions [61]. This is important as the biological effects differs between the types of radiation qualities as the particles traversing the tissues within the lower LET portion in the beam range are less damaging than the higher-LET portion of the beam that is strategically placed into the tumor region.

In the process of cell inactivation, high-LET irradiation has demonstrated to be far more effective than low-LET radiation [62, 63]. The reasoning behind this is likely due to the complexity of DNA damage associated with each radiation quality. While low-LET radiations, such as X-rays, can induce DSBs with associated base damage or SSBs, they rarely induce closely localized DSBs. On the other hand, high-LET radiations, such as carbon-ions or Fe-ions, deposit their energy in densely ionized tracks within the cells they traverse. This results in DSBs occurring in very close proximity to each other, ie. DSBs occurring within a few helical turns of the DNA. These high-LET induced DSBs are known to be very difficult for the cell to repair and often result in their death [30, 64, 65]. In addition, there are many other fallbacks to using low-LET radiations which decrease their ability in efficiently treating tumors that high-LET radiations do not possess which will be further discussed in the later sections.

Of the various types of charged particles used in radiotherapy, protons and carbon-ions have been most widely utilized. In comparison to photon beams, charged particle beams demonstrate higher cure rates with less complications [66, 67]. This is attributed to their precision of dose deliverance, thus limiting the dose given to normal tissues adjacent to the tumor. However, protons and heavier ions being much more massive than electrons, require

bigger and more costly accelerators (cyclotrons) to produce enough kinetic energy to treat deeply-seated tumors [68]. As a result, the equipment required for production of charged particle radiation is far more expensive than that for photons. Although, with technological advancements reducing the price of cyclotrons, it is likely to result in a wider use of charged particle therapy in the future [69].

Furthermore, the therapeutic value, i.e. the killing of tumor cells, of charged particle therapy is in part defined through their relative biological effectiveness (RBE). The concept of RBE was developed to compare the efficacy of different radiation types. Thus, the RBE is the ratio of a given dose of charged particles at a specific depth passing through air, water, or a biological tissue relative to the dose of x-rays or gamma rays required/known to produce an equal biological effect (usually 250 kVp X-rays or Co-60 gamma rays) [41]. In other words, it is the ratio of doses to reach the same level of effect when comparing two radiation modalities [70]. Generally, the heavier the particle is the larger RBE value it will have, i.e. a carbon-ion will have a larger RBE value than a proton, which in turn has a larger value than a photon [71].

## 1.5 Concept of the Bragg Peak

Unlike X-ray or gamma ray radiotherapy which utilizes massless photons, protons and carbon-ions used in particle radiotherapy are a form of electrically charged particles known as ions. When compared to photon beams, charged particle radiotherapy offers superior dose distribution which allows for more precisely targeting the tumor cells which may be deeply seated within the body [68].

This is due to the fact that when charged particles penetrate matter, they immediately start transferring their kinetic energy into the medium in which they traverse, as previously mentioned, the amount of energy being transferred is known as the LET [72]. The LET increases

as the particle slows down until it depletes all its kinetic energy and comes to rest. As a result, a characteristic depth vs dose curve is produced with relatively low dose being distributed at beam entrance which abruptly increases to a peak as the particle comes to a stop. Following this peak, the imparted dose dramatically falls [73].

The depth at which this drastic deposition of energy in a well-defined range and where most of the particle beam's energy is deposited along the beam path is known as the "Bragg peak," which typically found at the end of the beams range (Figure 1.2). This was named after the Nobel prize-winning British physicist William H. Bragg [74]. Moreover, the narrow region of the Bragg peak where a significant amount of energy from a particle beam is deposited into the tissue, is the point at which LET is at its highest value. This is very important in radiotherapy as ion beam's ability to form a Bragg peak provides for sparing a greater volume of normal tissue as compared to conventional photon radiotherapy as a result of their charge and increased mass.

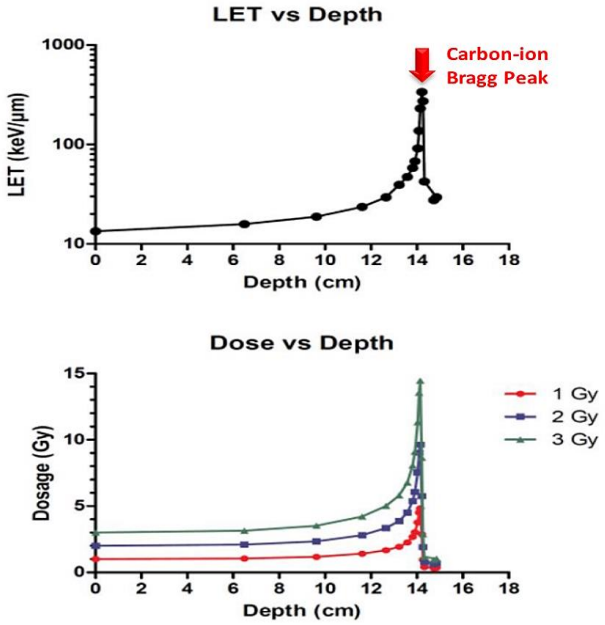


**Figure 1.2. Identification of the carbon-ion Bragg peak.** LET (keV/µm) (**Top**) and dose (Gy) (**Bottom**) distribution throughout the full range of the 290 MeV/n carbon-ion monoenergetic beam with indicated Bragg peak location. Radiation physics quantitative values of dose and LET per depth were kindly provided from HIMAC staff at NIRS.

## 1.6 The Spread-out Bragg Peak (SOBP)

In charged particle radiotherapy, such as with carbon-ion and proton beams, the Bragg peak can be manipulated to incorporate the entire tumor volume. This allows for the maximum dose of radiation to be delivered to all the malignant cells. This is done by the beam delivery technique known as the spread-out Bragg peak (SOBP) [71].

The SOBP technique takes advantage of the fact that charged particles can be magnetically steered rather than physically collimated as with conventional X-rays. Therefore, the narrow beam of charged particles can be deflected in the lateral direction and the tumor can be painted with the planned radiation dose. This technique also takes advantage of the fact that the initial kinetic energy and particle charge influences the depth of the penetrations with more energetic particles capable of penetrating deeper, and larger charged particles penetrating less deep with the same initial kinetic energy. Thus, by utilizing beams of particle(s) with different initial kinetic energies, i.e., using the same particle with different initial energies, a region of uniform dose in the beam direction can be created to cover the tumor in the longitudinal spread. By combining these two advantages, it allows for clinicians to utilize the SOBP technique to cover a tri-dimensional tumor with radiation doses while being able to minimize the amount of dose delivered to the surrounding normal healthy tissue [75].

When designing the SOBP for the clinical carbon-ion beam used in carbon-ion radiotherapy (CIRT), three factors must be considered which are the physical dose (Gy), RBE and dose in $Gy_{(RBE)}$ which is known as the biological dose. The biological dose is defined as the product of the physical dose and the RBE. At the national institute of radiological sciences (NIRS) for CIRT the biological dose has been defined as the product of the physical dose and the RBE of the radiation at 10% surviving fraction for human salivary gland (HSG) tumor cells [76, 77]. The

biological response flatness along the SOBP was confirmed by measuring the physical dose and dose-averaged LET, along with the biological cell survival experiments throughout the SOBP [78].

In order to achieve a uniformed biological dose $Gy_{(RBE)}$ across the SOBP, the physical dose (Gy) is decreased as the RBE rises. However, another important factor to consider in the design of the SOBP is the LET. The reason for this is that the RBE for most cell and tissue systems is known to increase with the LET over the carbon-ion beam's LET range. However, for a specified LET of a defined charged particle beam, the RBE values may vary widely between different cell lines with major changes in the LET and RBE values occurring predominately in the terminal 10 mm of the particles range [73]. Moreover, when using the SOBP in the beam delivery, the dose at a given position is overlapped by the different depth-dose distributions resulting from the varying incident energy. Thus, the LET generated by each monochromatic carbon-ion beam energy cannot be used when calculating the RBE, leading to the concept of dose-averaged LET to be used in this calculation [77, 79]. At a given position of x in the SOBP, the dose ($D_{SOBP}(x)$) and the dose-averaged LET ($LET_{SOBP}(x)$) can be calculated by the following equations:

$$\boldsymbol{Dose_{SOBP}(x) = \sum_{j} \omega_j d_j(x)}$$

$$\boldsymbol{LET_{SOBP}(x) = \frac{\sum_j LET_j(x)\omega_j d_j(x)}{D_{SOBP}(x)}}$$

In which $d_j(x)$, $w_j(x)$ and $LET_j(x)$ represent the dose profile, weighting factor and the LET value from the $j^{th}$ incident beam energy at the position x within the SOBP.

## 1.7 Direct and Indirect Actions of Radiation

Ionizing radiation can act either directly or indirectly to induce DNA damages (Figure 1.3). Direct action involves the direct energy transfer from the radiation to the DNA molecule, which can lead to either its excitation or ionization and cleaving their chemical bonds [80]. For radiation to act indirectly, the incident radiation ionizes the surrounding water molecules to produce reactive oxygen species (ROS), such as hydroxyl radicals, causing DNA damage in a processes termed "water radiolysis" [81]. For low-LET gamma irradiation the water radiolysis of cellular water rapidly generates ROS of hydroxyl radicals ($^{\bullet}OH$) and ionized water ($H_2O^+$) as well as hydrogen radicals ($H^{\bullet}$) and hydrated electrons ($e_{eq}^-$). Within one picosecond ($10^{-12}$s), superoxide ($O_2^{\bullet-}$) and hydrogen peroxide ($H_2O_2$) are formed as secondary ROS products of IR [82].

For both high- and low-LET radiations, a significant portion of the ionizing radiation-induced DNA damage is contributed to the radiolysis of water and the generation of ROS, although this contribution is known to be greater with low-LET radiations. With indirect action these ROS diffuse through the aqueous environment and chemically damage the DNA. Although, indirect damage is not only unique to radiation, as the hydroxyl attack from the radiolysis of water is identical to that of spontaneously occurring biological events [83].

The presence of molecular oxygen is required for the maximum ROS-related damage. This is important as it may limit the effectiveness of radiotherapy to treat hypoxic tumor cells. Quantifying the effect of oxygen is done through the oxygen enhancement ratio (OER) which seeks to assess the amount of dose necessary to result in an equivalent biological endpoint with or without the presence of oxygen [84]. For low-LET photons and protons, the OER is typically estimated at around 3, meaning that cell killing is roughly 3-fold greater in normoxic vs anoxic

conditions. Although, for high-LET radiations, such as carbon-ion and other heavy ions, the estimated OER varies with LET and can range from 1.0 – 2.5 depending on the ion charge and LET [85]. Thus, high-LET radiations can more effectively kill cells in the hypoxic cores of tumors as compared to low-LET radiations.

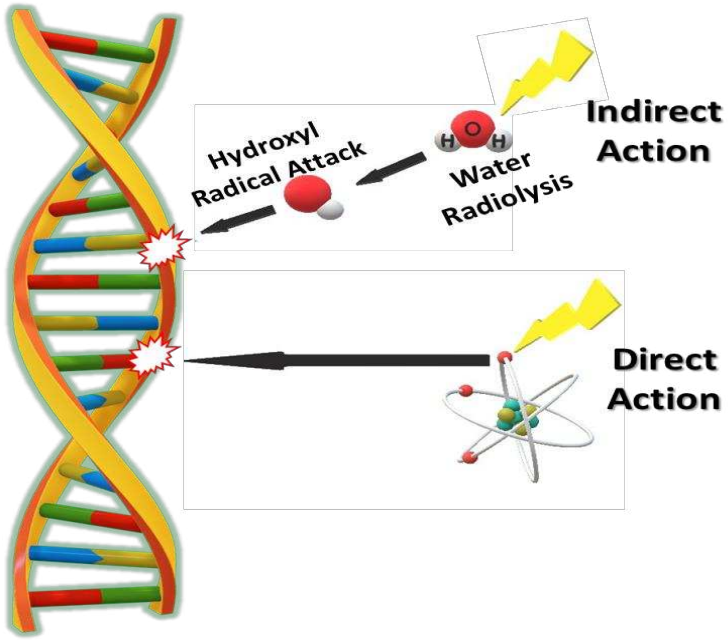


**Figure 1.3. Indirect and Direct actions of ionizing radiation DNA damage.** Indirect action involves the ionization of the surrounding water molecules within the cell to produce reactive oxygen species, the most consequential being hydroxyl radical ions in a process known as water radiolysis. Low-LET ionizing radiation is known to work mostly through this indirect action. Direct action involves the ionization of secondary electrons that directly interact with the DNA molecule to induce its damage. High-LET ionizing radiation DNA damage is known to be mostly contributed to this direct action.

X-rays are known as low-LET radiation and are sparsely ionizing, meaning ionizations by X-rays are sparsely produced in a large targeted volume, and over a wide range (Figure 1.4A) [80]. A large amount (around 2/3) of low-LET-induced DNA damage is believed to be contributed to this indirect action, as the amount of DNA damage within cells has been observed to decrease in the presence of increasing concentrations of the hydroxyl radical scavenger dimethyl sulfoxide (DMSO) [86]. Moreover, prior research conducted by J.F. Ward, et al. has suggested that the indirect action of cell killing is not due to individual hydroxyl free radicals produced from the

ionizing radiation's radiolysis of water but is due to the interaction of volumes of high radical density with DNA to cause locally multiply damaged sites (LMDS)[87].

On the other hand, for direct damage to occur with X-ray radiation the photon must directly "hit" the DNA molecule [88]. In contrast to low-LET radiations, high-LET radiations, such as carbon-ion or Fe-ion beams, are known to be densely ionizing as they dissipate their energy rapidly, producing very short and dense tracks of ionization (Figure 1.4B) [80]. Prior studies have demonstrated that there is an increase in direct action contribution for high-LET-induced DNA damage as the particulate can cause direct damage through electromagnetic interactions with the DNA molecule [89, 90]. Furthermore, as LET increases, more energy is deposited in short tracks, as it is densely ionizing, and the radical concentrations from the radiolysis of water are higher. This leads to more radial-radical reactions occurring and resulting in the formation of more bimolecular products, such as hydrogen peroxide ($H_2O_2$) and molecular oxygen ($O_2$) [91, 92]. This has been demonstrated in prior Monte Carlo simulations by J. Meesungnoen et al. in which they suggested that high-LET radiolysis of liquid water produced an excess of *in situ* molecular oxygen which was not observed with lower-LET radiations [93].

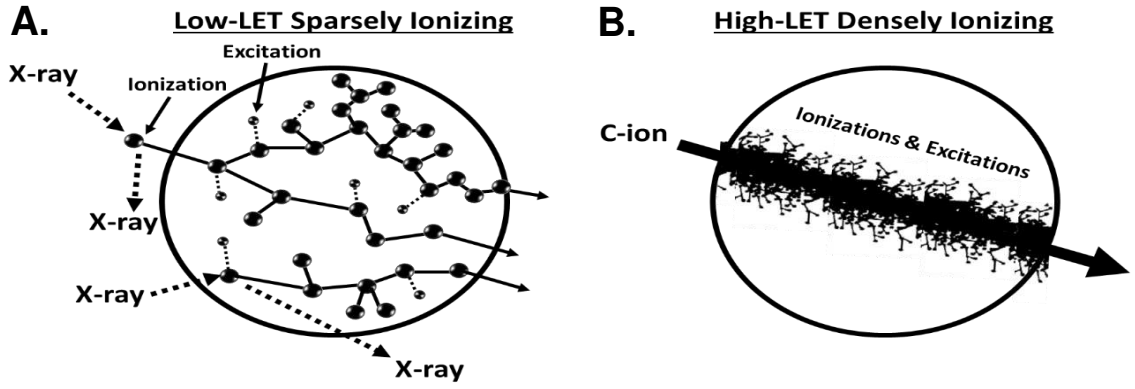


**Figure 1.4. Ionization density by radiation quality. (A)** Low-LET ionizing radiation, such as X-rays or gamma-rays, is sparsely ionizing in which the X-ray induced ionizations are sparsely produced over a large target volume and over a wide range. The ionization with excitation is due to Compton scattering or the photoelectric effect, depending on the photon energy. **(B)** High-LET ionizing radiation, such as carbon-ions, is densely ionizing meaning these particles deposit their energy in rapidly in very short and dense tracks of ionization.

## 1.8 Complexity of DNA Damage from Low- and High-LET Radiations

Radiation quality (low- or high-LET) mainly affects the complexity of the DSB and the complexity of the DSB increases with LET. Ionizing radiation will induce a fraction of the DNA damage sites with two or more DNA lesions formed within one or two helical turns of the DNA. When these sites are induced by a single radiation track, they are known as clustered damage or multiple damage sites (MDS) and also include DSBs [88]. Clustered damage sites are a signature of ionizing radiation in contrast with isolated, endogenously induced lesions, which tend to be homogeneously distributed. The two basic groups of complex DNA damage are DSBs and non-DSBs (Figure 1.5). The non-DSBs clusters can be a mixture of damaged bases and SSBs that are found in close proximity to each other [94]. On the other hand, prior studies have suggested that the clustered damage that includes DSBs are most likely due to the energy depositions of at least two to five ionizations localized within 1 – 4 nm [95]. Moreover, the complexity and yield of radiation-induced clustered DNA damage is known to increase with increasing ionizing density (higher LET) of the radiation [81, 96].

For low-LET sparsely ionizing radiation, it is considered that about 70% of the deposited energy induces isolated lesions, increasing the oxidative stress on the cell and about 30% of the deposited energy induces the clustered damage sites [97, 98]. On the other hand, for high-LET densely ionizing radiation, it is considered that about 90% of its deposited energy induces these clustered damage sites including DSBs. This is because unlike low-LET radiations, such as X-rays, that deposit their energy uniformly over tissue, high-LET radiations, such as carbon-ions, deposit significant amounts of energy along the traversal path constituting a characteristic track structure [99]. Thus, the distribution of dose from the high-LET particles creates large clusters of ionization events along the particle track, resulting in much more complex DNA damage which

can lead to more consequential biological effects when compared to low-LET radiation [75, 100]. This has been demonstrated in a prior study that observed as the LET of the radiation increased so did the complexity of the clusters, which reflected the number of lesions that were present [101]. In addition, it has also been shown that the clustered damage sites including DSBs have a reduced reparability when compared to individual lesions [102, 103]. This is believed to be due to the spatial distribution of the lesions when they are formed in clusters, which also contributes to more effectively killing the tumor cells as a result of the difficulty that the cell has in repairing these clustered lesions.

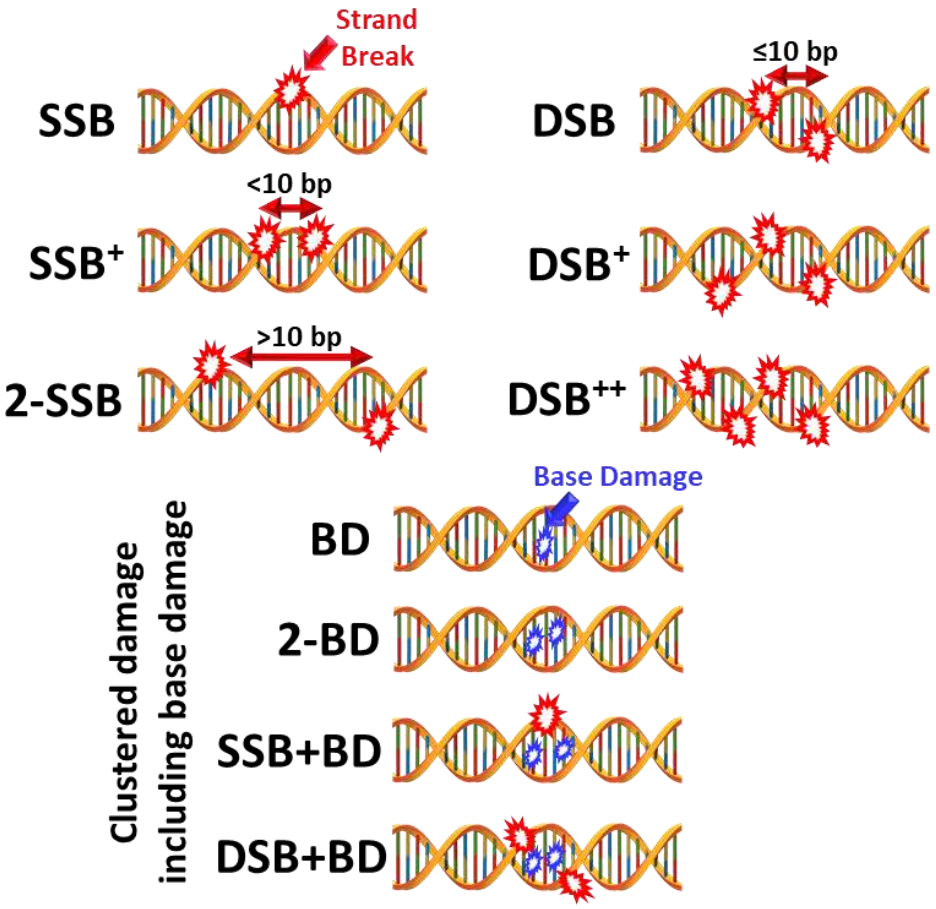


**Figure 1.5. Model of DNA damage induced by low- and/or high-LET radiation qualities.** If two SSBs are more than 10bp apart, it is denoted by 2-SSB. If two SSBs are within 10bp apart but on the same strand of DNA, it is denoted by $SSB^{+}$. If two SSBs are on opposite strands within 10bp of each other, it will be considered a DSB. Forms of complex DSBs are denoted as $DSB^{+}$ and $DSB^{++}$ with increasing DSB complexity, respectively. Non-DSBs include an SSB, $SSB^{+}$, 2-SSB, and SSB+BD.

## 1.9 Radiation-induced DNA Damage Response (DDR) and DSB Repair Pathways

The first response to radiation-induced DNA damage is cell signaling (intracellular and extracellular) in order to signal for DNA damage repair mechanisms. If the damage remains unrepaired, the cells can activate either cell-cycle arrest or cell-death processes in order to avoid possible mutations. However, if repaired incorrectly, the cell may be able to survive but the incorrect repair may result in a mutation that can lead to cancer [104]. Therefore, the DNA damage repair process is the key component of the cellular response to radiation. It has been demonstrated that the clustered DNA damage is known to be more difficult for the cellular machinery to repair than the individual damage sites and post-irradiation unrepaired cluster DNA lesions may generate additional DSBs [105-107]. In addition, the slow repair component that is LET-dependent is mainly due to the complex-type of DSB and the difficulty of repairing the high-LET particle-induced DSBs is attributed to the nature of the clustered DNA damage that is induced by the dense ionizations along the high-LET particle track [101]. Therefore, the identification, quantification and detection of clustered DNA damage as well as how cells process these types of damage is critical for understanding the biological effects of ionizing radiation on humans. To further understand the consequences of ionizing radiation exposure, it is important to evaluate the initial damage that is induced, determine the rates and repair pathways that are utilized as well as quantify the levels of the damage that remains after the cellular repair processes have completed.

Current advancements in immunostaining approaches and identification of essential components in each type of the DNA repair mechanisms have allowed us the opportunity to further address these radiation-induced DNA damage responses. These approaches have allowed us to visualize the recruitment and retention of DNA repair and their associated response proteins

at the sites of DNA breaks by fluorescence imaging of the ionizing radiation-induced foci (IRIF) [94]. Evaluation of these IRIF is important as it allows for the verification of the certain types of DNA lesions that are induced by each type of ionizing radiation quality as well as the spatial distribution of the different types of DNA lesions within the clustered DNA damage which enables us to address the complexity of the DNA damage that is induced.

SSBs can be visualized by immunostaining with antibodies against X-ray repair cross complementing 1 (XRCC1). XRCC1 is important as it acts as a scaffolding protein for other repair factors and physically interacts with several enzymes involved in SSB repair [108]. Therefore, XRCC1 can be used as a surrogate marker to identify the sites of SSBs within the clustered DNA lesions and can be used to evaluate the kinetics of the SSB repair. Base damage can also be visualized by immunostaining with antibodies against 8-oxoguanine DNA glycosylase (OGG1). OGG1 is important as it is the major DNA glycosylase responsible for the removal of 8-OxoG base lesions in DNA in mammalian cells [109]. Thus, the surrogate marker for base damages can be OGG1 and can be used to address the amounts of base damage within the clustered DNA lesions as well as predict the kinetics of the base damage repair.

As previously mentioned, the most consequential ionizing radiation-induced DNA lesions are DSBs. Therefore, the cell's ability or inability to efficiently repair these DSBs is essential to the fate of the cell's survival. As a result, addressing the DNA damage response proteins associated with DSBs is important in the evaluation of the biological effects resulting from the ionizing radiation induced DSBs. The two main DSB repair pathways in mammalian cells are homologous recombination (HR) and non-homologous end joining [94]. Each of these pathways is further discussed in mechanistic detail in the following sections and the pathway that is preferentially utilized with each radiation quality is further discussed in Chapter 4.

Surrogate markers for DSBs are γ-H2AX, phosphorylated DNA-dependent protein kinase (DNA-PK) and p53 binding protein 1 (53BP1). Each of these surrogate DSB markers can also be used to address the amounts of DSBs within the clustered DNA lesions and the DSB repair kinetics. A hallmark of DSB recognition and repair is the immediate phosphorylation of the histone H2AX by ATM or ATR at the sites of DSBs. The phosphorylated form of histone H2AX is known as γ-H2AX [110]. In addition, phosphorylated DNA-PK also localizes precisely at DSBs [111]. 53BP1 is a DNA damage response protein that responds to DSBs which forms discrete nuclear foci following ionizing radiation exposure and co-localizes with γ-H2AX and DNA-PK [112]. While indirect immunostaining with antibodies against γ-H2AX is the gold standard for identification of DSBs, direct live cell imaging of DSBs can be visualized by green fluorescent protein tagged DNA-PK (GFP-DNA-PK) and yellow fluorescent protein tagged 53BP1 (YFP-53BP1). Direct live cell imaging of the DSBs provides an additional advantage in more precisely estimating the amount of the DSBs induced by ionizing radiation and further insight into their initiation, repair kinetics and possible repair pathway choice.

### 1.9.1 Homologous Recombination (HR)

Homologous recombination (HR) DSB repair pathway requires a homologous sequence as a template for repair in order to remove the DSBs and faithfully restore the DNA sequence in their vicinity [113, 114]. HR repair pathway uses the sister chromatid as the template which results in gene conversion and is suggested to be a mostly error-free pathway that preferentially operates in the late S-phase [115]. Furthermore, since HR requires the sister chromatid as a donor for homologous sequence, it is limited to be only active in the S and G2 phases of the cell cycle and is thought to be actively suppressed in G1 cells in order to prevent loss of heterozygosity (LOH) [114, 116-118]. In the following sections the HR DSB repair pathway is

divided into its early steps and late steps. Furthermore, in a broad sense, the recombination processes can be further divided into synthesis-depended strand annealing (SDSA), canonical DNA double-strand break repair (DSBR), single-strand annealing (SSA), and break-induced replication (BIR) [113].

Depending on whether the flanking sequences of recombining DNA molecules are exchanged or not, the recombination can lead to either crossover or non-crossover recombination products. A crossover event is defined as when the distal arm of the broken DNA is swapped with the distal arm of the template DNA molecule. When crossovers occur between two homologous loci of the sister chromatids, there is an equal exchange between the sister chromatids. In this situation the crossover is mutagenically silent. However, crossovers that occur between two non-homologous loci of sister chromatids, such as repetitive sequences, gives rise to unequal sister chromatid exchanges. Similarly, when crossovers occurring between non-sister (homologous) chromosomes also leads to gross genome rearrangements. Another situation that can occur is when genetic information from one DNA molecule gets unidirectionally transferred into another DNA molecule, which is known as a gene conversion. Gene conversions can occur when a DNA sequence is copied from a donor template to the broken DNA molecule which can happen during DSBR, SSA, or BIR [33]. Mutagenic gene conversions are dangerous as they can give rise to a loss of heterozygosity (LOH), which is a key driver for tumorigenesis [119].

#### 1.9.1.1 HR – Early Steps

The necessary requirement for the initiation of HR is DNA end-restriction. In this step a long single-stranded 3'-DNA overhang is formed in order to start the search for homology (Figure 1.6) [120]. This is accomplished through a variety of factors including the MRN complex (MRE11-RAD50-NBS1), the C-terminal interacting protein 1 (CtIP), Exonuclease 1 (EXO1),

DNA2, and the Bloom's syndrome helicase (BLM). In the first step of this process to execute their function during HR initiation, the MRN complex is recruited to the DSB site, where it binds and cooperates with CtIP to promote end-resection [121, 122].

The MRN complex is comprised of the Rad50 proteins, meiotic recombination protein 11 (MRE11), and the Nijmegen breakage syndrome 1 (NBS1). Rad50 is comprised of three domains; the zinc hook domain, the coiled-coil domain that is comprised of two alpha-helices, and the head domain containing the amino terminus and carboxylic acid terminus. In the formation of the MRN complex, the dimerization of two Rad50 proteins initiates the binding of two MRE11 (MRE11/Mre11) proteins with one bound to each of the head domains of the Rad50 proteins [123]. Following the binding of the MRE11/Mre11 proteins, a single NBS-1 protein then binds to the MRE11/Mre11 proteins, thus forming the complete MRN complex. Each free end of the DNA in the DSB will then be bound by its own MRN complex [124].

The MRN complex is important as it allows for the detection of the DSB in order to initiate the HR DSB repair pathway. It does this through NBS-1 activation of the serine-threonine kinase enzyme, Ataxia telangiectasia mutated (ATM) [125]. It has been proposed that the dimerization of two ATM enzymes allows for one of the ATM enzymes within the dimer to bind to NBS-1. This leads to the activation of the ATM enzymes within the dimer through autophosphorylation on a Ser-1981 residue of the ATM enzyme that is directly attached to the NBS-1 protein which allows for the ATM enzyme to phosphorylate the serine residues of other proteins [126]. Following the autophosphorylation of the ATM enzymes, the ATM enzyme not directly attached to NBS-1 detaches and the remaining ATM enzyme directly attached to NBS-1 phosphorylates the histone H2AX on Ser-139 [127]. While there are several of the P13k-like kinases that may be able to perform this function, including ATM, ATR, and DNA-PK, it is

ATM that has emerged as the master kinase for both the direct phosphorylation of H2AX and many other phosphorylation events that are required for the protein complexes at sites of DNA damage, particularly in response to ionizing radiation [128]. Phosphorylated H2AX leads to it undergoing a conformational change and is now known as γ-H2AX. Furthermore, this active ATM enzyme can phosphorylate many other H2AX histones on Ser-139, resulting in an amplification of the signal for γ-H2AX to recruit many other proteins and enzymes involved in the DSB repair [129].

An important enzyme recruited by γ-H2AX is checkpoint kinase 2 enzyme (ChK2). When ChK2 binds to γ-H2AX it becomes active and recruits the p53 protein. Prior to the recruitment of p53, it is inactivated by being bound to mdm2 which binds to the transactivation domain of p53. For p53 to become active, ATM phosphorylates Ser-395 of mdm2 and Ser-15 of the p53 transactivation domain and Chk2 further phosphorylates the p53 transactivation domain on Ser-20. These phosphorylation's allow for the dissociation of mdm2 on p53, which activates p53. Active p53 proteins then form a tetramer and promote the increased expression of genes involved in the DSB repair machinery which upregulates the number of these proteins involved in the DSB repair process [112].

Following this process, end-resection is initiated in HR by the binding of CtIP to NBS-1 of the MRN complex [121]. Each MRN complex then moves away from the DSB site by around 100–200 base pairs (bps). The MRN complex then undergoes a conformational change which allows for MRE11 to make an endonuclease cut on the DNA strand which contains its 5'-broken end facing into the DSB site [130]. Following the endonuclease cut, the MRN complex then moves back towards the DSB site where MRE11 preforms 3' to 5'-exonuclease activity to remove all the nucleotides of the same DNA strand that it made its endonuclease cut, creating a

3’-ssDNA overhang of around 100–200 bps within the DSB site. Next, other 5’ to 3’-exonuclease enzymes, such as EXO1 or DNA2, will then further remove the nucleotides on the MRE11 endonuclease cut DNA strand to produce a long 3’-ssDNA overhang of around 1000 bps [131]. It is thought that this end-resection defines the point of no-return in the decision to process the DSB lesion by the HR repair pathway and thus the formation of the long ssDNA overhang regions are frequently used as a surrogate for ongoing HR [132].

Following the formation of this long ssDNA overhang, replication protein A (RPA) binds to the long ssDNA overhang. RPA is a heterotrimeric complex which is comprised of RPA70, RPA32, and RPA14 and exhibits high affinity for binding to ssDNA regions. RPA is then replaced by RAD51 recombinase, forming a RAD51 nucleoprotein filament on the DNA. However, mediator proteins are required for the replacement of RPA by RAD51. Such mediator proteins involved in this process are Breast cancer susceptibility gene 2 (BRCA2) and a group of five RAD51 paralogs (RAD51B, RAD51C, RAD51D, XRCC2 and XRCC3) [120]. Interestingly, high-levels of expression of RAD51 have also been observed in a wide variety of human malignancies, as it is a key factor in the HR repair pathway [133].

Upon formation of the RAD51 coated ssDNA, the stability of this nucleoprotein filament is very important for the further execution of the HR repair pathway. Thus, the RAD51 nucleoprotein filament can be negatively regulated when HR is disadvantageous. One such way for this to happen is when the PARI protein is together with a RECQL5 helicase. When the PARI protein and RECQL5 helicase are together, they act as a negative regulator of RAD51 filament formation. Another way to interfere with the RAD51 filament stability is by the “anti-recombinase” proteins BLM and RTEL1. These proteins have a negative impact on the already formed RAD51 filament and facilitates its dissociation [134]. Furthermore, CDK-mediated

regulation of HR involves the phosphorylation of Ser-3291 of BRCA2, which counteracts the interaction with RAD51 and thus can also negatively regulate the activity of the HR repair pathway [135].

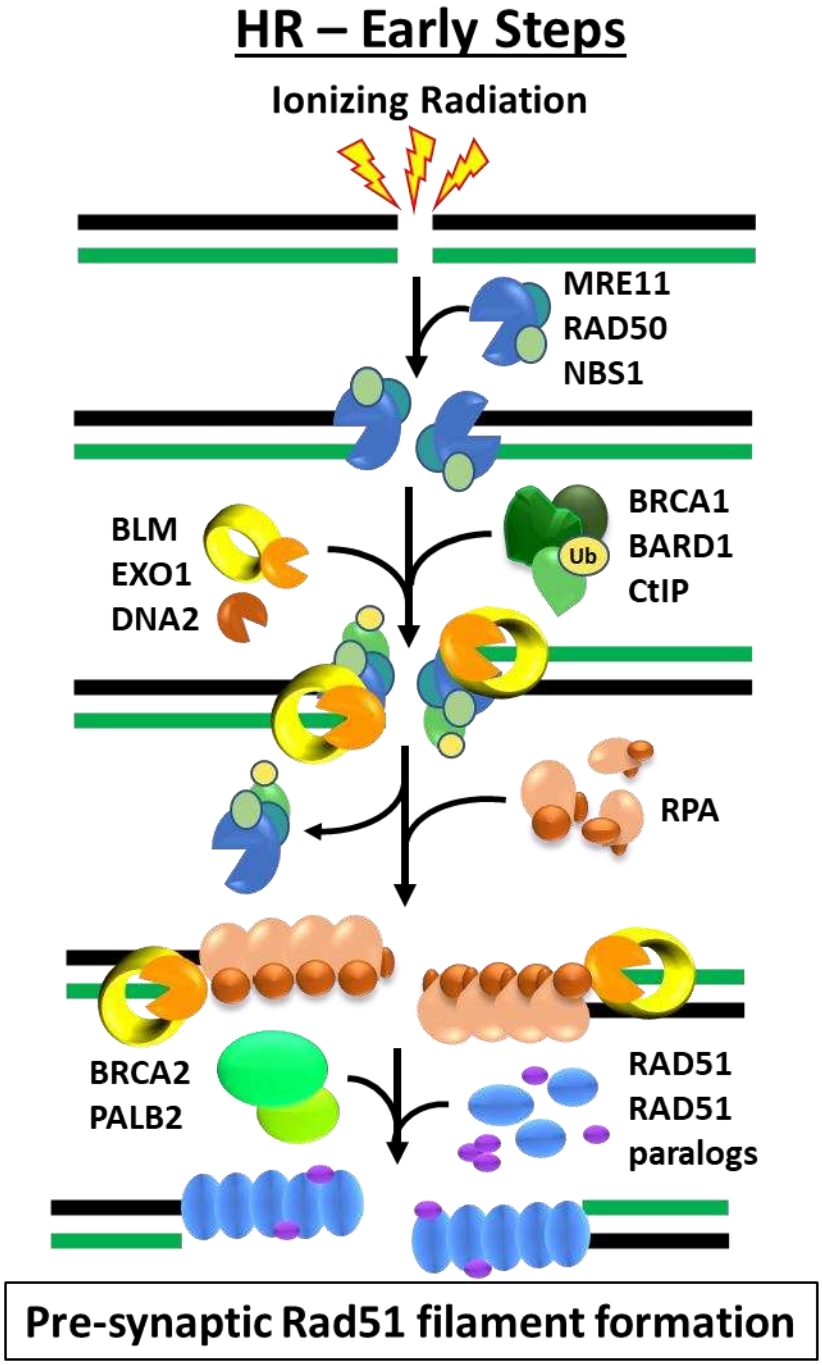


**Figure 1.6. Early Steps in HR.** The initial events leading to the formation of pre-synaptic RAD51 nucleoprotein filament (see text for more details).

#### 1.9.1.2 HR – Late Steps

As mentioned previously, the RAD51 nucleoprotein filament is very important for the HR DSB repair pathway to progress. The RAD51 nucleoprotein filament functions to invade the intact dsDNA molecule in order to search for homologous sequences and forms a structure that is known as the displacement loop (D-loop). Once homology is found (synapsis), the DNA will then start elongating the 3'-end of the invading strand. In order for the elongation process to commence, RAD51 must be removed in the synaptic complex from the very 3'-tip of the invading DNA strand to reveal the 3'-OH group for priming which is facilitated by RAD54 and RAD54B [136]. Following this point, HR can be completed by one of two sub-pathways known as synthesis-dependent strand annealing (SDSA) or canonical DSB repair (DSBR) (Figure 1.7) [113]. The stability of the D-loop is known to determine which of these two pathways HR will undergo [33].

In SDSA, the joint molecule intermediate is destabilized (D-loop is disrupted), and the nascent DNA is annealed to the other end of the broken DNA molecule. In this sub-pathway, the elongation of the invading 3'-end can continue over a limited distance, followed by the displacement of the newly synthesized stretch and re-ligation with the original DNA end resulting in the repair of the DSB. This process is the most frequent event during HR repair in higher eukaryotic cells and is equivalent to gene conversion. Furthermore, SDSA is one of the least mutagenic recombination sub-pathways as it results in a non-crossover repair product, i.e. gene conversion [33].

On the other hand, in DSBR, second end-capture can occur, and the D-loop is stabilized which becomes a substrate for annealing with the second resected DSB end. Following second end capture, DNA synthesis and ligation gives rise to a central intermediate of the DSBR sub-pathway with the formation of a double Holliday junction (dHJ) [137]. Because both DNA

molecules are physically linked at the junction points the Holliday junctions need to be processed prior to the separation of both DNA molecules. If these Holliday junctions are not processed it may lead to defects in chromosome segregation and can be one of the mechanisms responsible for genome instability [138]. Depending on the resolution of the dHJ by specialized resolving enzymes, GEN1 and MUS81/EME1, this will result in either crossover or non-crossover (gene-conversion) outcomes [139, 140].

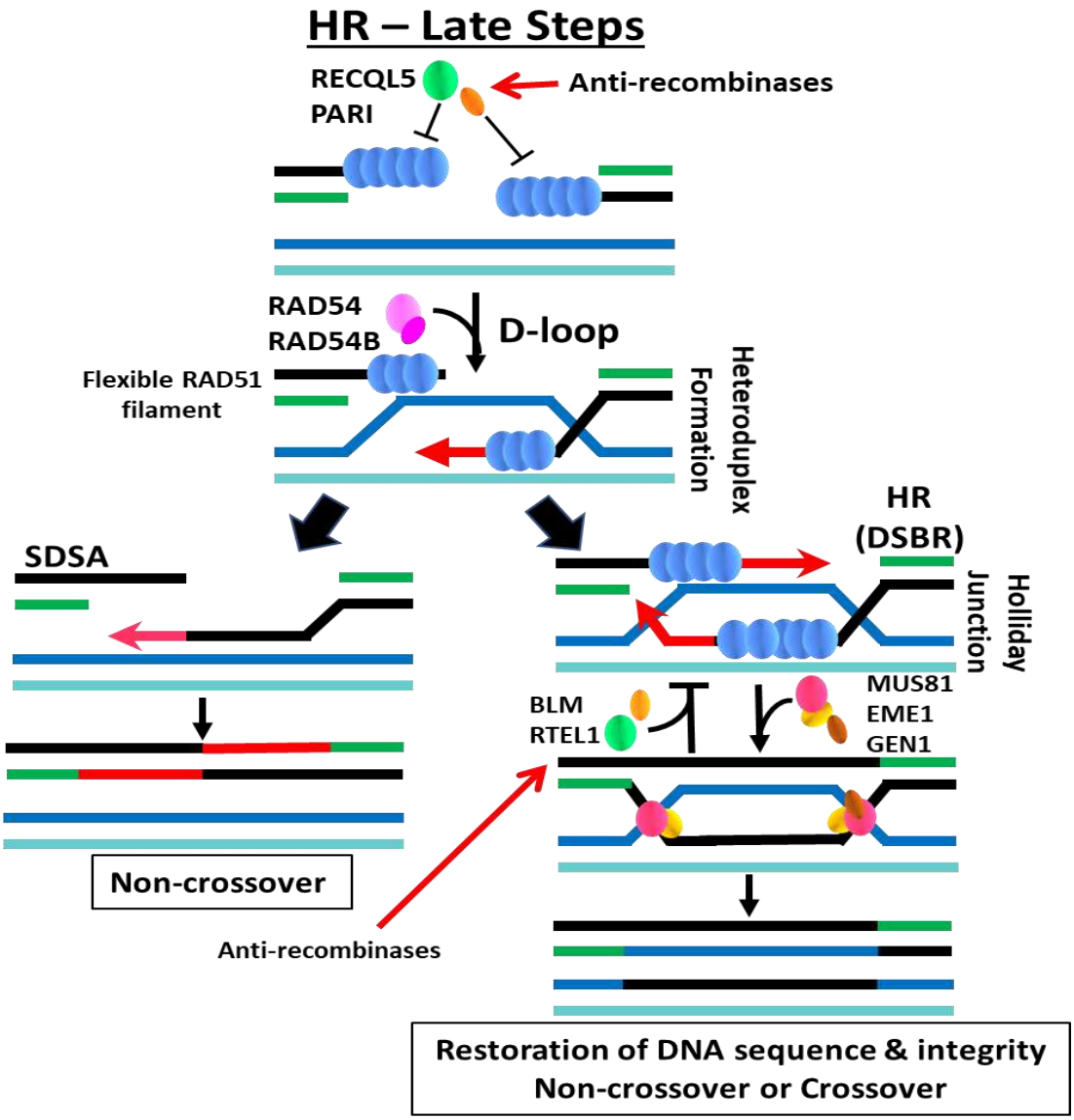


**Figure 1.7. Late steps in HR.** The formation of the D-loop structure and the two sub-pathways, SDSA and DSBR (see text for more details).

#### 1.9.1.3 Single-Strand Annealing (SSA)

The single-strand annealing (SSA) process involves DNA end resection to reveal repetitive DNA sequences, which are then subsequently annealed. The resulting DNA ends that essentially "stick out" are cleaved and the strands are ligated. Thus, SSA is a very mutagenic repair process as it leads to the deletion of the DNA sequence between the homologous regions. SSA is restricted in its use and is only used in situations when two repeats flank the break site and can restore the integrity of the DSBs within repetitive DNA sequences. Conceptually, SSA is similar to MMEJ, further discussed below. However, SSA is typically grouped with the recombination pathways due to its enzyme requirements. Moreover, SSA differs from MMEJ as it requires extensive DNA end restriction. Although, the extent of SSA in repairing ionizing radiation induced DSBs remains uncharacterized but its use is likely to be small [141].

#### 1.9.1.4 Break-Induced Replication (BIR)

The break-induced replication (BIR) pathway is used to repair one sided DSBs. In BIR, DNA synthesis proceeds all the way to the end of the template DNA. Thus, BIR copies the sequence of the entire chromosome arm. The genetic result of BIR is a nonreciprocal crossover. For this reason, BIR is a unique pathway for repairing one-ended DSBs that result from collapsed DNA replication forks. Moreover, BIR is characterized by the initiation of replication through the formation of a replication fork that replicates the entire chromosome past the DSB, which can cause extensive LOH [142, 143]. BIR can also allow for telomer lengthening in the absence of telomerase [144].

### 1.9.2 Nonhomologous End-Joining (NHEJ)

In contrast to HR, NHEJ involves direct ligation of two DSB ends with little to no sequence homology required. Thus, this process is quick and does not require a repair template, such as the

sister chromatid, so it is not limited to any phase of the cell cycle and NHEJ is known to be the primary pathway of DSB repair in G1-/early S-phase cells [115]. However, NHEJ typically leads to loss of genetic information which results in short deletions at the site of the DSB. Because NHEJ does not require a template, if multiple DSBs are present, ligation of the incorrect ends can also generate large deletions or chromosomal rearrangements [29]. Furthermore, NHEJ can only repair two-ended DSBs and abnormal structures, i.e., "dirty" ends, at the DSB site may inhibit this DSB repair process. Therefore, NHEJ represents a fast but potentially mutagenic DSB repair process. In addition, NHEJ can be subdivided into two pathways of DNA-PKcs dependent nonhomologous end-joining (D-NHEJ) and microhomology-mediated end-joining (MMEJ) [145].

#### 1.9.2.1 DNA-PKcs Dependent Nonhomologous End-Joining (D-NHEJ)

D-NHEJ catalyzes a simple rejoining reaction between two DNA ends that is irrespective of their origin and does not require homology at the free DNA ends (Figure 1.8) [38]. It is for this reasoning that NHEJ is operational through the cell-cycle. This process is initiated by the binding of the KU heterodimer to the DNA ends. The KU heterodimer is comprised of two subunits, KU70 and KU80. When these subunits come together, they are perfectly designed to bind to the free DNA ends. It is the high affinity of the KU heterodimer for the free DNA ends that makes it the perfect initiation factor for the D-NHEJ DSB repair pathway [146]. In addition, the binding of the KU heterodimer blocks nucleolytic processing of the DNA ends that is required in order to initiate other forms of DSB repair pathways, such as HR. Importantly, the KU heterodimer is essential in recruiting the catalytic subunit of the DNA-PKcs to form an active DNA-PK holoenzyme and when this holoenzyme is bound to DNA it results in almost a 10-fold increase in the DNA-PKcs kinase activity [147].

The binding and dimerization of DNA-PKcs is responsible for the immobilization of the two DNA ends and therefore facilitates the rejoining reaction [148]. The prerequisite for its dissociation from the DNA damaged sites and the recruitment of other repair factors is the phosphorylation of the DNA-PKcs at multiple residues, which is dependent on the nature of the DNA lesions. Furthermore, due to ionizing radiation-induced DSBs containing damaged nucleotides at their ends ("dirty" ends), DNA-PK activation aids in recruiting multiple proteins that are involved in the limited DNA end-processing which is required to generate the ligatable DNA ends such as, Artemis, DNA polymerase μ (pol μ), DNA polymerase λ (pol λ) and TDK. However, this end-processing can result in sequence changes at the junctions generated by D-NHEJ which makes mutations very likely. In addition, translocations and other chromosomal rearrangements, which are the hallmarks of genomic instability, can also be induced due to indiscriminately rejoining the DNA ends in the D-NHEJ repair pathway.

The final step in D-NHEJ is ligation. This is mediated exclusively through the ligation complex LIG4/XRCC4 which consists of DNA Ligase 4 (LIG4) and the X-ray cross complementing 4 protein (XRCC4). This ligation complex is assisted by the auxiliary factor XLF (Cernunnos) in order to mediate the ligation. This results in a quick and efficient restoration of DNA integrity but often comes at the cost of DNA sequence information loss [132].

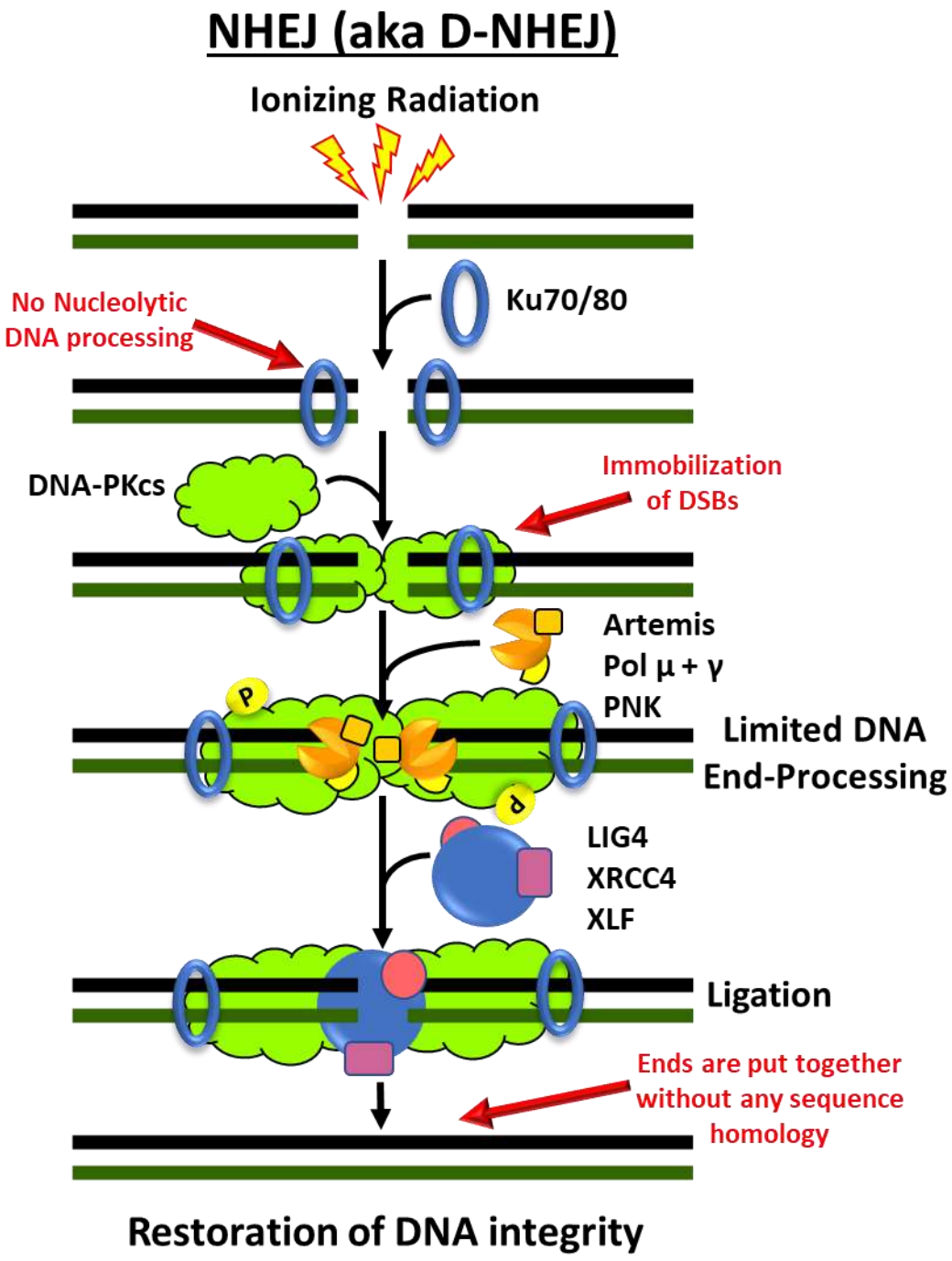


**Figure 1.8. Schematic representation of DSB repair by DNA-PKcs dependent non-homologous end joining (D-NHEJ).** D-NHEJ DSB repair process is initiated by the binding of the KU heterodimer to the DNA ends within the DSB site which then recruits DNA-PKcs to form an active DNA-PK holoenzyme. DNA-PK activation aids in the recruitment proteins involved in the limited DNA end-processing that is required to generate the ligatable DNA ends. Then the LIG4/XRCC4 complex exclusively mediates the ligation and is assisted by the ligation mediator XLF. At the end of this DSB repair process the DNA integrity at the site of the DSB is restored but the DNA sequence at the junction may be altered.

#### 1.9.2.2 Microhomology-Mediated End-Joining (MMEJ)

As with D-NHEJ, the microhomology-mediated end-joining (MMEJ) DSB repair pathway is incapable of restoring the DNA sequence information at the site of the DSB (Figure 1.9). In addition, it is also active in all phases of the cell-cycle, but MMEJ activity is significantly increased during S and G2 phases. Although, unlike D-NHEJ, the MMEJ pathway is yet to be fully characterized and has been considered a backup pathway for D-NHEJ [28, 149]. In addition, MMEJ occurs independently of the key D-NHEJ factors and usually involves short stretches of microhomology (2 – 20 nt) between the two broken DNA ends in order to mediate the DSB repair, hence the reasoning behind this pathways name [150]. MMEJ is also a much slower process than D-NHEJ and has a higher probability to join unrelated DNA ends. Therefore, it is highly error-prone with a high probability to cause translocations and other genomic rearrangements. Furthermore, MMEJ-derived mutations have appeared to be associated with cancer development and may support tumor progression. This is particularly observed when D-NHEJ or HR DSB repair pathways are found to be compromised [151]. Thus, the activation of MMEJ may contribute to the evolution of cancer and may be a potential target in specialized cancer therapies.

An important protein that is implicated in MMEJ is poly (ADP-ribose) polymerase 1 (PARP-1). PARP-1 plays a main role in the repair of SSBs, and it has been demonstrated that it can effectively compete with the KU heterodimer for DNA end-binding [152]. Prior studies have demonstrated that PARP-1 facilitates the repair of DSBs by MMEJ and is strongly suppressed by poly (ADP-ribose) polymerase 2 (PARP-2) [153]. In contrast to D-NHEJ, MMEJ benefits from microhomology at the DNA break sites, which is best found when the DNA ends become resected. The DNA end-resection in MMEJ is facilitated by the MRN complex (MRE11-

RAD50-NBS1) and CtIP. Interestingly, both of these are also involved in DNA end-resecting during HR [154]. As previously mentioned, MMEJ activity is significantly increased during S- and G2-phases, which is probably due to the increased activity of these DNA end-resection enzymes in these cell-cycle phases. Thus, it may be possible that MMEJ may also be a backup to HR in G2- and S-phases.

Ligation of MMEJ is mediated by DNA Ligase III (LIG3) [155]. Moreover, it has also been demonstrated that DNA Ligase I (LIG1) is known to contribute to this ligation process as well [155]. LIG 3 is known to ensure the ligation of both DNA strands during the DSB repair. Interestingly, when LIG3 is in complex with XRCC1 it also participates in the repair of SSBs and DNA base damages, meaning that XRCC1 may also be implemented in MMEJ. However, the role of XRCC1 in LIG 3 function during MMEJ is not clear [156, 157].

Regulatory proteins have also been implicated in the MMEJ pathway. In chronic myelogenous leukemia (CML), in which several of the D-NHEJ activities are suppressed, both LIG3 and the Werner syndrome helicase (WRN) were found to be upregulated. Under these conditions it was reported that WRN and LIG3 form a stable complex that is recruited to the DSB sites, therefore, activating the ligation process [158]. Histone H1 is another factor implicated in MMEJ, which stimulates the rejoining activity of LIG3 possibly by facilitation the synapsing of DNA molecules [159]. The extent of the MMEJ pathway in the repair of radiation induced DSBs is still unknown but as it shares many factors with other DNA damage repair pathways further investigation into MMEJ is important as it may reveal fundamental aspects behind the biological effects of ionizing radiation.

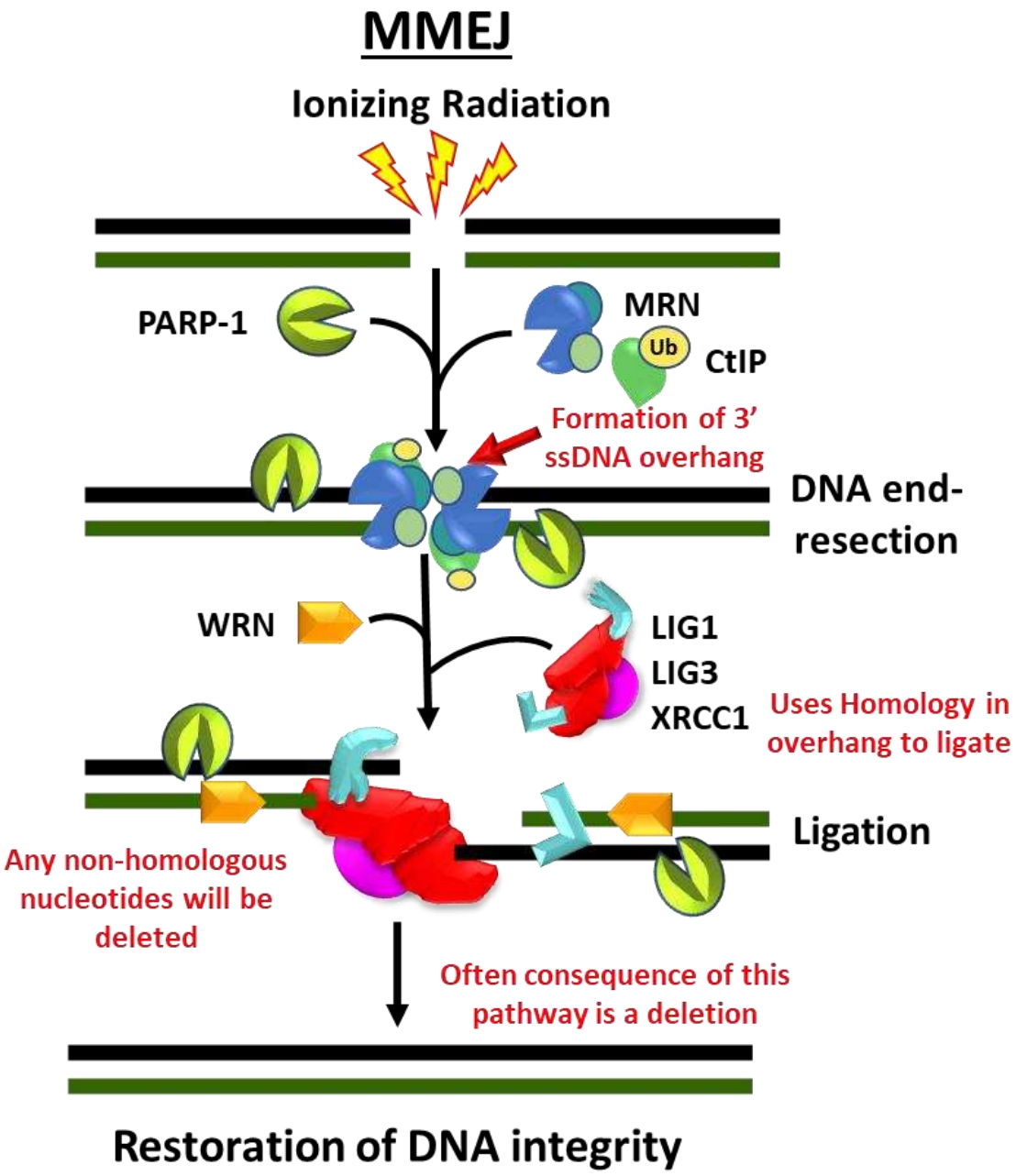


**Figure 1.9. Repair of DSBs by microhomology-mediated end joining (MMEJ).** The factors implicated in this pathway include PARP-1, the MRN complex, CtIP and WRN. DNA end-resection creates a short 3' ssDNA overhang and is mediated by the MRN complex, CtIP and PARP-1. Ligation is mediated by LIG3 or LIG1. The restoration of DNA integrity through MMEJ DSB repair pathway is associated with sequence information loss at the junction as well as by an increased risk of joining unrelated DNA ends which generate translocations and other genomic rearrangements.

## 1.10 Low-LET Radiobiology

Low-LET ionizing radiation induced DNA damage is known to be caused mainly through indirect action via water radiolysis and the production of ROS species, such as hydroxyl radicals. It has been suggested that indirect action accounts for nearly 2/3$^{rd}$ of its DNA damage while only around 1/3$^{rd}$ of its associated damage is contributed to direct action [97, 98]. Due to its high reliance on indirect action, low-LET radiations, including photon and proton beams, have an OER (oxygen enhancement ratio) that is generally estimated to be around 3. This means it is roughly 3 times less effective in oxygen deprived (hypoxic) conditions [85]. This is a critical factor in the success of the radiotherapy treatments as hypoxia is one of the main features of solid tumors and correlates directly with poor prognosis in cancer patients [52, 160]. Therefore, the lack of oxygen in hypoxic tumors directly affects the indirect action of low-LET radiation as it decreases the formation of ROS, promoting low-LET radioresistance. As a result, radiotherapy using low-LET ionizing radiation is less effective under hypoxic conditions, which often occur in tumors. Therefore, low-LET radiation's reliance on oxygen may reduce the cell killing of the hypoxic cancer cells, thereby reducing the efficiency of this form of radiotherapy treatment [6].

As previously mentioned, ionizing radiation is known to produce all types of DNA lesions. However, the occurrence of damaged bases and SSBs are known to occur far greater than that of DSBs. Prior studies using HPLC-MS/MS have calculated the exact number of DNA lesions that were induced by ionizing radiation per Gy/cell [161]. Although, it is generally accepted that the DNA damage induced by 1 Gy low-LET ionizing radiation per diploid mammalian cell to be estimated around 150 DNA-protein crosslinks, 1000 – 2000 damaged bases with purine damage < pyrimidine damage, 500 – 1000 SSBs, and 20 – 40 DSBs [88]. This is important as DSBs are the main factor responsible for ionizing radiation induced cell death but

occur much less frequent than the other DNA lesions. Therefore, less induction of DSBs per Gy dosage means less cell death, meaning that higher dosages may be required to increase the effectiveness of this type of cancer therapy. This is problematic as increasing the dosage of low-LET ionizing radiation may also increase the risk to the surrounding normal health cells. However, technological improvements have been made which allow for more accurate targeting of the tumor tissue to allow for a higher dosage of radiation to be focused within the targeted area, which is further discussed in the following low-LET photon radiotherapy section.

Another fall back to using low-LET radiation for radiotherapy arises from the radiosensitivity of the cells being specific to certain phases within the cell cycle. Radiosensitivity is governed by the amount of DNA damage following treatment, as well as the individual capacity to correctly repair the damage [162]. For low-LET radiation, the cells are most resistant while in S-phase and are most sensitive while in late G2/M-phases of the cell cycle. This is true for both low-LET photon (X-rays or gamma rays) as well as the more effective low-LET proton irradiations. This has been demonstrated in mammalian cells following low-LET proton irradiation as these cells portrayed high radiosensitivity shortly before and during mitosis but demonstrated radiation-resistance during DNA synthesis with maximum resistance occurring towards the end of the S-phase [163, 164]. These results further demonstrated that proton-induced DNA damage was cell cycle specific to the reproductive M-phase and G1 of interphase, while resistant to S-phase cells. The reliance on the specific phases within in the cell cycle in order to induce the most DNA damage, likely due to cell cycle specific checkpoints and DNA repair processes, is of particular concern, as some tumor cells which are low cycling or quiescent, are often localized in oxygen deprived tissues and are considered the most resistant to low-LET proton or X-ray radiations [73]. Thus, these tumor cells have a larger capacity to

recover from the low-LET-induced DNA damage, as their metabolic activity may be more readily equipped in dealing with the low-LET-induced radicals, thus allowing for their continued proliferation and failure to effectively kill all of the tumor cells.

While DSBs are known to be the major factor to induce radiation cell death, their repair is essential for cell survival. The major pathway for low-LET photon induced DSBs is believed to be NHEJ, which is active throughout all phases of the cell cycle. Prior studies have demonstrated that around 70% of the DSBs induced by either X-ray or gamma ray irradiations are repaired by NHEJ in human cells, in contrast to around 30% being repaired through HR, even when in G2 phase of the cell cycle when HR is active [165, 166]. This is believed to be a result of the low-LET radiation being sparsely ionizing and produces a higher amount of simple DSBs, in contrast to high-LET with produces more complex DSBs. On the other hand, it has been demonstrated that homology-directed repair is a requirement for developing S-phase radioresistance [167].

### 1.10.1 Low-LET Photon Radiotherapy

Photons are massless particles of energy and can be used in radiotherapy via either X-ray or gamma ray irradiation sources. X-rays and gamma rays have the same basic properties but originate from different parts of the atom. Simply, X-rays are emitted from processes outside of the nucleus while gamma rays originate from inside the nucleus. In other words, X-rays are generated by a linear accelerator that excites electrons, while gamma rays are from the decay of substances, such as cobalt-60 or cesium-137 [15]. Photons are the original ionizing radiation source used for radiotherapy. Following the discovery of X-rays in November 1895, physicians quickly began using X-rays for treating skin lesions within the first few months of 1896 and were also used to treat a patient with breast cancer in January of 1896 [168]. However, clinicians did

not have a clear understanding of the beams' physical or biological characteristics [169]. This lack of understanding led to much morbidity and poor cancer control, which became the driving force for radiobiologists to study the effects of X-rays on cells and for physicists to dive into the properties behind these radiations [170].

Since then, photon radiotherapy has advanced greatly. Such advancements are a result of both technical improvements and treatment planning. One such improvement came with the ability to use high-energy photons which has allowed for improving the target-to-entrance dose and with the sparing of the radiosensitive skin. This is due to the initial dose buildup, that is mainly caused by the forward scattered Compton elections, which shifts the peak dose by a few centimeters away from the surface of the patient's body [19].

Another technical improvement involved the development of intensity-modulated radiation therapy (IMRT). IMRT was first introduced in the 1990s and has since dramatically improved both the clinical outcome in prostate cancers as well as the radiation side effects involved with the radiotherapy treatments of many other cancers. IMRT utilizes inverse planning, in which you begin with a desired dose distribution and arrive at a specification of the required fluence modulation to create it. Fluence in radiotherapy is defined as the total number of particles that are crossing over a sphere unit cross section which surrounds a point source of ionizing radiation over the defined surface area [171]. Inverse planning differs from conventional forward planning, which mostly depends on geometric relationships between the tumor and nearby sensitive structures, as it is less dependent on the geometric parameters but more on the specification of the target tumor volumes and sensitive structures, as well as, their dose constraints [172].

IMRT enables for more accurate targeting of the tumor tissue as it allows for the delivery of radiation via fields that have non-uniform radiation fluence which when added together within a patient can produce a dose distribution with a concave shape [173]. This is done with the use of motor-driven multileaf collimators (MLC) which can move individually allowing for multiple fields to aid in the sparing of normal tissue as you can change the dose in each of the different fields [172]. Originally the MLC was developed for field shaping in 3D conformal radiotherapy. The MLC consists of a large number of highly absorbing tungsten "leaves" that can be moved against each other, thus, creating a large variety of field openings which are able to be shaped to conform with the projection of the target tumor volume [174].

The initial use of IMRT made an immediate impact on treating human cancers, such as prostate and oral tumors, with X-ray radiotherapy. In prostate tumors, IMRT has allowed for higher dosages which has led to a better tumor control [175]. In oral tumors, it has also allowed for better sparing of salivary glands and a decreased incidence of xerostomia [176]. Furthermore, in both veterinary and human medicine IMRT has demonstrated to decrease the acute radiation effects [177]. While the use of IMRT with X-rays has provided for enhanced tumor targeting, these beams are still composed of photons and their absorption characteristics in tissues remain unchanged, leading to the development of further technical advancements.

Stereotactic radiation therapy (SRT) is another technical improvement to help enhance the effectiveness of photon radiotherapy. Some tumor types that are not sensitive to fractionated radiotherapy, such as lung cancers, are very sensitive to SRT. Unlike conventional finely fractionated radiation therapy (FFRT), that spares normal tissue by fractionation, SRT spares the normal tissue by avoidance. Specifically, SRT spares normal tissues by minimizing dose to the normal tissue and administering large doses/fraction to only the tumor [178]. This technical

approach utilizes hypofractionation, meaning very few fractions given per treatment (1 – 5 fractions/treatment), and requires a planning system that can facilitate a rapid drop-off in dose between the tumor and normal tissue [179]. Therefore, SRT requires a system to stereotactically verify the position of a tumor and normal structures, which means during the treatment plan you must have a stereotactic to verify that the patient is in the same position. SRT can be subdivided into stereotactic body radiation therapy (SBRT) and stereotactic radiosurgery (SRS), also known as gamma knife. These differ in the dosage per fraction and the number of fractions given per treatment [180]. In treating intracranial or extracranial disorders with SRS, the tumor targets are irradiated with a dosage of 15 – 25 Gy in 1 – 2 fractions. On the other hand, when treating extracranial tumors with SBRT, the target tumors are irradiated with a dosage of 30 – 60 Gy in 2 – 5 fractions [181]. However, SRT is not appropriate for all tumor types. The tumor must be well defined, meaning you cannot use SRT to treat microscopic diseases, and you must have an adequate distance between the tumor and critical normal tissue structures.

While these advancements have helped improve photon radiotherapy most of the problems that arise from photon therapy are a direct result of the physical characteristics of the photon interactions with the tissue. The depth-dose distribution rises initially as the locally deposited dose, as well as the secondary electrons that are liberated by the incident photons build up their fluence, to a maximum followed by a the fluence and dose declining exponentially as a function of depth and the photons are absorbed beyond their target until they exit the body [72]. As a result, this leads to a relatively shallow depth of maximum dosage, which makes it difficult to treat deeply seated tumors without effecting the surrounding normal tissue which can be detrimental in treating such tumors within sensitive areas, such as in the head and neck. In addition, because photons do not have an electric charge, they cannot be magnetically or

electrically focused, requiring thick collimators to laterally shape the photon beam to cover the tumor target. Moreover, scattering interactions occur when the photons leave the collimator and prior to reaching their target regions, leading to a lateral spread outside of the collimated field. The result of this is an induction of a lateral penumbra region where the radiation dose is deposited in areas outside of their targeted region, contributing to irradiation of the surrounding normal tissue and increasing the risk of radiation-induced adverse effects [75]. The penumbra is defined as the width of the dose band lateral to the field edge for the dose to decrease from 80% to 20% [73]. Collectively, these factors make treating deeply seated tumors with high curative doses that are situated near at-risk structures very difficult with photon radiotherapy, as these doses may present substantial risk to these structures, such as DNA damage possibly resulting in mutation.

In addition, the low-LET physical properties of photon radiotherapy, as previously described, also hinder its cell killing abilities due to its high dependence on oxygen, cell cycle phase specificity and being sparsely ionizing. It has also been hindered due to the risk of inducing secondary cancers in long-term survivors of pediatric cancers following treatment with photon radiotherapy [182].

### 1.10.2 Low-LET Proton Radiotherapy

Compounding interest in the use of protons for radiotherapy began in 1946 with a paper written by Robert R. Wilson. In his paper he proposed that protons accelerated by machines could be used for medical purposes and scientific investigations. He reasoned that among the charged particles, protons offered the longest range for a given energy and were at the time the simplest and most practical for medical use [183]. Protons were first used clinically at Berkeley in 1954 and the development of the world's first hospital-based proton facility began in 1970 at

the Loma Linda University Medical Center (LLUMC) [184]. However, only in the mid-1980s with the development of the required computer competence and the needed imaging technology did a hospital-based proton facility become feasible and the first hospital based proton treatment center at LLUMC was established in 1990 [169].

Proton therapy is a type of charged particle (ion) therapy that is distinguished from x-ray or gamma ray treatments that utilize massless photons, as a proton is 1,836 times heavier than an electron. Proton beam irradiation accounts for about 85% of the cancer patients that receive particle therapy today [37]. Charged particles, such as protons and carbon-ions, have several unique factors that contribute to an overall superior delivery of radiation dose when compared to photon beams which include: (1) the ability to use the spread-out Bragg peak (SOBP) beam delivery method, providing an enhanced dose distribution and lateral focusing; (2) magnetic steering of the ion beams; (3) dose verification via available imaging and (4) superior LET. These properties help provide for optimal delivery of maximally safer and curative doses of radiation to the tumor while at the same time enhance the sparing of the surrounding normal tissues [75].

While proton beams have several physical advantages over the conventional photon beams, such as X-rays, they have a similar biological response due to both of these irradiation sources being clinically considered as low-LET [37]. Although, when compared to photon beams, proton beams are known to provide a superior depth vs dose distribution [68]. This is because photons have an infinite range, with the dose decreasing exponentially with depth. In contrast, the depth of penetration of protons in matter is finite and the range is a function of the proton energy as well as the electron density of the irradiated material [185]. This is a result of protons being charged particles, as previously explained, they demonstrate an increasing energy deposition

(LET) as they travel through the medium, leading to a maximum known as the Bragg peak, which is located near the end of the range of the proton beam. Prior to the Bragg peak, protons demonstrate a dose level that is modest as compared to photon beams and following the Bragg peak their deposited dosage drastically falls. As a result, therapeutic proton beams used in radiotherapy demonstrate LET values ranging from 0.4 – 30 keV/μm, as the LET increases up to its maximum at the proton Bragg peak [186]. Furthermore, the depth of the proton Bragg peak can be adjusted accordingly to the depth and extent of the target tumor volume by choosing the appropriate proton beam energies [187].

However, unlike other charged particle therapies, such as carbon-ion radiotherapy, protons are clinically known to be low-LET particles as their biological effects are still constrained by the low-LET properties previously described [73]. Although, proton beams have a slightly higher RBE than photon beams, as it is generally accepted that the average RBE value for proton beams is ~1.1. On the other hand, as the proton RBE increases with LET, a prior study using the endpoint of cell survival has demonstrated that the SOBP proton's beam RBE is ~1.1 in the entrance region, which increases to ~1.15 in the center of the SOBP, ~1.35 in the mid region of the SOBP and ~1.7 in the distal fall-off region of the SOBP [70].

Furthermore, like photons, protons can be intensity modulated. This is important as incorporating the intensity modulation concepts into proton therapy may help to further improve the proton dose distribution [188]. In contrast to photon IMRT, where large volumes of healthy tissue are irradiated, proton irradiation is already associated with smaller irradiation volumes of normal tissues [185, 189]. Intensity modulated proton therapy (IMPT) can also increase the dose conformality of proton therapy [190]. In addition, IMPT may also be able to reduce the sensitivity of the resulting dose distributions to delivery errors, as well as, some of the techniques

in IMPT may be utilized to reduce the total integrated dose that is delivered to the patient [174]. Another advantage to proton radiotherapy over conventional photon radiotherapy is, like carbon-ion beams, proton beams can be comprised of a selected spectrum of proton energies in order to distribute the Bragg peaks over the entire tumor volume with a uniform dose in the spread-out Bragg peak (SOBP) technique of beam delivery.

#### 1.10.2.1 Proton Radiotherapy Facilities

As per end of 2019, the total number of patients treated with protons has been 222,425 [191]. Currently, as of April 2021, there are 95 proton therapy facilities in clinical operation worldwide. In the USA, the only option for charged particle radiation therapy is with the low-LET proton facilities, with 40 of these facilities currently in clinical operation [192]. The reason behind only offering proton therapy over carbon-ion therapy in the USA is largely due to the differences in cost. While the current infrastructure required to generate and maintain a clinical proton beam is both bulky and more expensive than conventional photon therapy, these facilities are still less expensive to operate than the infrastructure required for generating high-LET heavy ions, like carbon-ion beams used in carbon-ion radiotherapy. However, as the benefits of utilizing proton therapy over photon therapy have continued to demonstrate that they outweigh their higher cost, this has led to more construction of these facilities. Although, increasing reports of the advantages of using high-LET particles, such are carbon-ions, over the low-LET protons, may further induce a change from proton beam facility construction to the more effective carbon-ion beam facilities [193].

## 1.11 High-LET Radiobiology

The use of high-LET heavier ions in cancer therapy was initially proposed as the heavier ion beams were believed to have radiobiological properties that could lead to superior results

than with the use of X-ray or proton beams in radiotherapy [194]. The main reason for using high-LET heavy charged particles in radiotherapy, such as carbon-ion beams, is due to their favorable depth vs dose profile which is superior to both low-LET proton and photon beams. While the physical properties of high-LET heavy ion beams are similar to low-LET proton beams, as in they both contain a Bragg peak, the heavy ion beams have reduced lateral scattering and longitudinal straggling [19, 195].

In contrast to low-LET photon and proton beams, high-LET heavy charged particles exhibit less multiple coulomb scattering as they travel through matter, leading to a sharper lateral penumbra. Moreover, in charged particle therapy not all the ions stop exactly at the same depth (at the Bragg peak) due to the stochastic nature of energy loss as the ions travel through the tissue which causes a range of uncertainty resulting in a widening of the Bragg peak in a longitudinal direction. However, this range of uncertainty is reduced as the atomic mass of the ion is increased, meaning there is less longitudinal stagging for heavier high-LET ion beams than with the low-LET proton beams [75]. Collectively, these factors allow for the heavy ion beams to be placed closer to at risk organs laterally, while still maintaining a high degree of organ sparing.

Other biological effects of high-LET ions such as, the reduced dependence on fractionation, not being limited by cell-cycle phase specificity, inducing dense ionizations along the particle track creating complex DNA damages, as well as, the reduced oxygen enhancement ratio (OER), have also made these ions very beneficial when treating tumors that display photon and proton radioresistance [196, 197]. Furthermore, these biological effects also provide heavy ions with larger RBE values, as RBE is a complex function involving the LET, particle type, tissue/cell type, cell cycle phase, dose per fractions, oxygenation state, and the endpoint that is

examined [75]. This means that the heavy ion beams with their higher RBE values are more effective at producing the same adverse biological effects, such as cell death, at equivalent doses of the low-LET photon or proton beams.

However, as heavy ions, such as carbon-ions, can be either lower- or higher-LET depending on their speed as they traverse through the medium, as previously explained, the RBE is variable and increases as a function of depth with its highest RBE value at the very distal edge of the Bragg peak. For other ions such as neon, oxygen, and helium, the distribution of the RBE values corresponds to different portions of the Bragg peak. Generally, the greater RBE values can be correlated with increasing LET, as in the case of carbon-ions, a maximum peak for the RBE is observed at LET values of ~100 keV/μm. This variation in RBE values is a result of the density of ionization events along the particle track. Thus, high-LET portions within the heavy ion beam range that are known to be densely ionizing results in complex DNA damage that is very difficult for the cell to repair and the type of DSB repair pathway, NHEJ or HR, that is most important in repairing the high-LET radiation induced complex DSBs still remains uncertain (Figure 1.10). In addition, the complex DNA damage, specifically complex DSBs, is believed to contribute to a substantial portion of the differences in the observed RBE values between the low- and high-LET radiations [39].

The complexity of DNA damage and the ability for the cell to efficiently repair the damage, particularly regarding DSBs, also plays a role in the sensitivity of mammalian cells to ionizing radiation. Prior research has demonstrated that the radiosensitivity of cells to high-LET radiation is cell cycle independent, in contrast to low-LET radiation, in which the radiosensitivity is cell cycle dependent as it portrays radioresistance in S- and early G2-phases of the cell cycle [198]. As previously mentioned, the low-LET ionizing radiation resistance is due to producing

simple DSBs as well as the occurrence of both NHEJ (which occurs in all phases of the cell cycle) and HR (which only occurs during S and G2-phases) (Figure 1.10).

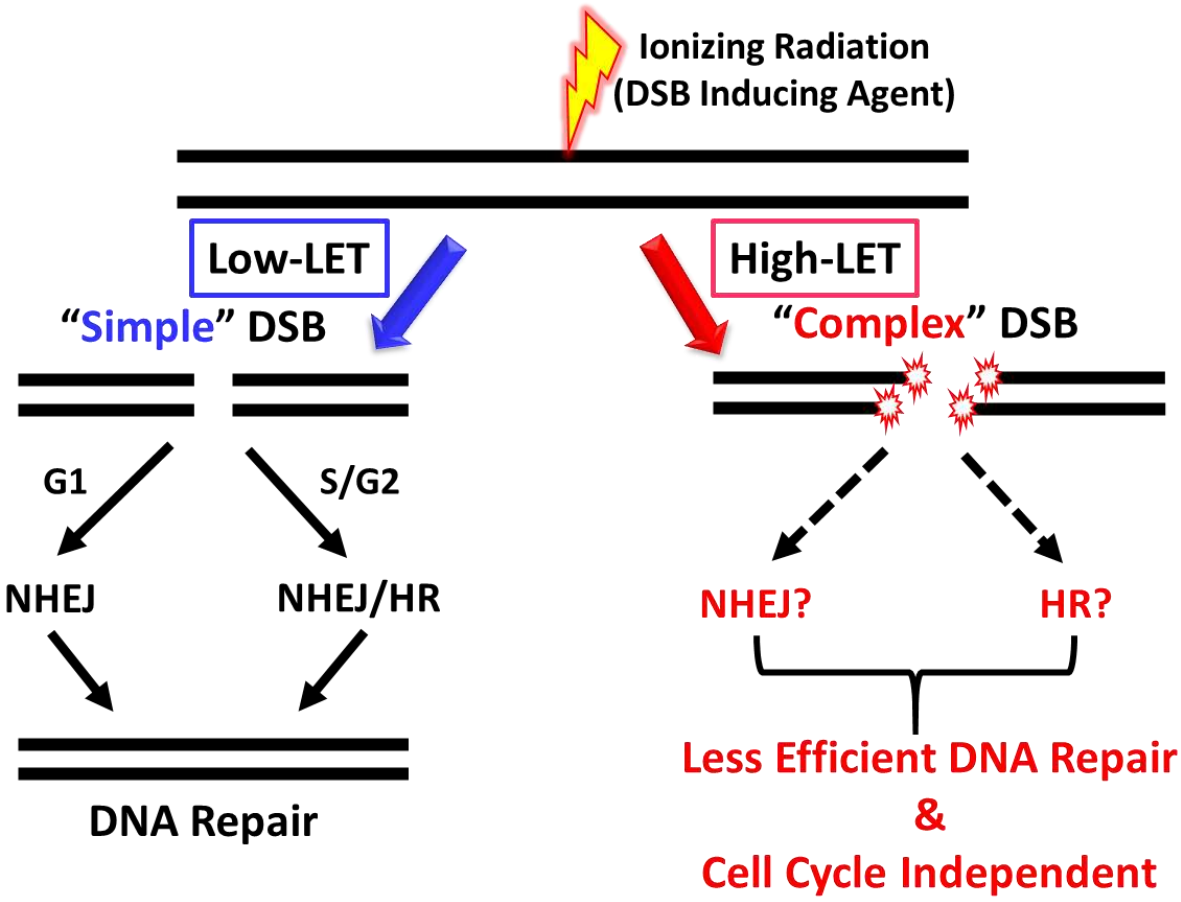


**Figure 1.10. DSB repair of low- and high-LET radiation-induced DNA damage.** Low-LET radiation is known to produce simple DSBs that are typically repaired by NHEJ or HR. While NHEJ is active throughout the full cell cycle, HR is limited to S- and G2-phases, in which the cells are most radioresistant to low-LET radiation. High-LET radiation is known to produce complex DSBs and is independent of cell cycle radioresistance. Complex DSBs demonstrate a less efficient repair response which leads to an increase in DNA damage remaining unrepaired for long periods of time following high-LET irradiation and eventually may promote genome instability if improperly repaired or cell death if left unrepaired. The repair mechanism used to resolve these high-LET induced complex DSBs is also poorly understood.

However, while high-LET radiation is known to be independent of cell cycle phase radioresistance, recent studies have suggested that S-phase cells are more sensitive to high-LET ionizing radiation [199]. The propose mechanism behind this increased S-phase sensitivity of high-LET radiation is thought to be due to the inhibition of the Ku-dependent NHEJ repair via the induction of high-LET complex DSBs. As high-LET radiation can penetrate deeper into the

nucleosome than low-LET radiation, it can induce greater amounts of short DSB fragments (<40 bps) at the same dose than low-LET radiation. Thus, the large number of short DSB fragments prevent the efficient loading and binding of the Ku heterodimer, an D-NHEJ factor, onto the broken DNA ends. Since, Ku binding to the DSBs is the first step in D-NHEJ, this leads to the suppression of D-NHEJ-mediated repair of the DSBs at these clustered damage sites [200]. However, there is still much debate into which DSB repair pathway, NHEJ or HR, is most essential in repairing the high-LET induced DSBs as there has been compelling evidence in support of each of these pathways, which will be further discussed in chapter 4.

High-LET ionizing radiation also demonstrates a lower oxygen enhancement ratio (OER). This is important as ionizing radiation can either work directly or indirectly, as previously explained. While low-LET radiation is mostly known to work indirectly, in which the radiolysis of water creates reactive oxygen species (ROS) that induce the DNA damage, high-LET radiation is known to work mostly through direct action, in which the ionizing radiation directly transfers its energy to the DNA molecule, making it less dependent on the ROS production and oxygen concentrations [80, 81]. However, the radiolysis of water and the generation of ROS is still considered to induce a significant proportion of DNA damage for both low- and high-LET radiation. As mentioned previously, molecular oxygen is required to maximize the ROS-related damage [75]. Thus, the quantification of the affect that oxygen has with each radiation quality is done through the OER. As OER addresses the amount of dose necessary to result in an equivalent biological endpoint with or without the presence of oxygen, it is a similar concept to RBE [84].

While the OER for low-LET photons and protons is generally estimated to be around 3, the OER for high-LET particles, such as carbon and other heavy ions, varies with their LET and

can range from 2.5 to 1.0 depending on the ion charge and respected LET value [85]. Simply, this means that high-LET ionizing radiations have less dependence on the presence of molecular oxygen in order to induce their biological effects as compared to low-LET ionizing radiations. Therefore, the use of high-LET heavy ions is beneficial in radiotherapy as these ions are more effective at killing cells in the hypoxic and necrotic cores of the tumors, in contrast to low-LET radiations in which these hypoxic conditions contribute to their low-LET radioresistance.

High-LET heavy ions also have the additional advantage over photon therapy in their dose verification methods. This is a result of when heavy ions, such as the nuclei of carbon atoms, travel through matter, both the ion projectile and the traversed matter undergo nuclear interactions. This is beneficial in dose verification as some of these nuclear interactions produce positron emitting nuclei that can be imaged by a positron emission tomography (PET) scanner [75]. However, these nuclear interactions also provide a disadvantage of using high-LET heavy ions as they produce secondary low Z fragmented ions that have a large forward momentum that allows them to travel beyond the range of where the incident ions stop (at their Bragg peak). Thus, these fragmented ions create a characteristic low dose tail behind the Bragg peak and result in a complex radiation field of mixed radiation qualities, which is further discussed below [75, 201].

### 1.11.1 High-LET Carbon-ion Radiotherapy (CIRT)

The superior biological and physical advantages of high-LET heavy ion beams over low-LET X-ray or proton beams, as discussed in the previous section, made them very desirable for their use in radiotherapy. In 1975, the University of California San Francisco Medical Center (UCSF) and UC Lawrence Berkeley National Laboratory (LBNL) began a collaborative clinical study to determine the efficacy of heavy charged particles in the treatment of human cancers.

From 1975 – 1992 patients at LBNL were treated with several High-LET ions including helium (He; Z=2), carbon (C; Z=6), nitrogen (N; Z=7), oxygen (O; Z=8), neon (Ne; Z=10), silicon (Si; Z=14), and argon (Ar; Z=18) [202]. With the goal of overcoming hypoxia, one of the major factors of cancer radioresistance, the use of very heavy ions, such as argon, was justified as these ions contain very high-LET which has been demonstrated to be required in order to achieve this goal [203, 204]. However, the relatively high entrance LET values of many of these heavy ions led to unacceptable patient toxicities. Although, out of these heavy ions, carbon-ion beams demonstrated to be a quality compromise as it portrayed LET values between 10 and 13 keV/µm in the entrance channel and fairly high-LET values throughout the spread-out Bragg peak (SOBP) region of 40 – 80 keV/µm [205]. Unfortunately, after pioneering the field of using charged particles in radiotherapy, the LBNL cyclotron was closed in 1992. However, the promising results of using carbon-ion beams in radiotherapy at LBNL shortly led to their use at National Institute of Radiological Sciences (NIRS). In 1994, NIRS began treating patients with carbon-ion beams using their Heavy Ion Medical Accelerator in Chiba (HIMAC) and have pioneered carbon-ion radiotherapy (CIRT) world-wide.

Therapeutic carbon-ion beams used in radiotherapy are typically accelerated to 100 – 400 MeV/n and have LET values ranging from 10 – 80 keV/µm, with a maximum peak of LET values of ~100 keV/µm at the distal edge of their Bragg peak [37]. As previously mentioned, RBE correlates with LET, thus, the accepted RBE for carbon-ions used in clinical radiotherapy is typically estimated to be between 2.5 – 3, although values even as high as 5 have been reported [84]. In addition, fast ions (at the entrance) will have a lower RBE than slow ions in the target region due to LET being proportional to $z^2/\beta^2$ (where z is the ion effective charge and β is its relative velocity) [203, 206-208]. As a result, for carbon-ion beams the RBE is variable and

increases as a function of depth. Therefore, the highest values of RBE are within the beam regions in which it is at its highest LET, i.e., at the Bragg peak.

As previously discussed, carbon-ions are significantly higher in their ionization density (resulting in complex DSB that enhance its cell killing effect), LET and RBE, as well as, significantly lower in their lateral scattering and OER in comparison to low-LET protons. Not only does this provide CIRT with more efficient cell killing but also contributes to the carbon-ion beam having a superior physical dose distribution and deposition around the carbon-ion Bragg peak. This results in the carbon-ion Bragg peak being tighter at the beam edge as compared to the proton Bragg peak.

In addition, as both proton and carbon-ion beams have the ability for utilizing the SOBP technique of beam delivery, the increased RBE of carbon-ions is attributed to their increased LET, which is most pronounced in the carbon-ion SOBP. This leads to a superior radiobiological dose distribution in terms of a higher peak to plateau ratio for the high-LET carbon-ion beam in contrast to the low-LET proton beam (Figure 1.11) [209]. In addition, these factors give carbon-ions the potential for dose escalation to the tumor, while still respecting the normal tissue constraints [60]. Therefore, these high-LET biological and physical properties along with carbon-ion beams not being cell cycle specific in radioresistance and their ability to treat low-LET radioresistant tumors, have made them the ideal charged particle as well as specific heavy ion candidate for cancer radiotherapy.

Technological advancements in CIRT facilities such as, raster scanning and improved motion monitoring, have continued to improve the accuracy of CIRT [210, 211]. Further improvements in CIRT include a further reduction in the number of fractions, the spacer gel used and treatment planning allowing urethral-sparing and nerve-sparing [212]. However, the biggest

hindrance in the wide-spread adoption of CIRT is due to the high initial investment cost in building a CIRT facility along with the costs of maintenance and treatments as these costs are far greater than the costs for photon and proton treatment facilities. To help reduce this cost many CIRT paradigms involve hypofractionation, in which fewer fractions are given within the treatment regimen but each fraction contains higher dosages (Gy), which has improved its efficiency and cost-effectiveness as well as reduces the overall treatment times [213, 214]. However, the justification for further expanding expensive CIRT facilities world-wide involves more research demonstrating its advantages over other therapies as well as positive clinical data that will further outweigh its benefits over its high cost.

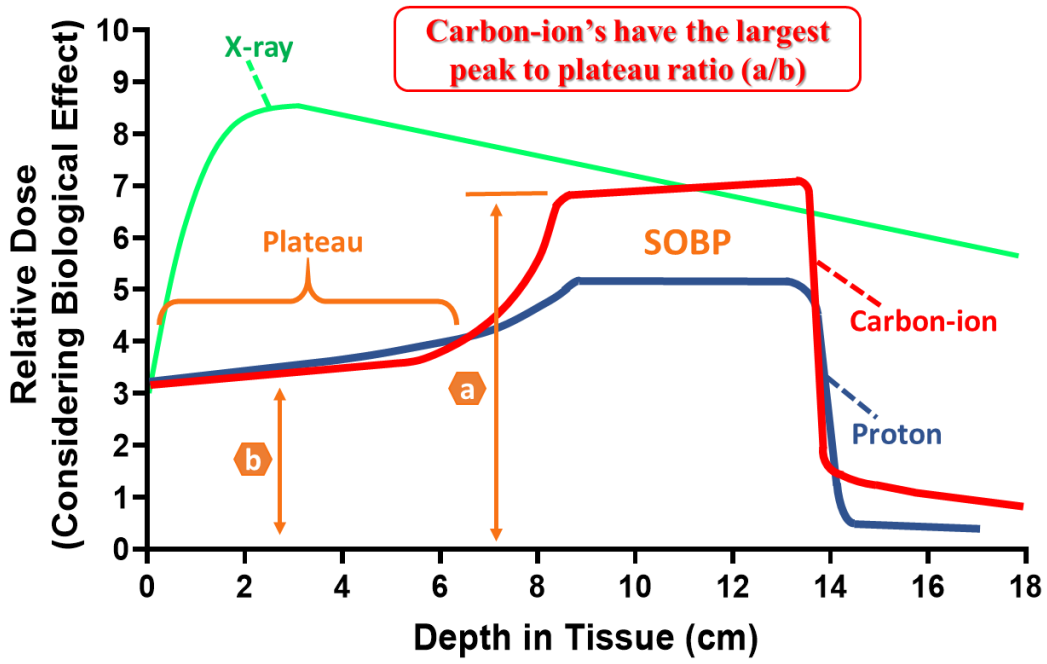


**Figure 1.11. Graphical representation of the relative dose vs depth in tissue from different beam sources of ionizing radiation.** Carbon-ion beams provide superior depth-dose distributions which allows for better spearing of the surrounding normal tissue outside of the targeted SOBP region and more effective cell killing within its SOBP region

#### 1.11.1.1 Carbon-ion Nuclear Fragmentation Tail

Apart from the high cost of CIRT, another hindrance for the wide-spread adoption of CIRT involves the characteristic carbon-ion nuclear fragmentation tail. Unlike protons, carbon-

ions in a typical tumor treatment undergo nuclear fragmentation which generates a mixed field of radiation qualities throughout their beam range that extends in the post Bragg peak regions, as only around 50% of the initial carbon-ions reach the end of their range (at the Bragg peak), while the others undergo these nuclear interactions producing the lighter fragmentation ions [19, 195].

Even though the stopping process of the high-energy carbon-ions penetrating a thick absorber is directed by collisions with atomic elections, nuclear interactions lead to significant effects at large penetration depths, even though the probability of these interactions is much smaller. The nuclear fragmentation ions are a result of the high energy carbon-ions undergoing nuclear interaction reactions as they traverse through the medium. These interactions can either result in a central head-on collision, in which there is a complete disintegration of both the projectile (carbon-ion) and target nuclei, or in peripheral collisions which result in partial fragmentations. However, for geometrical reasons, peripheral collisions are the most frequent nuclear reactions occurring along the stopping path of the carbon-ions, leading to the carbon-ion beam particle losing one or several nucleons [19, 215].

There are several important aspects of heavy ion nuclear fragmentation that must be considered when using heavy ion beams, such as carbon-ion beams, in radiotherapy. First, the nuclear reactions cause a loss of the primary beam particles and results in a build-up of lower-Z fragments. These effects become more and more important with increasing penetration depth, such as when treating deeply seated tumors. Furthermore, the secondary fragmentation ions are known to move at relatively the same velocity as the primary carbon-ions but are capable of traveling for longer ranges which produce a dose tail behind the Bragg peak, which is defined as the carbon-ion nuclear fragmentation tail (Figure 1.12) [216-218]. Lastly, the angular distributions of the fragments are mainly determined by the reaction kinematics and are forward

directed but are much broader than the lateral spread of the primary carbon-ions caused by multiple Coulomb scattering [19, 219, 220].

To investigate the fragmentation characteristics of heavy ions, a comparative experimental study was conducted in which they examined $^{10}$B, $^{12}$C, $^{14}$N, $^{15}$O, $^{16}$O, $^{18}$F, $^{19}$Ne and $^{20}$Ne-ions with kinetic energies ranging between 200 – 670 MeV/μm [221]. Their results demonstrated that the total (nuclear) cross section for reactions changing the proton number (Z) was found to be even smaller for $^{12}$C-ions than that of $^{10}$B-ions, while the value for $^{14}$N-ions was relatively high and that at larger penetration depths, a substantial fraction of each of the primary ions was lost by nuclear reactions. Although, regarding fragmentation, carbon-ions offered the best conditions. For example, only 38% of the primary 400 MeV/μm $^{20}$Ne-ions were observed to reach the Bragg peak at 16 cm depth in water while 52% of $^{12}$C were observed at the same range. In addition, the positron-emitting fragments $^{10}$C and $^{11}$C were found very useful for *in-vivo* range monitoring via positron emission tomography (PET) techniques [75]. The fragmentation-ions from a single $^{12}$C-ion have since been further identified with the most abundant type of secondary fragments being known to be helium-ions followed by hydrogen, lithium, beryllium and boron-ions, respectively [222]. While these fragmentation-ions are known to travel at relatively the same velocity and in the same direction, it is important to further investigate each of their individual properties in the post Bragg peak region as they can differ in the energy in which they carry and thus produce differences in the biological effects of the cells that each of them may transverse [223].

Therefore, the extent of the carbon-ion nuclear fragmentation tail to induce DNA damage needs to be explicitly studied so it can be included in the patient treatment planning system in order to avoid or limit the possible unanticipated adverse biological effects in the surrounding

normal healthy tissues. In addition, the extent of DSB complexity from each of the fragmentation-ions must also be further investigated. The reasoning for this is due to the primary high-LET carbon-ions being known to produce complex DSBs that are very difficult for the cell to repair leading to their cell death, however, if the lighter fragmentation-ions induce DSBs that are less complex than those from the primary ions, this may result in DSBs that may not be sufficient for cell death but may result in misrepair that has the potential to lead to genomic instability ultimately resulting in secondary induced cancers.

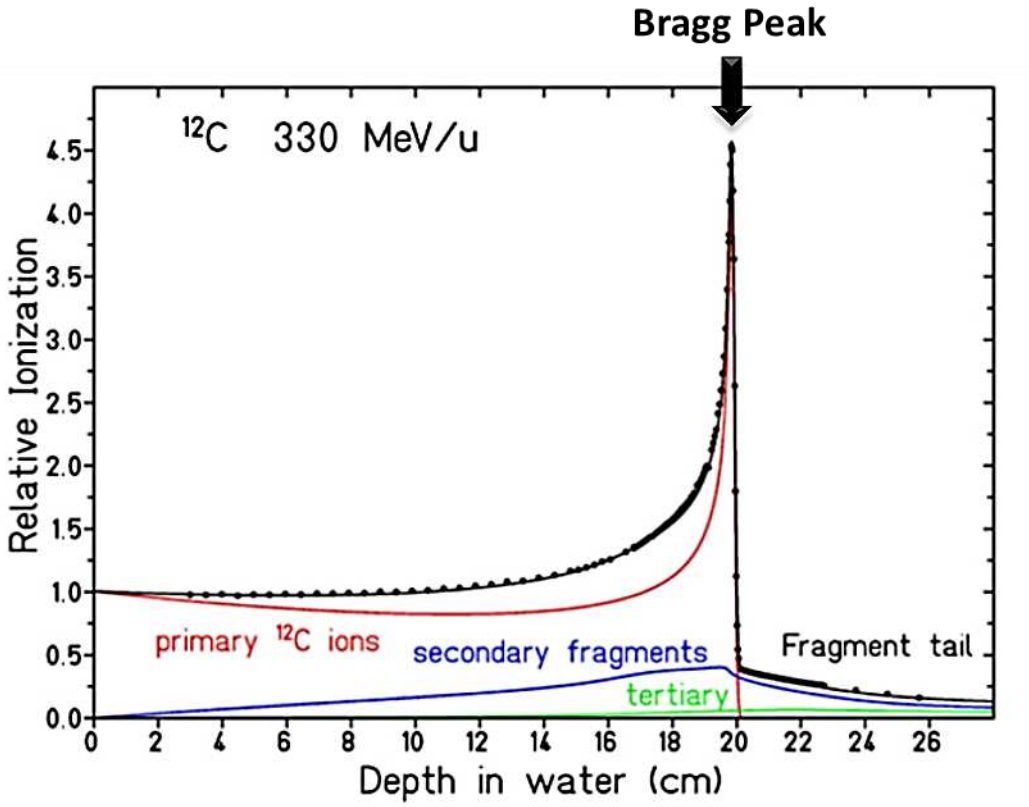


**Figure 1.12. Bragg curve for 330 MeV/n monoenergetic carbon-ion beam in water measured at GSI compared with model calculation.** Black line is the total calculated Bragg curve. Red, blue and green lines are the contributions from the primary particles and the fragments of secondary and tertiary fragmentations, respectively. The small dose beyond the Bragg peak (fragment tail) is caused by the high-energy nuclear fragmentations. Figure adapted from E Haettner *et al* 2013 [218].

#### 1.11.1.2 Risks of secondary induced cancers following CIRT

Due to the long latency of ionizing radiation-induced secondary cancers along with CIRT being the newest form of radiotherapy resulting in a relatively short follow up in the

accumulation of patient data, the risk of secondary tumors following CIRT treatment is still uncertain. While several animal studies have been conducted to address the risk of CIRT secondary induced cancers, the experimental long-term studies within humans are limited by the short timeframes with this newer radiotherapy treatment option. However, there is still much debate into the amount of risk that should be associated with CIRT in the development of these secondary radiation-induced malignancies.

In animal studies, a group from NIRS analyzed the genomes of T-cell lymphomas that arose in mice following CIRT and X-ray therapy. While these secondary tumors shared many common mutations, they found that large interstitial chromosomal mutations were much more common in the CIRT-induced secondary tumors [224]. In human studies, a group in 2016 examined the blood samples of patients receiving either IMRT alone or IMRT and CIRT boost for prostate cancer at HIT and GSI and examined the inter- and intra-change cytogenetic damage in each of the blood samples. In this study no differences were observed in the quality or quantity of chromosomal damage between the two treatment types. Therefore, they concluded that there is not a difference in the risk of late normal tissue complications or secondary malignancies with CIRT in comparison with IMRT [225].

In a retrospective cohort study, the authors reviewed the records of patients who received CIRT for prostate cancer between June 27, 1995 and July 10, 2012 at NIRS in Japan and retrieved the records of patients diagnosed and treated for prostate cancer between January 1, 1994 and December 31, 2012 from Osaka Cancer Registry. The results of this study suggested that the patients with localized prostate cancer treated with CIRT appeared to have a lower risk of subsequent primary cancers (secondary radiation-induced cancers) than those treated with photon radiotherapy [21]. With limited solid clinical data, mathematical modeling has also been

used to estimate the risk of secondary induced cancers [226]. Using this approach, the risk of secondary breast cancers was examined and was estimated to be comparable in Hodgkin's lymphoma patients treated with proton radiotherapy or CIRT in linear quadratic or the linear-no-threshold models [227].

While these studies are very important, the progressive long-term follow-up of thousands of patients that have been treated at NIRS has not yet provided any evidence of an increased risk in secondary CIRT-induced cancers. These results demonstrate promising evidence against the concerns of possible higher risks of secondary cancer induction for CIRT than for proton or photon radiotherapy [228, 229]. However, further understanding in the biology of ionizing radiation-induced secondary tumors and estimating the clinical risk to the normal tissue damage surrounding the target tumor area that may give rise to these secondary tumors is a cornerstone in establishing the case for further development of CIRT world-wide.

#### 1.11.1.3 Cancers effectively treated with CIRT

As mentioned previously, the location and radioresistance of certain tumors has created many implications in their treatment. However, CIRT has shown very promising results in effectively treating these tumors in which the other radiotherapy modalities have fallen short. This is due to the high-LET properties of CIRT, such as superior depth-dose distribution and superior biological effects, which has given CIRT the ability to treat tumors that are in close proximity to at risk organs as well as the low-LET photon and proton resistant tumors. Most notably these tumors include osteosarcomas and soft tissue sarcomas (STS), head and neck (including skull base) tumors, prostate cancers, cervical cancers, hepatocellular carcinomas (HCC), pancreatic cancers, glioblastoma (GBM), as well as, showing promising results in pediatric cancers along with recurrent and previously irradiated tumors [75].

Most of the published data for osteosarcomas and STS patients that are treated with CIRT at NIRS comes from unresectable or recurrent patients that were previously considered incurable or expected to have poor outcomes following treatment. For unresectable bone and soft tissue sarcomas treated with CIRT it was reported that the patients at 3 years had local control (LC) and overall survival (OS) of 73% and 47%, respectively, with no >3 acute reactions [230]. In addition, they reported that for unresectable retroperitoneal sarcomas, CIRT yielded at 5 years a LC and OS of 69% and 50%, respectively, with no patients developing grade 3 or higher toxicities as well as no gastrointestinal track complications being reported with a median follow up of 36 months. These results demonstrate the clear advantage of using CIRT in treating these tumors as most treatments involving surgical therapy with or without radiotherapy have 5-year LC and OS of 28 – 71% and 36 – 64%, respectively [231].

Cancers within the head and neck have demonstrated to be very difficult to treat with conventional radiotherapy due to the abundance of histologies that are X-ray resistant and are in a very small space where normal tissue sparing becomes very important. Therefore, the physical and biological properties of CIRT make it essential in treating these tumors and have demonstrated great success in treating these tumors with reduced acute and late reactions as compared to conventional radiotherapy [232]. CIRT has also demonstrated to be superior to proton therapy in the treatment of mucosal melanomas as it has been reported to have better local control, but the long-term survival is still reported to be poor which is likely due to the high distant metastasis rate of these melanomas [67, 233]. CIRT has also demonstrated to be superior to proton therapy for treating skull base tumors. Utilizing raster scanning CIRT to a medium of 60 GyE dosage has demonstrated a 5-years LC and OS of 89% and 98% for chondrosarcomas and 70% and 88% for chordomas, respectively, with mild acute and late toxicities as well as no

grade >3 reactions. On the other hand, proton radiotherapy demonstrated 5-year OS of 91% and 62% for skull base chondrosarcomas and chordomas, respectively but with a very high grade toxicity of 94% [234].

CIRT has clearly shown to be highly effective and far superior to the other radiation modalities in treating prostate cancer. A large multi-institutional retrospective analysis of 2157 patients treated with CIRT for prostate cancer with over half of the patients being high-risk and one third being intermediate-risk prostate cancer reported excellent results for both of these groups. Most interestingly, for patients of the high-risk group it was reported that they had a 92% and 99% 5-year biochemical recurrence-free survival and cancer-specific survival with no grade >3 toxicities [235].

Hepatocellular carcinomas (HCC) are the third leading cause of cancer death world-wide. While there are many treatment options available for HCC, the benefit of these treatments has demonstrated to be transient, and the overall survival has not been very good. The major limitation in treating HCC is the degree of liver cirrhosis. This is because any compromise of the liver function, such as radiation-induced hepatic insufficiency, in the healthy normal liver tissue can possibly be fatal. Using stereotactic body radiation therapy (SBRT) has portrayed improvements in the tolerability and outcomes as compared to conventional X-ray radiotherapy with IMRT, but the long-term outcomes are still considered to be poor [236]. On the other hand, in a clinical trial at NIRS it was reported that CIRT using 15 fractions in 5 weeks was feasible, well tolerated and provided very favorable outcomes for HCC patients who are recurrent after initial treatment or were deemed not amenable to any other treatment approach [237]. In addition, in a meta-analysis it was further demonstrated that charged particle radiotherapy had

superior survival, local control and less toxicity as compared to conventional X-ray therapy using IMRT [238].

Pancreatic cancer is the fifth leading cause of death world-wide. The only curative treatment for this type of cancer is known to be surgery. However, this treatment option only applies to a small number of pancreatic cancer patients as most of the patients usually present advanced unresectable pancreatic cancer. Low-LET radiotherapies have demonstrated to be very ineffective in treating this type of cancer as high levels of hypoxia and radioresistance has contributed to local failure being a major form of cancer recurrence [239]. For this reasoning, CIRT with its improved RBE and lower OER has provided for a much more effective treatment option in pancreatic cancer patients. CIRT in combination with Gemcitabine has been used to treat unresectable locally advanced pancreatic cancers (LAPC). The results of this treatments presented a 2-year OS of 48% with excellent tolerability at the given dose level which is much higher than with the other treatment options for LAPC (carbon-ion radiation delivered to 55.2 GyE in 12 fractions over 3 weeks and Gemcitabine escalated to 1000 mg/m$^2$ in the 3 weeks) [240].

Locally recurrent tumors that have previously been treated with or without conventional X-ray therapy have been very difficult to treat due to their increased tumor resistance after recurrence as well as in achieving normal tissue dose constraints in the previously irradiated tumors. Therefore, CIRT is a very attractive tool for treating these locally recurrent tumors. The benefits of CIRT in these cases was demonstrated as 52 patients with previously irradiated adenoid cystic carcinoma of the head and neck were re-irradiated with CIRT and the treatments were well tolerated without grade >2 toxicity and with excellent control and survival rates [241]. A group at NIRS also demonstrated the effectiveness of CIRT on recurrent previously resected

but not irradiated rectal cancers. In this study the dose was escalated to 73.6 GyE in 16 fractions over 4 weeks and they reported no grade >3 toxicities and also portrayed an excellent local control [242].

As there are far more examples demonstrating the benefits of using CIRT over other radiotherapy or cancer treatment modalities than those listed here, these cases portray clear clinical evidence of why it is important for CIRT to be more available to patients world-wide.

#### 1.11.1.4 Carbon-ion Radiotherapy Facilities

As of 1994 to per end of 2019, there have been a total of 34,138 patients treated with CIRT [191]. Currently, as of April 2021, there are a total of 12 CIRT facilities in clinical operation world-wide. Countries in which CIRT is currently available are Austria (1 facility), China (2 facilities), Germany (2 facilities), Italy (1 facility), and Japan (6 facilities) [192]. Although, there are 6 more CIRT facilities currently under construction which are located in China (1 facility planned start in 2021), France (1 facility planned start in 2023), Japan (1 facility planned start in 2021), South Korea (2 facilities planned start in 2022 and 2025), Taiwan (1 facility planned start in 2022) [243].

Despite the clear benefits behind the high-LET properties and clinical data support of CIRT, as mentioned previously, the biggest obstacle that has hindered the wide-spread adoption of CIRT facilities around the world is due to the high initial investment cost in the construction of these facilities as well as the maintenance and treatment costs. Moreover, CIRT re-introduction into the USA has been hampered by the concerns with respect to the cost effectiveness along with the lack of FDA certification and approved reimbursement [244]. However, this issue of a higher cost was also present when proton beam radiotherapy facilities were first introduced over X-ray radiotherapy facilities. The higher investment cost of proton

therapy facilities in comparison to photon therapy facilities, hindered proton facility world-wide establishment until further research into the benefits of utilizing proton beams over the conventional X-ray beams in radiotherapy became the driving force behind protons widespread use and facility construction [245].

A few studies have evaluated the cost-effectiveness of CIRT. In one such study they demonstrated that if the local control rate for skull base chordoma achieved with CIRT exceeds 70.3%, then CIRT had overall treatments costs that are lower than those for conventional X-ray therapy for patients with skull base chordomas. There results also showed that the incremental cost-effectiveness ratio for CIRT was estimated to be €2,539 ($3024.88) per 1% increase in survival, or about €7,692 ($9,163.98) per additional life-year. This group concluded that their results support that CIRT, although more expensive, is at least as cost-effective as advanced photon therapies for patients with skull base chordomas. They also stated that CIRT offers substantial benefits for the patients over conventional photon and proton therapies such as improved control rates and less severe side effects [246]. Another such study also concluded that CIRT was a cost-effective treatment as compared to multi-modality treatment in locally recurrent rectal cancer [247].

As more and more accumulating evidence is coming forth regarding the clear advantages of high-LET CIRT over both low-LET proton and X-ray radiotherapy methods, this has triggered international interest into comparative trials with CIRT along with investments into pre-clinical radiobiological research in the USA [37]. In fact, while there are no CIRT facilities neither operational nor under construction in the USA currently, the Mayo Clinics in Jacksonville, Florida has advanced plans for building the first CIRT dedicated facility in the USA. This would

bring about the return of heavy ion radiotherapy to the USA following the end of the LBNL pilot trial that ended in 1992 [212].

#### 1.11.1.5 National Institute of Radiological Sciences (NIRS)

The National Institute of Radiological Sciences (NIRS) in Chiba, Japan, pioneered radiotherapy with the use of carbon-ions as previously mentioned. Following the LBNL pilot trials, NIRS built the world's first medically dedicated heavy ion accelerator, called the Heavy Ion Medical Accelerator in Chiba (HIMAC). The construction of HIMAC began in 1988 and was completed in 1993 [248]. They then started clinical application of 290 MeV/n carbon-ions in 1994 and as of December 2019 they have treated 13,489 patients [191, 248]. Currently, NIRS is now part of the national institute for quantum and radiological science and technology (QST) and has reached a treatment capacity of between 900-1000 patients per year [249, 250].

CIRT at NIRS/QST is typically given 4 times per week for 3 weeks with a total average of 13 fractions. Although, the number of fractions given may vary accordingly with tumor size and location [68]. Despite the current cost for patients for a CIRT treatment course (3.2 million yen/~28,000 USD), the clinical effectiveness demonstrated at their facility has led to a continuous increase in the number of patients from both within and outside of Japan [249].

#### 1.11.1.6 Opportunities for further improving the efficacy of CIRT

In order to increase the benefits of CIRT to further out weight its high costs and enhance the drive in its widespread adoption, it is important to further improve the efficacy of CIRT. This can be done through the usage of radiosensitizers either by increasing the DNA damage associated with CIRT to increase its cell killing ability in the target region or by exploiting the DNA repair pathways utilized at specific depths within the carbon-ion beam range. However, in both

methods it is important for the damage to be concentrated within the target region, such as within the SOBP, to minimize damage to the surrounding normal healthy tissue.

As DNA damage, such as DSBs, are regarded as the critical target for ionizing radiations, as they are the main component behind ionizing radiation-induced cell death, the use of small molecules that can enhance the induction of DSBs at sub-cytotoxic doses will cause decreased cell survival in the CIRT-irradiated target cells. One such way to use these small molecules is to increase the contribution of the indirect action of the high-LET carbon-ion ionizing radiation. As mentioned previously, indirect action involves the radiolysis of water which produces ROS, the most damaging of which being the hydroxyl radical ($^{\bullet}OH$). Additionally, within one ps ($10^{-12}$ s) superoxide ($O_2^{\bullet-}$) and hydrogen peroxide ($H_2O_2$) are also formed as secondary ROS bimolecular products [82].

The intracellular stoichiometry of these reactive species can also be affected by subsequent chemical cascades leading to the generation of additional cell-damaging molecules [251]. This can be done through metal catalysis via the Fenton reaction by intracellular ferrous and/or cuprous ions which converts the secondary ROS products, $O_2^{\bullet-}$ and $H_2O_2$, to form additional amounts of the more damaging $^{\bullet}OH$ [252]. Thus, using transition metals as radiosensitizers via increasing the intracellular concentrations of transition metals will thus increase the amounts of hydroxyl radical ion production. Furthermore, as LET increases, more energy is deposited in short tracks, as it is densely ionizing, and the radical concentrations from the radiolysis of water are higher. This leads to more radial-radical reactions occurring and resulting in the formation of more of the bimolecular products, such as hydrogen peroxide ($H_2O_2$) and molecular oxygen ($O_2$) [91, 92]. Thus, the difference in the number of bimolecular products produced between the

radiation qualities (low- vs high-LET) can be exploited by increasing the intracellular concentrations of transition metals at non-cytotoxic dosages.

Another way to enhance CIRT effectiveness is by inducing combined lethality. Since DNA damage is the critical target for ionizing radiation, with the most consequential damage being DSBs, the final and most important mechanism following ionizing radiation-induced DSBs is the process of cellular DSB repair [253]. Thus, proper DSB repair is required for the cells survival and pharmacological or genetic inhibition of the DSB repair pathways will result in an increased radiotoxicity. The method of inhibiting the DNA repair pathways following ionizing radiation has been used with the PARP inhibitor Olaparib and the ATR inhibitor to VX-970 (Berzosertib) in order to prevent the repair of SSBs thus exacerbating the ionizing radiation-induced DNA damage [254, 255]. However, as DSBs are known to be the major factor to induce cell death as well as the DSB repair complexity increases with increased LET, it is important to focus on the DSB break repair pathways such as NHEJ or HR. This can be done by selectively inhibiting components within these DSB repair pathways following CIRT-induced DSBs. Previous studies have also demonstrated this method to be an enticing and promising combined modality therapy to enhance the treatment of primary tumors [256, 257].

## 1.12 Purpose and Specific Aims

With growing international interest in CIRT, it is important to not only identify the accuracy in which the carbon-ion beam deposits its dose but to also enhance its efficiency for inducing cell death. The biggest hurdle in the expansion of high-LET CIRT world-wide is due to the higher cost of construction and maintenance of these facilities as compared to the costs required for the less effective low-LET X-ray and proton radiotherapy facilities. To overcome this hurdle, the biological benefits of using high-LET CIRT must greatly outweigh its high costs as well as

outweigh the benefits of using the other low-LET radiotherapies such as with X-rays or proton beams. This evidence in supporting these benefits of CIRT comes from both the clinical and radiobiological studies.

In order to increase the benefits of CIRT, there are several important factors that need to be addressed. First, the accuracy in which the carbon-ion beam distributes its DSBs around its Bragg peak must be evaluated, as DSBs are the major factor behind radiation-induced cell death. Moreover, the extent in which the carbon-ion nuclear fragmentation ions induce DSBs in the post-Bragg peak regions must also be evaluated. This is a very important area in the study of CIRT, as these DSBs are outside of the target Bragg peak region, thus, they would be induced in the normal healthy tissue during CIRT. Therefore, the extent of this damage must be considered during treatment planning as it is an associated risk factor for CIRT-induced secondary tumors. Next, enhancing the efficiency of CIRT to induced tumor cell death is another important factor that must be implemented to increase this therapies benefits. This can be done by increasing the amount of CIRT-induced DNA damage, inhibiting the mechanisms behind the CIRT-induced DNA damage repair or a combination of both methods.

In this study we aim to provide evidence for the accuracy in which CIRT distributes its DSBs throughout the full carbon-ion beam range, including the distribution of the DSBs within the post-Bragg peak range, in a single biological system. It is important for the full carbon-ion beam range to be addressed as it is comprised of both low- and high-LET radiation qualities, depending on the depth within the beam range, as previously explained, which produce differences in their biological effects. It is also important to address the DSB distribution in a single biological system as obstructions from materials within the beam path or changes in the medium which the beam travels (air, plastic, media, etc.) may alter the accuracy in which the

DSBs would be distributed as well as the range in which the carbon-ion nuclear fragmentation ions would be induced clinically. We have created such a system which has enabled us to visually observe and quantitate the DSB distributions in a single biological system. This has allowed us to be able to differentiate the radiation qualities throughout the carbon-ion beam range as well as in the post-Bragg peak region utilizing fluorescently labeled γ-H2AX foci as a surrogate marker for DSBs.

We also aimed to provide evidence for methods that can enhance the effectiveness of CIRT to increase the cell death in its target region. In our first method, we demonstrated that the use of the transition metals copper and cobalt in solution with DNA increased the DNA damage in an LET and dose dependent manner. The proposed mechanism behind our results was via the Fenton reaction increasing the indirect action of DNA damage from the ionizing radiation, as previously explained. In another method, we sought to identify the DSB repair pathways that are preferentially utilized at different depths within the carbon-ion beam range. This is important as identifying any possible shifts within the carbon-ion beam range that the preferred DSB repair pathway changes, particularly in the high-LET target region, would provide fundamental knowledge into which pathway should be inhibited to increase the cell death within the target region. In order to do this, we utilized CHO mutant cell lines which were deficient in each of the major DSB repair pathways (NHEJ and HR) and addressed the differences in their survival fractions throughout the full carbon-ion beam range via our modified method of the cell survival assay, as explained in the following sections.

### 1.12.1 Chinese Hamster Ovary (CHO) cell line

Experiments involving cell culture within this study utilized the Chinese Hamster Ovary (CHO) cell line. We utilized this cell line for several reasons including the nature of their

relatively small colony sizes made them ideal to evaluate specific colonies at individual depths within our cell culture flasks to address changes in survival fractions at different depths within the carbon-ion beam range, as further explained in section 1.11.2.1. Furthermore, the CHO cell line has been established as a very useful model in radiation cytogenetics and tissue culture studies due to their low chromosome number (2n=22), quick doubling time (~14 – 17 hrs) and relatively small colony size [258]. CHO cells are also widely used in many other scientific aspects, such as in the study of genetics, toxicity screening, nutrition and gene expression and to express recombinant proteins. In fact, CHO cells are the most commonly used mammalian host for industrial production of recombinant protein therapeutics with nearly 70% of all recombinant protein therapeutics produced today being made in CHO cells [259].

CHO cells are an epithelial cell line derived from cells of the ovaries of Chinese hamsters. In 1919, Chinese hamsters were first used as a laboratory specimen in place of mice for typing pneumococci. Then in 1957, Dr. Theodore T. Puck of the Department of Medicine at the University of Colorado, successfully isolated an ovary cell from a female Chinese hamster while he was investigating the usefulness of various cells in somatic cell genetics. This led to him establishing the first CHO cells in culture plates [258]. Dr. Puck discovered that these cells were very resilient and their relatively fast generation times made them a great candidate for *in-vitro* cultivation. CHO cells soon became important for studying genetic defects, such as chromosomal abnormalities, due to having karyotype heterogeneity amongst their cell populations thus allowing for a low rate of spontaneous transformation, which has also made them ideal for quantitating radiation-induced micronuclei as well [259].

CHO cells have also been well established in the field of DNA damage and repair. This is due to the isolation of CHO mutant cell lines which are deficient in a variety of DNA damage

repair mechanisms which have been highly utilized in both non-ionizing and ionizing radiation research [260, 261]. Specifically, CHO mutant cell lines deficient in DSB repair have been critical in studying the repair mechanisms and associated factors that are essential in the DSB repair processes, such as NHEJ and HR, following ionizing radiation induced DSBs. CHO mutant cell lines that are defective in NHEJ mediated DSB repair include V3 (DNA-PKcs mutant), Xrs-6 (Ku80 mutant), Xrs-5 (Ku80 mutant) and XR-1 (XRCC4 mutant) [262]. CHO mutant cell lines that are defective in HR mediated DSB repair include 51D1 (Rad51D mutant) and irs1SF (XRCC3 mutant) [263, 264].

### 1.12.2 Cell Survival (Clonogenic) Assay

The main goal behind radiotherapy is to stop tumor cell growth. Thus, cell survival is a commonly used endpoint for *in-vitro* experiments. The two most essential measures of cell survival include: (1) its cellular viability, defined as the ability of a cell to preserve its physical and metabolic integrity, and (2) its clonogenicity, defined as the ability of a cell to undergo cellular division [35]. For stem cells within healthy normal tissues their capacity for continued proliferation is a prerequisite for the continued integrity and function of the normal tissue. On the other hand, continued proliferation of cancerous cells within a tumor is very problematic and these cells must be eradicated. For a tumor to be eradicated, the tumor cells must be effectively "killed" in the sense that these cells lose their ability to divide, thus eliminating their ability to cause further growth and spread of the malignancy [265].

The *in-vitro* cell survival assay, which is also known as the clonogenic assay or colony formation assay, is based on the ability of a single cell to grow into a colony after treatment. Thus, a clonogenic cell is defined as a surviving cell that has retained its reproductive integrity and is able to proliferate indefinitely to produce a colony, in which a colony is defined to consist

of at least 50 cells [265]. This assay has become very useful in a wide range of different scientific applications as it allows for the detection of all the cells that have retained their capacity for producing large numbers of progeny following any treatment that can cause cell reproductive death resulting from damage to DNA, damage to chromosomes, apoptosis, mitotic catastrophe, etc. Many studies have performed this assay and their results have provided fundamental information about the differences in sensitivity to radiation and chemotherapeutic agents among tumors and normal tissues as well as the modification of treatment effectiveness under various conditions and modes of application. Thus, this assay has also become the essential method of choice in determining the effect of cell reproductive death after treatment with various sources of ionizing or non-ionizing radiation, as only a fraction of the seeded cells are able to produce colonies [266].

The cell survival assay was first described in 1956 by Puck and Marcus. They published a seminal paper that described a cell culture technique for assessing culture dish plated single mammalian cell's ability to form colonies with a suitable medium. The selected medium was supplemented with many heavily irradiated "feeder" cells, which served to condition the microenvironment of the much smaller number of cells to be tested for their colony formation. Their experiments portrayed the first radiation-dose survival curve for HeLa cells in culture irradiated with X-rays. Results from their experiments demonstrated that these mammalian cells were much more radiosensitive than previously assumed for cells in tissues and had a mean lethal dose range of 1 – 2 Gy, paving the way for this method to be implemented in future radiation experiments [266, 267].

### 1.12.2.1 Cell Survival Assay – General approach

In the general approach to the cell survival assay, cells harvested from a stock culture will be plated at appropriate pre-determined dilutions into their respected cell culture dish or flask, for untreated controls or treatment dishes/flasks. Following plating, these cells will be incubated for generally around 1 – 3 hours to allow for cell attachment. After confirmed attachment, the appropriate cells will undergo the experimental treatment method, which must be performed before the cells start replicating. Directly after treatment, both untreated and treated cells in their respected cell culture dish or flask will be re-plated (seeded) at an appropriate concentration into a separate respected cell culture dish/flask. They will then be placed in an incubator and left for a time equivalent to at least six potential cell divisions. This time differs according to the cell lines doubling time as well as concentration of seeded cells but is typically 1 to 2 weeks for CHO cells. Following this incubation period, the cells in each cell culture dish/flask are fixed and stained and the resulting colonies are quantified (Figure 1.13).

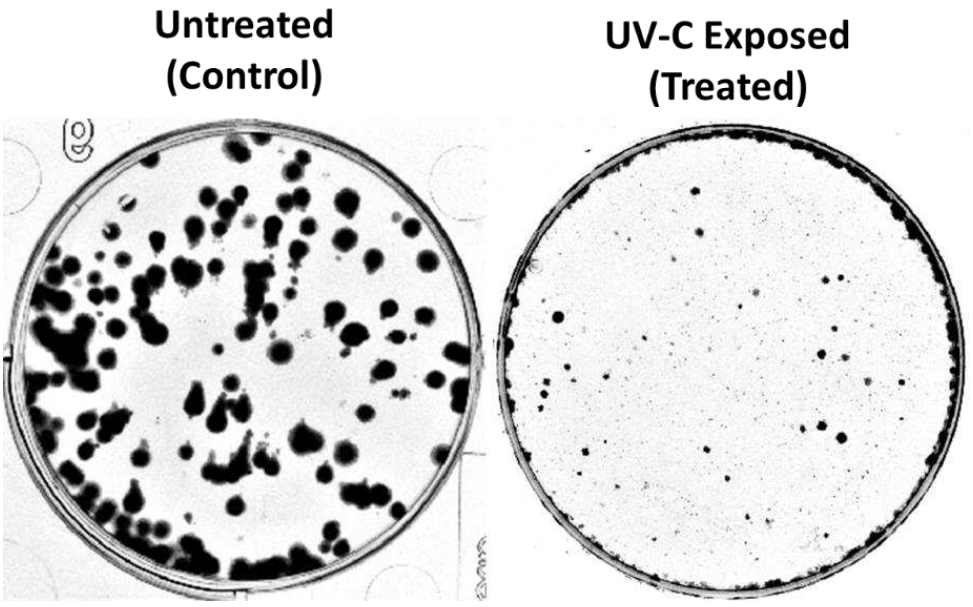


**Figure 1.13. Colony formation following treatment incubation period.** (**Left**) Colony formation of untreated (control) cells portraying the cell clonogenicity without treatment. (**Right**) UV-C treated cells that have retained their capacity for producing large numbers of progeny, i.e., retained their clonogenicity.

In the untreated cell culture dish or flask, these cells will not undergo treatment but are essential to determine the plating efficiency (PE) of each cell line that is used in the experiment. The PE indicates the percentage of untreated cells seeded that grow into colonies after the incubation period. This is an important step in the cell survival assay as different cell lines may vary in their PE's [265]. For example, CHO cells are known to possess a PE of 70 – 100% while PC3 (human prostate tumor) cells have a PE of 50 – 60% [266]. In other words, PE is the ratio of the number of colonies formed to the number of cells seeded, as displayed by the following equation:

$$\boldsymbol{PE = \left(\frac{\#\ of\ colonies\ formed}{\#\ of\ cells\ seeded}\right) x100\%}$$

In the treatment dish/flask, also seeded with the same number of cells used to address the PE, the cells that can form colonies after the incubation period following treatment are said to have survived as they have retained their reproductive integrity. Evaluating the number of these cells that have formed colonies allows for the calculation of the survival fraction (SF) [265]. Simply, the SF is the number of colonies that arise after treatment of the cells, expressed in terms of PE and displayed by the following equation:

$$\boldsymbol{SF = \frac{\#\ of\ colonies}{\#\ of\ cells\ seeded\ \times \left(\frac{PE}{100}\right)}}$$

Using this information, a cell survival curve can be constructed. For ionizing radiation, this depicts the relationship between the fraction of cells retaining their reproductive integrity and absorbed dose. Survival curves for mammalian cells are usually presented with dose plotted on a linear scale and surviving fraction on a logarithmic scale. In general, low-LET radiations, X-rays or gamma rays, produce a survival curve with an initial slope, followed by a bending

region or shoulder, after which it tends to straighten again at higher doses which generally does not occur until doses exceeding those used as daily fractions in radiotherapy have been reached. Furthermore, high-LET radiations, heavy-ions such as carbon-ions or Fe-ions, generally produce a straight line on a log-linear plot. In other words, high-LET radiation treatment survival approximates to an exponential function of dose (Figure 1.14) [265].

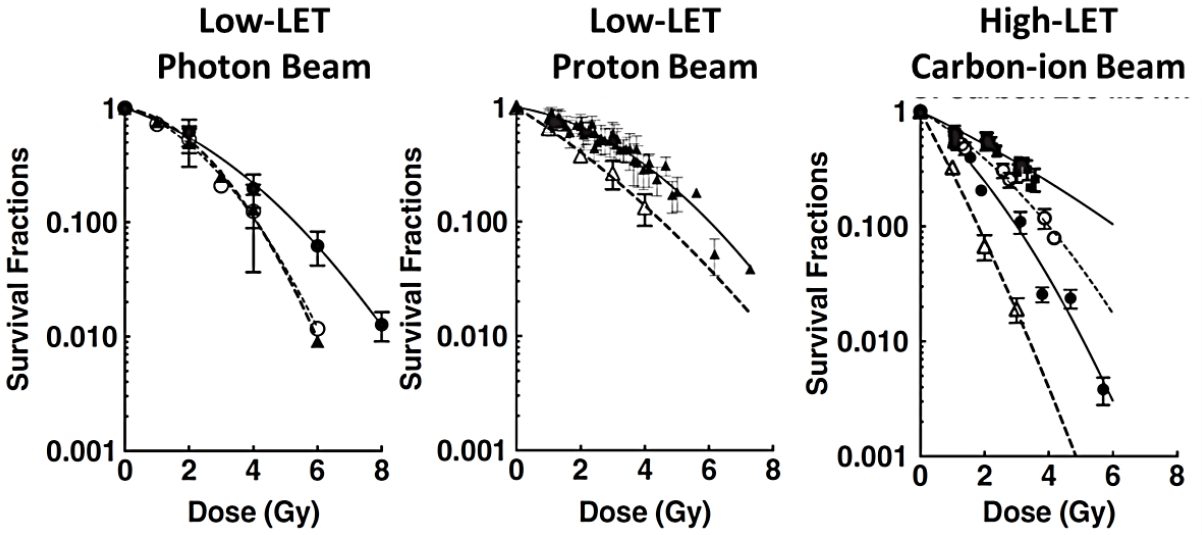


**Figure 1.14. Cell survival curves following irradiations from beam sources of different radiation qualities.** Left and middle graphs represent low-LET irradiations from photon beams, X-ray or gamma ray, and proton beams, respectively. Both of their survival curves demonstrate an initial slope proceeding into a curved region and straightening out at higher dosages. The right graph represents high-LET carbon-ion irradiation with a survival curve producing a straighter line. Figure taken from Fujisawa *et al.* 2013 [4].

### 1.12.2.2 Cell Survival Assay – Experimental modification

In order to address differences in the cell survival at different carbon-ion beam depths we had to design a method that could incorporate the full carbon-ion beam range in a single biological system. With the general approach to the cell survival assay this was not possible, as calculating the survival fraction required re-plating of the cells following treatment which would disrupt the placement that each cell was at within the carbon-ion beam range during irradiation. To solve this issue, we redefined how to calculate the survival fraction as described below.

The irradiation procedure for our experiments was similar to that used in the general approach for the cell survival assay. Cultured cells were trypsinized and re-suspended into growth medium. Once re-suspended, 60 mL of media containing 30,000 cells were placed into their appropriately labeled T-175 cell culture flask a few hours prior to irradiation and attachment was confirmed. Each flask was then irradiated independently with their respected dosage. For all flasks, the beam entry point was at the bottom of the flask (non-capped end).

However, instead of replating the cells immediately following irradiation, all cells were incubated for a period of 7 days for colony formation. After the culturing period, each culture flask was then washed with 0.9% NaCl, fixed in 100% ethanol and stained with 0.1% crystal violet. To quantify the survival fraction at each of our evaluated depths, they were scored for every millimeter along the width of the flask either possessing a surviving colony or not possessing a surviving colony, in which a surviving colony was defined as a colony containing >50 cells, and the average value was calculated for each depth (Figure 1.15).

Quantifying the cell survival at increasing depths in our flask with varying doses, allowed for us to determine the range at which each initial dosage could be considered lethal, as we would be able to observe a dramatic decrease in survival fractions between these depths. Furthermore, we could also address the carbon-ion beams observed biological Bragg peak, defined as the observed depth possessing the lowest number of colony formation, as well as how the survival differed in the post-Bragg peak depths at different dosages to observe the biological effects of carbon-ion nuclear fragmentation. Moreover, this method could also allow for extrapolating the differences in which DNA repair mechanisms and associated factors were preferentially utilized at different carbon-ion beam depths by utilizing CHO mutant cell lines that are deficient in different types of each of the DNA repair processes.

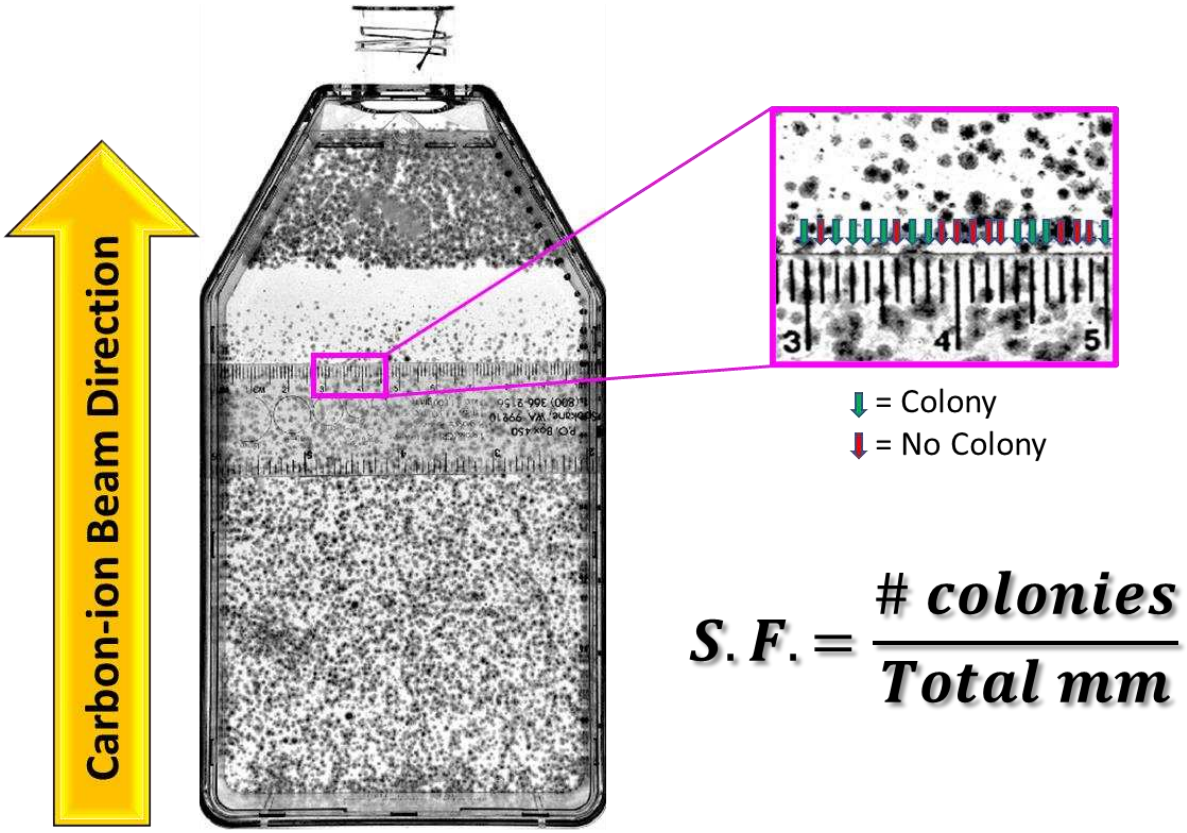


**Figure 1.15. Method for calculating the survival fraction at each depth within the carbon-ion beam range in a single biological system.** At each specified depth, surviving colony or no colony was addressed for every millimeter across the width of the flask. A surviving colony was defined as one containing >50 cells. The survival fraction was equal to the number of surviving colonies over the total width of the flask (mm).

### 1.12.3 γ-H2AX Assay

The γ-H2AX assay has become the gold standard for the detection of DSBs. Detection of these DSBs following irradiation is important in terms of cell killing as it is the critical lesion induced by ionizing radiation and their analysis provides essential insights into fundamental and translational radiobiology [268]. This assay is an immunocytochemical assay with antibodies recognizing γ-H2AX which is found at sites of DSBs.

The principle behind this assay involves the histone variant H2AX, which is known as the histone guardian of the genome [269]. H2AX is systematically found and ubiquitously distributed throughout the human genome and is involved in several important biological functions including: (1) concentration of the DNA damage signaling and repair proteins at the

sites of DSBs, (2) signal amplification and transduction in order to enhance the sensitivity of the DNA damage induced at the G2 cell cycle checkpoint, (3) implementation of an Artemis-dependent pathway (DNA-PKcs dependent NHEJ) that is required for the processing of a subset of radiation-induced DSBs, (4) promotes sister chromatid-dependent recombinational repair (HR) through the recruitment of cohesion, (5) aids in chromatin remodeling which assists the DSB processing, and (6) acts as a chromatin anchor to prevent dissociation of the DSB ends and enhances the repair fidelity [269-274]. At sites of ionizing radiation induced DSBs, as previously mentioned, H2AX becomes rapidly phosphorylated via ATM at serine 139. The phosphorylated form of H2AX then undergoes a conformational change and is referred to as γ-H2AX [127].

As phosphorylated γ-H2AX is implicated in the DSB repair pathway along with ATM being able to phosphorylate many H2AX histones, this leads to large numbers of γ-H2AX molecules being concentrated at the sites of DSBs, forming readily visible nuclear foci. Fluorescent staining of the cells' nuclei for these γ-H2AX molecules, via antibody recognition, allows for the visualization of the formation of these foci, thus allowing for the quantification of the DSBs and forming the basis for this sensitive biological dosimeter of ionizing radiation.

This assay also allows for visualizing differences between radiation qualities (low- or high-LET) (Figure 1.16). This is due to low-LET ionizing radiation sparsely depositing its energy meaning that these DSB sites are far more spread out within the cell [75]. In contrast, high-LET ionizing radiation densely deposits large amounts of its energy which creates close localizations of the DSB sites in a characteristic track structure as it traverses through the cell [275]. Thus, these track structures can be clearly visualized by immunofluorescence techniques utilizing antibodies directed against DSBs, such as done with this assay. Not only does this assay allow for the tracking of the induced DSBs but also allows for the study of DNA repair events at

these break sites. These closely localized DSBs (clustered or complex DSBs) are known to be refractory to repair and can be addressed by the persistence of the DSB marker, γ-H2AX, for long periods of time following ionizing radiation-induced DNA damage. This is due to the dephosphorylation of γ-H2AX and dispersal of γ-H2AX foci in irradiated cells correlates with the kinetics in the repair of the DSBs [276, 277]. In addition, the ionizing radiation-induced foci (IRIF) formed after high-LET radiation are known to be brighter and larger in dimension in comparison to those generated following low-LET radiations [278, 279].

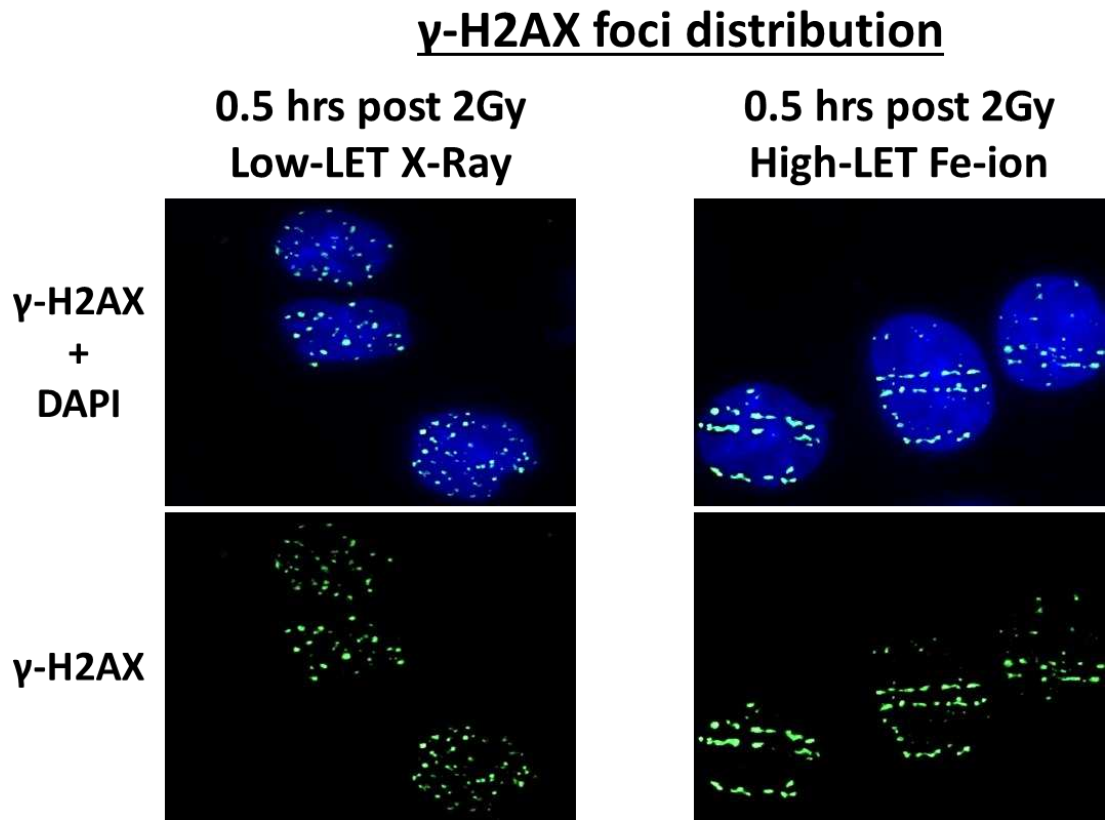


**Figure 1. 16. Image depiction of γ-H2AX foci distribution within the cell nucleus 0.5hrs following 2 Gy irradiation of low- or high-LET beam sources.** (**Left**) These high-LET γ-H2AX foci clusters are larger, brighter and are in close proximity to each other within each track structure. Low-LET X-ray irradiation demonstrates randomly distributed DSBs. These low-LET γ-H2AX foci clusters are smaller, less bright and portray large spacing between them. (**Right**) High-LET Fe-ion irradiation produces the high-LET characteristic track structure distribution of the DSBs. Each γ-H2AX foci is represented as a green dot and is a surrogate marker for DSBs. The cells nuclei is stained with DAPI and indicated in blue.

#### 1.12.3.1 γ-H2AX Assay – Experimental setup

The issue with the γ-H2AX assay within our experimental setup is that it requires for the cells to be attached to glass microscope slides and replating the cells following irradiation in our single biological system capable of incorporating the full carbon-ion beam range would require loss in the position of the cells at their respected beam depths during irradiation. In order to resolve this issue, the top of each cell culture flask was cut off, under sterile conditions, and labeled poly-L-lysine coated glass microscope slides were placed within each flask in the orientation depicted in Figure 1.17.

Following addition of the microscope slides, each flask was sterilized in a biosafety cabinet via exposure to UV-C light for 1 – 3 hrs, as contamination is the major concern for this method of setup. Once sterilized, the top of each flask was then returned to its respected flask, sealed with parafilm and stored in the refrigerator until its required use. No flask was stored for more than 1 week. Prior to addition of cells for each experiment, each flask's top was removed, the flasks were re-sterilized via exposure to UV-C light for 1 – 3 hrs and each respected flask top was returned and sealed with parafilm. This approach allows for not only staining the cells for the γ-H2AX assay, but also retains their positioning within the cell culture flask to observe the differences in the DSB distribution at different carbon-ion beam depths as further discussed in the next chapter.

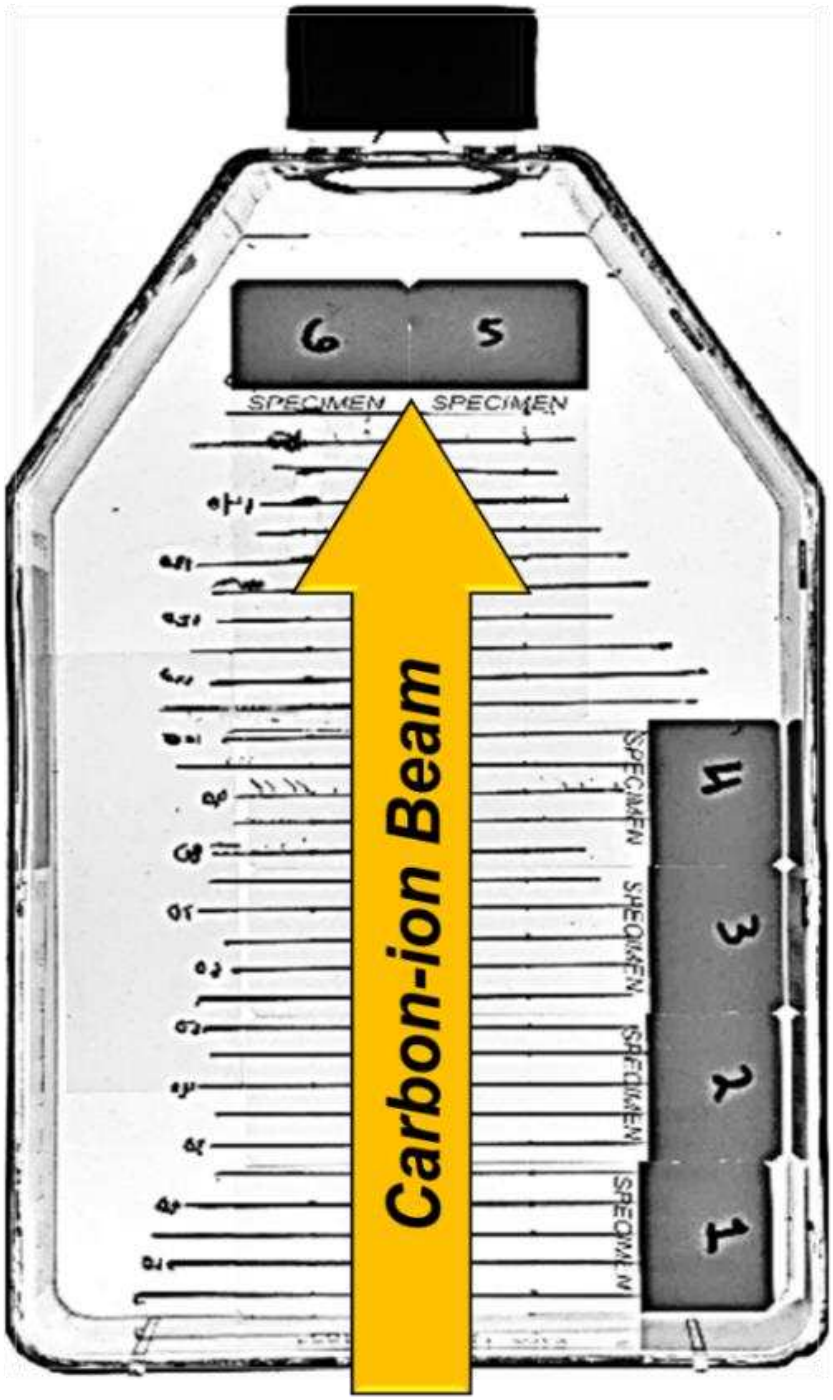


**Figure 1.17. Depiction of the γ-H2AX assay experimental setup.** Prior to addition of cells into the T-175 cell culture flask, 6 poly-L-lysine coated glass microscope slides were placed in the indicated orientation. This allows for the cells to retain their positions within the flask following carbon-ion beam irradiation in order to appropriately examine the DSB distribution at each depth within the carbon-ion beam range.

# CHAPTER TWO

## BIOLOGICAL EFFECTS OF CARBON-IONS AND THEIR ASSOCIATED NUCLEAR FRAGMENTATION-IONS THROUGHOUT THE FULL MONOENERGETIC CARBON-ION BEAM RANGE IN A SINGLE BIOLOGICAL SYSTEM

**Summary:** DNA double-strand breaks (DSBs) are the main actor behind ionizing radiation induced cell death. The number and proximity of DSBs with each other is known to increase with an increase in the linear-energy transfer (LET) of the ionizing radiation. High-LET heavy ions, such as carbon-ions, are known to induce these DSBs in very close proximity to each other, known as complex DSBs, producing a high-LET characteristic track structure in the cellular nucleus that the carbon-ion beam traverses. These complex DSBs are known to be very difficult for the cell to faithfully repair. However, as the carbon-ion beam traverses through the medium it undergoes nuclear interactions producing nuclear fragmentation ions that can travel much further distances than the carbon-ion Bragg peak, resulting in a mixed field of radiation qualities that can produce distinct differences in their biological effects. In addition, the biological effects of the primary carbon-ions can differ depending on the depth in which they are at within the full range of the carbon-ion beam. In this study we utilize our unique method of irradiation that can incorporate the full 290 MeV/n monoenergetic carbon-ion beam range within a single biological system to address the cell survival and DSB distribution at different beam depths as well as identify possible nuclear fragmentation ion-induced DSBs, specifically in the post-Bragg peak regions. Using γ-H2AX as a surrogate marker for DSBs via the γ-H2AX assay we quantified the number of γ-H2AX foci within each cell at each depth by foci cell intensity, individual foci number, foci cluster size and the number of track positive cells as well as the number of tracks per cell. We differentiated between tracks induced by either the primary carbon-ions and possible

fragmentation-ions in the post-Bragg peak region by addresses each of these values for each individual track at each depth. Our cell survival results identified that the biological Bragg peak was at 140 mm, as this depth demonstrated the lowest cell survival fraction regardless of initial treatment dosage. On the other hand, our γ-H2AX assay results demonstrated a significant increase in γ-H2AX foci distribution from 140 – 142.2 mm, termed the Foci Bragg Peak Range, with a peak at 142 mm. In the post-Bragg peak depths (143 – 155 mm) we observed clear differences in the track structures of track positive cells within the same depths and separated these tracks as being produced from possible heavy or light fragmentation ions. Our results suggested that the light-ions can travel further distances than the heavy-ions. Comparison of the γ-H2AX foci results with the cell survival results suggests that cell death from high-LET radiation is likely due to the density of DSBs within the track structures rather than just the presence of a track structure. Results of this study provide fundamental insight into the specificity of the carbon-ion beam to distribute DSBs around its Bragg peak as well as into the biological effects associated within the mixed radiation qualities associated with the full carbon-ion beam range.

## 2.1 Introduction

Carbon-ion ($^{12}$C-ion) beams have been very effective in their use in cancer radiotherapy due to their excellent physical dose-distribution and deposition around the Bragg peak. $^{12}$C-ions at the Bragg peak demonstrate high linear energy transfer (LET) which provides a high density of energy deposition per unit length [280]. This allows for $^{12}$C-ions to more accurately target the tumor tissue, enhance the cell killing effect within the target tissue and induce less damage to the surrounding normal tissue than with the use of protons or other conventional radiotherapy techniques [71, 281, 282]. Heavy particle irradiations, such as carbon-ions, are also known to be

high charge and energy (HZE) ions which use ionizing radiation (IR) to induce DNA damage. While the distribution of the DNA damage within the full $^{12}$C-ion beam range is very important clinically the biological effects of HZE ions is also of great concern for astronaut health as they may be continuously bombarded by these ions during space missions [283, 284].

The most consequential of the IR-induced DNA damage lesions are DNA double-strand breaks (DSBs). These DSBs are known to be the major actor responsible for radiation-induced cell death when left unrepaired [88]. However, misrepair of non-lethal DSBs may give rise to genome instability thus increasing the risk of cancer development [285]. This is important as the outcome of the IR-induced DSB may be associated with the type of radiation quality which is defined by its LET and determined by the particle type, charge and energy [64]. Sparsely ionizing low-LET radiations, such as X-rays, may induce DSBs with associated base damage or single-strand breaks (SSBs) but seldomly portray closely localized DSBs. On the other hand, high-LET heavy ions, such as $^{12}$C- or Fe-ions, deposit their energy within densely ionizing tracks that are created by the particle's traversal through the cell. These high-LET radiations frequently induce close localizations of DSBs that are within a few helical turns of DNA and can be closely localized along the ions track. This formation of multiple close-proximity DSBs following high-LET irradiation has also been demonstrated in prior studies using clusters of γ-H2AX foci as a surrogate for DSBs and high-resolution microscopy [30, 64, 65]. In addition, these closely localized DSBs fall within the category of complex DSBs and are known to be very difficult for the cell to repair [39, 286].

While many studies have focused on the incident $^{12}$C-ions and/or the high-LET $^{12}$C-ions at the Bragg peak, prior studies have mentioned the need for a single biological system capable of incorporating the full $^{12}$C-ion beam length to more accurately portray differences between the

biological effects at each depth within the beams range [222, 287]. This is because the $^{12}$C-ion beam used in carbon-ion radiotherapy (CIRT) is composed of both low- and high-LET regions. CIRT works as a result of when ions penetrate matter, they immediately start transferring their kinetic energy, quantified as LET. The LET increases as the ion slows down until it depletes all its kinetic energy at the end of the ions range, known as the Bragg peak. Following this Bragg peak the LET and deposited dosage dramatically falls. However, the primary $^{12}$C-ions may undergo nuclear inelastic reactions with the cells or other materials they transverse creating fragmentation-ions. These fragmentation-ions can travel at nearly the same velocity and direction as the primary $^{12}$C-ions but are capable of transporting energy over longer distances past the $^{12}$C-ion Bragg peak [288].

Even though these fragmentation-ions have different spatial distributions and biological properties they may still be considered as high-LET radiation but may not be capable of inducing lethal DSBs to the same degree as the primary $^{12}$C-ions. Therefore, they may cause harmful effects to the normal tissues, such as an elevated risk of secondary tumors resulting from the misrepair of the fragmentation-ion induced DSBs [21, 289]. However, observation of the biological effects from the fragmentation-ions in the post Bragg peak regions has been very difficult as obstructions from materials within the beam path or changes in the medium which the beam travels (air, plastic, media, etc.) may alter the accuracy in which these fragments would be induced clinically.

In a recent study conducted by McFadden *et al.*, they sought to investigate the differences in DNA damage between the primary $^{12}$C-ions and the fragmentation-ions by comparing the DSB response in different regions of the $^{12}$C-ion beam, at the $^{12}$C-ion beam entrance (incident $^{12}$C-ions) and spread-out Bragg peak (SOBP) (high-LET $^{12}$C-ions). In this study, they imaged

live cells on 3 cm x 3 cm coverslips expressing fluorescently labeled 53BP1 foci as a surrogate marker for DSBs directly following SOBP $^{12}$C-ion beam irradiation with a confocal microscope placed in the beam path. Prior to irradiation they set their SOBP width to 4 cm (4 to 8 cm depth) in water, and their samples were positioned either at the entrance (0.7 cm depth) or in the SOBP (7.2 cm depth). They concluded that this method allowed for them to separate fragments from the primary $^{12}$C-ions in the SOBP region and assign them to a single focus in order to segregate the DNA damage response from either ion class using the radiation-induced foci (RIF) intensity, number per unit fluence and induction cross section [287].

However, the results of this study may be skewed due to the gap left between the samples as the Z-value (proton number) of the medium that the carbon-ion beam traverses may change as it travels from sample, through the gap and to another sample. Prior studies have demonstrated that due to the nuclear interactions along the $^{12}$C-ion beam path as it traverses through a single medium, only around 50% of the primary $^{12}$C-ions are observed at their Bragg peak [75]. While this method is very good for live cell imaging, this gap may have altered the accuracy of the deposited dosages as well as the actual quantity of fragmentation-ion induced DSBs due to the possibility of lower $^{12}$C-ion nuclear fragmentations being induced via decreased nuclear interactions along the full $^{12}$C-ion beam range.

In order to address these issues and appropriately observe the biological effects from $^{12}$C-ions at increasing depths within the full $^{12}$C-ion beam range as well as from $^{12}$C-ion nuclear fragmentation-ions we have created a novel method capable of observing the DSB distribution within the full monoenergetic $^{12}$C-ion beam range in a single biological system using fluorescently labeled γ-H2AX foci as a surrogate marker for DSBs. To the best of the authors knowledge, this is the first study in which the full $^{12}$C-ion beam range DSB distribution has been

evaluated in a single biological system. Here we demonstrate that our system is capable to not only identify the depths within the beam range that show characteristics of high-LET radiation but also demonstrate how the DSB distribution changes as the beam approaches the Bragg peak as well as can observe the heterogeneity of the DNA damage in the post-Bragg peak depths resulting from the $^{12}$C-ion nuclear fragmentation-ions.

## 2.2 Results

### 2.2.1 Identification of biological Bragg peak depth and the biological effects of the $^{12}$C-ion nuclear fragmentation tail via the cell survival assay

All experimental flasks were irradiated with horizontal orientation to the $^{12}$C-ion beam source (Figure 2.1A). Consistent with our prior work, we observed a decrease in survival at our first evaluated depth with an increase of initial beam entry irradiation treatment dosage [290]. Under all initial beam irradiation treatment dosages of 1, 3, 5 or 10 Gy, the depth of 14.0 cm (140 mm) portrayed the lowest survival fraction (Figures 2.1B–G). Thus, we defined this as the biological Bragg peak depth. This is consistent with a prior study using a different method to observe the full 290 MeV/n $^{12}$C-ion beam range that also reported the lowest survival fractions at the depth of 14.0 cm with initial dosage increases of 0.5, 1 and 2 Gy [71].

Significant increases or decreases in survival fractions within the $^{12}$C-ion beam range for each initial beam entry irradiation treatment dosage was determined by comparing each of the evaluated depths to the first evaluated depth at 1.0 cm (10 mm) from the $^{12}$C-ion beam entry into the flask, representing the incident $^{12}$C-ions (Figures 2.1C-F). A range of significant decrease was observed with initial irradiation treatment dosages of 2, 3 and 5 Gy between the depths of 11.0 – 14.2 cm, 11.0 – 14.2 cm and 8.0 – 14.2 cm, respectively ($P<0.05$). However, 10 Gy $^{12}$C-ion irradiation treatment dosage did not demonstrate a significant decrease. A range of

significant increase was observed with the initial irradiation treatment dosages of 3, 5 and 10 Gy between the depths of 14.4 – 18.0 cm, 14.3 – 18 cm and 14.4 – 18 cm, respectively ($P<0.05$). However, 2 Gy $^{12}C$-ion irradiation treatment dosage did not demonstrate a significant increase.

Survival fractions in depths directly following our biological Bragg peak depth (14.0 cm) decreased as our initial irradiation treatment dosage increased, as portrayed in Figures 2.1C-F with the depths of 14.2 and 14.3 cm indicated by the red and blue arrows, respectively. Our results also demonstrated that the average depth of colony reappearance following the biological Bragg peak increased as the initial irradiation treatment dosage increased (Figure 2.1H). Reappearance of colony formation was observed for the initial treatment dosages of 2, 3, 5 and 10 Gy at the depths of 141.8 ± 0.22 mm, 142.6 ± 0.19 mm, 142.9 ± 0.04 mm and 143.7 ± 0.35 mm, respectively. As compared to the depth of colony reappearance for the initial treatment dosage of 2 Gy, statistical significance increased with an increase in initial treatment dosage of 3, 5 and 10 Gy ($P<0.05$, $P<0.01$ and $P<0.001$, respectively). These findings demonstrate that the biological Bragg peak depth is consistent throughout a wide range of initial treatment dosages and suggest that $^{12}C$-ion nuclear fragmentation may be responsible for cell death in the post-Bragg peak region as these fragmented ions are known to be capable of traveling greater distances with relatively the same velocity [222].

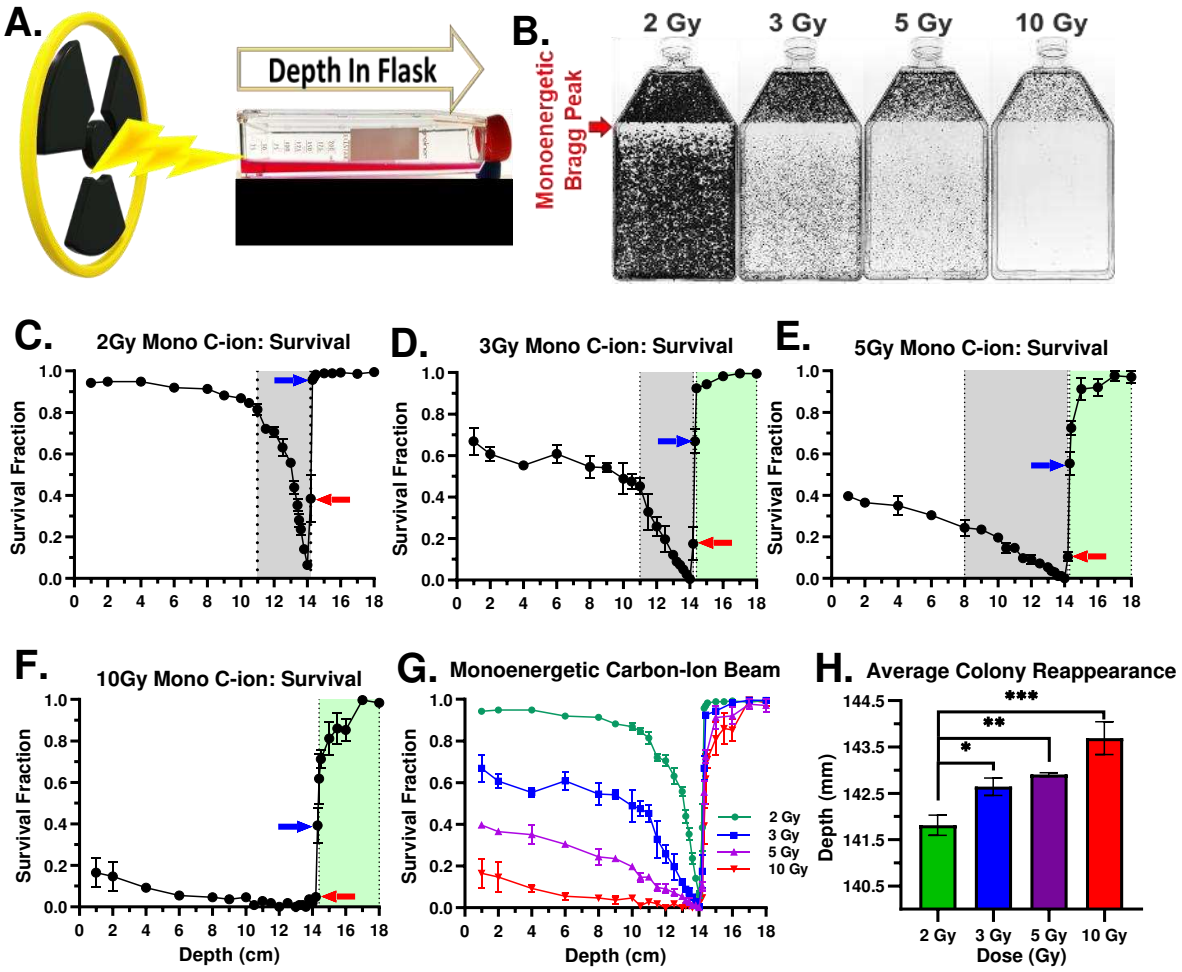


**Figure 2.1. Cell survival vs depth of the full monoenergetic $^{12}$C-ion beam range at increasing initial dosages in CHO-10B2 cells.** **(A)** Horizontal Irradiation setup. **(B)** Images of cell culture flasks following irradiation of 2, 3, 5 or 10 Gy initial dosage. **(C-F)** Survival fraction vs depth following irradiation of each initial dosage. Red and blue arrows indicate survival fraction at 14.2 and 14.3 cm, respectively. Areas highlighted in gray or green represent a significant decrease ($P<0.05$) or significant increase ($P<0.05$) compared to the closest analyzed depth near beam entry at 1.0 cm, Bonferroni multiple comparisons test. **(G)** Merge of all cell survival curves. **(H)** Average colony reappearance depth at each initial dosage. * = $P<0.05$, ** = $P<0.01$, *** = $P<0.001$. Error bars indicate standard errors of the means from a minimum of three independent experiments per each initial dosage.

### 2.2.2 Identification of foci Bragg peak range and DSB distribution across the full beam range following 2 Gy 290 MeV/µm monoenergetic $^{12}$C-ion treatment irradiation

To further investigate the biological effects on a molecular level behind our results obtained in the clonogenic assays we observed the DSB distribution via the γ-H2AX assay at increasing depths within the $^{12}$C-ion beam range. For all γ-H2AX assay experiments we utilized the free cycling CHO-10B2 cell line, which was fixed and stained for γ-H2AX expression at 0.5

hrs following their respected irradiation. This time point was selected as prior studies have indicated the strongest induction of γ-H2AX foci was observed at 0.5 hrs in CHO cells in different stages of the cell cycle, as well as, in multiple tumor cell lines following X-ray, $^{12}$C-ion or Fe-ion beam irradiation [64, 276, 291]. We examined the full $^{12}$C-ion beam range capable in our system (10-155 mm) for experiments involving 2 Gy $^{12}$C-ion irradiation treatment dosage as it contained the largest survival fraction ratio of entrance depth (10 mm) to biological Bragg peak depth (140 mm) in our clonogenic assays (Figures 2.1C, 2.2B,C & 2.3B). We also examined the depths from 115-155 mm (Slides 5 and 6) for experiments involving $^{12}$C-ion beam irradiation with a treatment dosage of 10 Gy as our clonogenic assay results demonstrated that this initial irradiation treatment dosage possessed the largest biological effects post-Bragg peak (Figures 2.1B-D, 2.2D & 2.3C). For experimental controls, we used unirradiated cells as the negative control, 2 Gy and 4 Gy X-ray beams for low-LET positive controls and 2 Gy Fe-ion beams for high-LET positive control (Figure 2.2A).

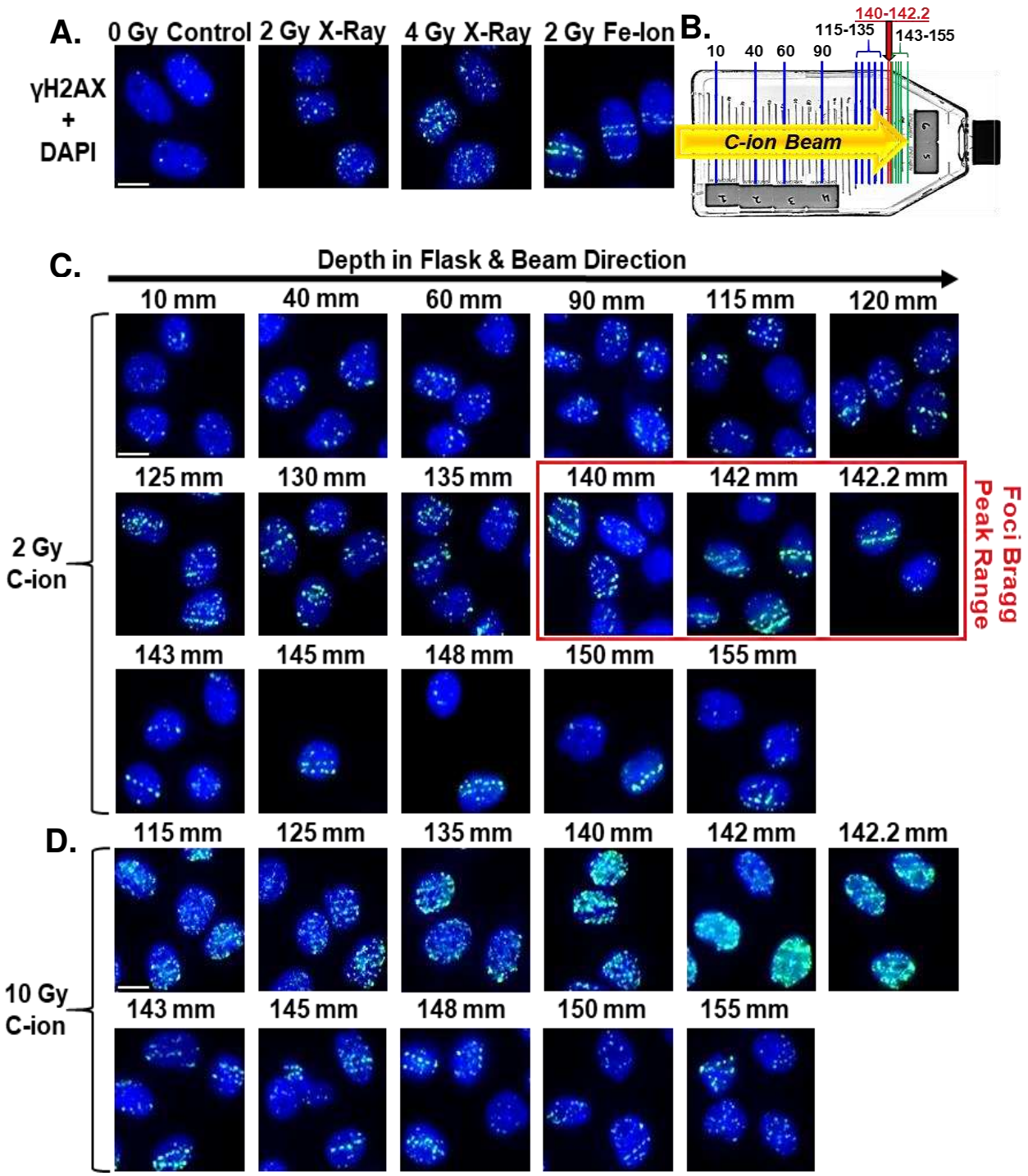


**Figure 2.2. Images of γ-H2AX foci cluster formation in DAPI stained nucleus at each depth without deconvolution following 0.5 hrs post monoenergetic 290 MeV/n $^{12}$C-ion or control irradiations in free cycling CHO-10B2 cells.** **(A)** Cluster formation in controls. Negative control = unirradiated (0Gy). Positive controls = low-LET X-ray of 2 and 4 Gy, and high-LET Fe-ion of 2 Gy. **(B)** Depiction of slide placement to determine beam depth in flask following $^{12}$C-ion irradiation. **(C)** Cluster formation of 2 Gy $^{12}$C-ion full beam range (10mm-155mm). **(D)** Cluster formation of 10 Gy $^{12}$C-ion in proximal, at and post Bragg peak ranges (115-155mm). Indicator bar represents 10 µm. Red box represents depths within the Foci Bragg Peak Range (FBPR).

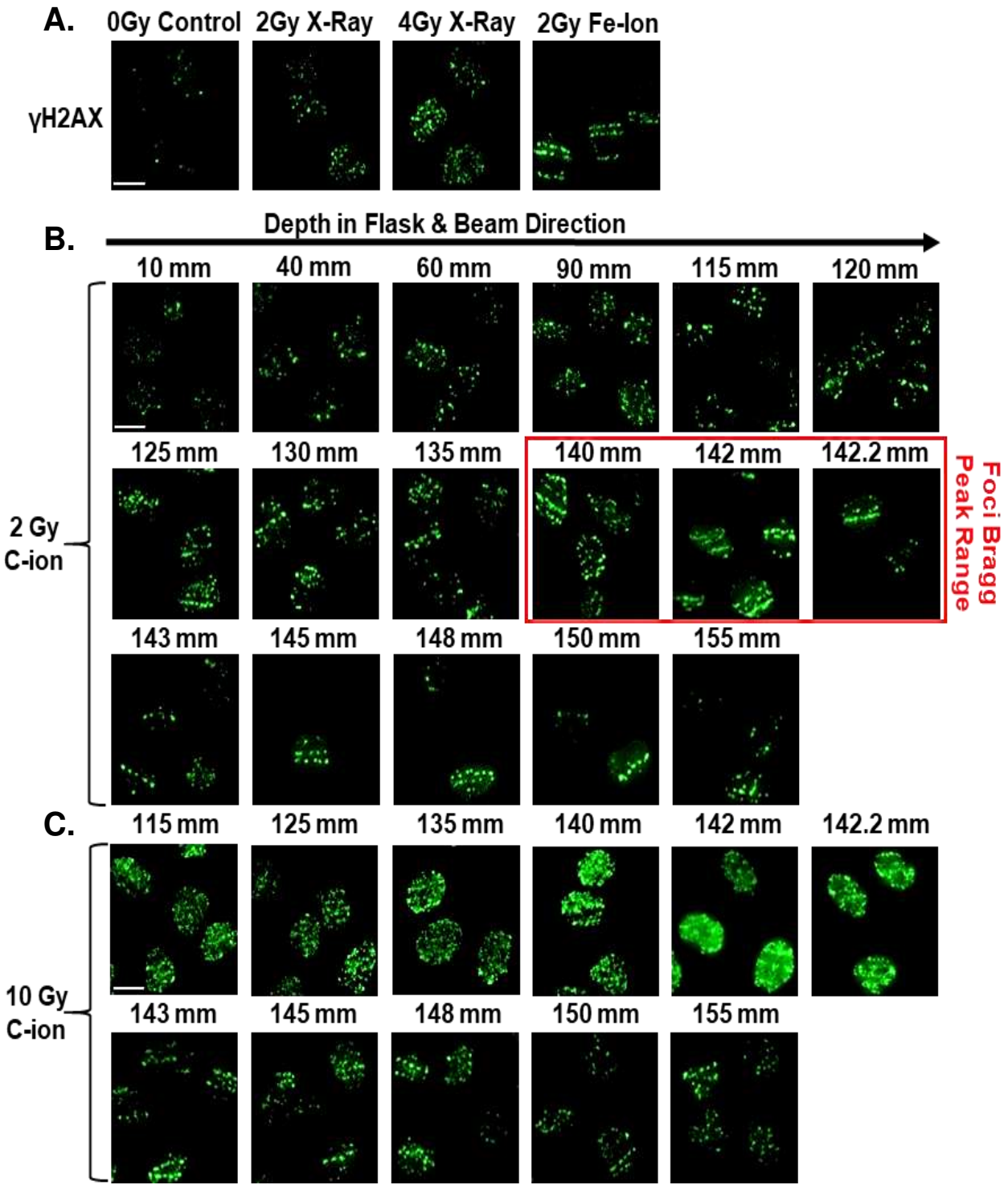


**Figure 2.3. γ-H2AX foci distribution without deconvolution. (A)** Cluster formation in controls. Negative control = unirradiated (0Gy). Positive controls = low-LET X-ray of 2 and 4 Gy, and high-LET Fe-ion of 2 Gy. **(B)** Cluster formation of 2 Gy $^{12}$C-ion full beam range (10mm-155mm). **(C)** Cluster formation of 10 Gy $^{12}$C-ion in proximal, at and post Bragg peak ranges (115-155mm). Indicator bar represents 10 µm.

As shown in Figure 2.4, the acquired z-stack images captured with our Zeiss Axioplan microscope were merged and deconvoluted via Metamorph software prior to γ-H2AX foci cluster analyzation. Briefly for cluster size scoring, the clusters within each cell were counted if they were found to be greater than 0.8, 1.2 or 2.4 µm in width and/or length, i.e., irregular shaped clusters may have lengths >2.4 µm but also contain multiple widths of > 1.2 µm and/or > 0.8 µm. Individual numbers of foci within each cluster were identified as pixel clumps demonstrating higher pixel intensities. Intensity values of each cell was also obtained from the original image without deconvolution to eliminate possible counting bias. For each individual experiment, at least 50 CHO-10B2 cells were analyzed at each depth as well as in each of our controls. As with our clonogenic assay, statistical significance of each depth in these experiments and for controls were determined by comparison to the first evaluated depth closest to beam entry at 10 mm, representing the incident $^{12}$C-ions.

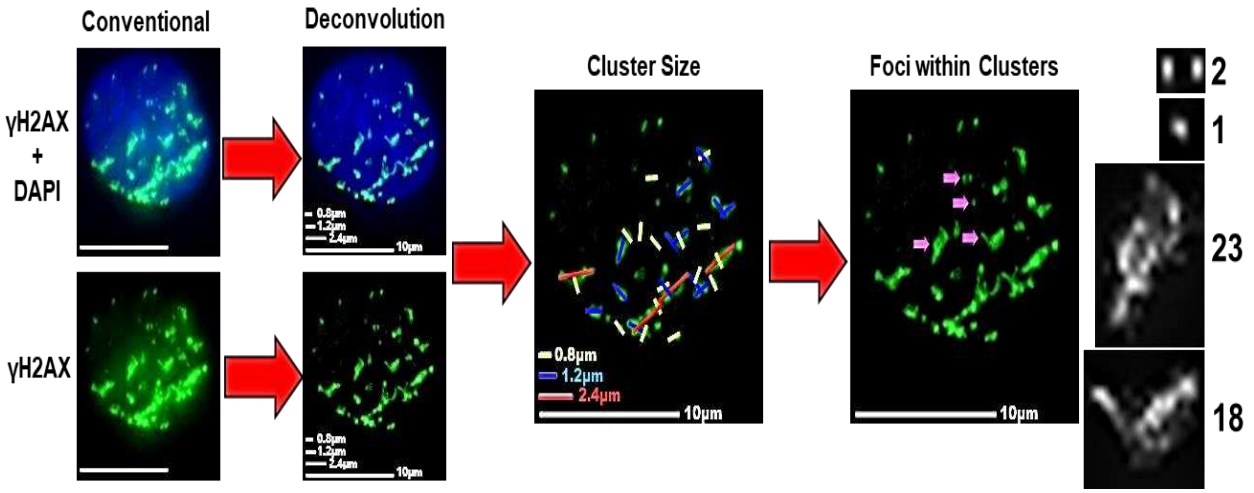


**Figure 2.4. Method of γ-H2AX foci analysis.** Depiction of γ-H2AX + DAPI image using Zeiss Axioplan microscope followed by deconvolution with Metamorph software prior to analysis and method representation of foci cluster size scoring and foci counting in each cell. Foci clusters were scored as greater than 0.8, 1.2 or 2.4 µm in width and/or length represented as yellow, blue or red lines, respectively. Foci counting was determined by differences in pixel intensity across each cluster.

In our positive controls, only 4 Gy X-ray and 2 Gy Fe-ion beams were found to have a significant increase in the mean intensity distribution per cell (A.U.) (10 mm: $7.91x10^5 \pm 6.8x10^4$ A.U. → 4 Gy X-ray: $1.84x10^6 \pm 1.9x10^5$ A.U.; 2 Gy Fe-ion:$.67x10^6 \pm 1.6x10^5$ A.U.) ($P<0.001$). In our unirradiated negative control, a statistically significant decrease was observed ($1.95x10^5 \pm 1.4x10^4$ A.U.) ($P<0.05$) (Figure 2.5A).

Our results following 2 Gy $^{12}$C-ion irradiation treatment dosage reporting the values for mean intensity distribution per cell, the average foci number per cell and the average number of clusters by size per cell at each depth demonstrated a consistent trend in the distribution of the γ-H2AX foci throughout the 2 Gy $^{12}$C-ion experimental beam range (Figures 2.5A,B,D). This observed trend involved a gradual increase in each of the respective values from beam entry depth at 10 mm to 120 mm, which increased at a higher rate as the depth approached the biological Bragg peak at 140 mm, with the first instance of statistical significance beginning at 135 mm ($P<0.05$) and reaching a significant peak value at 142 mm ($P<0.001$). Importantly, our results demonstrated a high degree of significance in these values for the depths ranging between 140 – 142.2 mm, as compared to each respected value at 10 mm ($P<0.001$). Therefore, we defined this range as our Foci Bragg Peak Range (FBPR). Our results also demonstrated similarities in the average number of clusters by size per cell between the depths within the FBPR and our high-LET control, 2 Gy Fe-ion, as these depths and control were the only ones observed to be highly significant for all three cluster sizes ($P<0.001$).

Following the FBPR, a rapid decrease in these values was observed, as portrayed in Figure 2.5A showing a highly significant decrease in the mean intensity values between the depths of 142 and 143 mm (142 mm: $2.45x10^6 \pm 3.6x10^5$ A.U. → 143 mm: $1.40x10^6 \pm 3.7x10^5$ A.U.) ($P<0.001$). Although, for the mean intensity and average foci per cell values our results

demonstrated that the depth of 143 mm was still considered significant as compared to 10 mm (143 mm: 141.0 ± 4.6 A.F./C) ($P<0.01$). Following the depth of 143 mm, these values continued to moderately decrease up to the last evaluated depth at 155 mm in which they returned to values slightly less than those observed at 10 mm (155 mm: $7.68x10^5 \pm 5.6x10^4$ A.U., 77.4 ± 5.0 A.F./C). On the other hand, beginning at 148 mm until our last evaluated depth of 155 mm our results demonstrate that each depth within this range contained smaller values of the average number of clusters with sizes >0.8 and >1.2 µm than those reported at 10 mm (10mm: 8.47 ± 1.8 Cls>0.8, 3.05 ± 1.3 Cls>1.2 µm → 148mm: 7.19 ± 1.1 Cl>0.8, 2.51 ± 0.5 Cl>1.2 µm).

Next, each depth within our experimental 2 Gy $^{12}$C-ion beam range was further examined for the percentage of cells containing foci numbers within the ranges of <100, 100 – 149, 150 – 200 or >200, as well as, for the percentage of cells containing at least one foci cluster >2.4 µm (Figures 2.5C,D). Consistent with the forementioned trend, our results demonstrated that as the beam approaches the biological Bragg peak depth of 140 mm, which displayed the lowest percentage of cells containing <100 foci/cell (1.21 ± 2.1%), there is a continuous shift in the percentage of cells falling within the higher foci number ranges as well as a continuous increase in the percentage of cells containing foci clusters >2.4 µm.

Prior to the FBPR, depths from 125 – 135 mm were found to have a significant increase in cells containing foci within the range of 100 – 149 foci/cell (10mm: 14.43 ± 13.6% → 125mm: 46.52 ± 15.5, 135mm: 46.94 ± 1.9%) ($P<0.01$). Moreover, the percentage of cells containing foci within the range of 150 – 200 foci/cell were found to have a significant increase between the depths of 135 – 143 mm (10mm: 0.00 ± 0.0% → 135mm: 24.33 ± 7.7%, 143mm: 21.11 ± 1.4%) ($P<0.01$). However, the depths between 130 – 143 mm were found to have a significant increase in the percentage of cells containing clusters >2.4 µm (10mm: 0.54 ± 0.9

%Cl>2.4 → 130mm: 24.63 ± 6.3, 143mm: 47.93 ± 12.1%Cl>2.4) ($P<0.05$ – $P<0.001$, respectively). Depths within the FBPR (140 – 142.2 mm) along with our high-LET control, 2Gy Fe-ion, were the only depths observed displaying a significant increase in the percentage of cells containing >200 foci per cell with a peak value at 142 mm (10mm: 0.00 ± 0.0% → 140mm: 57.23 ± 24.9, 142mm: 69.91 ± 12.2, 142.2mm: 40.24 ± 11.5%; 2Gy Fe-ion: 30.15 ± 6.6%) ($P<0.001$).

Collectively, these results demonstrate that at precisely 10 mm prior to the FBPR the $^{12}$C-ion beam rapidly increases in the number of induced DSBs within the cells the $^{12}$C-ions transverse, as represented by the γ-H2AX foci within each cell. The number of DSBs then reaches its peak at 142 mm. Within 1 mm following this peak there is a sudden drop in the amount of induced DSBs that continues to steadily decline the further away the beam proceeds. Furthermore, depths within the FBPR closely resembled that of our high-LET positive control, 2 Gy Fe-ion, demonstrating that these depths contain $^{12}$C-ions with LET values which may be similar or greater than those of the incident Fe-ions LET values.

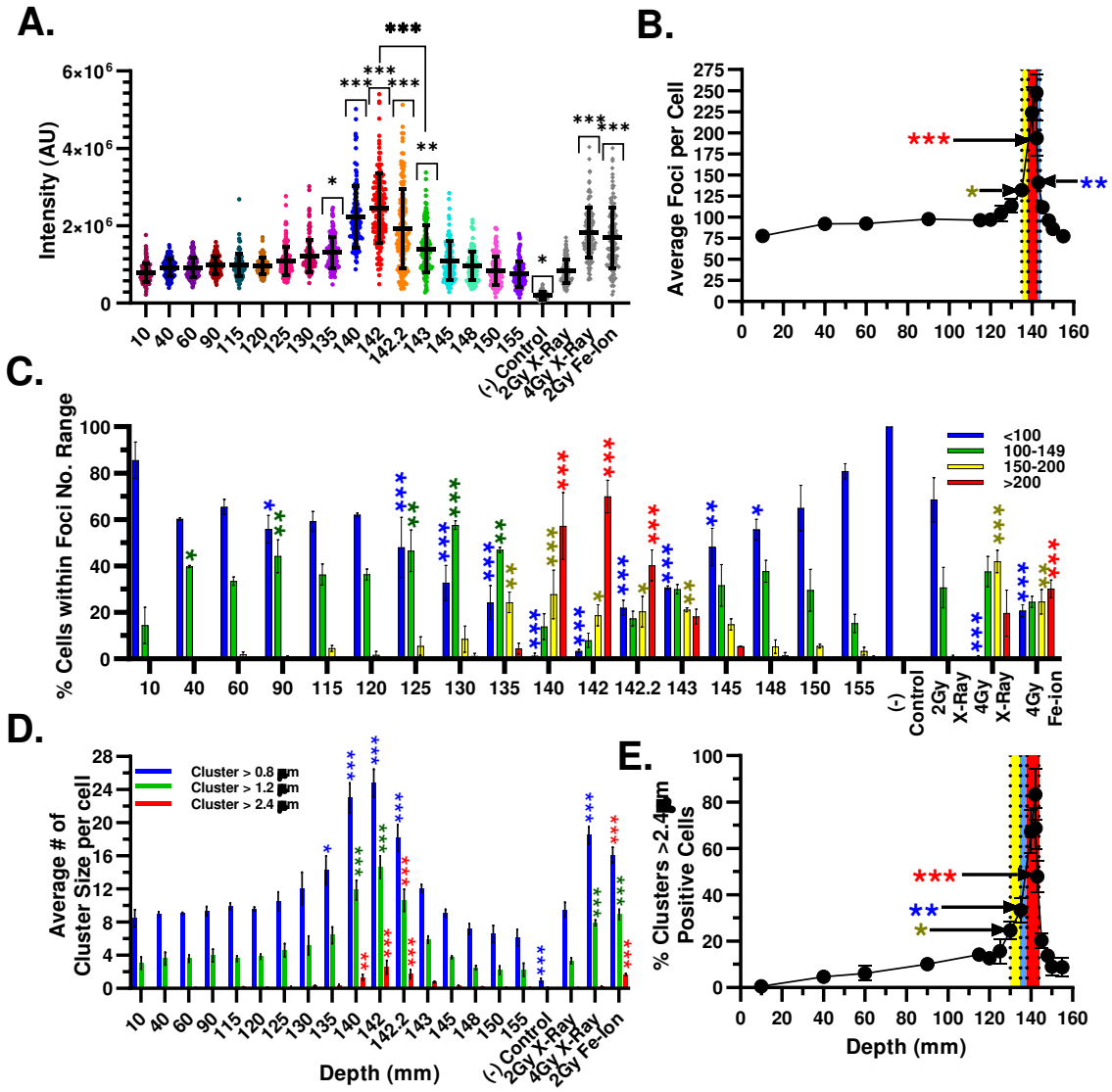


**Figure 2.5. Full beam range of γ-H2AX foci number and cluster size vs depth following 2Gy monoenergetic 290 MeV/n $^{12}$C-ion irradiation.** **(A)** Intensity distribution per cell at each respected depth in flask and in each control. **(B)** Average number of foci per cell at each respected depth in flask. **(C)** % of cells within each foci number range of <100 (blue), 100-149 (green), 150-200 (yellow) and >200 (red) foci/cell. **(D)** Average number of cluster sizes per cell within each range of 0.8 (blue), 1.2 (green) or 2.4 (red) µm in width and/or length. **(E)** % of cells containing clusters >2.4 µm at each depth. Statistical significance was determined at each depth as compared to its respected value or indicated range at 10 mm, Bonferroni multiple comparisons test, * = P<0.05, ** = P<0.01, *** = P<0.001. Figures **(B,E)** statistical significance is indicated in yellow, blue or red for *, ** or ***, respectively. Error bars indicate standard deviation **(A)** or the standard errors of the means **(B-D)** from a minimum of 50 cells analyzed per each depth per experiment and at least three independent experiments per each irradiation treatment.

### 2.2.3 Identifying depths within the 2 Gy $^{12}$C-ion beam range containing high-LET track structures

High-LET radiation is known to deposit a large amount of energy in a small distance which causes dense ionizations along a track, while low-LET radiation is known to deposit their energy more sparsely within a cell [292]. Therefore, to further identify the depths within the carbon-ion beam range which contain high-LET $^{12}$C-ions capable of inducing these track structures, we quantitatively evaluated each depth for the percent of high-LET track positive cells and analyzed each of the track positives cells intensity (Figures 2.6A,B). High-LET track structures were observed from 115 mm until our last capable experimental depth at 155 mm following 2 Gy $^{12}$C-ion irradiation treatment dosage. As expected within our controls, only the high-LET positive control, 2 Gy Fe-ion, portrayed track positive cells which also demonstrated a highly significant increase in both the percentage of track positive cells and mean value of the intensity distribution as compared to the initial track positive depth at 115 mm following 2 Gy $^{12}$C-ion irradiation treatment dosage (115mm: 14.21 ± 2.3%, 1.19x$10^6$ ± 4.3x$10^5$ A.U. → 2Gy Fe-ion: 74.76 ± 2.9%, 1.93x$10^6$ ± 7.1x$10^5$ A.U.) ($P<0.001$).

Our results demonstrated a significant increase in the percentage of cells containing track structures in the depths between 135 – 143 mm (37.9 ± 14.7% – 40.5 ± 13.3%) and in the track positive intensity distribution from 140 – 143 mm (2.43x$10^6$ ± 8.0x$10^5$ A.U. – 1.75x$10^6$ ± 6.1x$10^5$ A.U.) ($P<0.05$). Consistent with our high-LET positive control, our FBPR (140 – 142.2 mm) also demonstrated a high degree of significance for both values (73.1 ± 6.4% – 57.6 ± 5.2%; 2.43x$10^6$ ± 8.0x$10^5$ A.U. – 2.48x$10^6$ ± 9.2 A.U.) with a peak at 142 mm (81.3 ± 8.1%; 2.61x$10^6$ ± 8.7 A.U.) ($P<0.001$). We further confirmed the peak depth to be at 142 mm by irradiating our cells with 10 Gy $^{12}$C-ion beam irradiation treatment dosage and examined the

average intensity of all cells at each track positive depth identified following 2 Gy $^{12}$C-ion beam irradiation treatment dosage (Figure 2.6C).

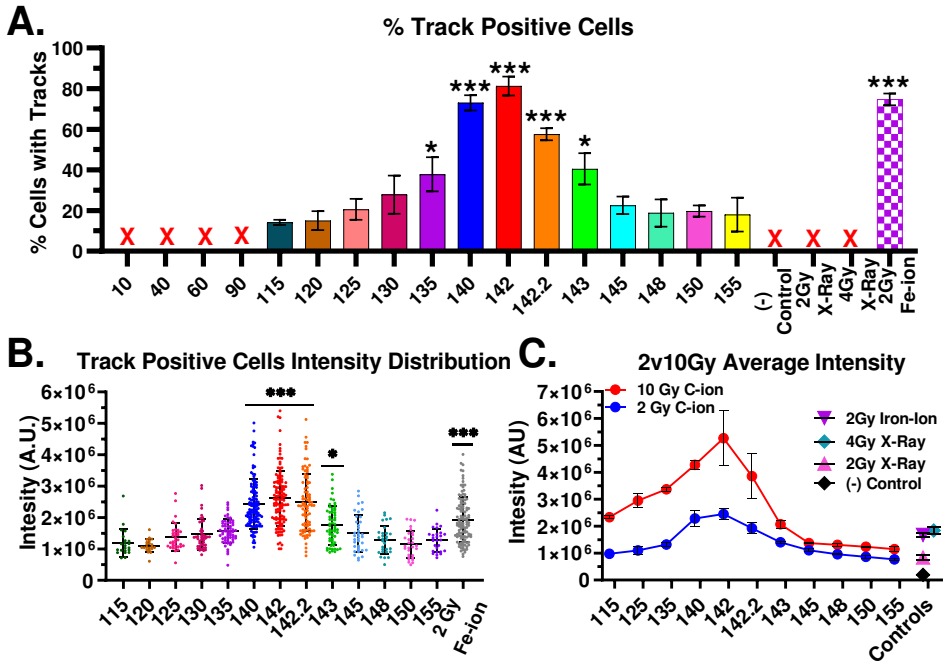


**Figure 2.6. Identification of track positive depths in the $^{12}$C-ion beam range. (A)** % of cells containing at least one-track structure at each depth or in control. **(B)** Intensity distribution of track positive cells. **(C)** Average intensity comparison of 2Gy and 10Gy $^{12}$C-ion beam in track positive depths identified in A and controls. Statistical significance of each depth as compared to its respected value at 115 mm. Bonferroni multiple comparisons test, * = P<0.05, ** = P<0.01, *** = P<0.001. Error bars indicate standard errors of the means from a minimum of 50 individual cells analyzed per depth per experiment from at least three independent experiments per irradiation treatment.

Within the track positive depths following 2 Gy $^{12}$C-ion irradiation treatment dosage, our results also demonstrated an increase in the percentage of cells containing multiple tracks, reaching a peak at 142 mm and then declining in the number of tracks per cell in the proceeding depths (Figure 2.7A). Cells containing 4 tracks/cell were only observed in the depths within the FBPR (140 – 142.2 mm) as well as in our positive control, 2 Gy Fe-ion. As compared to 115 mm, only the depths of 140 and 142 mm were observed to have a high degree of significant increase in the percentage of cells containing 2, 3 and 4 tracks/cell (140 mm: 21.0 ± 4.2, 24.08 ± 5.2 and 9.3 ± 2.4%; 142 mm: 32.0 ± 7.0, 24.62 ± 6.7 and 8.7 ± 5.2%, respectively) (P<0.001).

Although, 140 mm was observed to have a higher percentage of cells with 4 tracks/cell than 142 mm. Moreover, we observed a shift throughout the FBPR as the highest percentage of cells fell from 3 to 2 to 1 track/cell for the depths of 140, 142 and 142.2 mm, respectively.

Our results also identified two key differences in the individual tracks within the cells between each of our FBPR depths. These differences involved the foci number ranges per track and the foci cluster sizes within each track. From the initial track positive depth of 115 mm, we observed a consistent increase in the number of tracks containing 60 – 99 foci/track with a significant increase ranging between 135 – 142 mm with a peak at 140 mm (115mm: 1.00 ± 1.7%; 135mm: 20.67 ± 1.5%, 140 mm: 55.67 ± 7.4%, 142mm: 43.67 ± 17%) ($P<0.01$ – $P<0.001$, respectively) (Figure 2.7B). Tracks containing 100 – 150 foci/track had a significant increase throughout all FBPR depths with a peak at 142 mm (115mm: 0.00 ± 0.0%; 140mm: 19.67 ± 17.6%, 142mm: 34.0 ± 13.1%, 142.2mm: 23.0 ± 5.3 %) ($P<0.05$, $P<0.001$ and $P<0.01$, respectively). Tracks containing >150 foci/track, demonstrated a notable increase throughout our FBPR with a statistically significant peak at 142.2 mm (115mm: 0.00 ± 0.0%; 142.2mm: 23.0 ± 5.3%) ($P<0.05$). Out of all track positive depths, 142.2 mm also contained the lowest percentage of its tracks within the range of <60 foci/track and the highest percentage of its tracks within the ranges of 100 – 150 and >150 foci/track, possibly indicating that the $^{12}C$-ions at this depth contained the highest LET values (Figure 2.7C).

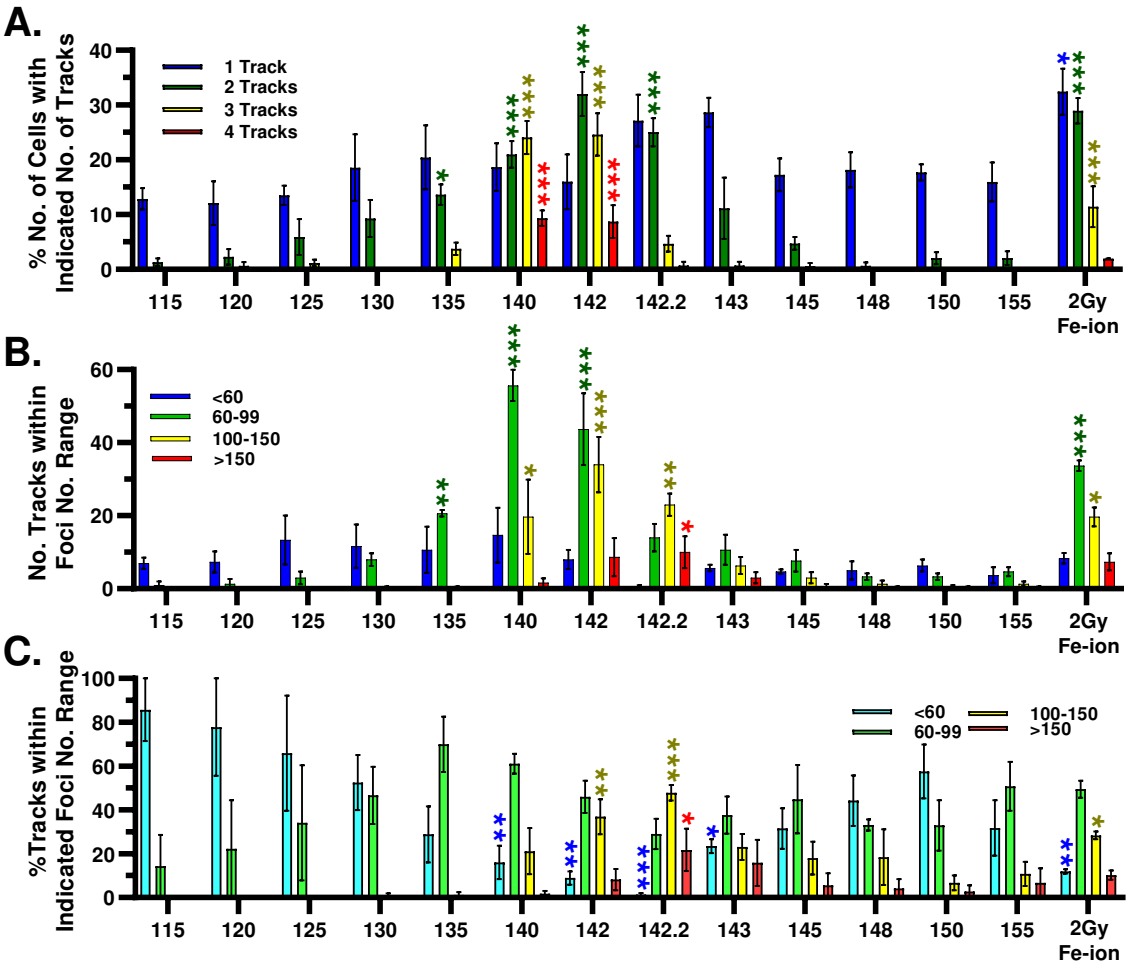


**Figure 2.7. Analysis of track positive depths in the $^{12}$C-ion beam range. (A)** % of cells containing either 1 (blue), 2 (green), 3 (yellow) or 4 (red) tracks at each track positive depth following 2Gy $^{12}$C-ion or Fe-ion beam irradiation. **(B)** Foci number ranges per track per track positive depth. **(C)** % of tracks within indicated foci number range. Statistical significance of each depth as compared to its respected value at 115 mm. Bonferroni multiple comparisons test, * = P<0.05, ** = P<0.01, *** = P<0.001. Error bars indicate standard errors of the means from a minimum of 50 individual cells analyzed per depth per experiment from at least three independent experiments per irradiation treatment.

Next, we examined the foci cluster sizes within each track (Figure 2.8A). Our results demonstrated that within each track, the average number of foci clusters with sizes >0.8, 1.2 and 2.4 µm all portrayed a significant increase from 142 – 143 mm with a peak at 142.2 mm (115mm: 6.47 ± 1.9, 2.72 ± 0.6 and 0.16 ± 0.2 → 142mm: 9.78 ± 1.2 (P<0.05), 5.92 ± 0.8 (P<0.001) and 1.05 ± 0.6 (P<0.05); 142.2mm: 12.11 ± 1.8, 7.78 ± 1.7 and 1.40 ± 0.7 (all P<0.001); 143mm: 9.61 ± 1.3 (P<0.05), 5.53 ± 1.0 (P<0.01) and 1.00 ± 0.4 (P<0.05),

respectively). On the other hand, all depths within the FBPR demonstrated to have a significant increase in the number of tracks containing at least one cluster of size >2.4 µm, with a peak at 142 mm (115mm: 1.00 ± 1.0 #Cl>2.4 → 140mm: 36.67 ± 17.5 #Cl>2.4, 142mm: 60.0 ± 31.6 #Cl>2.4, and 142.2mm: 35.67 ± 7.5 Cl>2.4) (P<0.01, <0.001, <0.01, respectively) (Figure 2.8B). This shift is likely due to a higher percentage of tracks containing more than two clusters of size >2.4 µm were observed at the depths of 142.2 and 143 mm (Figure 2.8C). Furthermore, 142.2 mm was also the most similar to our high-LET control, 2 Gy Fe-ion, regarding the distribution in percentages of tracks containing 0, 1, 2 and >2 clusters of size >2.4 µm/track.

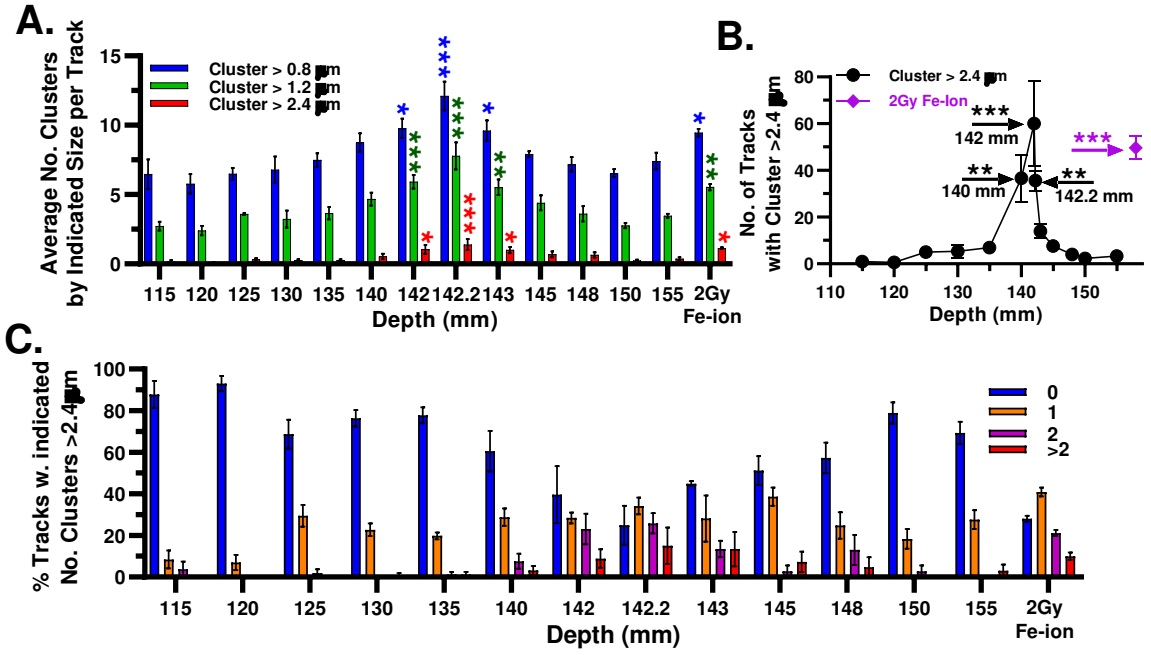


**Figure 2.8. Analysis of tracks by γ-H2AX foci cluster size. (A)** Average number of clusters that are >0.8, >1.2 or >2.4 size µm per track. **(B)** Number of tracks containing at least one cluster with size >2.4 µm. **(C)** % of tracks containing indicated number of clusters with size >2.4 µm. Statistical significance of each depth as compared to its respected value at 115 mm. Bonferroni multiple comparisons test, * = P<0.05, ** = P<0.01, *** = P<0.001. Error bars indicate standard errors of the means from a minimum of 50 individual cells analyzed per depth per experiment from at least three independent experiments per irradiation treatment.

These results demonstrate that the peak depth for the high-LET track structures is at 142 mm and suggest that while the tracks/cell may decrease from the proximal to distal end of the FBPR (140 to 142.2 mm), the density of ionizations causing the DSBs in the tracks at the distal

end and adjacent depth (142.2 and 143 mm) may increase. Thus, the tracks at these depths may be the result of higher-LET $^{12}$C-ions or possibly heavy fragmentation ions traveling further than the Bragg peak.

### 2.2.4 Analysis of all cells within Post-foci Bragg peak range depths

The individual cells within each post-FBPR depths (143 – 155 mm) varied widely in their γ-H2AX foci distributions. To further evaluate these differences, it was important to investigate these depths following a higher initial treatment dosage of 10 Gy $^{12}$C-ion beam irradiation. Our results demonstrated a decrease in the mean intensity values of all cells at each depth as the $^{12}$C-ion beam progressed further in the post-FBPR direction regardless of initial irradiation treatment dosage (Figure 2.9A). However, the mean intensity values of cells within all post-FBPR depths following 10 Gy $^{12}$C-ion irradiation treatment dosage were found to be significantly higher than those irradiated with 2 Gy $^{12}$C-ion treatment dosage ($P<0.001$). On the other hand, this was not observed for the mean intensity values of only track positive cells as our results only demonstrated a significant increase in the depths of 143, 148 and 150 mm with the degree of significance decreasing as the depths proceeded further post-FBPR ($P<0.001$, $P<0.01$, $P<0.05$, respectively) (Figure 2.9B).

Under both irradiation dosages our results demonstrated a significantly higher average number of clusters >2.4 μm at 143 mm as compared to the furthest evaluated post-FBPR depth of 155 mm for both initial irradiation treatment dosages of 2 and 10 Gy $^{12}$C-ion beams (Figure 2.9C). We also observed that the percentages of cells within certain foci number ranges demonstrated significant differences only at the depths of 143 and 145 mm (Figure 2.9D). Moreover, a significant decrease in the percentage of cells containing <100 foci/cell was observed at both of these depths (**2Gy:** 155 mm: 80.79 ± 5.6% → 143 mm: 30.65 ± 1.3%; 145

mm: 48.19 ± 14.0%) (P<0.001, P<0.05, respectively) (**10Gy:** 155 mm: 47.13 ± 13.4% → 143 mm: 5.33 ± 4.6%; 145 mm: 19.36 ± 8.4%) (P<0.001, P<0.01, respectively). On the other hand, a significant increase was observed in the percentage of cells containing 150 – 200 and >200 foci/cell only at 143 mm (**2Gy:** 155 mm: 3.30 ± 5.6, 0.63 ± 1.1% → 143 mm: 21.11 ± 1.3, 18.2 ± 5.4%, respectively) (P<0.001) (**10Gy:** 155 mm: 14.54 ± 13.4, 7.09 ± 1.9%; 143 mm: 33.79 ± 3.7, 44.33 ± 7.6%, respectively) (P<0.05, P<0.001, respectively). In addition, 143 mm following 10 Gy $^{12}$C-ion irradiation treatment dosage also demonstrated a higher percentage of cells in the ranges of 150 – 200 and > 200 foci/cell as compared to our high-LET positive control, 2 Gy Fe-ion (10Gy $^{12}$C-ion: 33.80 ± 3.7%, 44.33 ± 7.6%; 2Gy Fe-ion: 24.59 ± 9.2%, 30.15 ± 6.6%, respectively). However, 145 mm only demonstrated a significance increase following 2 Gy $^{12}$C-ion irradiation treatment dosage in the percentage of cells containing 150 – 200 foci/cell (145 mm: 14.83 ± 14.0%) (P<0.01).

While there were many similarities in the depths that were found to be significant, there were key differences in the highest percentage of cells falling into certain foci number ranges following each respected irradiation treatment dosage. Our results demonstrated that only following the treatment of 2 Gy $^{12}$C-ion irradiation dosage the highest percentage of cells were in the range of <100 foci/cell at all post-FBPR depths. On the other hand, following 10 Gy $^{12}$C-ion irradiation treatment dosage, the highest percentage of cells at 143 mm was in the range of >200 foci/cell and the depths from 145 – 150 mm had their highest percentage of cells being in the range of 100 – 149 foci/cell, while only the depth of 155 mm had its highest percentage of cells as <100 foci/cell. These results are consistent with the survival fractions observed throughout the post-Bragg peak depths following each respected dosage and suggest that cells containing foci numbers within the ranges of <100 foci/cell and somewhere between 100 – 149 foci/cell are

likely to survive. In addition, our results demonstrate that the contribution of the primary $^{12}$C-ions or their possible fragmentation ions to induce DSBs reduces the further away they are from the FBPR.

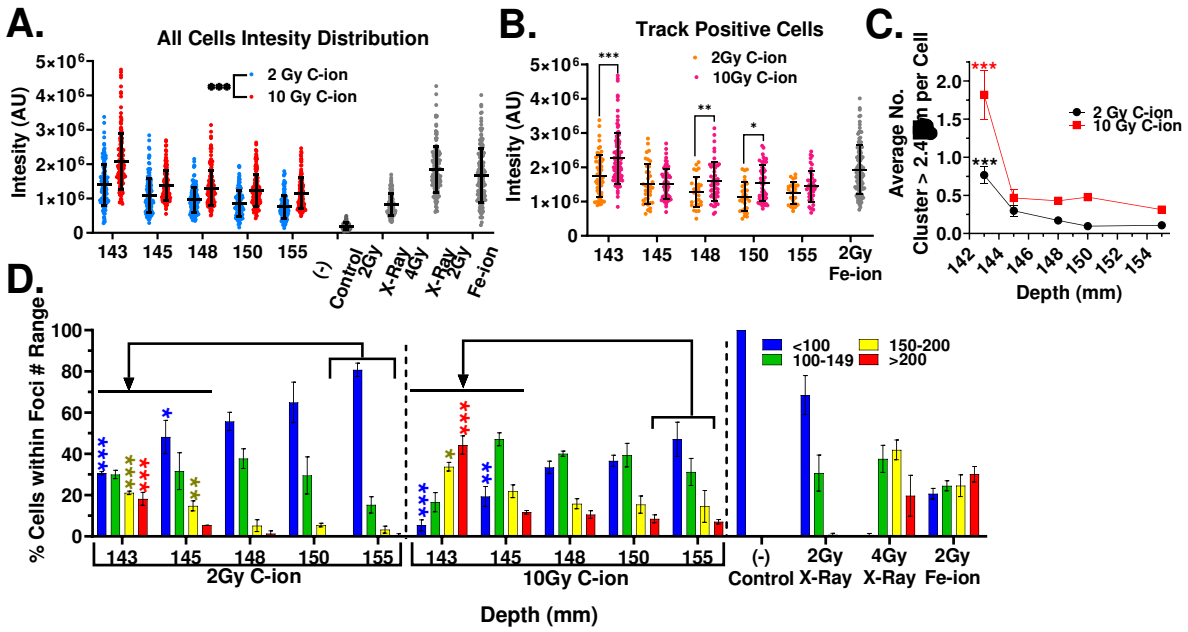


**Figure 2.9. Evaluating all post-FBPR cells following 2 or 10 Gy $^{12}$C-ion irradiations.** **(A)** Intensity distribution of all cells at each post Bragg peak depth. **(B)** Intensity distribution of only track positive cells at each post Bragg peak depth. **(C)** Average number of clusters >2.4 µm following 10 Gy (Red) or 2 Gy (Black) $^{12}$C-ion irradiation. **(D)** % Cells within each indicated foci number range per depth. **(A,B)** Statistical significance between 2 and 10 Gy mean intensity values at each depth determined by Student standardized two-tailed t-test. **(C,D)** Statistical significance as compared to each respected value at 155 mm. Bonferroni multiple comparisons test, * = P<0.05, ** = P<0.01, *** = P<0.001. Error bars indicate standard errors of the means from a minimum of 50 cells analyzed per depth per experiment and at least three independent experiments per irradiation treatment.

### 2.2.5 Analysis of post-FBPR track positive cells and high-LET track structures

While high-LET track structures were detected in all post-FBPR depths (143 – 155 mm) following either 2 or 10 Gy $^{12}$C-ion beam irradiation treatment dosages, we were able to observe distinctively visible differences between the track positive cells within the same depth. This was likely due to the property differences between each of the $^{12}$C-ion nuclear fragmentation ions, as it has been previously reported that heavier-ions produce denser foci distributions within in their tracks than the lighter-ions [223] (Figure 2.10). Using the same methodology for track structure

analysis as before, we evaluated each post-FBPR depth to differentiate between the heavy-ion and light-ion induced track structures and statistical significance was determined as compared to the furthest evaluated depth at 155 mm for each respected value and respected treatment dosage.

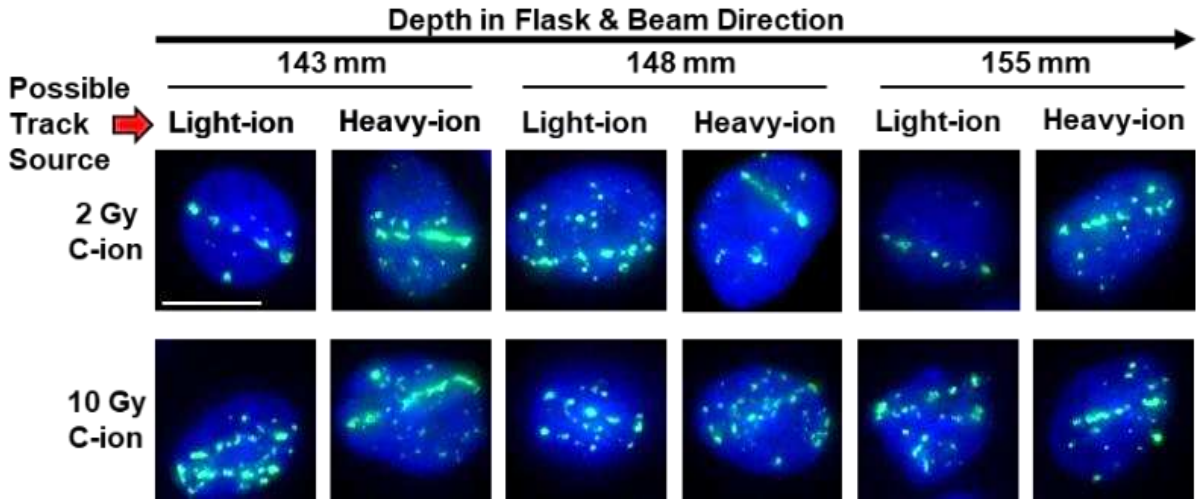


**Figure 2.10. Differences in the post-Bragg peak track structure within the same depth.** Image portrayal of post Bragg peak track structures variation due to $^{12}$C-ion nuclear fragmentation following either 2Gy (Top) or 10Gy (Bottom) $^{12}$C-ion irradiation. Possible track structure sources defined by density of foci within each track with lighter ion induced tracks having lower density (Left) and heavier ion induced tracks having higher density (Right).

Evaluation of each post-FBPR depth by the percentage of cells containing 0, 1, 2, 3 or 4 tracks/cell following both 2 and 10 Gy initial $^{12}$C-ion beam irradiation treatment dosages demonstrated a correlation between an increasing percentage of cells containing 0 tracks with a decrease in percentage of cells containing 1 or more tracks per cell as the depths proceeded further post-FBPR up to 148 mm, where they remained relatively consistent in the number of tracks per cell until our furthest evaluated depth at 155 mm (Figure 2.11A). At 143 mm, following 2 Gy $^{12}$C-ion irradiation treatment dosage, our results demonstrated a significantly lower percentage of cells containing 0 tracks and a significantly higher percentage of cells containing 1 track (155 mm: 81.99 ± 8.3%, 15.95 ± 6.2%; 143 mm: 59.52 ± 13.3%, 28.66 ± 4.7%, respectively) ($P<0.05$).

On the other hand, at both 143 and 145 mm following 10 Gy $^{12}$C-ion irradiation treatment dosage, there was a significantly lower percentage of cells containing 0 tracks (155 mm: 72.07 ± 4.0%; 143 mm: 29.15 ± 8.1%; 145 mm: 54.10 ± 3.4%) ($P<0.001$, $P<0.01$, respectively). Although, 143 mm demonstrated a significantly higher percentage of cells containing 2, 3 and 4 tracks/cell (155 mm: 4.47 ± 2.7%, 0.00%, 0.00%; 143 mm: 25.18 ± 4.2%, 11.26 ± 1.1%, 2.64 ± 2.3%, respectively) (2 and 3 tracks/cell $P<0.001$, 4 tracks/cell $P<0.05$). In addition, 143 mm with 10 Gy $^{12}$C-ion irradiation treatment dosage produced very similar percentages of cells containing each number of tracks/cell as with our high-LET positive control, 2 Gy Fe-ion (**0 Tracks:** 10Gy $^{12}$C-ion: 29.15 ± 8.1%, Fe-ion: 25.24 ± 2.9%; **1 Track:** 10Gy $^{12}$C-ion: 31.78 ± 7.1%, Fe-ion: 32.4 ± 7.3%; **2 Tracks**: 10Gy $^{12}$C-ion: 25.18 ± 4.2%, Fe-ion: 28.94 ± 4.0%; **3 Tracks:** 10Gy $^{12}$C-ion: 11.26 ± 1.1%, Fe-ion: 11.44 ± 6.4%; **4 Tracks:** 10Gy $^{12}$C-ion: 2.64 ± 2.3%, Fe-ion: 1.94 ± 0.1%).

Our post Bragg peak results also demonstrated that following 2 Gy $^{12}$C-ion irradiation treatment dosage, no depths containing tracks within any of our foci number ranges were found to be significant with respect to 155 mm (Figure 2.11B). On the other hand, following 10 Gy $^{12}$C-ion irradiation treatment dosage, the depth of 143 mm demonstrated a significantly greater number of tracks within the foci number ranges of 60 – 99 and 100 – 150 foci/track (155 mm: 9.33 ± 2.1, 2.33 ± 2.1 tracks; 143 mm: 35.67 ± 5.0, 21.0 ± 8.7 tracks, respectively) ($P<0.001$). However, these were not found to be significant when observed as the percentage of tracks containing these foci number ranges at 143 mm (Figure 2.11C). Our results also demonstrated that following 10 Gy $^{12}$C-ion irradiation treatment dosage, 143 mm portrayed a similar number of tracks within these foci per track number ranges with our high-LET control, 2 Gy Fe-ion (33.67 ± 2.5, 19.67 ± 4.5 #tracks, respectively).

We observed that both 2 Gy and 10 Gy $^{12}$C-ion irradiation treatment dosages demonstrated a similar number of tracks within the highest foci number/track range, >150 foci/track, at 143 and 145 mm (143 mm: 3.0 ± 2.6, 3.67 ± 3.8; 145 mm: 0.67 ± 1.2, 0.67 ± 1.2 # of tracks, respectively). However, following 145 mm the number of tracks within this range remained around 0.33 tracks for 2 Gy $^{12}$C-ion irradiation treatment dosage, in contrast to 10 Gy $^{12}$C-ion irradiation treatment dosage, in which it remained around double this value at 0.67 tracks. Moreover, following 10 Gy $^{12}$C-ion irradiation treatment dosage, the highest percentage of tracks were those within the foci number range of 60 – 99 at all post-FBPR depths. On the other hand, following 2 Gy $^{12}$C-ion irradiation treatment dosage, this range was the highest for all depths except at 148 and 150 mm, which contained the highest percentage of tracks within the range of <60 foci/track.

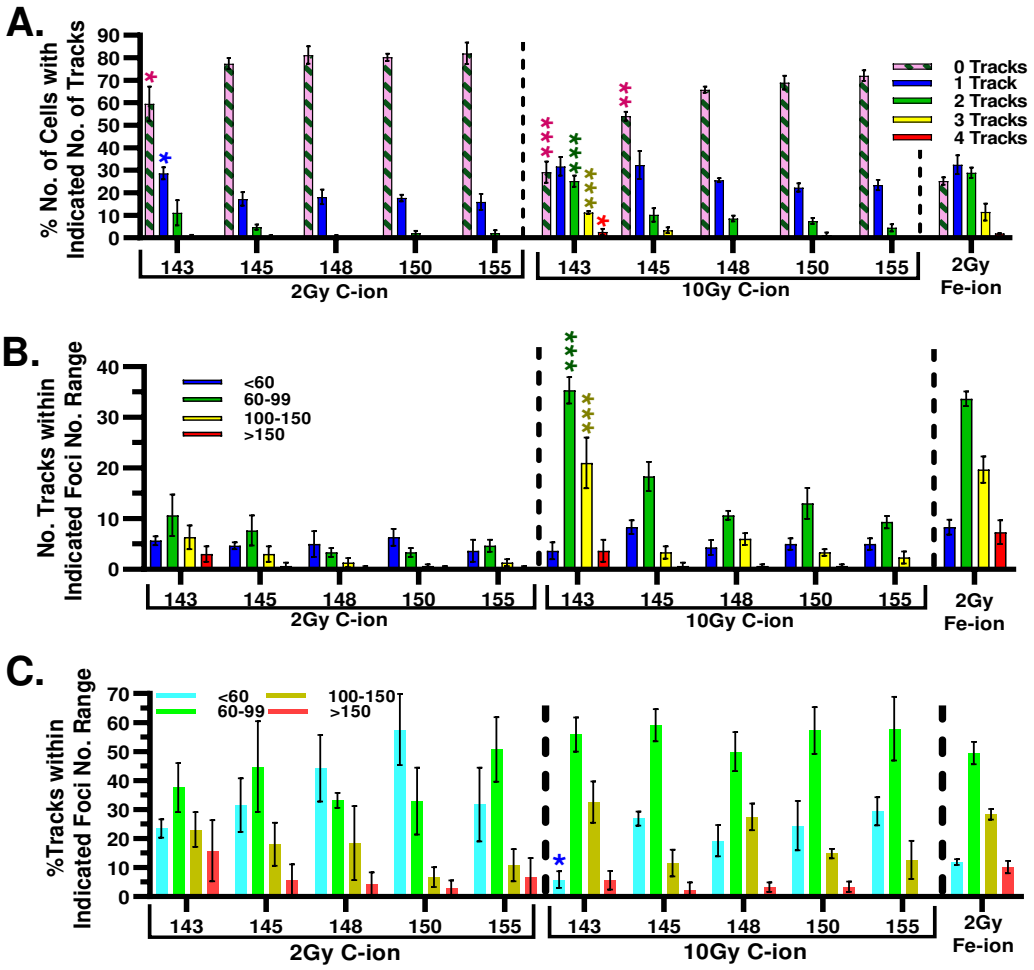


**Figure 2.11. Post Bragg peak tracks per cell and Foci number range per track. (A)** % number of cells with 0, 1, 2, 3 or 4 tracks in post Bragg peak depths. **(B)** Foci number ranges per track in post Bragg peak depths. **(C)** % Tracks within each indicated foci number range per depth. Statistical significance as compared to its respected value at 155 mm for each respective dosage by Bonferroni multiple comparisons test * = P<0.05, ** = P<0.01, *** = P<0.001. Error bars indicate standard errors of the means from a minimum of 50 cells analyzed per depth per experiment and at least three independent experiments per irradiation treatment.

### 2.2.6 Differentiating post-FBPR high-LET track structures by foci cluster size per track

We further differentiated the high-LET track structures by their cluster size, as larger cluster sizes represented denser foci distributions within the heavy-ion induced tracks. Our results demonstrated that the average number of clusters of each cluster size of >0.8 µm, >1.2 µm and >2.4 µm per track were similar regardless of initial treatment dosage at all post-FBPR depths (Figure 2.12). This was most notable at the depth of 143 mm (**2 Gy:** 9.61 ± 1.3, 5.53 ± 1.0, 1.00 ± 0.4 clusters/track; **10 Gy:** 9.18 ± 1.2, 5.53 ± 1.2, 1.01 ± 0.4 clusters/track,

respectively). Although, 2 Gy and 10 Gy $^{12}$C-ion irradiation treatment dosages demonstrated differences in which cluster size per track was observed to be significant as compared to each initial beam treatment dosage's respected furthest evaluated depth of 155 mm. Following 2 Gy $^{12}$C-ion irradiation treatment dosage, at the depth of 143 mm, a significant increase was observed for the clusters per track of sizes > 0.8 µm and >1.2 µm (155 mm: 7.41 ± 1.0, 3.46 ± 0.3 clusters/track, respectively) (P<0.05). On the other hand, at the same depth following 10 Gy $^{12}$C-ion irradiation treatment dosage, the clusters per track of sizes > 0.8 µm and >2.4 µm were found to be significantly greater (155 mm: 6.97 ± 0.7, 0.39 ± 0.2 clusters/track, respectively) (P<0.05).

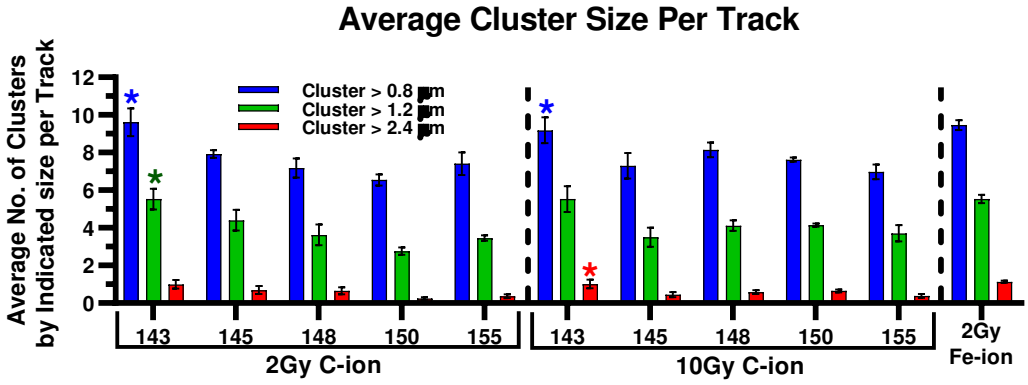


**Figure 2.12. Differentiating track structures by cluster size.** Average cluster size per track in post Bragg peak depths. Statistical significance as compared to its respected value at 155 mm for each respective dosage by Bonferroni multiple comparisons test * = P<0.05, ** = P<0.01, *** = P<0.001. Error bars indicate standard errors of the means from a minimum of 50 cells analyzed per depth per experiment and at least three independent experiments per irradiation treatment.

Next, we examined each of our cluster sizes per track individually and observed what percentage of tracks contained a specific number range of each cluster size. With cluster size of >0.8 µm, our results demonstrated that all post-FBPR depths, regardless of initial $^{12}$C-ion beam irradiation treatment dosage, had the highest percentage of tracks in the range containing 5 – 10 clusters/track (Figure 2.13A). Although, both 2 and 10 Gy $^{12}$C-ion irradiation treatment dosages demonstrated similar values of the percentage of tracks containing 11 – 15 clusters of size >0.8

um at 143 mm as with our high-LET positive control, 2 Gy Fe-ion (2Gy $^{12}$C-ion: 21.89 ± 15.4%; 10Gy $^{12}$C-ion: 24.80 ± 9.0%; 2Gy Fe-ion: 25.10 ± 4.6%).

However, clusters of size >1.2 µm differed in their percent distribution per track between 2 and 10 Gy $^{12}$C-ion irradiation treatment dosages. Following 10 Gy $^{12}$C-ion irradiation treatment dosage, all post-FBPR depths had their highest percentage of tracks within the range of 3 – 6 clusters >1.2 µm/track. In addition, only with 10 Gy $^{12}$C-ion irradiation treatment dosage, the depth of 143 mm demonstrated to be most like our positive high-LET control, 2 Gy Fe-ion. On the other hand, following 2 Gy $^{12}$C-ion irradiation treatment dosage, the highest percentage of tracks switched from containing 3 – 6 clusters >1.2 µm/track to containing greater than 3 clusters >1.2 µm/track at the depth of 150 mm (Figure 2.13B).

Evaluation of the largest cluster size (>2.4 µm) demonstrated a significant decrease in the number of cluster size >2.4 µm positive tracks from 143 – 145 mm following 10 Gy $^{12}$C-ion irradiation treatment dosage but was not observed following 2 Gy $^{12}$C-ion irradiation treatment dosage for these respected depths (10Gy: 143 mm: 41.67 ± 8.1 → 145 mm: 10 ± 3 Cl >2.4 µm Tracks) ($P<0.001$) (Figure 2.13D). Although, we observed a significantly lower percentage of tracks containing 0 clusters >2.4 µm/track at the depth of 143 mm as compared to 155 mm following both 2 and 10 Gy $^{12}$C-ion irradiation treatment dosages (155 mm: 69.31 ± 9.3, 66.16 ± 9.4%; 143 mm: 44.91 ± 2.1, 34.89 ± 9.2%, respectively) ($P<0.05$) (Figure 2.13C). Moreover, 143 mm with each respected treatment dosage demonstrated the highest percentage of tracks containing 2 or greater than 2 clusters >2.4 µm/track in all post-FBPR depths. However, following 10 Gy $^{12}$C-ion irradiation treatment dosage, 143 mm was the only depth with its highest percentage of tracks containing 1 cluster >2.4 µm/track and again was observed to be the most like the positive high-LET control, 2 Gy Fe-ion. In addition, following 2 Gy $^{12}$C-ion

irradiation treatment dosage, the depths of 150 and 155 mm demonstrated a large spike in the percentage of tracks not containing any clusters >2.4 µm/track, which was consistent with the switch in the highest percentage of tracks containing the lowest number range for clusters >1.2 µm/track appearing at these depths.

These results demonstrated that the post-FBPR induced track structures may be differentiated by cluster size as the heavy ion induced tracks may contain one or more clusters of size >2.4 µm/track. This is consistent with the $^{12}$C-ion induced track structures observed in Figure 2.8C, with an increase in this cluster size/track up to its peak value as the beam approached the end of the FBPR (142.2 mm) following 2 Gy $^{12}$C-ion irradiation treatment dosage.

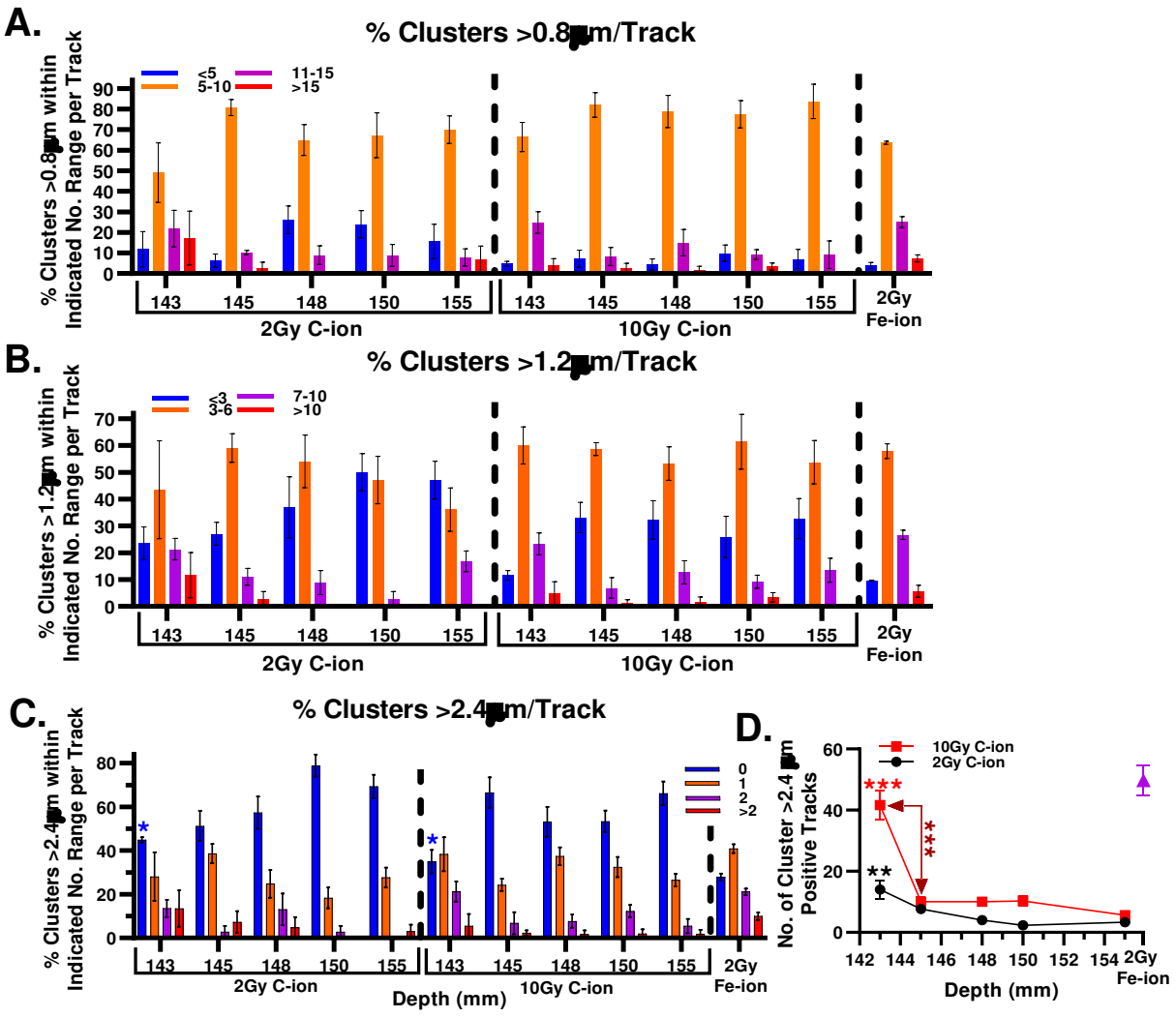


**Figure 2.13. Individual cluster size per track**. **(A – C)** % clusters of sizes >0.8, >1.2 or >2.4 µm within each respected indicated number range per track. **(D)** Number of Tracks with at least one cluster >2.4 µm. Statistical significance as compared to its respected value at 155 mm unless specified for each respective dosage by Bonferroni multiple comparisons test * = P<0.05, ** = P<0.01, *** = P<0.001. Error bars indicate standard errors of the means from a minimum of 50 cells analyzed per depth per experiment and at least three independent experiments per irradiation treatment.

### 2.2.7 DSB Distribution Correlation with Cell Survival

To address the similarity between the γ-H2AX foci distribution with the survival fractions at each respected depth we examined the average intensity per cells, percentage of cells containing clusters that were of size >2.4 µm and the percentage of track positive cells following either 2 or 10 Gy $^{12}$C-ion initial irradiation treatment dosages (Figures 2.14A,B). This γ-H2AX

foci data was selected for comparison as it was the least plausible data that may be subjected to differences within its interpretation, i.e., better image resolution may provide with more accurate foci number counts.

Correlation with survival was then determined by evaluating the combined 2 and 10 Gy $^{12}$C-ion data within three ranges in respect to the biological Bragg peak depth (140 mm), as previously determined via the clonogenic assay. The first evaluated range was from the first evaluation depth at beam entry that represented the incident $^{12}$C-ions up to the biological Bragg peak depth that represented the highest-LET $^{12}$C-ions (10 – 140 mm). Other evaluated ranges consisted of the depths post-biological Bragg peak (142 – 155 mm) and depths within the full foci experimental evaluated range (10 – 155 mm) (Figure 2.14C).

Our results demonstrated that for the depths ranging up to the biological Bragg peak depth, the percentage of track positive cells had the highest correlation with cell survival ($R^2$=0.99), closely followed by the percentage of cells containing clusters of size >2.4 µm ($R^2$=0.95) and that the lowest correlation was with average foci/cell intensity ($R^2$ = 0.89). However, the inverse was observed for the depths within both the post biological Bragg peak range as well as the full foci experimental range, as the highest correlation was determined to be with the average foci/cell intensity ($R^2$=0.87, 0.71) followed by percent clusters >2.4 µm positive cells ($R^2$=0.82, 0.57) and percent track positive cells ($R^2$=0.73, 0.52), respectively. These results suggest that cell death from high-LET radiation may not only depend on the presence of a track structure but the density of ionizations within the track structure(s), i.e., containing large cluster sizes.

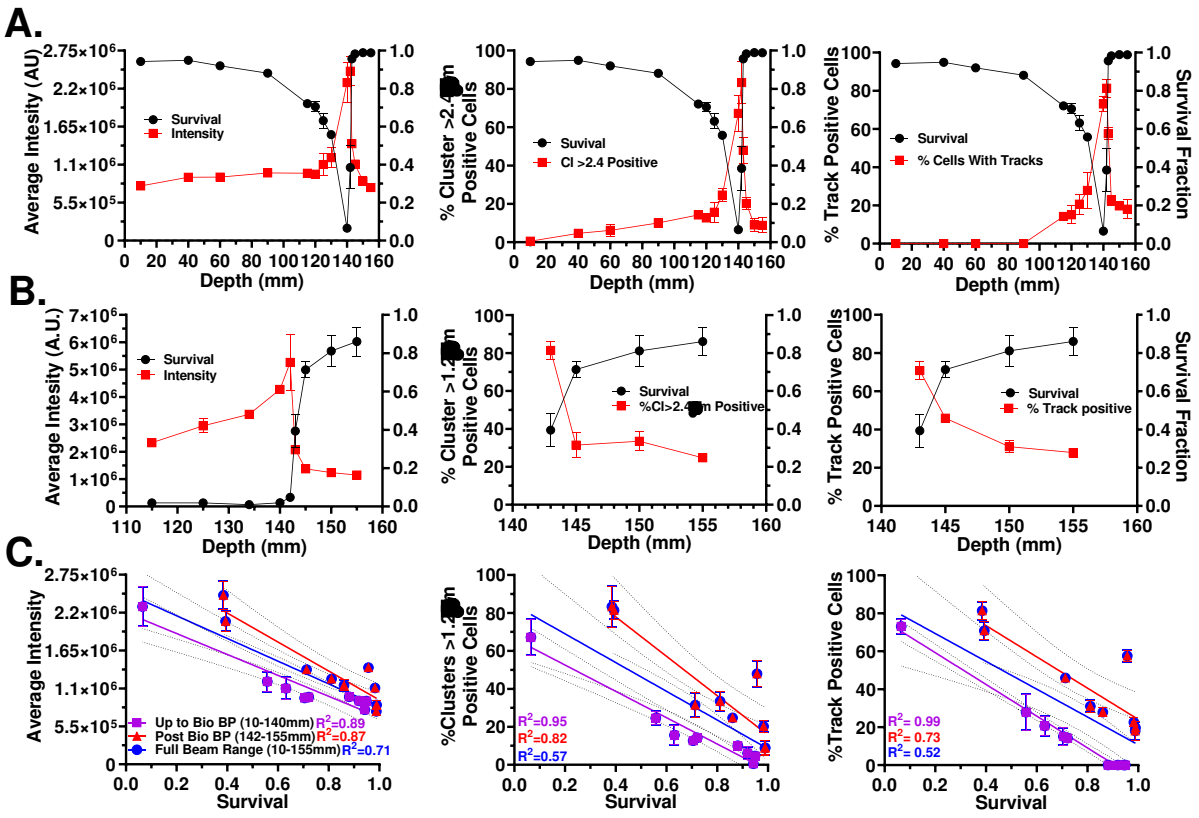


**Figure 2.14. γ-H2AX foci comparison with Survival. (A)** 2 Gy $^{12}$C-ion irradiation showing full beam range comparison of survival (**Black**) with average intensity (Left), % Cluster > 2.4µm positive cells (Middle), and % Track positive cells (Right) (**Red**). **(B)** 10 Gy $^{12}$C-ion irradiation comparison of survival (**Black**) with average intensity within the track positive depth range (Left), post FBPR depths % Cluster > 2.4µm positive cells (Middle), and post FBPR depths % Track positive cells (Right) (**Red**). **(C)** Correlation between survival and average intensity (Left), % Cluster > 2.4µm positive cells (Middle), and % Track positive cells (Right) incorporating both 2 and 10 Gy $^{12}$C-ion data. Correlation addressed as up to biological Bragg peak (10 – 140mm) (**Purple**), Post biological Bragg peak (142 – 155mm) (**Red**), and Full beam range (10 – 155mm) (**Blue**) with respected $R^2$ values. $R^2$ values were derived from simple linear regression analysis via GraphPad Prism 8 software. Error bars indicate standard errors of the means from a minimum of 50 individual cells analyzed per depth per experiment from at least three independent experiments per irradiation treatment.

## 2.3 Discussion

We have developed a novel method to observe the biological effects with minimal interference within the full 290 MeV/n monoenergetic $^{12}$C-ion beam range and have demonstrated that this method can be used to investigate the DSB distribution within cells at increasing beam depths, differentiate between radiation quality (low- vs high-LET), as well as identify differences between the $^{12}$C-ion nuclear fragmentation induced high-LET track

structures in the post-Bragg peak region, previously not possible in a single biological system. Our results also provide key insights behind how the DSB distribution can influence cell survival at each depth within the $^{12}$C-ion beam range.

Our cell survival results demonstrated an excellent representation of the $^{12}$C-ion beam's depth vs dose distribution which is consistent with prior studies describing this beam to have a sharp increase in the deposited dosage the closer the beam approaches to the $^{12}$C-ion Bragg peak [71, 290] (Figure 2.15). We observed a sharp decrease in survival fractions the closer the beam approached to the depth containing the lowest survival fraction at 140 mm in depth (Figure 2.1G). Therefore, we defined this depth at 140 mm as the biological Bragg peak. Following the biological Bragg peak, a sharp increase in survival was observed. However, there was a notable decrease in survival in the post-Bragg peak depths with an increase in initial irradiation treatment dosage (Figures 2.1C – F). One possible reason for this may be due to the number of $^{12}$C-ions that travel further than the biological Bragg peak increases as the initial irradiation treatment dosage increases. Another possible reason explaining this observation may be due to $^{12}$C-ion nuclear fragmentation, as these fragmentation ions are known to be capable of traveling longer distances past the Bragg peak [288]. Therefore, as the initial dosage increases, the number of fragmentation-ions may also increase.

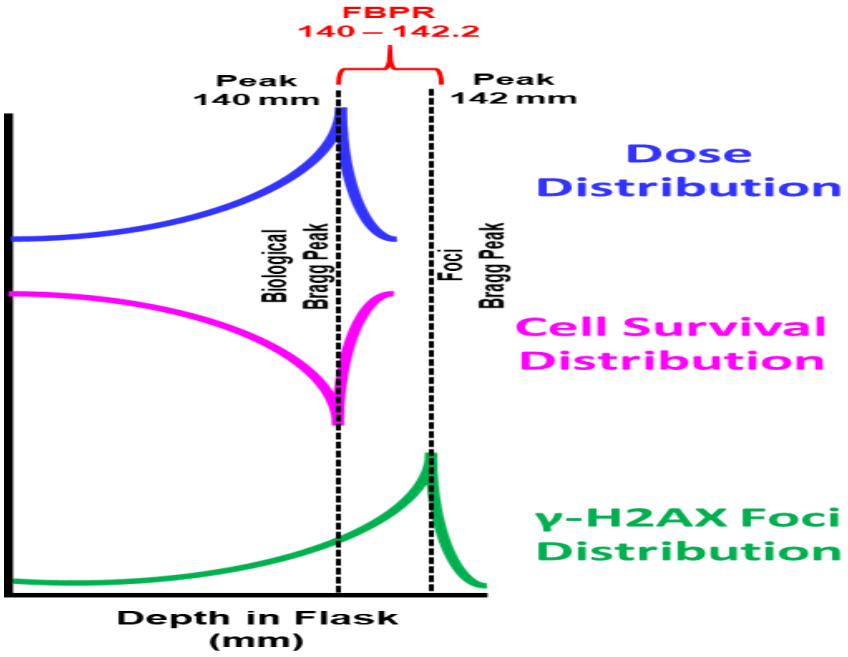


**Figure 2.15. Schematic representation of differences in peak depths.** Dose and cell survival fraction distribution demonstrate similar distributions with peak at 140 mm (Biological Bragg peak depth). γ-H2AX foci distribution demonstrated a peak depth at 142 mm. Foci Bragg peak range (FBPR) identified as between the depths of 140 – 142.2 mm.

To further investigate the biological effects behind our cell survival results on a molecular level, we analyzed the DSB distribution at increasing depths throughout the full $^{12}$C-ion beam range. DSB distribution was important for us to analyze as DSBs are known to be the main actor responsible for radiation-induced cell death [88]. To do this we fluorescently stained the cells for γ-H2AX foci, as a surrogate marker for DSBs and examined the γ-H2AX foci clusters at increasing depths within the beam range following either 2 or 10 Gy initial $^{12}$C-ion beam irradiation dosages (Figures 2.2 & 2.3) [293]. In addition, prior studies have demonstrated that the γ-H2AX foci clusters following high-LET heavy particle irradiation are larger and more diffuse than those arising after low-LET X-ray irradiation and are also deposited in tracks [294, 295]. It has also been demonstrated that γ-H2AX foci peak at 0.5 hrs post irradiation [296, 297]. Thus, we evaluated the γ-H2AX foci at this time point since the focus of the current study was to examine the initial biological effects induced by both the low- and high-LET components within

the full $^{12}$C-ion beam range. Our results agree with these prior studies as the γ-H2AX foci clusters in our low-LET positive control cells following 2 and 4 Gy X-ray irradiations were observed to be more spherical in shape and smaller than those arising in our high-LET positive control cells following 2 Gy Fe-ion beam irradiations as these foci were larger, more irregular shaped and mostly deposited into tracks. Due to the irregular shape of the foci clusters following the high-LET irradiation, we also concluded that the most accurate representation of the cluster sizes was to measure them by their lengths and/or widths.

To help distinguish between the radiation qualities within the $^{12}$C-ion beam range we separated the clusters sizes within the cells at each depth as being either >0.8, >1.2 or >2.4 μm (Figure 2.4). The reasoning behind each foci cluster size and procedure for identifying individual foci numbers within each cluster is further explained in materials and methods section. Intensity values of each cell were also obtained from the original image without deconvolution to eliminate possible counting bias (Figure 2.5A). This approach allowed us to differentiate between individual cells as well as individual tracks by foci number ranges and foci cluster sizes at each depth.

The mean values of the intensity distribution/cell, average foci/cell and the percentage of cells containing clusters of size >2.4 μm/cell demonstrated an inversely proportional trend with our cell survival results. These values began to rapidly increase 15 mm prior to reaching their peak value at 142 mm and significantly decreased 1 mm following this peak ($P<0.001$), which was followed by a steady decline in each value as the depths proceeded further away (Figures 2.5A,B,E). We observed that the depths ranging from 140 – 142.2 mm demonstrated a high degree of significant increase for each of these respected values with the peak again being at 142 mm ($P<0.001$). Therefore, we referred to this range as our foci Bragg peak range (FBPR). In

addition, all depths within our FBPR portrayed their highest percentage of cells being those containing >200 foci/cell (Figure 2.5C). Although, following the biological Bragg peak depth (140 mm), the percentage of cells containing <100 foci/cell increased as the depths progressed further away. This may explain why we observed an increase in survival fractions at these depths in our cell survival assay, even though the foci data demonstrated a consistent peak in foci/cell at 142 mm.

We then evaluated each depth for the presence of high-LET characteristic track structures. These track structures first appeared at 115 mm and were observed up to our last evaluated depth at 155 mm. A high degree of significant increase in both the percentage of track positive cells and the track positive cell mean value of intensity distribution was observed throughout the FBPR, again we observed a peak in both of these values at 142 mm ($P<0.001$) (Figures 2.6A,C). To confirm this peak depth, as it differed from our biological Bragg peak depth at 140 mm, we irradiated our cells with 10 Gy $^{12}$C-ion beam irradiation treatment dosage. However, the density of the γ-H2AX foci clusters made 10 Gy irradiated cells unfeasible to distinguish between the number of foci within each cell as well as the number of tracks per cell in the depths prior to the distal end of the FBPR (142.2 mm) (Figure 2.2D). Although, we were able to observe the average intensity of the foci clusters within the cells at each depth. The average intensity values confirmed that the peak depth was indeed at 142 mm, which was followed by a steep drop off in the values of average foci cluster intensity (Figure 2.6C).

Following 2 Gy $^{12}$C-ion irradiation treatment dosage, we demonstrated that the percentage of cells containing a greater number of tracks per cell increased as the beam approached the peak depth at 142 mm (Figure 2.7A). While a high degree of significant increase was observed in the percentage of cells containing 2 tracks/cell throughout the FBPR depths,

only 140 and 142 mm demonstrated a high degree of significant increase in the percentage of cells containing 3 and 4 tracks/cell ($P<0.001$). Interestingly, cells containing 4 tracks/cell were only observed in the FBPR as well as in our high-LET positive control, 2Gy Fe-ion. This suggested that the $^{12}C$-ions in this range may contain similar or greater LET values than that of the incident Fe-ions. We also observed that as the beam proceeded through the FBPR, the highest percentage of cells at each depth fell from 3 to 2 to 1 track(s)/cell (from 140 to 142 to 142.2 mm, respectively). Following the FBPR, we observed very few cells containing more than 2 tracks/cell and a decrease in the percentage of cells containing 1 and 2 tracks/cell from 143 to 145 mm. However, depths from 148 – 155 mm remained relatively consistent with the percentage of cells containing 1 or 2 tracks/cell.

Further investigation revealed key differences between each of the track positive depths involving the foci number ranges and cluster sizes per each individual track. These differences may be explained by the varying energy levels of the $^{12}C$-ions at each depth, as demonstrated in a prior study conducted by Sridharan et al., in which they irradiated cells with three different high charge and energy (HZE) particles (Fe, Si and Ti) at multiple energy levels. In this study, it was reported that as the energy level of each HZE particle was increased, there was an observable difference in each of their respected γ-H2AX foci track structures [297]. This became most apparent throughout our FBPR, as we observed that out of all the track positive depths each increasing depth within the FBPR contained a different peak value for the number of tracks within an increasing foci number range, as the peak values for the number of tracks containing 60 – 99, 100 – 150 and >150 foci/track were at 140, 142 and 142.2 mm, respectively. Moreover, throughout the FBPR, the number of tracks containing <60 foci/track were observed to decrease while the number of tracks containing >150 foci/track were observed to increase. This was

consistent with the observed increase in each foci cluster size range and our high-LET control, 2Gy Fe-ion, containing large numbers of tracks with >150 foci/track and clusters of size >2.4 μm (Figures 2.7 & 2.8). These results demonstrated that while the number of tracks per cell decreased throughout the FBPR, the number of foci per track and cluster size per track increased.

However, these results may have been due to the particles being able to centrally or peripherally traverse the cells because the plane of individual cells differs throughout the FBPR [64]. Even though the respected average dose to the population may be the same at each individual depth, the depths containing more tracks per cell may have a higher number of tracks that peripherally traversed the cells, making these tracks shorter and possibly demonstrating a lower number of foci/tracks then if they had centrally traversed the cell. We resolved this by quantifying the number of tracks containing at least one of our largest cluster sizes (>2.4 μm) regardless of how many of these clusters a track might have at each depth (Figure 2.8B). Our results demonstrated a sharp increase in the number of these tracks from 135 – 140 mm with a significant increase throughout the FBPR and a peak at 142 mm ($P<0.01$ and $P<0.001$, respectively). We also observed a sharp decrease from 142.2 – 143 mm which gradually decreased in the following depths. Furthermore, tracks in the cells following irradiation with our high-LET control, 2Gy Fe-ion, fell in between the depths of 140 and 142 mm, suggesting that the $^{12}$C-ions at 142 mm may have higher LET values than the incident Fe-ions.

While consistent trends were observed in the depths up to the end of the FBPR (10 – 142.2 mm) following 2 Gy $^{12}$C-ion irradiation treatment dosage, the individual cells within each depth throughout the post-FBPR (143 – 155 mm) demonstrated wide variabilities in their γ-H2AX distribution. To further investigate these variations and how they might contribute to cell death, we also observed the post-FBPR following 10 Gy $^{12}$C-ion irradiation treatment dosage.

We chose this dosage as it demonstrated the largest differences in the survival fractions between each depth within this respected region (Figure 2.1F). Under both irradiation conditions, we observed a higher percentage of the cells falling in both the lower foci number ranges and being track negative as well as having a decrease in the average number of foci clusters of size >2.4 µm/cell as the beam proceeded from 143 – 155 mm (Figure 2.9). This was consistent with our observed increase in survival at these depths following 10 Gy $^{12}$C-ion irradiation treatment dosage.

On the other hand, the percentage of track positive cells in the post-FBPR depths was not as consistent with survival at each respected depth, as compared to the track positive depths up to the end of the FBPR. This was likely due to the individual track positive cells within the same depth demonstrating observable inconsistencies between their track structures in the post-FBPR (Figure 2.10). The possible reasoning behind these track structure variations within the same depths is likely due to $^{12}$C-ion nuclear fragmentation. This reasoning is consistent with a prior study conducted by Arico et al., in which they investigated the fragmentations from a single $^{12}$C-ion and reported that the most abundant types of secondary fragments were helium-ions followed by hydrogen, lithium, beryllium and boron-ions, respectively [222]. While these fragmentation ions are known to travel at relatively the same velocity and in the same direction, they can differ in the energy in which they carry and thus produce differences in the track structures of the cells they transverse [223].

While we could not definitively differentiate the post-FBPR high-LET track structure induction resulting from $^{12}$C-ions or their fragmentation-ions, we could distinguish if the tracks were a possible result of light- or heavy-ions by the density of their foci distributions along each track. We defined heavy-ion induced tracks containing foci number ranges within 100 – 150 and

>150 foci/track and possessing 2 or more foci clusters of size >2.4 µm/track (Figures 2.11B,C & 2.13C). These parameters were chosen as a prior study demonstrated that the ionization cluster size distributions were larger following heavy-ion irradiation ($^{12}$C-ion) than with light-ion irradiation (He-ion) as well as we observed tracks within these foci number ranges first appearing either within or directly prior to our FBPR following 2 Gy $^{12}$C-ion irradiation treatment dosage (Figures 2.7 & 2.8) [223]. Using these parameters, we observed that the abundance of suspected heavy-ions capable of depositing their energy in dense tracks at each depth following 2 Gy $^{12}$C-ion irradiation treatment dosage became more apparent following irradiation at the higher treatment dosage of 10 Gy, which may further explain the observed decrease in survival at these post-FBPR depths following 10 Gy $^{12}$C-ion irradiation treatment dosage.

Interestingly, 143 mm following 10 Gy $^{12}$C-ion irradiation treatment dosage was similar to the depth of 142.2 mm following 2 Gy $^{12}$C-ion irradiation treatment dosage in both survival and track structure analysis as well as similar to our high-LET control, 2 Gy Fe-ion, in track structure analysis. Although, this shift was not observed for any of the proceeding post-FBPR depths. These results demonstrated that a high percentage of heavy-ion tracks were at 143 mm which diminished as an increasing percentage of light-ion tracks were observed as the depths proceeded further away. One possible reasoning for this is that the lighter ions were more capable of traveling farther distances than the heavier ions. This reasoning also demonstrates how the foci distributions density within the tracks can influence cell survival in the post-FBPR, as we observed that the cell survival increased with an increase in post-Bragg peak depth.

Lastly, we sought to determine if the underlying factor between the foci distribution correlation with cell death was due to the number of foci per cell (via average intensity per cell),

the foci density per cell (via percentage of cluster >2.4 μm positive cells), the presence of a track structure (via percentage of track positive cells), or a combination of these (Figure 2.14C). For depths ranging up to the biological Bragg peak (10 – 140 mm), we observed that the presence of a track structure and foci density highly correlated with the cell death ($R^2$= 0.99 and 0.95, respectively). On the other hand, post-biological Bragg peak depths (142-155 mm) had the highest correlation with the number of foci/cell followed by the foci density/cell and the lowest correlation with the presence of a track structure ($R^2$= 0.87, 0.82 and 0.73, respectively). These results agreed with our post-FBPR track structure analysis and further supported that the cell death from the high-LET radiation may be dependent on the density in which the foci are distributed within their tracks.

However, the reasoning behind having the lowest cell survival at the biological Bragg peak depth of 140 mm but the highest number of foci at 142 mm, may have been due to the overkill effect. The overkill effect is when a single particle deposits much more energy than is required to kill a cell. This results in it killing less cells per absorbed dose. The overkill effect is known to occur when the LET value is greater than 100 keV/μm [298]. In addition, at very high-LET values, such as with those required for the overkill effect, the percentage of non-hit cells has been observed to increase. This increase in non-hit fraction of cells with an increasing LET has been suggested to be caused by enhanced clustering of ionization and DNA damage within the hit cells which lowers the energy efficiency for producing DNA damage in the non-hit cells [299]. Therefore, the carbon-ions at 142 mm may have LET values high enough to produce this overkill effect, thus providing the explanation behind why we observed an increase in cell survival at this depth.

In conclusion, we developed a novel method to address the DSB distribution throughout the full $^{12}$C-ion beam range in a single biological system using γ-H2AX as a surrogate marker for DSBs. Using this approach, we confirmed that the biological Bragg peak depth was at 140 mm and demonstrated how the high-LET track structures change both in the number of tracks/cell and foci density per track as the beam approached the Bragg peak. We also confirmed the presence of track structures resulting from heavy- and light-ions in the post-FBPR regions, demonstrating the biological impacts from nuclear fragmentations and how it is the foci density within these track structures that may be critical for cell death. These results are of great interest as misrepair of the DSBs within the post-FBPR light-ion induced tracks may contribute to genetic instability possibly resulting in cancer cell propagation as we observed high survival within this region, suggesting that these DSBs were capable of being repaired. In addition, our results also provide the fundamental basis for further research into the DNA damage repair mechanisms throughout the full $^{12}$C-ion beam range that may be useful targets for combination cancer therapy techniques as well as provide valuable insight into the $^{12}$C-ion nuclear fragmentation induced DNA damage. Results of this study should be carefully considered during radiation treatment planning to limit the amount of healthy cell damage thus reducing the risk of cancer cell development in patients.

## 2.4 Materials and Methods

### 2.4.1 Cell culture and irradiation conditions.

Chinese hamster ovary (CHO) cells were kindly supplied by Dr. Joel Bedford (Colorado State University, Fort Collins, CO). Cells were grown and maintained in α-MEM (Invitrogen, Carlsbad, CA, USA) supplemented with 10% heat inactivated fetal bovine serum (Sigma), supplemented with antibiotics and antimycotics at 37 °C in incubators at 5% CO2 and 100%

humidity. Doubling times were approximately 12 hours for this cell line. Carbon-ions and Fe-ions were accelerated to 290 MeV/nucleon and 500 MeV/nucleon, respectively, using the Heavy Ion Medical Accelerator in Chiba (HIMAC) synchrotron at the National Institute of Radiological Sciences (NIRS), Chiba, Japan. Dose rates for carbon-ions and Fe-ions were set at 1 Gy/min. Monoenergetic 290 MeV/nucleon carbon-ions and 500 MeV/nucleon Fe-ions have LET values of 13 keV/μm and 200 keV/μm on entrance, respectively. Cell culture flasks or chamber slides were set up in a horizontal position (approximately 5 degrees) to carbon-ion or Fe-ion beam source, respectively, prior to irradiation. X-ray irradiation was performed at 200 kVp and 20 mA with Aluminum (0.5 mm)-Copper (0.5 mm) filters (Shimadzu, TITAN-320, NIRS) and dose rates were set at 0.5 Gy/min. Irradiations were carried out at room temperature. The beam characteristics and dosimetry using HIMAC have been described previously [300, 301].

### 2.4.2 Irradiation procedure for cell survival assays.

Cultured cells were trypsinized and re-suspended into growth medium. Once re-suspended, 60 mL of media containing 30,000 cells were placed into their appropriately labeled T-175 cell culture flask a few hours prior to irradiation and attachment was confirmed. All flasks were irradiated independently with a dosage of either 2, 3, 5 or 10 Gy. For all flasks, the beam entry point was at the bottom of the flask (non-capped end) (Figure 2.1A). Immediately following irradiation, all cells were incubated for a period of 7 days for colony formation. After this culturing period, each culture flask was then washed with 0.9% NaCl, fixed in 100% ethanol and stained with 0.1% crystal violet.

### 2.4.3 Survival fraction calculation for cell survival assays.

Survival fraction were calculated as described previously [290]. Briefly, to quantify the survival fraction at each of our evaluated depths, they were scored for every millimeter along the

width of the flask either possessing a surviving colony, defined as a colony containing >50 cells, or not possessing a surviving colony and the average value was calculated. This approach was repeated for a minimum of three independent experiments per each one of our initial dosages of 2, 3, 5 or 10 Gy.

### 2.4.4 Irradiation procedure for γ-H2AX assays.

For carbon-ion and X-ray irradiations: The top of each T-175 cell culture flask was removed, and 6 poly-L-lysine coated glass microscope slides were placed inside each flask as oriented in figure 2.2B. Tops were then returned to their respected flask and sealed with parafilm prior to addition of cells. Cultured cells were trypsinized and re-suspended into growth medium. Once re-suspended, 60 mL of media containing 9 million cells were placed into their appropriately labeled T-175 cell culture flask a few prior to irradiation and attachment was confirmed. For Fe-ion irradiations, 0.4 mL of media containing 50,000 cells were placed into each well of an 8 well Nunc Lab-Tek Chamber Slide System (Nalge Nunc, Naperville, IL, USA) a few hours prior to irradiation and attachment was confirmed. Chamber slides were placed with 4 of the 8 wells (one side) directly facing Fe-ion beam in horizontal orientation (approximately 5 degrees) to Fe-ion beam. Only wells of side directly facing Fe-ion beam were analyzed.

### 2.4.5 Immunofluorescence staining

Cells were washed in cold PBS and fixed for 15 min in 4% w/v paraformaldehyde and washed again in PBS. Cells were then permeabilized for 5 min in 0.2% v/v Triton X-100 (Sigma-Aldrich, Japan) in PBS, and washed twice in PBS. Slides were treated with 10% goat serum for 1 hr at 37 °C for blocking. Antibodies were diluted with 10% w/v goat serum in PBS. Cells were incubated with 1:300 mouse anti-γH2AX antibody (Millipore, Billerica, USA) for 1 h at 37 °C, washed three times in PBS and incubated with 1:500 Alexa Fluor 488 goat anti-mouse IgG

antibody (abcam, Cambridge, MA, USA) for 1 h at 37 °C, and washed four times in PBS. DAPI (49,6-diamidino-2-phenylindole) (Roche, Indianapolis, IN, USA) was then applied to stain the DNA.

### 2.4.6 γ-H2AX foci analysis by Zeiss Axioplan microscopy with and without Metamorph deconvolution

Microscopic images were captured with an Zeiss Axioplan microscope using a 60X objective. Since the depth of CHO cells is approximately, 2–3 μm, 20 slices within 4 mm were taken with Z-series stacks. 20 deconvoluted or non-deconvoluted images were stacked into a single-layer image to analyze γ-H2AX foci. Non-deconvoluted stacked images were analyzed for foci intensities. Deconvoluted stacked images were analyzed for foci cluster sizes and the number of individual foci. For this analysis images taken by the Zeiss Axioplan were deconvoluted and processed using Metamorph software (Molecular Devices LLC., San Jose, CA, USA) via 2D no-neighbors deconvolution.

### 2.4.7 γ-H2AX foci scoring

Foci scoring was carried out blindly with at least 50 cells/each depth or control/experiment. Unless stated otherwise all foci analysis represents the mean and SEM from at least 3 independent experiments. Foci cluster sizes within the cells at each depth or in controls were scored as being either >0.8, >1.2 or >2.4 μm in length and/or width. Foci length was measured within Metamorph software following image processing. These sizes were chosen as the largest cluster size observed in unirradiated cells was 0.8 μm with a very low frequency of occurrence and very few clusters within the cells were observed as >2.4 μm following high dose 4 Gy X-ray irradiation in contrast to many clusters of this size being present following high-LET 2 Gy Fe-ion irradiation (Figures 2.2A & 2.5D). In addition, a prior study using a higher image

resolution than used in our study demonstrated the presence of many individual γ-H2AX foci within each cluster following 2Gy Fe-ion beam irradiation [64]. Thus, with use of our conventional lower image resolution via Zeiss Axioplan microscope with deconvolution we addressed the individual foci number within the clusters by zooming in on each individual cluster by 300% and scanning the pixel intensities across each cluster. Pixels demonstrating a drastic decrease in intensity values portrayed the separation between the individual foci. This allowed us to determine the number of foci within each cluster (Figures 2.4). To eliminate possible counting bias, intensity values of each cell within each depth was also obtained from the stacked image without deconvolution (Figure 2.5A).

### 2.4.8 Statistical analysis

All experimental data was derived from at least 3 independent experiments. For experiments involving γ-H2AX foci, at least 50 cells per each depth or control per experiment were analyzed. Statistical significance was determined using one-way analysis of variance (ANOVA) followed by Bonferroni multiple comparisons test or Student's two-tailed t test by GraphPad Prism 8$^{TM}$ software (GraphPad, La Jolla, CA, USA). * = $P<0.05$, ** = $P<0.01$, *** = $P<0.001$. Analysis was carried out between entry depth (10mm) versus others unless stated otherwise.

# CHAPTER THREE

## METAL IONS MODIFY *IN-VITRO* DNA DAMAGE YIELDS WITH HIGH-LET RADIATION

**Summary:** $Cu^{2+}$ and $Co^{2+}$ are metals known to increase DNA damage in the presence of hydrogen peroxide through a Fenton type reaction. We hypothesized that these metals could increase DNA damage following irradiations of increasing LET values as hydrogen peroxide is a product of the radiolysis of water. The reaction mixtures contain either double- or single-stranded DNA in solution with $Cu^{2+}$ or $Co^{2+}$ and was irradiated either with X-ray, carbon-ion or iron-ion beams or treated with hydrogen peroxide or bleomycin at increasing radiation dosages or chemical concentrations. DNA damage was then assessed by gel electrophoresis followed by band intensity analysis. DNA in solution with metals demonstrated the most DNA damage when treated with hydrogen peroxide followed by irradiation with low-LET (X-ray), high-LET (carbon-ion and iron-ion), respectively, and demonstrated the least damage with treatment of bleomycin. $Cu^{2+}$ portrayed greater DNA damage than $Co^{2+}$ following all experimental conditions. The metals effect caused more DNA damage and was observed to be LET dependent for single-strand break formation but inversely dependent for double-strand break formation. These results suggest that $Cu^{2+}$ is more efficient than $Co^{2+}$ at inducing both DNA single-strand and double-strand breaks following all irradiations and chemical treatments.

### 3.1 Introduction

The major actor responsible for radiation induced cell death is DNA double-strand breaks (DSBs), from localized single-strand breaks (SSBs). Generally, 1 Gy of radiation produces 20-40 DSBs and a few thousands of SSB in cells [302]. Radiation-induced DNA damages are caused by direct action or indirect action through the radiolysis of water. X-rays are known as low-LET

(linear energy transfer) radiation and are sparsely ionizing. A large amount of low-LET induced-DNA damage is believed to be contributed by hydroxyl radical mediated indirect action [303]. However, radiation induced cell death is not due to individual hydroxyl radicals but by the interaction of radicals at high density near DNA causing locally multiply damaged sites (LMDS) [87]. On the other hand, high-LET radiations, such as neutrons and heavy charged particles, are known to be densely ionizing and produce higher biological effectiveness [303]. There is an increase in direct action contribution for high-LET induced-DNA damage through stronger electromagnetic interactions with the DNA molecule [89, 90]. Furthermore, dense ionizations produced by high-LET radiation creates high radical concentrations from the radiolysis of water leading to more radial-radical reactions and resulting in the formation of greater G-values of hydroxyl radicals [304].

To further study the intracellular hydroxyl radical reactions produced from the indirect action of low-LET irradiation prior studies have demonstrated hydrogen peroxide as an appropriate alternate chemical source to ionizing radiation [305, 306]. H. J. Rhaese et al. portrayed at the molecular level that hydrogen peroxide causes the degradation of DNA in aqueous solutions [307] and the range of observed DNA lesions was found to be similar to the range of damage produced by hydroxyl radicals from ionizing radiation [308]. Mechanistically, M. E. Hoffmann et al. demonstrated that transition metal ions are essential for the formations of strand breaks in cells treated with hydrogen peroxide due to a Fenton-type reaction production of hydroxyl radicals [306].

Beyond hydrogen peroxide, another chemical that can be used to examine DNA damage is bleomycin, a radiomimetic drug currently used in human cancer therapy and its toxicity is mostly attributed to its ability to induce DSBs [309]. Bleomycin-mediated DNA degradation

requires the presence of a redox-active metal ion, such as $Fe^{2+}$ or $Cu^{+}$, as well as, molecular oxygen [310]. Bleomycin-mediated DNA degradation is sequence selective and results in preferential cleavage at certain $^{5'}GT^{3'}$ and $^{5'}GC^{3'}$ sequences [311]. Bleomycin contains at least four functional domains but of importance for this current study is the metal-binding domain, responsible for metal ion binding and molecular oxygen activation which must ultimately mediate the abstraction of hydrogen atoms from the DNA substrate, a critical step for DNA cleavage [311-313]. Several studies have demonstrated its metal-binding domain is able to bind numerous metal ions and this domain also constitutes the primary determinant of the sequence selectivity of DNA cleavage by metal-bleomycin complex (BLM) [313-315]. Thus, the type of metal which binds bleomycin can influence how efficiently it induces DNA breaks. Moreover, the qualitative order of stability of metallobleomycins at pH 7 among metals commonly found in cells is Cu(II)- > Fe(III)- > Zn- > Fe(II) > Cu(I)-BLM [316]. Following binding DNA, bleomycin produces two sets of oxidation products from B-form DNA substrates. One of the oxidation products results in frank DNA strand scission and the other oxidation product affords base release at the site of BLM-induced lesion with concomitant formation of a 4'-hydroxyapurinic acid moiety. Common to both pathways is the production of an initially formed C-4' radical intermediate resulting from the abstraction of a hydrogen atom from the DNA substrate by bleomycin. To induce the DNA lesion this radical intermediate can either combine with dioxygen, thus forming a hydroperoxyl radical, or it can undergo oxidation, thus forming a carbocation that reacts with water [310].

Yields of radicals in solution can be affected by factors including pH, temperature, solvents and substrates [317, 318]. As the hydroxyl radical scavengers, such as dimethyl sulfoxide (DMSO), attenuate radiation effects, the amount of hydroxyl radicals can interfere with

DNA damage yields [319]. In addition, superoxide dismutase and Catalase are endogenous enzymes that reduce final hydroxyl radical formation, which may also decrease the radiation effects from indirect action [320]. In order to better understand the underlying mechanisms behind DNA damage induced by each of these sources, as well as, enhancing their ability to induce DNA strand breaks, we can take advantage of Fenton-type reactions utilizing the transition metals copper and cobalt.

Prior studies have observed an increase in DNA strand breaks and a decrease in the molecular weight of DNA in mammalian cells treated with either copper or cobalt [321], as well as, these metals in complexes have also been observed to decrease survival following irradiation [322-324]. Moreover, Lloyd D.R. et al. demonstrated that the site-specific mechanisms in the formation of DSBs were due to the oxidative DNA damaged mediated by copper (II) Fenton reactions in solution with DNA and hydrogen peroxide [325]. Prior work from Lloyd D.R. et al. also demonstrated $^{32}$P-Postlabelling analysis of DNA treated with hydrogen peroxide and either copper(II), cobalt(II), chromium (VI), iron(II), nickel(II) or vanadium(III) resulted in in the detection of between four and eight radioactive TLC spots corresponding to DNA lesions and importantly the copper-Fenton system generated the highest total yield of these DNA lesions followed by cobalt-Fenton system [326].

In the present study, we observed how the amount of DSBs and SSBs are influenced by radiation sources increasing in LET values, as well as, by chemical treatment on naked double-strand DNA (dsDNA) and single-strand DNA (ssDNA) in solution. We also observed how the ROS generation may contribute to the mechanistic capabilities of copper and cobalt to further induce DSBs and SSBs when in solution with dsDNA or ssDNA following each of these conditions. Irradiation sources used in this study were X-ray (LET=2 keV/um), spread out Bragg

peak (SOBP) 290 MeV/n carbon-ion beams (LET=50 keV/μm) or monoenergetic 500 MeV/n iron-ion beams (LET=200 keV/um) each at increasing dosages (Gy). Chemical treatments used in this study were either hydrogen peroxide or bleomycin at increasing chemical concentrations. Results of this study will provide a better understanding into ROS generation and production of hydroxyl radical formation at increasing LET values. In addition, these results will provide evidence into the mechanism behind how copper and cobalt may enhance the induction of DSBs and SSBs following ionizing radiation and chemical treatments.

To the best of our knowledge this is the first study to compare the effects of copper and cobalt on DNA damage from ionizing radiations of increasing LET along with the effects from the chemicals of hydrogen peroxide or bleomycin at increasing chemical concentrations. We hypothesized that the transition metals copper and cobalt would be useful chemicals to enhance the indirect action contribution of DNA damage for high-LET radiations. This is due to the ability of hydrogen peroxide to undergo the Fenton-type reaction, thus resulting in the formation of the much more reactive hydroxyl radical, thereby, leading to an increase in DNA strand breaks. For the same reasoning, we also believed these chemicals would increase both DSBs and SSBs when in solution with hydrogen peroxide. Regarding molecular oxygen as also being a bi-product of high-LET irradiation as well as being an essential component for bleomycin-induced DNA damage, we also sought to address how these metals may influence bleomycin's efficiency to induce DNA cleavage. To test our hypothesis, we used *in-vitro* single- and double-stranded DNA and three different qualities of radiation with different LET values and two major chemicals to cause DNA damage to assess the metal effect for DNA damage.

## 3.2 Results

### 3.2.1 DNA DSB by ionizing radiation and metals

In order to address the DSB induction yield with ionizing radiation sources increasing in their LET value, we found that 30 ng of dsDNA from lambda phage in 10 µL of reaction solution demonstrated an appropriate representation of DSB yields at increasing treatment irradiation dosages. DSB formation yield measured with in-vitro dsDNA was higher in low-LET X-ray and decreased as LET value increased in carbon-ion and iron-ion, respectively. $D_{50}$ values (dose to achieve 50% intact DNA) were achieved with 44, 142, and 299 Gy, respectively. X-ray irradiation produced significant increase in DSBs with both metals compared to control (Figure 3.1A). Carbon-ion irradiation produced significant increase in DSB with addition of $Cu^{2+}$ or $Co^{2+}$ compared to control. Adding $Cu^{2+}$ produced a significant increase in DSB formation compare to adding $Co^{2+}$ (Figure 3.1B). Finally, iron-ion irradiation demonstrated an increase in DSB when adding either metals, most notably with $Cu^{2+}$, but this observed difference was not found to be significant under all experimental dosages (Figure 3.1C).

$D_{50,\,DSB}$, demonstrated fold increases of efficiency of DSB with addition of metal ions (Table 3.1). $D_{50,\,DSB}$ values with adding $Cu^{2+}$ were smaller than adding $Co^{2+}$ for all tested radiations. Therefore, adding $Cu^{2+}$ was more efficient at increasing DSB yields for tested radiation than adding $Co^{2+}$.

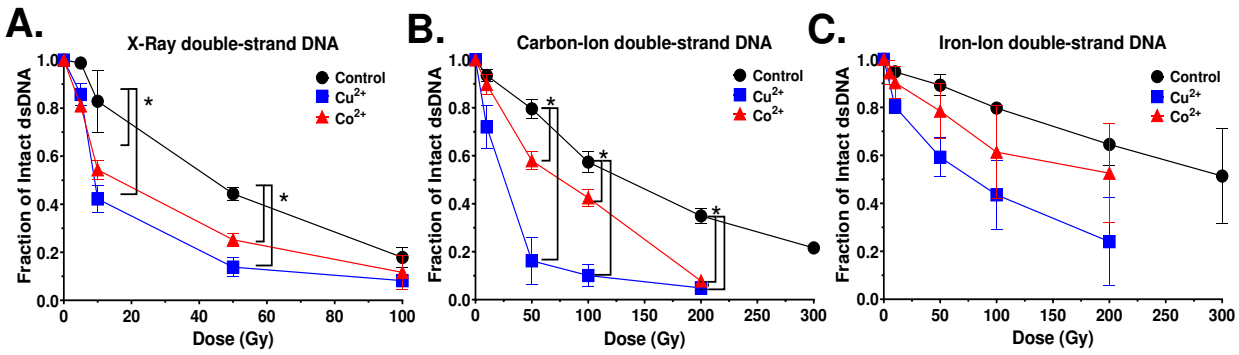


**Figure 3.1. $Cu^{2+}$ and $Co^{2+}$ effect on DNA DSBs at increasing radiation dosage (Gy) with radiation sources of increasing LET values.** **(A)** Low-LET X-ray for DSBs. **(B)** High-LET carbon-ion for DSBs. **(C)** High-LET iron-ion for DSBs. Error bars indicate standard error of the means from at least three independent experiments. * indicates statistical differences ($P < 0.05$).

**Table 3.1. $D_{50,DSB}$ and $IC_{50,DSB}$ values, radiation doses (Gy) or chemical concentration required for 50% intact dsDNA with or without metal ions**

| *Initial dsDNA amount ➔ 30 ng Lambda phage dsDNA in 10 µL reaction solution* | | | |
|---|---|---|---|
| **Source** | **Control** | **$Cu^{2+}$** | **$Co^{2+}$** |
| **X-ray** | **44 Gy** | **8.5 Gy** | **15.5 Gy** |
| **Carbon-ion** | **142.9 Gy** | **28.1 Gy** | **80.9 Gy** |
| **Iron-ion** | **299.1 Gy** | **80 Gy** | **187 Gy** |
| **Bleomycin** | **46625 nM** | **29882.4 nM** | **39560.6 nM** |
| **$H_2O_2$** | **20073 nM** | **22 nM** | **177 nM** |

### 3.2.2 DNA SSB by ionizing radiation and metals

Induction of SSB was measured with in-vitro ssDNA originated from M13 bacteriophage. In order to appropriately address the SSB yield from each ionizing radiation source, ~3X the amount of ssDNA (83 ng) was required in the 10 µL of reaction solution as compared with dsDNA in order to address the damage at comparable dosages as used with dsDNA.

For DSB, X-ray was the most efficient ionizing radiation source to cause SSBs as $D_{50, SSB}$ values of 57 Gy among tested radiation. $D_{50, SSB}$ values of high-LET radiation carbon-ion and iron-ion were 130 Gy and 160 Gy, respectively. Irradiation of X-ray was observed to produce a significant increase of SSB with adding $Cu^{2+}$ and $Co^{2+}$. Adding $Cu^{2+}$ and $Co^{2+}$ showed

significant increase of SSB formation compared to control (Figure 3.2A). Carbon-ion irradiation produced a significant increase of SSB formation with adding both metals compared to control (Figure 3.2B). Then, iron-ion irradiation also produced a significant increase of SSB formation with both metals (Figure 3.2C).

$D_{50, SSB}$ values demonstrated fold increases of efficiency of SSB with addition on metal ions (Table 3.2). $D_{50, SSB}$ values with adding $Cu^{2+}$ were smaller than adding $Co^{2+}$ for all tested radiation. Therefore, adding $Cu^{2+}$ was more efficient at increasing DSB yields for tested radiation than adding $Co^{2+}$.

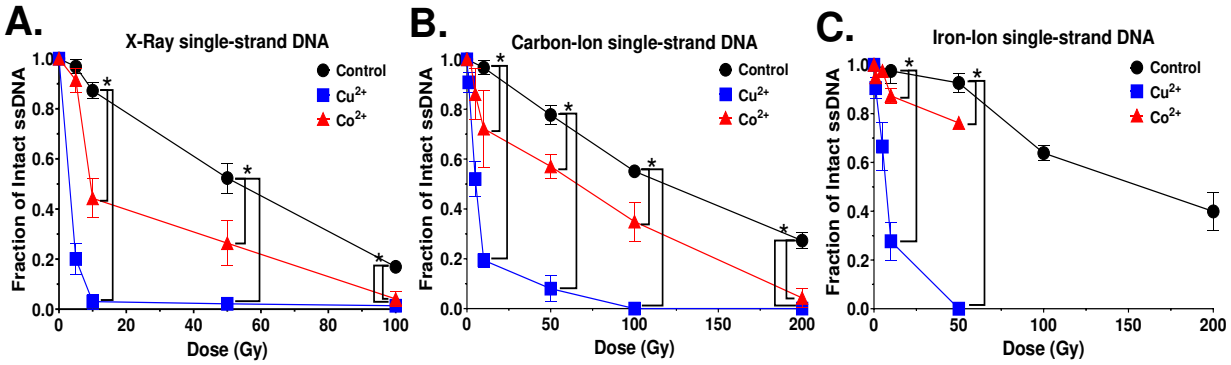


**Figure 3.2. $Cu^{2+}$ and $Co^{2+}$ effect on DNA DSBs at increasing radiation dosage (Gy) with radiation sources of increasing LET values.** **(A)** Low-LET X-ray for SSBs. **(B)** High-LET carbon-ion for SSBs. **(C)** High-LET iron-ion for SSBs. Error bars indicate standard error of the means from at least three independent experiments. * indicates statistical differences ($P < 0.05$).

**Table 3.2. $D_{50,SSB}$ and $IC_{50,SSB}$ values, radiation doses (Gy) or chemical concentration required for 50% intact ssDNA with or without metal ions.**

| *Initial ssDNA amount: 83 ng M13 bacteriophage ssDNA in 10 µL reaction solution* | | | |
|---|---|---|---|
| **Source** | **Control** | **$Cu^{2+}$** | **$Co^{2+}$** |
| **X-ray** | **57.5 Gy** | **3.1 Gy** | **9.6 Gy** |
| **Carbon-ion** | **129.8 Gy** | **2.9 Gy** | **65.0 Gy** |
| **Iron-ion** | **160.0 Gy** | **7.0 Gy** | **102.0 Gy** |
| **Bleomycin** | **8689.2 nM** | **4591.9 nM** | **26138.2 nM** |
| **$H_2O_2$** | **17237 nM** | **0.156 nM** | **1138 nM** |

### 3.2.3 DNA DSB by bleomycin and hydrogen peroxide with metals

To induce DNA damages, bleomycin or hydrogen peroxide ($H_2O_2$) were treated with DNA at room temperature for 30 min. Bleomycin is known to produce DSBs and SSBs [327]. Hydrogen peroxide produces SSBs [306]. Bleomycin presented concentration dependent DSB formation up to 1,413 μM with $IC_{50, DSB}$ value of 46,625 nM (Figure 3.3A and Table 3.1). At 14.1 μM, adding both metals enhanced DSB formation. Interestingly, from 70.6 μM of bleomycin, adding $Co^{2+}$ was observed to switch from sensitization to protection in comparison to control.

Hydrogen peroxide, up to 10 mM, did not produce a significant amount of DSBs without metals. Based on regression curves, $IC_{50, DSB}$ was calculated as 20 mM. By adding either metal ions, hydrogen peroxide treatment was observed to produce a significant increase of DSB formation (Figure 3.3B).

$IC_{50, DSB}$ values (chemical concentration required for 50% intact DNA) demonstrated fold increases of efficiency of DNA breaks with addition of metal ions (Table 3.1). Although $IC_{50, DSB}$ values of bleomycin were decreased slightly with metals, $IC_{50, DSB}$ values of hydrogen peroxide were severely decreased from 20073 nM to 22 nM ($Cu^{2+}$) and 177 nM ($Co^{2+}$). Therefore, bleomycin had minimum effects from metal ions to form DSB. On the other hand, hydrogen peroxide got severely affected by adding metals and copper ions affected stronger than cobalt ions for hydrogen peroxide.

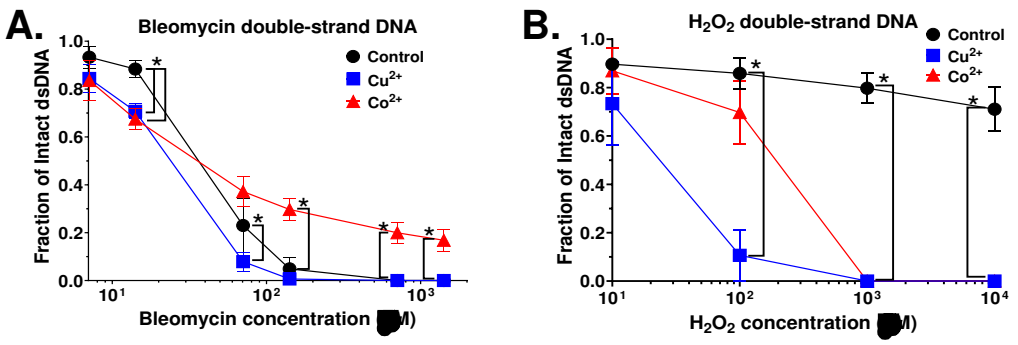


**Figure 3.3. $Cu^{2+}$ and $Co^{2+}$ effect on DNA DSBs at increasing drug concentrations of either Bleomycin or hydrogen peroxide.** **(A)** Bleomycin for DSBs. **(B)** Hydrogen peroxide for DSBs. Error bars indicate standard error of the means from at least three independent experiments. * indicates statistical differences ($P < 0.05$).

### 3.2.4 DNA SSB by bleomycin and hydrogen peroxide with metals

Bleomycin produced SSB in a concentration dependent manner. As with DSB formation, bleomycin demonstrated a shift from sensitivity to protection with adding $Co^{2+}$ in SSB formation above 7.1 μM. Adding $Cu^{2+}$ was observed to increase the sensitivity of bleomycin compared to control but these decreases in SSB formation were not observed to be significant (Figure 3.4A). Hydrogen peroxide produced dose dependent SSB formation up to tested 10 μM. A significance increase in SSB was observed with adding $Cu^{2+}$ at the lowest tested concentration of 100 pM. Adding cobalt ions increased SSBs but the effect was much smaller than adding copper (Figure 3.4B).

$IC_{50,\ SSB}$ values demonstrated fold increases of efficiency of DNA breaks with addition of metal ions (Table 3.2). Although $IC_{50,\ SSB}$ values of bleomycin showed a few times changes by adding metal ions, $D_{50,\ SSB}$ values of hydrogen peroxide were dramatically decreased with addition of metals. Therefore, bleomycin had minimum effects from metal ions to form SSB. On the other hand, hydrogen peroxide got severely affected by adding metals and copper ions affect was much stronger than with cobalt ions.

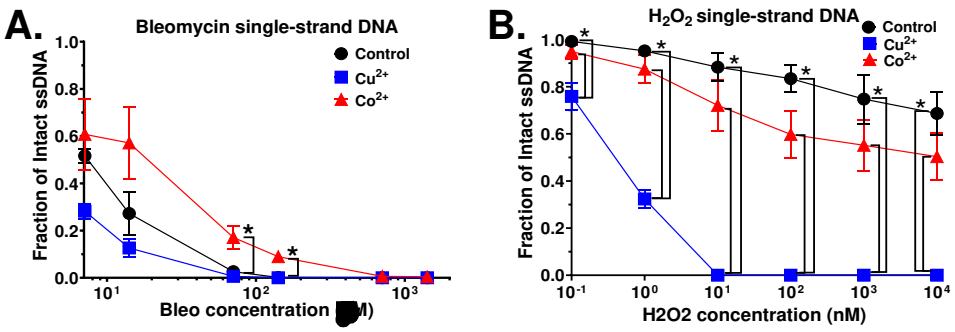


**Figure 3.4. $Cu^{2+}$ and $Co^{2+}$ effect on DNA SSBs at increasing drug concentrations of either Bleomycin or hydrogen peroxide. (A)** Bleomycin for SSBs. **(B)** Hydrogen peroxide for SSBs. Error bars indicate standard error of the means from at least three independent experiments. * indicates statistical differences ($P < 0.05$).

### 3.2.5 Metal enhancement ratio for DNA break formation

Metal enhancement ratio's (MER) were calculated from the $D_{50}$ and $IC_{50}$ values from Tables 3.1 and 3.2 and described in materials and methods section. For ionizing radiation with 30 ng of dsDNA in solution with 10 µL reaction solution, the MER demonstrated a fold reduction of 5.18x, 5.09x, and 3.74x with $Cu^{2+}$ and 2.84x, 1.77x, and 1.6x with $Co^{2+}$ following X-ray, carbon-ion, or iron-ion, respectively. Bleomycin showed the smallest MER values. The MER demonstrated a fold reduction of 914.94x with $Cu^{2+}$ and 113.41x with $Co^{2+}$ following $H_2O_2$ (Figure 3.5A).

For ionizing radiation with 83 ng of ssDNA in solution with 10 µL reaction solution, the MER demonstrated a fold reduction of 18.37x, 21.96x, and 22.92x with $Cu^{2+}$ and 5.97x, 2x, and 1.57x with $Co^{2+}$ following X-ray, carbon-ion and iron-ion, respectively. The MER values for SSB were greater values than for DSB. Bleomycin showed the smallest MER values. The MER demonstrated a fold reduction of 110493x with $Cu^{2+}$ and 15.15x with $Co^{2+}$ following $H_2O_2$. (Figure 3.5B).

Therefore, metal ions affected both SSB and DSB formation induced by tested chemicals and radiation. Hydrogen peroxide affected DNA damage the most followed by low-LET radiation and high-LET radiation and bleomycin affected the least. $Cu^{2+}$ presented stronger

effects than $Co^{2+}$. SSB formation was more enhanced by metal ions than DSBs. Metal effects for DNA damage was LET dependent for SSB formation but inversely dependent for DSB formation.

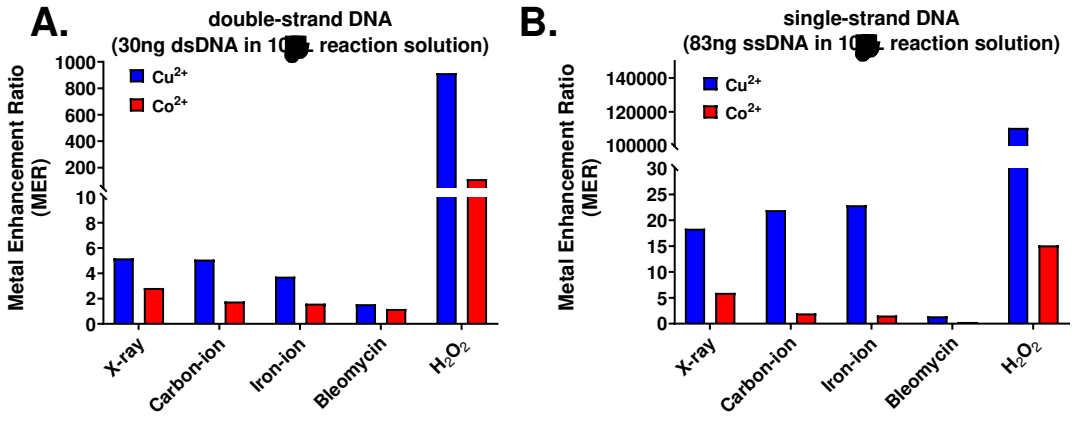


**Figure 3.5. Metal enhancement ratio (MER) for DNA break formation comparison between ionizing radiation and chemical treatment with metals in solution with DNA. (A)** MER for 30ng of dsDNA in 10µL of reaction solution. **(B)** MER for 83ng of ssDNA in 10µL of reaction solution.

## 3.3 Discussion

In the present study, we observed that the induction of DSBs and SSBs reduced with increasing LET values as low-LET X-ray irradiations were the most efficient inducers of DNA strand breaks per dose (Gy) followed by the high-LET carbon-ion and iron-ion beams, respectively (Tables 3.1 & 3.2). These results are in agreement with prior research utilizing cell lines which indicates that the number of SSBs produced is estimated to be lower in high-LET radiation [303]. In contrast to our results, other prior studies have demonstrated an increase in DSBs with increased LET in cells [102, 328]. It is hard to compare directly to our in-vitro DNA analysis in reaction solution and cells because DNA in cells has chromatin structure and are not naked forms because chromatin structure protects DNA from radiation [329].

In the presence of $Cu^{2+}$ or $Co^{2+}$, we observed an increase in the amounts of DSBs and SSBs for both low- and high-LET radiations (Figures 3.1 & 3.2). Interestingly, as the LET

increased the fold reduction of MER values decreased for both metals in dsDNA, as well as, with $Co^{2+}$ in ssDNA but increased for $Cu^{2+}$ in ssDNA (Figure 3.5). A possible explanation for these observed results may be due to $Cu^{2+}$'s ability over $Co^{2+}$'s to more efficiently interact with the hydrogen peroxide produced from the high-LET irradiations via Fenton-type reaction. Therefore, $Cu^{2+}$ Fenton-type reaction would result in the production of more hydroxyl radical formation, thus increasing the amounts of more randomly distributed SSBs (Figures 3.6). Moreover, metal ions are essential for the formations of strand breaks with hydrogen peroxide through Fenton-type reaction to produce hydroxyl radicals (Figures 3.3B & 3.4B) [306], as well as, site-specific mechanisms in the formation of DSBs mediated by $Cu^{2+}$-Fenton reactions (Figure 3.6) [317]. Our results also agreed with prior research that the $Cu^{2+}$-Fenton system generated a higher total yield of DNA lesions than with the $Co^{2+}$-Fenton system [326].

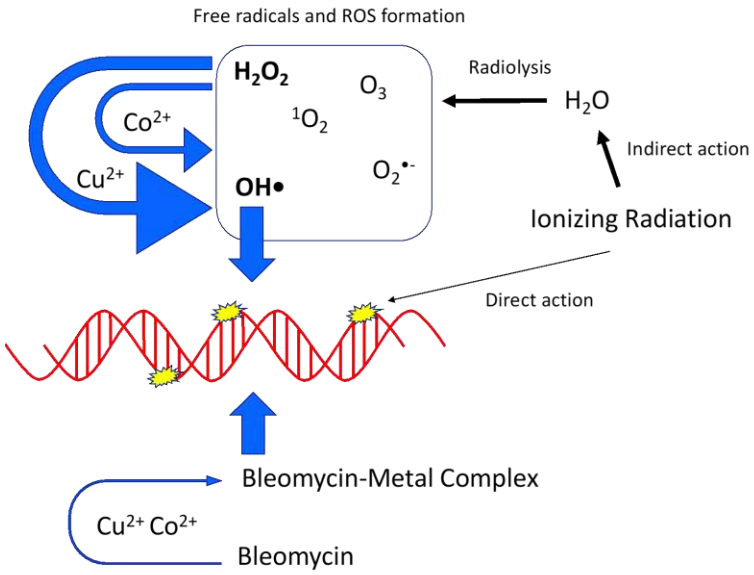


**Figure 3.6. Schematic of metals with each solution treatment.** Proposed mechanisms of metal enhancement of ionizing radiation, bleomycin and $H_2O_2$. Thickness of arrows associated with the degree of effects.

Importantly, although $Cu^{2+}$'s increased ability to induce hydroxyl radical ions through Fenton-type reaction, mammalian cells are not efficiently killed by SSBs caused by hydroxyl radicals from hydrogen peroxide. Hydroxyl radicals induced singly damaged sites are efficiently

and accurately repaired by cellular repair mechanisms in contrast to hydroxyl radicals produced via the radiolysis of water causing LMDS which are much more difficult for the cell to repair [319]. This is most likely due to DSBs being the major actor responsible for radiation-induced cell death which occur from localized SSBs [330]. Although, our hydrogen peroxide results were consistent with our ionizing radiation results in which $Cu^{2+}$ in solution with DNA not only increased SSBs but DSBs as well. This may suggest that the hydrogen peroxide produced from the ionizing radiation, importantly from our high-LET radiation sources, was in close enough proximity to the DNA which allowed for the Fenton-type reaction production of hydroxyl radical ions to induce these LMDS. Future experiments examining direct plasmid analysis to confirm how copper influences high-LET radiation-induced DNA damage and their complexity would be beneficial to further support this reasoning [326].

Finally, we observed how $Cu^{2+}$ and $Co^{2+}$ influence DNA breaks with bleomycin, a radiomimetic drug that binds with a metal and uses molecular oxygen to induce DSBs [309]. Prior studies have suggested that $Cu^{2+}$-bleomycin complex is inactive in the degradation of DNA [312, 331]. On the other hand, several studies have demonstrated that the $Cu^{2+}$-bleomycin complex does indeed produce DNA strand scission [332, 333]. Our results agree with the latter, in which $Cu^{2+}$ in solution with bleomycin and DNA was observed to more efficiently induce DSBs and SSBs than in solution with control (Figures 3.3A & 3.4A). On the other hand, we observed a concentration dependent switch from sensitization to protection for $Co^{2+}$ with bleomycin in both dsDNA and ssDNA. A possible reasoning behind this may be from the fact that it has been established that $Co^{2+}$-bleomycin binds efficiently only at certain sites of DNA and that cleavage does not occur at all bound sites [334]. Furthermore, our observed results may also be explained as prior studies have demonstrated that as the ratio of DNA to $Co^{2+}$-bleomycin

complex increases, the $Co^{2+}$-bleomycin complex becomes resistant to oxidation [36-39]. The MER values of bleomycin were the smallest among tested agents with metals. This suggested that bleomycin induced DNA damage is not strongly associated with hydroxyl radicals.

In conclusion, the present work demonstrates that $Cu^{2+}$ and $Co^{2+}$ may be useful tools to enhancing the indirect action of DNA damage for high-LET irradiations. Both metals were observed to be capable of increasing DNA strand breaks following irradiation. However, $Cu^{2+}$ was observed to be more efficient than $Co^{2+}$ at inducing these strand breaks. We propose the mechanism behind this observation is due to their interaction with hydrogen peroxide produced from the radiolysis of water via Fenton-type reaction. This was supported as we also observed this increase in DNA strand breaks with the metals in solution with hydrogen peroxide and DNA. These results suggest a possible mechanism of enhancement for the indirect action of DNA damage produced by high-LET radiation.

## 3.4 Materials and Methods

### 3.4.1 Irradiation conditions

Low-LET irradiations were conducted utilizing the X-ray generator TITAN 320 (200 kVp, 20 mA, 5 mm aluminum and copper filter). X-ray exposure rate was 3.1 Gy/min and LET value of 2 keV/μm [335]. For high-LET heavy ion irradiations, spread out Bragg-peak (SOBP) carbon-ions and monoenergetic iron-ions were accelerated to 290 and 500 MeV/n, respectively, using HIMAC. Dose rates for carbon-ions and iron-ions were set at 5 and 10 Gy/min, respectively. SOBP carbon-ions and monoenergetic iron-ions contained a LET value of 50 and 200 keV/μm, respectively [335].

### 3.4.2 DNA solution preparation and chemical treatment

A total of 10 μL of reaction solution was used containing 30 ng of double strand DNA (dsDNA) of lambda phage (New England BioLabs Inc, Ipswich, MA, USA, stock concentration of 500 ng/μL) or 83 ng of single strand DNA (ssDNA) of M13mp18 phage (New England BioLabs Inc, stock concentration of 250 ng/μL) with 10 mM Tris-HCl pH7.71 with or without 0.2 mM of $CuCl_2$ or $CoCl_2$.

For chemical treatment experiments, hydrogen peroxide or bleomycin was added to a total of 10 μL of reaction solution with or without metals. Once solution was made, they were incubated at 37°C for 30 min. Following irradiation or chemical treatment incubation 1mM EDTA was added to chelate excess metals within the solution and incubated at room temperature for 5 min [317].

### 3.4.3 Electrophoresis and DNA damage quantification

Electrophoresis was carried out as previously described [336-338]. Each sample was added with 6X loading dye (15% Ficoll (w/v), 10% glycerol (v/v), 0.25% bromophenol blue (w/v), and 0.25% xylene cyanol FF (w/v) in distilled water) and electrophoresis was carried out with an 1% (w/v) Agarose gel in 1X TAE buffer containing 0.01% (w/v) ethidium bromide and ran at 100 V and for 60 min in 1x TAE buffer. After electrophoresis and destained in distilled water, gels were imaged, and band intensity measurements were processed. Band intensities at intact DNA were then normalized to control that were not irradiated or treated without chemicals and calculated fraction of intact DNA after irradiation or chemical treatment.

$D_{50}$ and $IC_{50}$ values, dose or chemical concentration required to produce 50% intact DNA, were determined using regression curves generated by GraphPad Prism 8 (GraphPad

Software, San Diego, CA, USA). From these values, Metal enhancement ratios (MER) were calculated from $D_{50}$ ($IC_{50}$) of control values divided by $D_{50}$ ($IC_{50}$) of tested agents values.

### 3.4.4 Statistical analysis

All experiments were carried out with three or more independent experiments. Data points were expressed as a mean with standard errors of the means. All experimental data were analyzed via GraphPad Prism 8. One-way analysis of variance (ANOVA) and Turkey's multiple comparison test was conducted for statistical significance. Differences with *P* values of less than 0.05 were considered statistically significant.

# CHAPTER FOUR

## THE PREFERRED DSB REPAIR PATHWAY SWITCHES FROM NHEJ TO HR AS THE CARBON-ION BEAM APPROACHES THE SOBP

**Summary:** The cellular carbon-ion radiation-induced DNA double-strand break (DSB) repair pathway choice is an essential component behind the fate of the cell's survival. The two main DSB repair pathways in mammalian cells are non-homologous end joining (NHEJ) and homologous recombination (HR). It has been suggested that the balance between which of the two repair pathways is preferentially utilized depends on the DSB complexity. In the case of the carbon-ion beam, the DSB complexity increases within the carbon-ion spread-out Bragg peak (SOBP) as the linear energy transfer (LET) increases. Taking advantage of this increase in DSB complexity with an increase in the LET, we investigated the importance of each DSB repair pathway at each depth within the carbon-ion SOBP range in a single biological system using cell survival as an endpoint. We addressed the radiosensitivity of CHO mutant cell lines either deficient in NHEJ (V3) or HR (51D1) in comparison to the wild-type (10B2) cell line. Our results demonstrated that both NHEJ- and HR-deficient cells portrayed an increase in radiosensitivity throughout the full carbon-beam range. NHEJ-deficient cells had the greatest increase in radiosensitivity in the depths from beam entrance up to the proximal depth of the SOBP and demonstrated a dose-dependent increase in survival throughout the SOBP. HR-deficient cells had the greatest ratio of survival fraction at entrance depth to lowest survival fraction within the SOBP. Collectively, our results suggest that HR may be the most beneficial pathway to inhibit in order to enhance the cell killing effect of CIRT in the targeted cells within the SOBP while limiting unwanted damage to the surrounding cells. As demonstrated here,

studies on DSB repair pathway choice at varying depths within the full carbon-ion beam range provide important insight on potential targets to inhibit to enhance the efficiency of CIRT.

## 4.1 Introduction

Radiation therapy has developed into an essential cancer treatment modality as more than 2/3$^{rds}$ of cancer patients in the USA today receive some form of radiation therapy that can be used either alone or in combination with other cancer therapeutic modalities, such as surgery or chemotherapy [75]. The main goal behind radiotherapy is to precisely eliminate the tumor cells while minimizing the damage to the surrounding normal healthy cells. Of the radiation therapy methods available today, carbon-ion radiotherapy (CIRT) has demonstrated to be the most effective in the treatment of benign tumors due to it having optimal properties for producing both physically superior and biologically effective dose localization in the body of densely ionizing high-linear energy transfer (high-LET) radiation which provides it with superior depth-dose distribution around its Bragg peak [78]. The high-LET spectrum of the carbon-ion (C-ion) beam provides many biological advantages over the other low-LET radiotherapies, such as photon or proton beams, which include a higher relative biological effectiveness (RBE) [301, 339], reduced capacity in the DNA repair of cellular radiation induced lesions [340], a lower oxygen enhancement ratio (OER) [341], and has been demonstrated to be highly effective in treating radioresistant tumors [342].

CIRT uses ionizing radiation which induces a variety of DNA lesions, with DNA double-strand breaks (DSBs) being the most toxic due to unrepaired or mis-repaired DSBs can lead to cell death or genomic instability [343-345]. High-LET C-ions induce a high density of DSBs along their particle tracks, while low-LET photon beams induce sporadic DNA damage in their irradiated cells [346]. The high density of the DSBs induced by the high-LET C-ions produces

DSBs in very close proximity to one another, within one or two helical turns of the DNA, which are considered as complex DSBs and are known to be very difficult for the cell to faithfully repair [39, 286]. As a result, higher levels of cell death are induced by high-LET radiation as compared to low-LET radiation, even at the same physical dosages [346]. This is important as the C-ion beam used in CIRT is a mixture of both low- and high-LET radiation qualities. This is a result of the LET increasing the closer the beam approaches its Bragg peak, where it reaches its peak in LET value.

In eukaryotes, the two main pathways for DSB repair are homologous recombination (HR) and non-homologous end joining (NHEJ). NHEJ is a "quick and dirty" repair mechanism that is active throughout the full cell-cycle but is far less accurate than HR, as small deletions or insertions often occur at these NHEJ repaired DSB sites, which may result in mutations leading to cancer [29]. On the other hand, HR results in mostly error-free repair of the DSB lesions but is only active in late S/G2 phase of the cell cycle due to it requiring a homologous undamaged DNA as the repair template [347, 348]. Thus, the choice of the DSB repair pathway has been suggested to be controlled by the cell-cycle phase [349]. However, with ionizing radiation induced DSBs, it was previously demonstrated that NHEJ initially attempts to repair these DSBs in G2 but if the DNA damage complexity is too high and NHEJ does not ensue the rapid enjoining process, the repair pathway may switch from NHEJ to HR [165].

The choice of DSB repair pathway the cell preferentially utilizes following high-LET radiations, such as CIRT, is still open to debate as prior studies have demonstrated compelling evidence for both NHEJ and/or HR pathways. In one such study conducted by Takahashi et al., the authors showed that following CIRT and using cell survival as their endpoint, targeting the NHEJ repair pathway yielded higher radiosensitivity in cells than targeting HR [346]. This was

further supported in another study conducted by Zhou et al, in which they inhibited the DNA-dependent protein kinase catalytic subunit (DNA-PKcs), a central component in the NHEJ repair complex, and demonstrated that these cells had an increased radiosensitivity in cancer cells following C-ion irradiation. However, the authors also mentioned that most of the C-ion irradiation induced DNA damage was repaired within 24 hours following radiation in both of their cell lines with and without NHEJ inhibition [257].

On the other hand, a prior study conducted by Gerelchuluun et al. demonstrated that while the NHEJ pathway plays an important role in repairing the DSBs induced by both clinical proton and C-ion beams, the HR pathway following C-ion irradiation is more involved in the repair of DSBs [256]. It has also been demonstrated by Nakajima et al. that the cells that were pre-exposed to low dose ionizing radiation preferred to undergo HR following a challenging dose of ionizing radiation in G2 cells, while NHEJ repair kinetics in G1 were not affected by pre-ionizing radiation treatment. In this study, the authors suggested this was due to pre-exposure of ionizing radiation stimulated DNA DSB end resection which promotes the use of HR [65]. Wang et al. also demonstrated that high-LET radiation induces a large amount of short DSB fragments (<40 base pairs) which prevent the efficient loading and binding of the Ku heterodimer, an NHEJ factor, onto the broken DNA ends. Since, Ku binding to the DSBs is the first step in NHEJ, this leads to the suppression of NHEJ-mediated repair of the DSBs at these clustered damage sites and thus the preferred DSB repair pathway was suggested to become HR [200].

These conflicting studies may be the result of the C-ion beam used in CIRT being comprised of both low- and high-LET radiation qualities depending on the depth in which the beam traverses through the medium as it approaches its Bragg peak. Thus, it may be possible that each experiment may produce different results in the type of DSB repair mechanism that is

preferentially used depending on their evaluated depth within the C-ion beam range. In this study, we have overcome this issue by utilizing a single biological system capable of incorporating the full C-ion SOBP beam range in order to address which DSB repair pathway, NHEJ or HR, is preferentially utilized at different beam depths. We exposed Chinese hamster ovary (CHO) wild-type (WT) cells and CHO mutant cell lines deficient in either the NHEJ or HR pathway to C-ion spread-out Bragg peak (SOBP) beam at increasing treatment dosages and examined their radiosensitivity via our modified method of the cell survival assay. The results of this study are very important to determine which DSB repair process is most essential at each depth within the C-ion beam range, as this study will provide key insights into important targets that may be inhibited to enhance the efficiency of CIRT in killing the targeted tumor cells within the C-ion SOBP while limiting the damage to the surrounding healthy tissues.

## 4.2 Results

### 4.2.1 Identification of the biological spread-out Bragg peak (SOBP) range in WT cells

In order to determine the biological SOBP range, as with all cell survival experiments in this study, all experimental flasks were irradiated with 290 MeV/n C-ion SOBP beam delivery in horizontal orientation to C-ion beam source and the survival fraction at each depth was calculated and normalized with control (0Gy) at each depth with each respected cell line, as described in material and methods (Figure 4.1). Briefly, the Bragg peak of a monoenergetic C-ion beam of 290 MeV/n was spread out to 6 cm via ridge filters [301]. Previously, we have demonstrated that the biological Bragg peak depth for WT CHO cell line, 10B2, following 290 MeV/n monoenergetic C-ion irradiation was at 14.0 cm, as this depth demonstrated the lowest survival fraction within the full C-ion beam range [71, 290]. Consistently, our results demonstrated a decrease in survival fractions in the depths ranging from 8.0 – 14.0 cm under all

irradiation treatment dosages following the C-ion SOBP beam delivery. Thus, we define this range as our biological SOBP range.

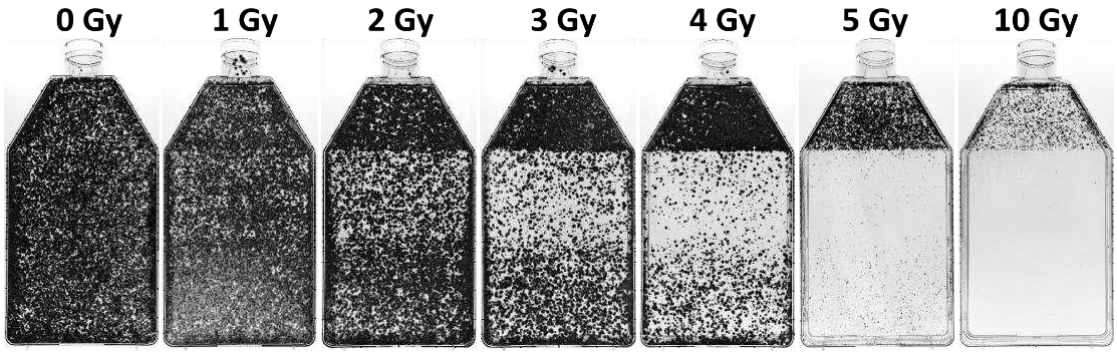


**Figure 4.1. Flask images of CHO WT cell line with increasing treatment dosages**. Images of flasks containing WT CHO cell line following horizontal C-ion SOBP irradiation and 7-day incubation of each respected treatment dosage.

Survival fractions of the CHO WT cell line, 10B2, were not consistent throughout the SOBP as we observed an increase in the survival fractions as the beam proceeded from the proximal to distal end of the SOBP, regardless of initial treatment dosage (Figures 4.2A). Significant increases or decreases in survival fractions within the C-ion beam range for each initial beam treatment irradiation dosage was determined by comparing evaluated depths to the first evaluated depth at 1.0 cm from the C-ion beam entry into the flask for all cell survival experiments in this study. The depth at 1.0 cm represented the incident C-ions.

Our results demonstrated that the range of significant decrease in survival fractions increased with an increase in initial treatment dosage from 1 to 4 Gy ($P<0.05$) (Figure 4.2B). Following 1 Gy treatment dosage, depths displaying a significant decrease were 8.5, 10.5, 12.0 and 12.5 cm ($P<0.05$). At this dosage, the depths with the most notable lowest survival fractions were at 8.5, 10.5 and 12.5 cm with mean values of $0.91 \pm 0.036$, $0.89 \pm 0.001$, and $0.89 \pm 0.015$, respectively. Following 2 Gy treatment dosage, the range of depths displaying a significant decrease were from 7.5 – 13.5 cm ($P<0.05$). At this dosage, the depths with the most notable

lowest survival fractions were at 8.0, 8.5 and 13.0 cm with mean values of 0.61 ± 0.122, 0.65 ± 0.094 and 0.68 ± 0.059, respectively. Following 3 Gy treatment dosage, the range of depths displaying a significant decrease were from 7.0 – 13.5 cm ($P<0.05$). At this dosage, the depths with the most notable lowest survival fractions were at 8.0, 8.5 and 10.5 cm with mean values of 0.38 ± 0.043, 0.40 ± 0.055 and 0.37 ± 0.023, respectively. Following 4 Gy treatment dosage, the range of depths displaying a significant decrease were from 6.8 – 13.5 cm ($P<0.05$). At this dosage, the depths with the most notable lowest survival fractions were at 8.5 and 10.5 cm with mean values of 0.16 ± 0.057 and 0.13 ± 0.009, respectively.

Range of significant increase in survival fractions decreased with an increase in initial treatment dosage from 4 to 10 Gy ($P<0.05$). Following 4 Gy treatment dosage, the range of significant increase was from 14.0 – 18.0 cm ($P<0.05$) with 14.0 cm having a mean value of 0.87 ± 0.079. Following both 5 and 10 Gy treatment dosages, the range of significant increase was from 14.2 – 18.0 cm ($P<0.05$) with 14.2 cm having a mean value of 0.84 ± 0.114 and 0.51 ± 0.114, respectively. Collectively, these results demonstrate that as the treatment dosage increased the survival fraction decreased both throughout the biological SOBP (8.0 – 14.0 cm) as well as in the adjacent post-SOBP depths (>14.0 cm).

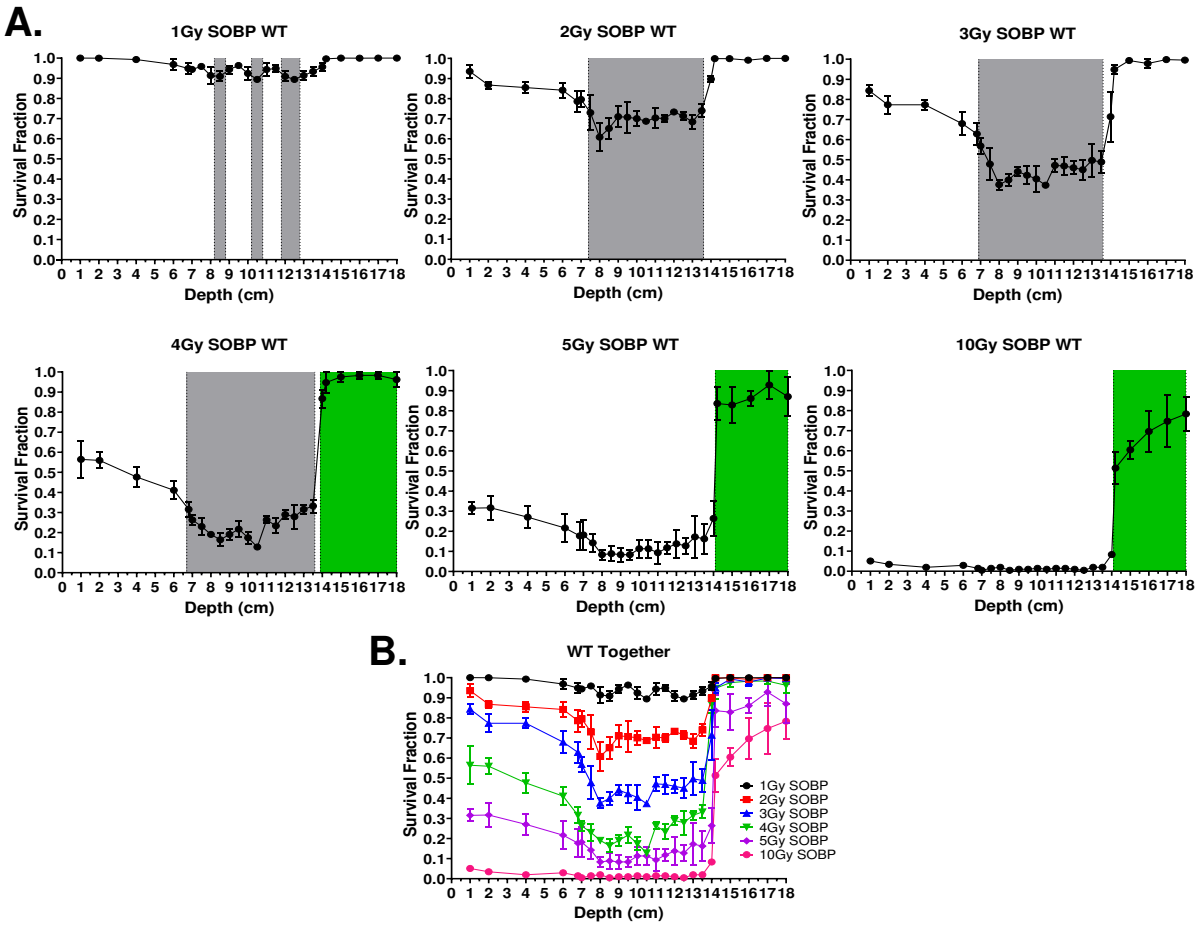


**Figure 4.2. Cell survival distribution of WT CHO cell line with increasing treatment dosages.** **(A)** Survival fractions at each depth following each respected treatment dosage. Areas highlighted in gray or green represent a significant decrease or significant increase, respectively ($P<0.05$), as compared to the closest analyzed depth near beam entry at 1.0 cm for each respective dosage, One-Way ANOVA followed by Bonferroni multiple comparisons test. **(C)** Merge of survival fractions following each respected dosage. Error bars indicated standard errors of the means from a minimum of three independent experiments per each initial dosage.

### 4.2.2 Importance of HR in the repair of C-ion irradiation-induced DSBs

Next, we sought out to determine the importance of the two main DSB repair pathways involved in the repair of C-ion radiation-induced DSBs, HR and NHEJ. First, we investigated the contribution of the HR mechanism for DSB repair throughout the full C-ion SOBP beam range by evaluating the survival fractions at each depth within our flasks with the CHO mutant cell line, 51D1, at increasing C-ion SOBP treatment dosages (Figure 4.3). This cell line has mutated Rad51D, which is an essential component in HR repair [33].

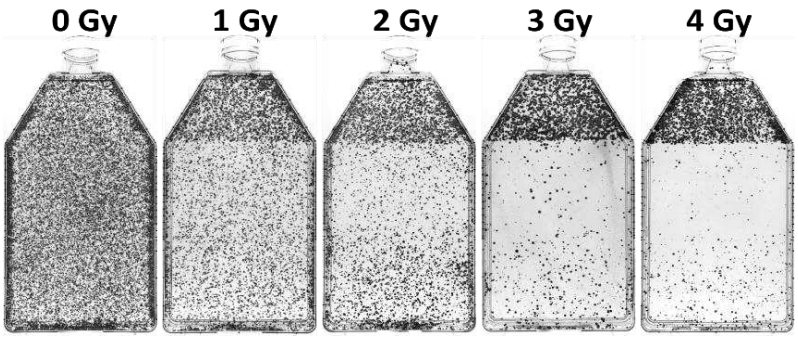


**Figure 4.3. Flask images of 51D1 cell line with increasing treatment dosages.** Images of flasks containing 51D1 cell line following horizontal C-ion SOBP irradiation and 7-day incubation of each respected treatment dosage.

The range of significant decrease in survival fractions increases with an increase in initial treatment dosage from 1 to 3 Gy ($P<0.05$) (Figures 4.4A,B). Following 1 Gy treatment dosage, depths displaying a significant decrease were 8.5, 9.0, 10.0 and 10.5 cm ($P<0.05$). At this dosage, the depths with the most notable lowest survival fractions were at 8.5, 10.0 and 10.5 with mean values of 0.35 ± 0.111, 0.36 ± 0.089 and 0.36 ± 0.107, respectively. Following 2 Gy treatment dosage, the range of depths displaying a significant decrease were from 7.0 – 11.5 cm as well as 12.5 cm ($P<0.05$). At this dosage, the depths with the most notable lowest survival fractions were at 8.0, 8.5 and 10.5 with mean values of 0.17 ± 0.039, 0.18 ± 0.076 and 0.14 ± 0.046, respectively. Following 3 Gy treatment dosage, the ranges of depths displaying a significant decrease were from 8.0 – 9.0 cm and from 10.0 – 11.5 cm ($P<0.05$). At this dosage, the depths with the most notable lowest survival fractions were at 8.0, 8.5 and 10.5 with mean values of 0.05 ± 0.009, 0.04 ± 0.009 and 0.05 ± 0.014, respectively.

A significant increase was observed for all treatment dosages. In contrast to WT cells, the range of significant increase in survival fractions increased with an increase in initial treatment dosage. Following both 1 and 2 Gy treatment dosages, the range of significant increase was from 15.0 – 18 cm ($P<0.05$) with mean values of 0.85 ± 0.045 and 0.77 ± 0.183 at 15.0 cm, respectively. Following 3 Gy treatment dosage, the range of significant increase was from 14.0 –

18 cm (P<0.05) with the mean value of 0.48 ± 0.083 at 14.0 cm. Following 4 Gy treatment dosage, the range of significant increase was from 14.2 – 18 cm (P<0.05) with the mean value of 0.61 ± 0.177 at 14.2 cm.

The HR-deficient mutant cell line, 51D1, demonstrated a similar pattern of survival fraction distribution as with the WT CHO cell line, 10B2. However, there was an increase in radiosensitivity at each respected treatment dosage as compared to the WT CHO cell line. These results suggest that HR is important for the DSB repair throughout the full C-ion beam range but is most important throughout the SOBP.

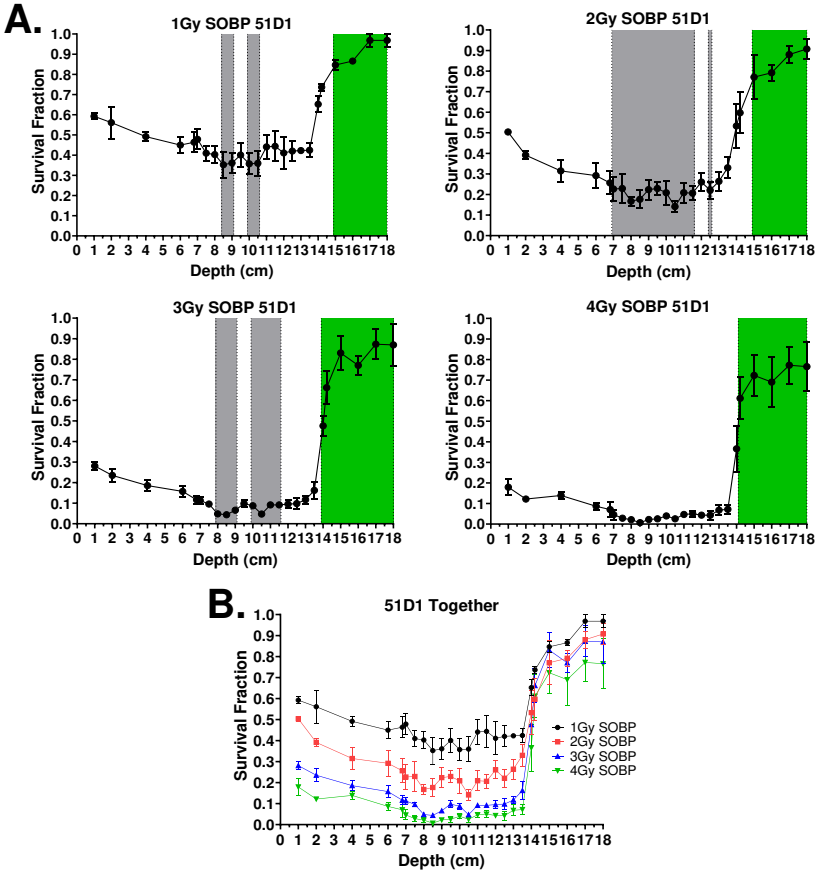


**Figure 4.4. Cell survival distribution of 51D1 cell line defective in HR with increasing treatment dosages.** **(A)** Survival fractions at each depth following each respected treatment dosage. Areas highlighted in gray or green represent a significant decrease or significant increase, respectively (P<0.05), as compared to the closest analyzed depth near beam entry at 1.0 cm for each respective dosage, One-Way ANOVA followed by Bonferroni multiple comparisons test. **(B)** Merge of survival fractions following each respected dosage. Error bars indicated standard errors of the means from a minimum of three independent experiments per each initial dosage.

### 4.2.3 Importance of NHEJ in the repair of C-ion irradiation-induced DSBs

To further investigate the DSB repair mechanisms utilized following C-ion radiation-induced DSBs, we next examined the survival distribution of the CHO mutant cell line, V3, that is deficient in the NHEJ DSB repair pathway following increasing C-ion SOBP treatment dosages (Figure 4.5). V3 has a mutation in DNA-dependent protein kinase catalytic subunit (DNA-PKcs), which is an essential component in the DNA-PKcs-dependent NHEJ pathway [350].

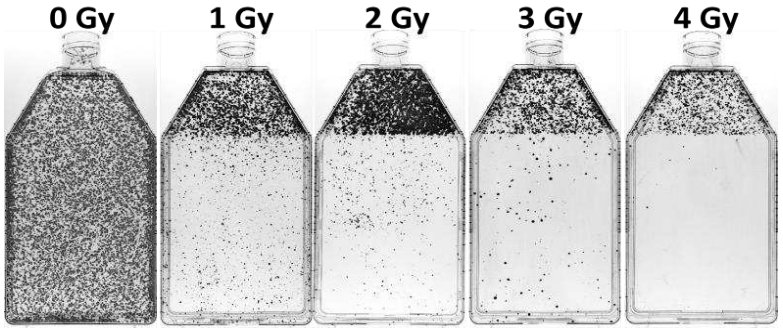


**Figure 4.5. Flask images of V3 cell line with increasing treatment dosages.** Images of flasks containing V3 cell line following horizontal C-ion SOBP irradiation and 7-day incubation of each respected treatment dosage

The V3 cell line did not portray a significant decrease at any of the treatment dosages as compared to the first evaluated depth (1.0 cm) at each respected treatment dosage (Figure 4.6A). However, a significant increase was observed under all treatment dosages. Following 1 Gy treatment dosage, the range of significant increase was from 14.2 – 18 cm ($P<0.05$) with a mean value of 0.80 ± 0.174 at 14.2 cm. Following 2, 3 and 4 Gy treatment dosages, the range of significant increase was from 14.0 – 18 cm ($P<0.05$) with mean values at 14.0 cm of 0.57 ± 0.023, 0.49 ± 0.188 and 0.27 ± 0.075, respectively.

Only following 1 Gy treatment dosage did the survival distribution of V3 cell line demonstrate a similar trend as with WT 10B2 cell line with a decrease in survival fractions up to the proximal half of the SOBP. Although, in the distal portion of the SOBP the survival fractions

of the V3 cell line increased to higher values than those observed at the initial evaluated depth at 1.0 cm (Figure 4.6B). For treatment dosages 2 – 4 Gy, survival fractions increased throughout the SOBP and the average survival within the SOBP was greater than the depths prior to the SOBP for each respected dosage, which was most notable following 2 Gy treatment dosage.

Collectively, the results with the NHEJ-deficient mutant cell line, V3, demonstrate that NHEJ is the most important for C-ion induced DSB repair in the depths prior to the SOBP. In addition, these results suggest that NHEJ becomes less important in the repair of C-ion induced DSBs as the depths proceed from the proximal to distal region of the SOBP (from 8.0 to 14.0 cm), in a treatment dose-dependent manner.

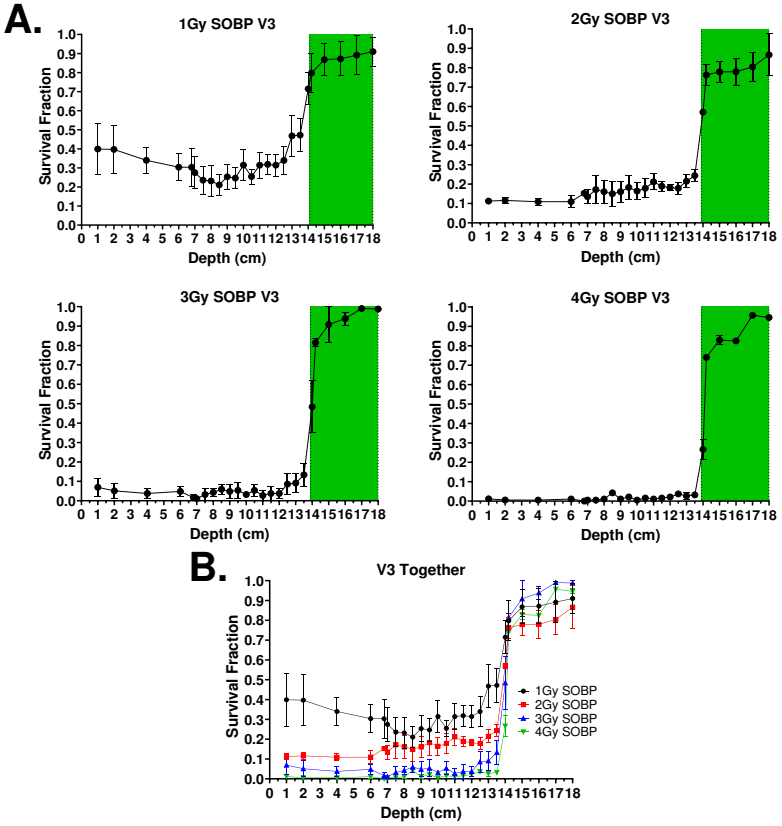


**Figure 4.6. Cell survival distribution of V3 cell line defective in NHEJ with increasing treatment dosages.** **(A)** Survival fractions at each depth following each respected treatment dosage. Areas highlighted in gray or green represent a significant decrease or significant increase, respectively ($P<0.05$), as compared to the closest analyzed depth near beam entry at 1.0 cm for each respective dosage, One-Way ANOVA followed by Bonferroni multiple comparisons test. **(B)** Merge of survival fractions following each respected dosage. Error bars indicated standard errors of the means from a minimum of three independent experiments per each initial dosage.

### 4.2.4 Comparing the radiosensitization between the two mutant cell lines defective in either NHEJ or HR

To investigate which DSB repair process was most important at different C-ion beam depths at each treatment dosage, we compared the survival fractions of each cell line at each depth of their respected treatment dosage (Figure 4.7). Comparison of each mutant cell line's survival fraction mean values with those from WT at each respected depth demonstrated significant differences between 51D1 (defective in HR) and V3 (defective in NHEJ) cell lines following 2 and 3 Gy treatment dosages (Figure 4.8). Following 2 Gy treatment dosage, 51D1 demonstrated significantly less of a difference from WT than V3 did from WT at the depths from 1.0 – 6.0 cm and at the depth of 9.0 cm ($P<0.05$). Following 3 Gy treatment dosage, 51D1 demonstrated significantly less of a difference from WT than V3 did from WT at the depths from 1.0 – 4.0 cm and at the depth of 9.0 cm ($P<0.05$).

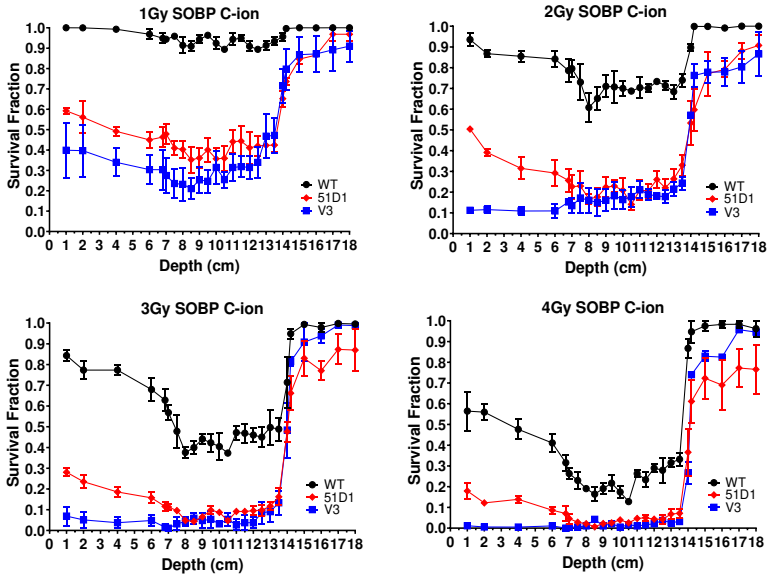


**Figure 4.7. Comparison of cell survival distribution of each cell line at increasing treatment dosages.** Wild type (10B2), 51D1 and V3 cell lines are indicated as black, red and blue, respectively. Error bars indicated standard errors of the means from a minimum of three independent experiments per each initial dosage.

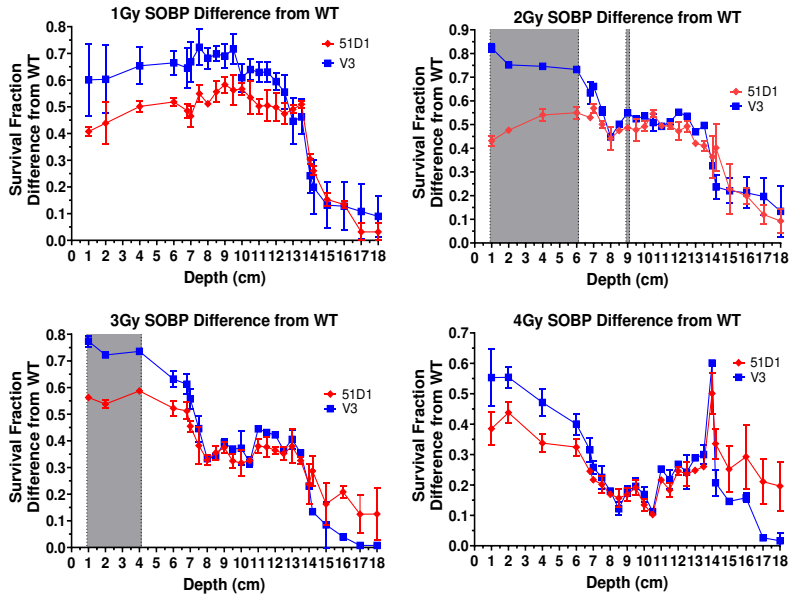


**Figure 4.8. Comparison of each mutant cell line's difference in mean value of survival fraction from WT at each depth following increasing treatment dosage.** Areas highlighted in grey represent a significant difference between each mutant cell line, Multiple t-tests followed by Bonferroni-Dunn method. Error bars indicated standard errors of the means from a minimum of three independent experiments per each initial dosage.

Next, the sensitization enhancement ratio (SER) for each cell line was calculated for the proximal (8.0 – 9.0 cm), mid (10.0 – 11.0 cm) and distal (12.0 – 13.0 cm) regions of the SOBP (Table 4.1). The SER was addressed by comparing the average $D_{10}$ values of each mutant cell line with the average $D_{10}$ value for the WT in each of their respected regions within the SOBP. $D_{10}$ values were defined as the treatment dosage required for 10% survival (0.1 survival fraction) in each region of the SOBP. The SER was calculated via the following equation:

$$\boldsymbol{SER_{SOBP\ region} = \frac{Average\ D_{10}WT_{SOBP\ region}}{Average\ D_{10}Deficient\ cells_{SOBP\ region}}}$$

In all regions of the SOBP, 51D1 had a smaller SER than that of V3. In the proximal region of the SOBP, 51D1 and V3 had an SER of 1.63 and 1.72, respectively. In the mid region of the SOBP, 51D1 and V3 had an SER of 1.55 and 1.65, respectively. In the Distal region of the SOBP, 51D1 and V3 had an SER of 1.57 and 1.67, respectively.

**Table 4.1. $D_{10}$ values and the Sensitization Enhancement Ratios (SER) within the SOBP**

| Cell Line | Proximal $D_{10}$ (Gy) | Mid $D_{10}$ (Gy) | Distal $D_{10}$ (Gy) | Proximal SER | Mid SER | Distal SER |
|---|---|---|---|---|---|---|
| **Wild-Type** | 4.67 ± 0.05 | 4.65 ± 0.16 | 5.10 ± 0.13 | 1.0 | 1.0 | 1.0 |
| **51D1** | 2.87 ± 0.10 | 3.00 ± 0.19 | 3.25 ± 0.11 | 1.63 | 1.55 | 1.57 |
| **V3** | 2.71 ± 0.06 | 2.82 ± 0.05 | 3.06 ± 0.16 | 1.72 | 1.65 | 1.67 |

$D_{10}$ value = Average treatment dosage required to produce 10% survival in either the proximal (8.0 – 9.0 cm), mid (10.0 – 11.0 cm) or distal (12.0 – 13.0 cm) regions of the SOBP

To examine how the importance of each repair pathway throughout the SOBP may differ from depths at the beam entrance, the ratio of the survival fraction at the entrance depth (1.0 cm) to the lowest survival fraction within each of the regions within the SOBP (proximal, mid and distal regions) was determined for WT, 51D1 and V3 (Figure 4.9). In all regions this ratio increased with an increase in treatment dosage for the WT and 51D1 cell lines but fluctuated with the V3 cell line. In addition, out of all regions and respected treatment dosages only the proximal region following 1 Gy treatment dosage did not portray 51D1 with the highest ratio but instead demonstrated that V3 had the highest ratio out of the three cell lines.

Each respected ratio was then compared for significant differences at each of their respected treatment dosages in each region of the SOBP. No significant difference was observed between the ratios of WT and V3 regardless of region or dosage. On the other hand, 51D1 demonstrated a significant difference between both WT and V3. In the proximal region of the SOBP, the ratio of 51D1 was significantly greater than both WT and V3 at 2, 3 and 4 Gy treatment dosages with $P<0.05$, $P<0.001$ and $P<0.05$ for WT, respectively, and $P<0.01$, $P<0.001$ and $P<0.01$ for V3, respectively. In the mid region of the SOBP, the ratio of 51D1 was significantly greater than WT with $P<0.05$ at both 2 and 3 Gy treatment dosages and significantly greater than V3 at 2, 3 and 4 Gy treatment dosages with $P<0.01$, $P<0.05$ and $P<0.05$, respectively. In the distal region of the SOBP, the ratio of 51D1 was significantly greater than WT only at 4 Gy treatment dosage with $P<0.05$ but was significantly greater than V3 at both 2

and 4 Gy treatment dosages with P<0.01 and P<0.001, respectively. Collectively, these results demonstrate that NHEJ is the most important DSB repair pathway leading up to the SOBP, while the importance of the HR DSB repair pathway increases from the proximal to distal regions of the SOBP or throughout the full SOBP as the treatment dosage increases.

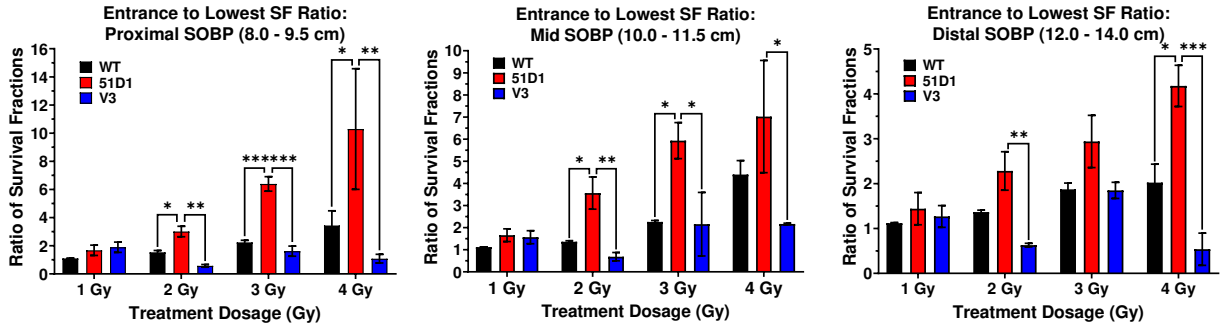


**Figure 4.9. Ratio of survival fraction at entrance depth at 1.0 cm to lowest survival fraction (SF) of each cell line in the in different regions of the SOBP at increasing treatment dosages.** Regions of SOBP were divided into Proximal (8.0 – 9.5 cm) (**Left**), Mid (10.0 – 11.5 cm) (**Middle**) and Distal (12.0 – 14.0 cm) (**Right**). Within each region the depth with the lowest survival fraction for each cell line was selected for ratio calculation. Error bars indicated standard errors of the means from a minimum of three independent experiments per each initial dosage. Significance determined by One-Way ANOVA followed by Tukey multiple comparison test, * = P<0.05, ** = P<0.01, *** = P<0.001.

## 4.3 Discussion

In the present study, utilizing our modified version of the cell survival assay we observed the survival fractions at increasing depths within the 290 MeV/n C-ion SOBP beam range with increasing treatment dosages. Previously, we demonstrated that the biological Bragg peak depth, the depth containing the lowest survival fractions throughout the full C-ion beam range, following monoenergetic 290 MeV/n C-ion beam irradiation was at 14.0 cm, regardless of initial treatment dosage [71, 290]. With the use of ridge filters, the 290 MeV/n monoenergetic C-ion beam is known to produce a SOBP of 6 cm [301]. Consistent with these previous findings, we observed a decrease in survival with the CHO WT cell line, 10B2, throughout the depths of 8.0 cm – 14.0 cm (Figure 4.2B). Thus, we defined this range as our biological SOBP.

However, survival fractions were not consistent throughout the SOBP as the survival fraction increased from the proximal to distal ends of the SOBP. These results correlate with what is known about the integrated dose (Gy) and linear energy transfer (LET) (keV/µm) distribution throughout the SOBP (Figure 4.10). The integrated dose is known to rapidly increase the closer the beam approaches its peak at the proximal end of the SOBP, at 8.0 cm, and steadily decreases until it reaches the distal end of the SOBP, at 14.0 cm, in which it rapidly decreases following this depth. In contrast, the LET slightly increases at the proximal end of the SOBP and rapidly increases the closer the beam approaches to the distal end of the SOBP, resulting in a large peak in LET at the depth of 14.0 cm, followed by a rapid decrease in LET [73].

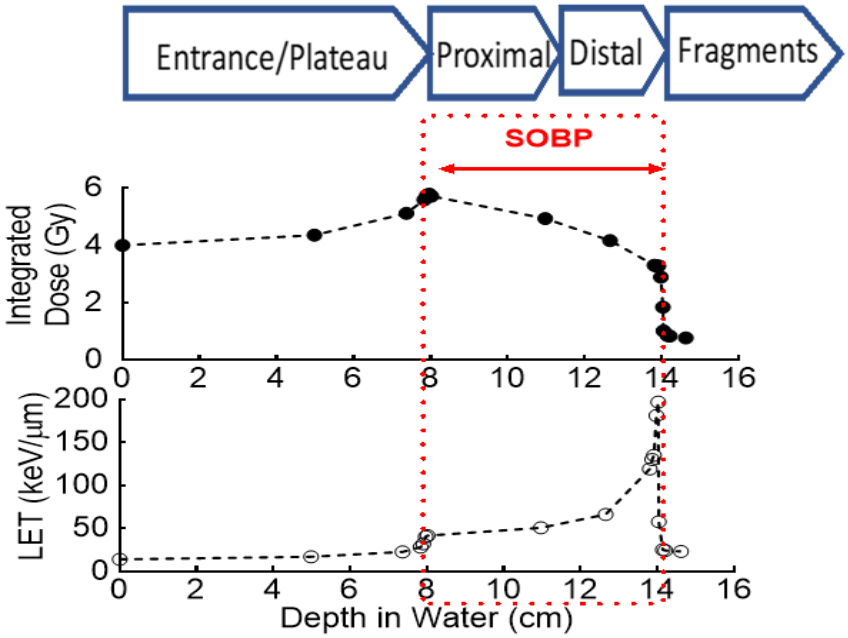


**Figure 4.10. Integrated dose (Gy) and LET (keV/µm) distribution throughout the full range of the 290 MeV/n C-ion SOBP beam at a treatment dosage of 4 Gy.** Figure adapted from Sunada et al. 2017 [351].

Our results demonstrated that the survival within the SOBP was the lowest when the dosage was at its highest, in the proximal end and was the highest when the LET was at its highest, in the distal end (Figures 4.2 & 4.10). These results suggest that the integrated dosage has a greater influence than the LET in the case of cell survival. Although, this may be due to

less cells being “hit” at the distal end of the SOBP, where there is higher LET but lower integrated dosage.

Next, we used our system to address the importance of HR and NHEJ pathways in repairing the C-ion irradiation induced DSBs at increasing depths within the C-ion SOBP beam range. This was accomplished by addressing the survival fraction at each depth utilizing cell lines that were defective in either the HR or NHEJ pathways. In order to account for differences in plating efficiencies between the cell lines, the survival fractions were normalized with their control (0 Gy) for each respected cell line, including WT, at each respected evaluated depth within our system. Prior studies have demonstrated that the occurrence and radiation quality (low- or high-LET) of ionizing radiation-induced DSBs are known to depend on the ionizing density that is associated with the radiation [103, 352, 353]. Therefore, as the ionization density increases within the C-ion SOBP beam range, this should exert a significant influence on the subsequent repair pathway choice. For this reasoning, in the current study we compared the contributions of the HR and NHEJ pathways in the repair of C-ion SOBP irradiation-induced DSBs in genetically established HR- or NHEJ -deficient cell lines.

HR is known to be a mostly error-free pathway that is only active in the S and G2 phases of the cell cycle [115]. In this study, we used the CHO mutant HR-defective cell line, 51D1, which is defective for Rad51D [263, 264]. Rad51D, otherwise known as Rad51 paralog D, is an essential component in the HR pathway as it is a mediator protein involved in the replacement of the replication protein A (RPA) with Rad51 to bind to the ssDNA overhang created in the initial steps of HR which allows for the HR pathway to continue [120]. The HR-defective cell line, 51D1, exhibited high levels of sensitivity at all depths throughout the C-ion SOBP beam range as compared to WT cells following each respective treatment dosage (Figure 4.7). These results are

consistent with prior studies who also demonstrated that HR-deficient cell lines demonstrated an increase in sensitivity compared to WT cells following C-ion beam irradiation [65, 167, 256, 264].

While 51D1 cells were more sensitive than WT cells, they demonstrated a similar pattern in the survival fraction distribution with that of WT cells throughout the full C-ion SOBP beam range. However, the increase in radiosensitivity was most notable throughout the C-ion SOBP. The sensitivity was also observed to decreased as the beam proceeded from proximal to distal regions of the SOBP as the 51D1 cells demonstrated their highest SER of 1.63 in the proximal region of the SOBP (8.0 – 9.0 cm) and an SER of 1.57 in the distal region of the SOBP (12.0 – 13.0 cm) (Table 4.1). In addition, out of all cell lines used in this study, 51D1 had the highest ratio of entrance depth survival fraction (1.0 cm) to lowest survival fraction within each region of the SOBP (proximal SOBP = 8.0 – 9.5 cm, mid SOBP = 10.0 – 11.5 cm and distal SOBP = 12.0 – 14.0 cm) for all treatment dosages, except for 1 Gy within the proximal SOBP region in which V3 had the highest ratio (Figure 4.9). This result is consistent with a prior study conducted by Sunada et al., in which they used an OptiCEll$^{TM}$ system to observe the cell survival throughout the full C-ion SOBP beam range. Data generated from this study demonstrate that this ratio was greater for V3 than 51D1 following 1 Gy treatment dosage as well as demonstrated that 51D1 cells demonstrated an increase in radiosensitivity as compared to WT [351].

Next, we examined the importance of the NHEJ DSB repair pathway throughout the full C-ion SOBP beam range. NHEJ is a simple, rapid and efficient DSB repair pathway that is active throughout the full cell cycle but is known to be error-prone [115, 354, 355]. In this study we used the CHO mutant NHEJ-deficient cell line, V3, which is defective in DNA-PKcs [262]. DNA-PKcs are known to play a key role in the NHEJ repair pathway and the phosphorylation

status of the DNA-PKcs indicates the level of kinase activity as well as the DNA end-binding ability, which assumably determines whether the cell will utilize either the NHEJ or HR pathway [356, 357]. The NHEJ-deficient cell line, V3, demonstrated the highest sensitivity of all cell lines used in this study. As with 51D1, V3 demonstrated its highest SER of 1.72 in the proximal region of the SOBP which decreased as the beam proceeded throughout the SOBP with the distal region having an SER of 1.67 (Table 4.1).

However, V3 cells demonstrated the most notable increase in sensitivity in the depths from beam entrance up to the SOBP. In contrast to 51D1 and WT cells, our results demonstrated that V3 cells had a dose dependent increase in survival throughout the SOBP as compared to survival in the depths prior to the SOBP, which was most apparent following 2 Gy treatment dosage (Figure 4.6). Moreover, in the depths prior to the SOBP, V3 cells demonstrated a higher difference in their survival from WT as compared to the difference between 51D1 and WT cells (Figure 4.7). Thus, these results suggested that NHEJ is very important in the depths from beam entrance up to the proximal region of the SOBP. The possible reason for this may be due to the complexity of the DSBs, as the DSBs may be less complex in this region of the C-ion SOBP range. This reasoning is consistent with the results of a prior study conducted by Yajima et al., in which they demonstrated that less complex DSBs are primarily repaired through NHEJ and the efficiency of NHEJ in repairing the DSBs diminishes as the DSB complexity increases and the preferred DSB repair pathway becomes HR [166].

Collectively, the results of this study demonstrate a potential benefit for inhibiting HR over the inhibition of NHEJ in order to enhance the effectiveness of CIRT. Even though both HR- and NHEJ-deficient cell lines, 51D1 and V3, respectively, portrayed an increase in radiosensitivity as compared to the WT cell line, 10B2, the NHEJ-deficient cell line, V3,

demonstrated to be highly sensitive within the depths from the entrance up to the proximal SOBP (1.0 – 8.0 cm) (Figures 4.6 & 4.8). Therefore, using drugs to inhibit the NHEJ DSB repair pathway may have greater unwanted damage to the surrounding normal tissue outside of the targeted tumor cells within the SOBP.

Clinical studies have also observed unfavorable outcomes in patients whose tumors strongly express RAD51, which suggests that human tumors may develop "addictions" to abnormally high RAD51 levels [133, 358, 359]. These studies support our results demonstrating HR-deficient cell line, 51D1, having an increase in radiosensitivity and suggest that inhibition of RAD51, thereby inhibiting HR DSB repair pathway, may be an important strategy to include in combination with CIRT. This strategy has been shown to be very appealing as prior reports have also demonstrated that HR inhibition via Gleevec-mediated inhibition of Rad51 expression and Rad51 siRNA may promote preferential sensitization of tumor cells relative to normal cells [360, 361]. One potential drug that has promising results in cell-based experiments is RI-1, where it demonstrated to specifically inhibit HR efficiency. RI-1 is a RAD51-inhibitory compound that inactivates RAD51 by directly binding to a protein surface at cysteine 319 that serves as an interface between protein subunits in RAD51 filaments [362]. In future studies, it would be beneficial to utilize our system with human cell lines treated with drugs such as RI-1 in combination with CIRT to examine the survival distribution throughout the full C-ion beam range and observe the extent of its radiosensitization ability as well as the effects it may have on the surrounding cells outside of the targeted SOBP region.

In conclusion, studies on how the HR and NHEJ pathways contribute to the repair of C-ion radiation induced DSBs are essential in our understanding of the responses of cancers to this type of radiotherapy as well as important for developing molecularly targeted radiosensitizing

therapies to incorporate during treatment to enhance the effectiveness of CIRT to eradicate the target tumor cells. Collectively, the results of this study utilizing a single biological system demonstrated that while NHEJ is important throughout the full C-ion SOBP range, the importance of NHEJ decreases as the importance of HR increases as the C-ion beam proceeds throughout the SOBP (Figure 4.11). Therefore, HR inhibition is a potentially optimal target to complement radiotherapy, and these results may contribute to the development of more effective C-ion radiation therapy.

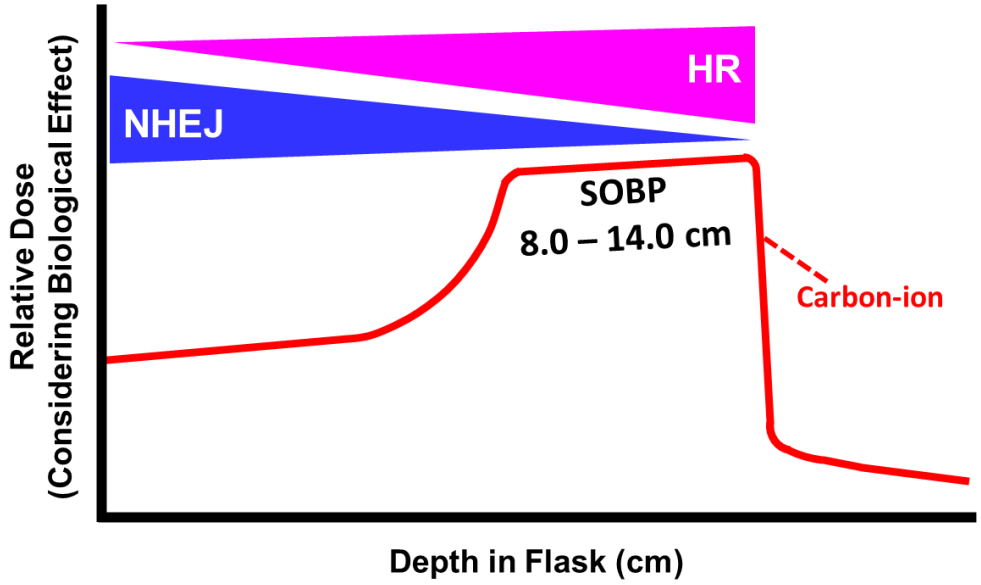


**Figure 4.11. Graphical representation demonstrating the importance of each DSB repair pathway throughout the carbon-ion SOBP beam range.** NHEJ is more important in depths prior to the SOBP. HR becomes more important in the depths within the SOBP.

## 4.4 Materials and Methods

### 4.4.1 Cell culture and irradiation conditions

Chinese hamster ovary (CHO) wild type (10B2) cells including kindly supplied by Dr. Joel Bedford (Colorado State University, Fort Collins, CO, USA). DNA repair deficient CHO mutants, V3 (DNA-PKcs) [262] and 51D1 (Rad51D) [263] were kindly supplied by Dr. Larry Thompson at the Lawrence Livermore National Laboratory (Livermore, CA, USA).

Cells were grown and maintained in α-MEM (Invitrogen, Carlsbad, CA, USA) supplemented with 10% heat inactivated fetal bovine serum (Sigma), supplemented with antibiotics and antimycotics (Anti-Anti; Invitrogen, Grand Island, NY, USA) at 37 °C in incubators at 5% CO2 and 100% humidity. Carbon-ions were accelerated to 290 MeV/nucleon, using the Heavy Ion Medical Accelerator in Chiba (HIMAC) synchrotron at the National Institute of Radiological Sciences (NIRS), Chiba, Japan. Carbon-ions accelerated at 290 MeV/n of initial energy have an LET of 13 keV/μm on entrance and were spread out with a ridge filter for 6 cm width of spread-out Bragg peak (SOBP) [363]. Dose rates for the carbon-ions were set at 1 Gy/min.

### 4.4.2 Irradiation procedure for cell survival assays

Cultured cells from each respected cell line were trypsinized and re-suspended into their respected growth medium. Once re-suspended, 60 mL of media containing 30,000 cells from each respected cell line were placed into their appropriately labeled T-175 cell culture flask a few hours prior to irradiation and attachment were confirmed. All flasks were irradiated independently with a dosage of either 1, 2, 3, 4, 5 or 10 Gy. Control flasks for each respected cell line were not irradiated. For all flasks, the beam entry point was at the bottom of the flask (non-capped end) (Figure 2.1A). Immediately following irradiation, all cells were incubated for a period of 8 days for colony formation. After this culturing period, each culture flask was then washed with 0.9% NaCl, fixed in 100% ethanol and stained with 0.1% crystal violet.

### 4.4.3 Survival fraction of cell survival assay calculation

Survival fractions were calculated as described previously [290]. Briefly, to quantify the survival fraction at each of our evaluated depths for each respected cell line, they were scored for every millimeter along the width of the flask either possessing a surviving colony, defined as a

colony containing >50 cells [364], or not possessing a surviving colony and the average value was calculated. Survival fractions for each respected depth, dosage and cell line was normalized with its respected control to account for differences in plating efficiencies between each cell line. This approach was repeated for a minimum of three independent experiments per each one of our initial treatment dosages of 0, 1, 2, 3, 4, 5 or 10 Gy per each respected cell line.

### 4.4.4 SER and entrance to lowest SOBP survival fraction ratios calculation

$D_{10}$ values (radiation dose to achieve 10% cell survival) were obtained from regression curves in either the proximal (8.0 – 9.0 cm), mid (10.0 – 11.0 cm) or distal (12.0 – 13.0 cm) regions of the SOBP. Sensitizer enhancement ratio (SER) was calculated using the $D_{10}$ values of each respected cell line at each respected region of the SOBP. Entrance to lowest SOBP survival fraction ratios were calculated as the survival fraction at the entrance evaluated depth (1.0 cm) divided by the lowest survival fraction within the proximal (8.0 – 9.5 cm), mid (10.0 – 11.5 cm) or distal (12.0 – 14.0 cm) regions of the SOBP.

### 4.4.5 Statistical analysis

All experimental data was derived from at least 3 independent experiments. Statistical significance was determined using one-way analysis of variance (ANOVA) followed by Bonferroni or Tukey multiple comparisons test by GraphPad Prism 8™ software (GraphPad, La Jolla, CA, USA). * = $P<0.05$, ** = $P<0.01$, *** = $P<0.001$. Analysis was carried out between entry depth (1.0 cm) versus others unless stated otherwise.

# CHAPTER FIVE

# CONCLUSIONS AND FUTURE DIRECTIONS

## 5.1 DSB distribution throughout the full monoenergetic carbon-ion beam range

Our novel method of cellular irradiation capable of incorporating the full 290 MeV/n carbon-ion beam range in a single biological system allowed us to investigate differences in the biological effects at increasing depths within the carbon-ion beam range. In the first part of this study, we investigated the DNA double-strand break (DSB) distribution using γ-H2AX as a surrogate marker for DSBs. We then correlated this distribution with cell survival following irradiation with the monoenergetic carbon-ion beam as well as examined its associated carbon-ion nuclear fragmentation induced DSBs in the post-Bragg peak depths.

Our cell survival results demonstrated that the biological Bragg peak was located at the depth of 140 mm. The results of the γ-H2AX assay demonstrated that the induction of DSBs increased as the beam approached its peak at 142 mm. Although, the depths from 140 – 142.2 mm all demonstrated to be highly significant in the induction of DSBs as compared to the initial evaluated depth at 10 mm ($P<0.001$), representing the incident carbon-ions. Thus, we defined this range as the foci Bragg peak range (FBPR). These results also demonstrated that the high-LET particles (carbon-ions or nuclear fragmentation ions), identified by their characteristic high-LET track structures within the cells, initially appeared at the depth of 115 mm and were observed until our last evaluated depth at 155 mm. The most tracks/cell was observed at the depth of 140 mm but the densest distribution of γ-H2AX foci was observed at the depth of 142 mm. This suggested that the highest dosage may have been at 140 mm, while the highest LET value may have been at 142 mm.

While the track structures within the cells demonstrated a relatively consistent increase in the density of the γ-H2AX foci distribution as the beam approached and preceded throughout the end of the FBPR, the track structures within the same post-FBPR depths differed in their density distribution of the γ-H2AX foci. These differences in the density of the γ-H2AX foci distribution within these cells track structures allowed us to differentiate between the possible lighter- and heavier-fragmentation ions. We observed that the lighter fragmentation ions were more capable of traveling farther distances in the post-FBPR depths than the heavy ions. Comparison of our γ-H2AX assay data with our cell survival data demonstrated that in the depths ranging from initial entry up to the biological Bragg peak (10 – 140 mm), the highest correlation was with the percentage of track positive cells, closely followed by the percentage of cells containing our largest foci cluster size of >2.4 μm. However, in the depths within the post-Bragg peak range (143 – 155 mm), the highest correlation was with the average foci/cell intensity followed by the percentage of cells containing our largest foci cluster size of >2.4 μm.

Collectively, these results suggested that the cell death from high-LET radiation may not be dependent only on the presence of a track structure but the density in which the DSBs that are near each other are induced within the cell. In other words, larger clusters of DSBs have a greater correlation with cell death than smaller clusters of DSBs within the track structures. Results of this study are important to not only deepen our understanding of the initial biological effects at different carbon-ion beam depths but also provide fundamental aspects to incorporate into carbon-ion radiation therapy (CIRT) treatment planning in order to limit unwanted cellular damage to the cells outside of the target region.

In future studies, it would be beneficial to address the kinetics of the DSB repair at each depth within the carbon-ion beam range by addressing the γ-H2AX foci distribution at multiple

time points. In addition, mutation frequency should also be investigated at each of these depths, specifically within the depths of the post-Bragg peak range. Results of these future studies will not only further our understanding into the biological effects throughout the full carbon-ion beam range but will also present important information to incorporate into the treatment planning associated risk. The associate risk is due to the mutational capabilities behind the carbon-ion nuclear fragmentation ions, as these ions can travel further distances past the targeted Bragg peak region. This is important as the fragmentation ion induced DSBs may not be complex enough to induce cell death, as with the primary carbon-ion induced DSBs seen at the Bragg peak, but instead may be improperly repaired leading to mutations that may ultimately result in a secondary induced malignancy.

## 5.2 Enhancing the indirect action of high-LET radiation induced DNA damage

In the next part of this study, we hypothesized that DNA in solution with the transition metals, $Cu^{2+}$ or $Co^{2+}$, would increase the DNA damage associated with high-LET radiation. The reasoning behind this hypothesis was due to the formation of the bimolecular product, $H_2O_2$, from the radiolysis of water, which is known to increase with an increase in LET [304]. Thus, we could exploit this increase in $H_2O_2$ via a Fenton-type reaction with the transition metals to produce larger quantities of the highly reactive hydroxyl radical ions, which are the main actor behind the indirect action of DNA damage with ionizing radiation. To test this hypothesis, we treated DNA in solution with each of the transition metals with ionizing radiation sources increasing in LET values, such as X-rays, carbon-ion and iron-ion beams, respectively, at increasing treatment dosages (Gy) or with chemical treatment of $H_2O_2$ or the radiomimetic drug, bleomycin, at increasing chemical concentrations.

The results of this study demonstrated that the addition of the transition metals, $Cu^{2+}$ and $Co^{2+}$, in solution with DNA increased both the DSBs and DNA single-strand breaks (SSBs), as compared to DNA in solution alone, under all irradiation conditions and chemical treatments. As expected, due to the reasoning behind our hypothesis, metals in solution with DNA demonstrated the most DNA damage in $H_2O_2$. However, metals in solution with DNA was observed to be LET dependent for SSB formation but inversely dependent for DSB formation. In addition, $Cu^{2+}$ was found to be more effective than $Co^{2+}$ at increasing the DNA damage under all irradiation conditions and chemical treatments.

Collectively, these results suggested that the addition of transition metals may be an effective option to increase the indirect action of DNA damage with high-LET radiation as well as $Cu^{2+}$ would be a more effective option than $Co^{2+}$. These results are important in CIRT as it provides a novel method for incorporating a non-toxic radiosensitizer, $Cu^{2+}$, to increase the damage associated to the cells within the high-LET target region. The importance of having a non-toxic radiosensitizer is due to the vascular leakage associated with the tumor. Future studies involving the treatment of human cell lines with $Cu^{2+}$ and addressing their increase in radiosensitivity would be beneficial as the cellular processes may produce a different response than that observed with DNA in solution with the metal.

## 5.3 Addressing the DSB repair pathway choice throughout the full carbon-ion SOBP beam range

In the last part of this study, we investigated the importance of each of the DSB repair pathways, non-homologous end joining (NHEJ) or homologous recombination (HR), at each depth within the full carbon-ion spread-out Bragg peak (SOBP) beam range. Utilizing the cell survival assay with our method of cellular irradiation as well as survival fraction calculation, we

identified the biological SOBP being within the depths from 8.0 – 14.0 cm using the wild-type Chinese hamster ovary (CHO) cell line, 10B2. Next, we compared the radiosensitivity between two DSB-repair deficient cell lines, V3 (NHEJ-deficient) and 51D1 (HR-deficient).

The results of this study demonstrated that both NHEJ- and HR-deficient cells (V3 and 51D1, respectively) portrayed an increase in radiosensitivity as compared to wild type cells (CHO 10B2) throughout the full carbon-ion SOBP beam range. In addition, the NHEJ-deficient cell line, V3, had the highest sensitization enhancement ratio (SER) throughout the SOBP. Although, V3 cells also demonstrated the greatest increase in radiosensitivity in the depths from beam entrance up to the proximal depth of the SOBP and demonstrated a dose-dependent increase in survival fractions throughout the SOBP. On the other hand, the HR-deficient cell line, 51D1, had the greatest ratio of the survival fraction at entrance depth to the lowest survival fraction within each of the SOBP regions (proximal, mid, and distal), meaning the sensitization effect for this cell line was higher within the SOBP in respect to the surrounding regions.

Collectively, these results suggested that the inhibition of the HR DSB repair pathway would be more beneficial to incorporate with CIRT than the inhibition of the NHEJ DSB repair pathway. This is because it would result in more effective cell killing within the targeted cells of the SOBP while limiting the damage to the surrounding healthy tissue. Studies on how the HR and NHEJ pathways contribute to the repair of carbon-ion radiation induced DSBs are essential in our understanding of the responses of cancers to this type of radiotherapy as well as important for developing molecularly targeted radiosensitizing therapies to incorporate during treatment to enhance the effectiveness of CIRT to eradicate the target tumor cells.

In future studies, it would be beneficial to repeat the γ-H2AX assay, as previously described, with human cell lines deficient in each of the DSB repair pathways and investigate the

kinetics behind their repair by evaluating the γ-H2AX foci distribution at increasing time points in each respected cell line following the carbon-ion SOBP beam irradiation. This assay could also be further modified to evaluate associate factors with each repair pathway, such as RPA with HR, that co-localizes with the γ-H2AX foci to further identify the repair processes that will be utilized at each DSB site at different depths within the full carbon-ion SOBP beam range.

# REFERENCES


1. Sidney, S., A.S. Go, and J.S. Rana, *Transition From Heart Disease to Cancer as the Leading Cause of Death in the United States.* Annals of Internal Medicine, 2019. **171**(3): p. 225-225.
2. Mahase, E., *Cancer overtakes CVD to become leading cause of death in high income countries.* Bmj-British Medical Journal, 2019. **366**: p. 2.
3. Weir, H.K., et al., *Heart Disease and Cancer Deaths - Trends and Projections in the United States, 1969-2020.* Preventing chronic disease, 2016. **13**: p. E157-E157.
4. Fujisawa, H., et al., *Comparison of human chordoma cell-kill for 290 MeV/n carbon ions versus 70 MeV protons in vitro.* Radiat Oncol, 2013. **8**: p. 91.
5. Bidram, E., et al., *A concise review on cancer treatment methods and delivery systems.* Journal of Drug Delivery Science and Technology, 2019. **54**: p. 101350.
6. Begg, A.C., F.A. Stewart, and C. Vens, *Strategies to improve radiotherapy with targeted drugs.* Nat Rev Cancer, 2011. **11**(4): p. 239-53.
7. Singleterry, J., *The Costs of Cancer.* American Cancer Society Cancer Action Network, 2017.
8. Chu, S.H., et al., *Current use of drugs affecting the central nervous system for chemotherapy-induced peripheral neuropathy in cancer patients: a systematic review.* Supportive Care in Cancer, 2015. **23**(2): p. 513-524.
9. Ewertz, M., C. Qvortrup, and L. Eckhoff, *Chemotherapy-induced peripheral neuropathy in patients treated with taxanes and platinum derivatives.* Acta Oncologica, 2015. **54**(5): p. 587-591.
10. Brigden, M. and M. McKenzie, *Treating cancer patients. Practical monitoring and management of therapy-related complications.* Canadian Family Physician, 2000. **46**(11): p. 2258.
11. Lee, C.S., E.J. Ryan, and G.A. Doherty, *Gastro-intestinal toxicity of chemotherapeutics in colorectal cancer: The role of inflammation.* World Journal of Gastroenterology, 2014. **20**(14): p. 3751-3761.
12. Coates, A., et al., *On the receiving end--patient perception of the side-effects of cancer chemotherapy.* Eur J Cancer Clin Oncol, 1983. **19**(2): p. 203-8.
13. Curigliano, G., et al., *Cardiac toxicity from systemic cancer therapy: a comprehensive review.* Prog Cardiovasc Dis, 2010. **53**(2): p. 94-104.
14. Monsuez, J.J., et al., *Cardiac side-effects of cancer chemotherapy.* Int J Cardiol, 2010. **144**(1): p. 3-15.
15. Baskar, R., et al., *Cancer and radiation therapy: current advances and future directions.* Int J Med Sci, 2012. **9**(3): p. 193-9.
16. Zehir, A., et al., *Mutational landscape of metastatic cancer revealed from prospective clinical sequencing of 10,000 patients.* Nature Medicine, 2017. **23**(6): p. 703-713.
17. Lengyel, E., et al., *Malignant mucosal melanoma of the head and neck.* Pathol Oncol Res, 2003. **9**(1): p. 7-12.
18. Mendenhall, W.M., et al., *Radiotherapy alone or combined with surgery for adenoid cystic carcinoma of the head and neck.* Head Neck, 2004. **26**(2): p. 154-62.

19. Schardt, D., T. Elsässer, and D. Schulz-Ertner, *Heavy-ion tumor therapy: Physical and radiobiological benefits.* Reviews of Modern Physics, 2010. **82**(1): p. 383-425.
20. Lomax, A.J., *Charged particle therapy: the physics of interaction.* Cancer J, 2009. **15**(4): p. 285-91.
21. Mohamad, O., et al., *Risk of subsequent primary cancers after carbon ion radiotherapy, photon radiotherapy, or surgery for localised prostate cancer: a propensity score-weighted, retrospective, cohort study.* Lancet Oncology, 2019. **20**(5): p. 674-685.
22. Radford, J.A., et al., *Screening for lung cancer in patients at high risk of this second cancer after treatment for Hodgkin lymphoma (HL).* Haematologica-the Hematology Journal, 2007. **92**: p. 1-2.
23. Jelena, Z., et al., *Carbon ions of different linear energy transfer (LET) values induce apoptosis & G2 cell cycle arrest in radio-resistant melanoma cells.* Indian J Med Res, 2016. **143**(Supplement): p. S120-S128.
24. Goodarzi, A.A., A. Anikin, and D.D. Pearson, *Chapter 33 - Environmental Sources of Ionizing Radiation and Their Health Consequences*, in *Genome Stability*, I. Kovalchuk and O. Kovalchuk, Editors. 2016, Academic Press: Boston. p. 569-581.
25. Costes, S.V., et al., *Spatiotemporal characterization of ionizing radiation induced DNA damage foci and their relation to chromatin organization.* Mutat Res, 2010. **704**(1-3): p. 78-87.
26. Dokic, I., et al., *Next generation multi-scale biophysical characterization of high precision cancer particle radiotherapy using clinical proton, helium-, carbon- and oxygen ion beams.* Oncotarget, 2016. **7**(35): p. 56676-56689.
27. Blaisdell, J.O., L. Harrison, and S.S. Wallace, *Base excision repair processing of radiation-induced clustered DNA lesions.* Radiation Protection Dosimetry, 2001. **97**(1): p. 25-31.
28. Nikjoo, H., et al., *Radiation track, DNA damage and response-a review.* Reports on Progress in Physics, 2016. **79**(11): p. 55.
29. Chang, H.H.Y., et al., *Non-homologous DNA end joining and alternative pathways to double-strand break repair.* Nature Reviews Molecular Cell Biology, 2017. **18**(8): p. 495-506.
30. Oike, T., et al., *Visualization of complex DNA double-strand breaks in a tumor treated with carbon ion radiotherapy.* Scientific Reports, 2016. **6**: p. 7.
31. Hanai, R., M. Yazu, and K. Hieda, *On the experimental distinction between ssbs and dsbs in circular DNA.* International Journal of Radiation Biology, 1998. **73**(5): p. 475-479.
32. Rothkamm, K. and M. Löbrich, *Evidence for a lack of DNA double-strand break repair in human cells exposed to very low x-ray doses.* Proceedings of the National Academy of Sciences, 2003. **100**(9): p. 5057.
33. Ranjha, L., S.M. Howard, and P. Cejka, *Main steps in DNA double-strand break repair: an introduction to homologous recombination and related processes.* Chromosoma, 2018. **127**(2): p. 187-214.
34. Olive, P.L., J.P. Banath, and R.E. Durand, *HETEROGENEITY IN RADIATION-INDUCED DNA DAMAGE AND REPAIR IN TUMOR AND NORMAL-CELLS MEASURED USING THE COMET ASSAY.* Radiation Research, 1990. **122**(1): p. 86-94.
35. Karger, C.P. and P. Peschke, *RBE and related modeling in carbon-ion therapy.* Physics in Medicine and Biology, 2018. **63**(1).

36. Polo, S.E. and S.P. Jackson, *Dynamics of DNA damage response proteins at DNA breaks: a focus on protein modifications.* Genes Dev, 2011. **25**(5): p. 409-33.
37. Tinganelli, W. and M. Durante, *Carbon Ion Radiobiology.* Cancers, 2020. **12**(10): p. 37.
38. Lieber, M.R., *The Mechanism of Double-Strand DNA Break Repair by the Nonhomologous DNA End-Joining Pathway.* Annual Review of Biochemistry, 2010. **79**(1): p. 181-211.
39. Asaithamby, A., B. Hu, and D.J. Chen, *Unrepaired clustered DNA lesions induce chromosome breakage in human cells.* Proc Natl Acad Sci U S A, 2011. **108**(20): p. 8293-8.
40. Lobrich, M. and P.A. Jeggo, *The impact of a negligent G2/M checkpoint on genomic instability and cancer induction.* Nat Rev Cancer, 2007. **7**(11): p. 861-9.
41. Furusawa, Y., *Heavy-Ion Radiobiology*, in *Carbon-Ion Radiotherapy: Principles, Practices, and Treatment Planning*, H. Tsujii, et al., Editors. 2014, Springer Japan: Tokyo. p. 25-37.
42. Jackson, S.P. and J. Bartek, *The DNA-damage response in human biology and disease.* Nature, 2009. **461**(7267): p. 1071-8.
43. Verheij, M., *Clinical biomarkers and imaging for radiotherapy-induced cell death.* Cancer Metastasis Rev, 2008. **27**(3): p. 471-80.
44. Vakifahmetoglu, H., M. Olsson, and B. Zhivotovsky, *Death through a tragedy: mitotic catastrophe.* Cell Death Differ, 2008. **15**(7): p. 1153-62.
45. Cohen–Jonathan, E., E.J. Bernhard, and W.G. McKenna, *How does radiation kill cells?* Current Opinion in Chemical Biology, 1999. **3**(1): p. 77-83.
46. Pajonk, F., E. Vlashi, and W.H. McBride, *Radiation resistance of cancer stem cells: the 4 R's of radiobiology revisited.* Stem cells (Dayton, Ohio), 2010. **28**(4): p. 639-648.
47. Bedford, J.S., *Sublethal damage, potentially lethal damage, and chromosomal aberrations in mammalian cells exposed to ionizing radiations.* International Journal of Radiation Oncology*Biology*Physics, 1991. **21**(6): p. 1457-1469.
48. Pawlik, T.M. and K. Keyomarsi, *Role of cell cycle in mediating sensitivity to radiotherapy.* International Journal of Radiation Oncology*Biology*Physics, 2004. **59**(4): p. 928-942.
49. Withers, H.R., *CELL-CYCLE REDISTRIBUTION AS A FACTOR IN MULTIFRACTION IRRADIATION.* Radiology, 1975. **114**(1): p. 199-202.
50. Withers, H.R., et al., *Accelerated repopulation in head and neck cancer*. 1988, United States: S Karger Publishers Inc.
51. Bese, N.S., P.A. Sut, and A. Ober, *The effect of treatment interruptions in the postoperative irradiation of breast cancer.* Oncology, 2005. **69**(3): p. 214-223.
52. Bertout, J.A., S.A. Patel, and M.C. Simon, *The impact of O2 availability on human cancer.* Nature Reviews Cancer, 2008. **8**(12): p. 967-975.
53. Thomlinson, R.H. and L.H. Gray, *THE HISTOLOGICAL STRUCTURE OF SOME HUMAN LUNG CANCERS AND THE POSSIBLE IMPLICATIONS FOR RADIOTHERAPY.* British Journal of Cancer, 1955. **9**(4): p. 539-&.
54. Nagasawa, H. and J.B. Little, *INDUCTION OF SISTER-CHROMATID EXCHANGES BY EXTREMELY LOW-DOSES OF ALPHA-PARTICLES - REPLY.* Cancer Research, 1993. **53**(9): p. 2188-2188.

55. He, M., et al., *Cytochrome-c mediated a bystander response dependent on inducible nitric oxide synthase in irradiated hepatoma cells.* British Journal of Cancer, 2012. **106**(5): p. 889-895.
56. Shao, C., et al., *Nitric oxide-mediated bystander effect induced by heavy-ions in human salivary gland tumour cells.* International Journal of Radiation Biology, 2002. **78**(9): p. 837-844.
57. Shao, C., et al., *Role of Gap Junctional Intercellular Communication in Radiation-Induced Bystander Effects in Human Fibroblasts.* Radiation Research, 2003. **160**(3): p. 318-323.
58. Tu, W., et al., *Both irradiated and bystander effects link with DNA repair capacity and the linear energy transfer.* Life Sciences, 2019. **222**: p. 228-234.
59. Amaldi, U. and G. Kraft, *Radiotherapy with beams of carbon ions.* Reports on Progress in Physics, 2005. **68**(8): p. 1861.
60. Schulz-Ertner, D. and H. Tsujii, *Particle radiation therapy using proton and heavier ion beams.* J Clin Oncol, 2007. **25**(8): p. 953-64.
61. Weber, U. and G. Kraft, *Comparison of carbon ions versus protons.* Cancer J, 2009. **15**(4): p. 325-32.
62. Blakely, E.A., et al., *Inactivation of human kidney cells by high-energy monoenergetic heavy-ion beams.* Radiat Res, 1979. **80**(1): p. 122-60.
63. Cox, R., et al., *Mutation and inactivation of mammalian cells by various ionising radiations.* Nature, 1977. **267**(5610): p. 425-7.
64. Nakajima, N.I., et al., *Visualisation of gamma H2AX Foci Caused by Heavy Ion Particle Traversal; Distinction between Core Track versus Non-Track Damage.* Plos One, 2013. **8**(8).
65. Nakajima, N.I., et al., *Pre-Exposure to Ionizing Radiation Stimulates DNA Double Strand Break End Resection, Promoting the Use of Homologous Recombination Repair.* Plos One, 2015. **10**(3): p. 15.
66. Ramaekers, B.L., et al., *Systematic review and meta-analysis of radiotherapy in various head and neck cancers: comparing photons, carbon-ions and protons.* Cancer Treat Rev, 2011. **37**(3): p. 185-201.
67. Demizu, Y., et al., *Particle therapy for mucosal melanoma of the head and neck.* Strahlentherapie und Onkologie, 2014. **190**(2): p. 186-191.
68. Tsujii, H., *History of Charged Particle Radiotherapy*, in *Carbon-Ion Radiotherapy: Principles, Practices, and Treatment Planning*, H. Tsujii, et al., Editors. 2014, Springer Japan: Tokyo. p. 3-10.
69. Ma, C.M. and R.L. Maughan, *Within the next decade conventional cyclotrons for proton radiotherapy will become obsolete and replaced by far less expensive machines using compact laser systems for the acceleration of the protons.* Med Phys, 2006. **33**(3): p. 571-3.
70. Paganetti, H., *Relative biological effectiveness (RBE) values for proton beam therapy. Variations as a function of biological endpoint, dose, and linear energy transfer.* Phys Med Biol, 2014. **59**(22): p. R419-72.
71. Genet, S.C., et al., *Comparison of cellular lethality in DNA repair-proficient or -deficient cell lines resulting from exposure to 70 MeV/n protons or 290 MeV/n carbon ions.* Oncol Rep, 2012. **28**(5): p. 1591-6.

72. Mohan, R. and D. Grosshans, *Proton therapy - Present and future.* Adv Drug Deliv Rev, 2017. **109**: p. 26-44.
73. Suit, H., et al., *Proton vs carbon ion beams in the definitive radiation treatment of cancer patients.* Radiother Oncol, 2010. **95**(1): p. 3-22.
74. Brown, A. and H. Suit, *The centenary of the discovery of the Bragg peak.* Radiotherapy and Oncology, 2004. **73**(3): p. 265-268.
75. Mohamad, O., et al., *Carbon Ion Radiotherapy: A Review of Clinical Experiences and Preclinical Research, with an Emphasis on DNA Damage/Repair.* Cancers, 2017. **9**(6): p. 30.
76. Kamada, T., *The Characteristics of Carbon-Ion Radiotherapy*, in *Carbon-Ion Radiotherapy: Principles, Practices, and Treatment Planning*, H. Tsujii, et al., Editors. 2014, Springer Japan: Tokyo. p. 13-16.
77. Kase, Y., et al., *Biological dose calculation with Monte Carlo physics simulation for heavy-ion radiotherapy.* Physics in Medicine and Biology, 2006. **51**(24): p. N467-N475.
78. Kanai, T., et al., *Irradiation of Mixed Beam and Design of Spread-Out Bragg Peak for Heavy-Ion Radiotherapy.* Radiation Research, 1997. **147**(1): p. 78-85.
79. Kim, C.H., et al., *Practical biological spread-out Bragg peak design for a carbon beam.* Journal of the Korean Physical Society, 2015. **67**(8): p. 1440-1443.
80. Pouget, J.-P. and S.J. Mather, *General aspects of the cellular response to low- and high-LET radiation.* European Journal of Nuclear Medicine, 2001. **28**(4): p. 541-561.
81. Ward, J.F., *DNA damage produced by ionizing radiation in mammalian cells: identities, mechanisms of formation, and reparability.* Prog Nucleic Acid Res Mol Biol, 1988. **35**: p. 95-125.
82. Singh, A. and H. Singh, *Time-scale and nature of radiation-biological damage: Approaches to radiation protection and post-irradiation therapy.* Progress in Biophysics and Molecular Biology, 1982. **39**: p. 69-107.
83. Wallace, S.S., *Biological consequences of free radical-damaged DNA bases.* Free Radic Biol Med, 2002. **33**(1): p. 1-14.
84. Weyrather, W.K. and J. Debus, *Particle Beams for Cancer Therapy.* Clinical Oncology, 2003. **15**(1): p. S23-S28.
85. Tinganelli, W., et al., *Influence of acute hypoxia and radiation quality on cell survival.* Journal of Radiation Research, 2013. **54**(suppl_1): p. i23-i30.
86. Johnson, G.E., *Mammalian Cell HPRT Gene Mutation Assay: Test Methods*, in *Genetic Toxicology: Principles and Methods*, J.M. Parry and E.M. Parry, Editors. 2012, Springer New York: New York, NY. p. 55-67.
87. Ward, J.F., *Biochemistry of DNA Lesions.* Radiation Research, 1985. **104**(2s): p. S103-S111.
88. Lomax, M.E., L.K. Folkes, and P. O'Neill, *Biological consequences of radiation-induced DNA damage: relevance to radiotherapy.* Clin Oncol (R Coll Radiol), 2013. **25**(10): p. 578-85.
89. Holley, W.R., A. Chatterjee, and J.L. Magee, *PRODUCTION OF DNA STRAND BREAKS BY DIRECT EFFECTS OF HEAVY CHARGED-PARTICLES.* Radiation Research, 1990. **121**(2): p. 161-168.
90. Roots, R., et al., *CHARACTERIZATION OF HYDROXYL RADICAL-INDUCED DAMAGE AFTER SPARSELY AND DENSELY IONIZING IRRADIATION.* International Journal of Radiation Biology, 1985. **47**(2): p. 157-166.

91. Muroya, Y., et al., *High-LET Ion Radiolysis of Water: Visualization of the Formation and Evolution of Ion Tracks and Relevance to the Radiation-Induced Bystander Effect.* Radiation Research, 2006. **165**(4): p. 485-491.
92. Meesungnoen, J. and J.P. Jay-Gerin, *High-LET Ion Radiolysis of Water: Oxygen Production in Tracks.* Radiation Research, 2009. **171**(3): p. 379-386.
93. Meesungnoen, J. and J.-P. Jay-Gerin, *High-LET Radiolysis of Liquid Water with 1H+, 4He2+, 12C6+, and 20Ne9+ Ions: Effects of Multiple Ionization.* The Journal of Physical Chemistry A, 2005. **109**(29): p. 6406-6419.
94. Asaithamby, A. and D.J. Chen, *Mechanism of cluster DNA damage repair in response to high-atomic number and energy particles radiation.* Mutation Research-Fundamental and Molecular Mechanisms of Mutagenesis, 2011. **711**(1-2): p. 87-99.
95. Brenner, D.J. and J.F. Ward, *CONSTRAINTS ON ENERGY DEPOSITION AND TARGET SIZE OF MULTIPLY DAMAGED SITES ASSOCIATED WITH DNA DOUBLE-STRAND BREAKS.* International Journal of Radiation Biology, 1992. **61**(6): p. 737-748.
96. Goodhead, D.T., *Energy deposition stochastics and track structure: what about the target?* Radiation Protection Dosimetry, 2007. **122**(1-4): p. 3-15.
97. Nikjoo, H., et al., *Quantitative modelling of DNA damage using Monte Carlo track structure method.* Radiat Environ Biophys, 1999. **38**(1): p. 31-8.
98. Nikjoo, H., et al., *Track structure in radiation biology: theory and applications.* International Journal of Radiation Biology, 1998. **73**(4): p. 355-364.
99. Plante, I., A. Ponomarev, and F.A. Cucinotta, *3D visualisation of the stochastic patterns of the radial dose in nano-volumes by a Monte Carlo simulation of HZE ion track structure.* Radiation Protection Dosimetry, 2011. **143**(2-4): p. 156-161.
100. Hagiwara, Y., et al., *3D-structured illumination microscopy reveals clustered DNA double-strand break formation in widespread gamma H2AX foci after high LET heavy-ion particle radiation.* Oncotarget, 2017. **8**(65): p. 109370-109381.
101. Goodhead, D.T., *Initial events in the cellular effects of ionizing radiations: clustered damage in DNA.* Int J Radiat Biol, 1994. **65**(1): p. 7-17.
102. Jenner, T.J., et al., *INDUCTION AND REJOINING OF DNA DOUBLE-STRAND BREAKS IN V79-4 MAMMALIAN-CELLS FOLLOWING GAMMA-IRRADIATION AND ALPHA-IRRADIATION.* International Journal of Radiation Biology, 1993. **64**(3): p. 265-273.
103. Eccles, L.J., P. O'Neill, and M.E. Lomax, *Delayed repair of radiation induced clustered DNA damage: Friend or foe?* Mutation Research/Fundamental and Molecular Mechanisms of Mutagenesis, 2011. **711**(1): p. 134-141.
104. Hanahan, D. and R.A. Weinberg, *The Hallmarks of Cancer.* Cell, 2000. **100**(1): p. 57-70.
105. David-Cordonnier, M.H., et al., *Efficiency of incision of an AP site within clustered DNA damage by the major human AP endonuclease.* Biochemistry, 2002. **41**(2): p. 634-642.
106. Gulston, M., et al., *Processing of clustered DNA damage generates additional double-strand breaks in mammalian cells post-irradiation.* Nucleic Acids Research, 2004. **32**(4): p. 1602-1609.
107. Eccles, L.J., M.E. Lomax, and P. O'Neill, *Hierarchy of lesion processing governs the repair, double-strand break formation and mutability of three-lesion clustered DNA damage.* Nucleic Acids Research, 2010. **38**(4): p. 1123-1134.
108. Horton, J.K., et al., *XRCC1 and DNA polymerase beta in cellular protection against cytotoxic DNA single-strand breaks.* Cell Research, 2008. **18**(1): p. 48-63.

109. Rosenquist, T.A., D.O. Zharkov, and A.P. Grollman, *Cloning and characterization of a mammalian 8-oxoguanine DNA glycosylase.* Proceedings of the National Academy of Sciences, 1997. **94**(14): p. 7429-7434.
110. Olive, P.L., *Detection of DNA damage in individual cells by analysis of histone H2AX phosphorylation*, in *Cytometry, 4th Edition: New Developments*, Z. Darzynkiewicz, M. Roederer, and H. Tanke, Editors. 2004, Elsevier Academic Press Inc: San Diego. p. 355-373.
111. Chen, B.P.C., et al., *Cell cycle dependence of DNA-dependent protein kinase phosphorylation in response to DNA double strand breaks.* Journal of Biological Chemistry, 2005. **280**(15): p. 14709-14715.
112. Schultz, L.B., et al., *P53 Binding Protein 1 (53bp1) Is an Early Participant in the Cellular Response to DNA Double-Strand Breaks.* Journal of Cell Biology, 2000. **151**(7): p. 1381-1390.
113. Kowalczykowski, S.C., *An Overview of the Molecular Mechanisms of Recombinational DNA Repair.* Cold Spring Harbor Perspectives in Biology, 2015. **7**(11): p. 36.
114. Filippo, J.S., P. Sung, and H. Klein, *Mechanism of Eukaryotic Homologous Recombination.* Annual Review of Biochemistry, 2008. **77**(1): p. 229-257.
115. Rothkamm, K., et al., *Pathways of DNA Double-Strand Break Repair during the Mammalian Cell Cycle.* Molecular and Cellular Biology, 2003. **23**(16): p. 5706.
116. Onn, I., et al., *Sister Chromatid Cohesion: A Simple Concept with a Complex Reality.* Annual Review of Cell and Developmental Biology, 2008. **24**(1): p. 105-129.
117. Pâques, F. and J.E. Haber, *Multiple Pathways of Recombination Induced by Double-Strand Breaks in <em>Saccharomyces cerevisiae</em&gt.* Microbiology and Molecular Biology Reviews, 1999. **63**(2): p. 349.
118. Aylon, Y. and M. Kupiec, *New insights into the mechanism of homologous recombination in yeast.* Mutation Research/Reviews in Mutation Research, 2004. **566**(3): p. 231-248.
119. Fearon, E.R. and B. Vogelstein, *A genetic model for colorectal tumorigenesis.* Cell, 1990. **61**(5): p. 759-767.
120. West, S.C., *Molecular views of recombination proteins and their control.* Nature Reviews Molecular Cell Biology, 2003. **4**(6): p. 435-445.
121. Sartori, A.A., et al., *Human CtIP promotes DNA end resection.* Nature, 2007. **450**(7169): p. 509-514.
122. Kousholt, A.N., et al., *CtIP-dependent DNA resection is required for DNA damage checkpoint maintenance but not initiation.* Journal of Cell Biology, 2012. **197**(7): p. 869-876.
123. Stracker, T.H. and J.H.J. Petrini, *The MRE11 complex: starting from the ends.* Nature Reviews Molecular Cell Biology, 2011. **12**(2): p. 90-103.
124. Lamarche, B.J., N.I. Orazio, and M.D. Weitzman, *The MRN complex in double-strand break repair and telomere maintenance.* FEBS Letters, 2010. **584**(17): p. 3682-3695.
125. Carson, C.T., et al., *The Mre11 complex is required for ATM activation and the G2/M checkpoint.* The EMBO Journal, 2003. **22**(24): p. 6610-6620.
126. Bakkenist, C.J. and M.B. Kastan, *DNA damage activates ATM through intermolecular autophosphorylation and dimer dissociation.* Nature, 2003. **421**(6922): p. 499-506.

127. Rogakou, E.P., et al., *DNA Double-stranded Breaks Induce Histone H2AX Phosphorylation on Serine 139*.* Journal of Biological Chemistry, 1998. **273**(10): p. 5858-5868.
128. Stiff, T., et al., *ATM and DNA-PK Function Redundantly to Phosphorylate H2AX after Exposure to Ionizing Radiation.* Cancer Research, 2004. **64**(7): p. 2390.
129. Bekker-Jensen, S. and N. Mailand, *Assembly and function of DNA double-strand break repair foci in mammalian cells.* DNA Repair, 2010. **9**(12): p. 1219-1228.
130. Neale, M.J., J. Pan, and S. Keeney, *Endonucleolytic processing of covalent protein-linked DNA double-strand breaks.* Nature, 2005. **436**(7053): p. 1053-1057.
131. Garcia, V., et al., *Bidirectional resection of DNA double-strand breaks by Mre11 and Exo1.* Nature, 2011. **479**(7372): p. 241-244.
132. Mladenov, E., et al., *DNA Double-Strand Break Repair as Determinant of Cellular Radiosensitivity to Killing and Target in Radiation Therapy.* Frontiers in Oncology, 2013. **3**(113).
133. Qiao, G.B., et al., *High-level expression of Rad51 is an independent prognostic marker of survival in non-small-cell lung cancer patients.* British Journal of Cancer, 2005. **93**(1): p. 137-143.
134. Karpenshif, Y. and K.A. Bernstein, *From yeast to mammals: Recent advances in genetic control of homologous recombination.* DNA Repair, 2012. **11**(10): p. 781-788.
135. Esashi, F., et al., *CDK-dependent phosphorylation of BRCA2 as a regulatory mechanism for recombinational repair.* Nature, 2005. **434**(7033): p. 598-604.
136. Li, X. and W.-D. Heyer, *RAD54 controls access to the invading 3'-OH end after RAD51-mediated DNA strand invasion in homologous recombination in Saccharomyces cerevisiae.* Nucleic Acids Research, 2008. **37**(2): p. 638-646.
137. Duckett, D.R., et al., *The structure of the holliday junction, and its resolution.* Cell, 1988. **55**(1): p. 79-89.
138. Wechsler, T., S. Newman, and S.C. West, *Aberrant chromosome morphology in human cells defective for Holliday junction resolution.* Nature, 2011. **471**(7340): p. 642-646.
139. Constantinou, A., et al., *Holliday junction resolution in human cells: two junction endonucleases with distinct substrate specificities.* The EMBO Journal, 2002. **21**(20): p. 5577-5585.
140. Wu, L. and I.D. Hickson, *The Bloom's syndrome helicase suppresses crossing over during homologous recombination.* Nature, 2003. **426**(6968): p. 870-874.
141. Cramer, K., et al., *BCR/ABL and Other Kinases from Chronic Myeloproliferative Disorders Stimulate Single-Strand Annealing, an Unfaithful DNA Double-Strand Break Repair.* Cancer Research, 2008. **68**(17): p. 6884.
142. Fan, R., et al., *Defective DNA Strand Break Repair after DNA Damage in Prostate Cancer Cells.* Cancer Research, 2004. **64**(23): p. 8526.
143. Llorente, B., C.E. Smith, and L.S. Symington, *Break-induced replication: What is it and what is it for?* Cell Cycle, 2008. **7**(7): p. 859-864.
144. Sakofsky, C.J. and A. Malkova, *Break induced replication in eukaryotes: mechanisms, functions, and consequences.* Critical Reviews in Biochemistry and Molecular Biology, 2017. **52**(4): p. 395-413.
145. Meek, K., et al., *The DNA-dependent protein kinase: the director at the end.* Immunological Reviews, 2004. **200**: p. 132-141.

146. Arosio, D., et al., *Studies on the mode of Ku interaction with DNA.* Journal of Biological Chemistry, 2002. **277**(12): p. 9741-9748.
147. Mladenov, E. and G. Iliakis, *Induction and repair of DNA double strand breaks: The increasing spectrum of non-homologous end joining pathways.* Mutation Research/Fundamental and Molecular Mechanisms of Mutagenesis, 2011. **711**(1): p. 61-72.
148. Meek, K., et al., *The DNA-dependent protein kinase: the director at the end.* Immunological Reviews, 2004. **200**(1): p. 132-141.
149. Iliakis, G., *Backup pathways of NHEJ in cells of higher eukaryotes: Cell cycle dependence.* Radiotherapy and Oncology, 2009. **92**(3): p. 310-315.
150. Seol, J.-H., E.Y. Shim, and S.E. Lee, *Microhomology-mediated end joining: Good, bad and ugly.* Mutation Research/Fundamental and Molecular Mechanisms of Mutagenesis, 2018. **809**: p. 81-87.
151. Bennardo, N., et al., *Alternative-NHEJ Is a Mechanistically Distinct Pathway of Mammalian Chromosome Break Repair.* Plos Genetics, 2008. **4**(6): p. 10.
152. Wang, M.L., et al., *PARP-1 and Ku compete for repair of DNA double strand breaks by distinct NHEJ pathways.* Nucleic Acids Research, 2006. **34**(21): p. 6170-6182.
153. Robert, I., F. Dantzer, and B. Reina-San-Martin, *Parp1 facilitates alternative NHEJ, whereas Parp2 suppresses IgH/c-myc translocations during immunoglobulin class switch recombination.* Journal of Experimental Medicine, 2009. **206**(5): p. 1047-1056.
154. Zha, S., C. Boboila, and F.W. Alt, *Mre11: roles in DNA repair beyond homologous recombination.* Nature Structural & Molecular Biology, 2009. **16**(8): p. 798-800.
155. Simsek, D., et al., *DNA Ligase III Promotes Alternative Nonhomologous End-Joining during Chromosomal Translocation Formation.* Plos Genetics, 2011. **7**(6): p. 11.
156. Wang, H., et al., *DNA Ligase III as a Candidate Component of Backup Pathways of Nonhomologous End Joining.* Cancer Research, 2005. **65**(10): p. 4020.
157. Della-Maria, J., et al., *Human Mre11/Human Rad50/Nbs1 and DNA Ligase IIIα/XRCC1 Protein Complexes Act Together in an Alternative Nonhomologous End Joining Pathway*.* Journal of Biological Chemistry, 2011. **286**(39): p. 33845-33853.
158. Sallmyr, A., A.E. Tomkinson, and F.V. Rassool, *Up-regulation of WRN and DNA ligase IIIα in chronic myeloid leukemia: consequences for the repair of DNA double-strand breaks.* Blood, 2008. **112**(4): p. 1413-1423.
159. Rosidi, B., et al., *Histone H1 functions as a stimulatory factor in backup pathways of NHEJ.* Nucleic Acids Research, 2008. **36**(5): p. 1610-1623.
160. Bristow, R.G. and R.P. Hill, *Hypoxia and metabolism: Hypoxia, DNA repair and genetic instability.* Nature Reviews Cancer, 2008. **8**(3): p. 180-192.
161. Reynolds, P., et al., *Disruption of PARP1 function inhibits base excision repair of a sub-set of DNA lesions.* Nucleic Acids Research, 2015. **43**(8): p. 4028-4038.
162. Vignard, J., G. Mirey, and B. Salles, *Ionizing-radiation induced DNA double-strand breaks: a direct and indirect lighting up.* Radiother Oncol, 2013. **108**(3): p. 362-9.
163. Masunaga, S. and K. Ono, *Significance of the response of quiescent cell populations within solid tumors in cancer therapy.* J Radiat Res, 2002. **43**(1): p. 11-25.
164. Pawlik, T.M. and K. Keyomarsi, *Role of cell cycle in mediating sensitivity to radiotherapy.* Int J Radiat Oncol Biol Phys, 2004. **59**(4): p. 928-42.
165. Shibata, A., et al., *Factors determining DNA double-strand break repair pathway choice in G2 phase.* Embo Journal, 2011. **30**(6): p. 1079-1092.

166. Yajima, H., et al., *The complexity of DNA double strand breaks is a critical factor enhancing end-resection.* DNA Repair, 2013. **12**(11): p. 936-946.
167. Tamulevicius, P., M. Wang, and G. Iliakis, *Homology-Directed Repair is Required for the Development of Radioresistance during S Phase: Interplay between Double-Strand Break Repair and Checkpoint Response.* Radiation Research, 2007. **167**(1): p. 1-11.
168. Grubbé, E.H., *Priority in the Therapeutic Use of X-rays.* Radiology, 1933. **21**(2): p. 156-162.
169. Slater, J.M., *From X-Rays to Ion Beams: A Short History of Radiation Therapy*, in *Ion Beam Therapy: Fundamentals, Technology, Clinical Applications*, U. Linz, Editor. 2012, Springer Berlin Heidelberg: Berlin, Heidelberg. p. 3-16.
170. Kaplan, H.S., *Basic principles in radiation oncology.* Cancer, 1977. **39**(S2): p. 689-693.
171. Price, R.A., *Intensity Modulated Radiation Therapy (IMRT)*, in *Encyclopedia of Radiation Oncology*, L.W. Brady and T.E. Yaeger, Editors. 2013, Springer Berlin Heidelberg: Berlin, Heidelberg. p. 374-384.
172. Webb, S., *The physical basis of IMRT and inverse planning.* The British Journal of Radiology, 2003. **76**(910): p. 678-689.
173. Nutting, C., *Intensity-modulated radiotherapy (IMRT): the most important advance in radiotherapy since the linear accelerator?* The British Journal of Radiology, 2003. **76**(910): p. 673-673.
174. Bortfeld, T., *IMRT: a review and preview.* Physics in Medicine and Biology, 2006. **51**(13): p. R363-R379.
175. Ling, C.C., et al., *Conformal radiation treatment of prostate cancer using inversely-planned intensity-modulated photon beams produced with dynamic multileaf collimation.* International Journal of Radiation Oncology*Biology*Physics, 1996. **35**(4): p. 721-730.
176. Studer, G., et al., *IMRT in oral cavity cancer.* Radiation Oncology, 2007. **2**(1): p. 16.
177. Freedman, G.M., et al., *Intensity Modulated Radiation Therapy (IMRT) Decreases Acute Skin Toxicity for Women Receiving Radiation for Breast Cancer.* American Journal of Clinical Oncology, 2006. **29**(1): p. 66-70.
178. Prezzano, K.M., et al., *Stereotactic body radiation therapy for non-small cell lung cancer: A review.* World Journal of Clinical Oncology, 2019. **10**(1): p. 14-27.
179. Fogh, S.E., et al., *Hypofractionated stereotactic radiation therapy: an effective therapy for recurrent high-grade gliomas.* Journal of clinical oncology : official journal of the American Society of Clinical Oncology, 2010. **28**(18): p. 3048-3053.
180. Leksell, L., *Stereotactic radiosurgery.* Journal of Neurology, Neurosurgery & Psychiatry, 1983. **46**(9): p. 797.
181. Kim, M.-S., et al., *Radiobiological mechanisms of stereotactic body radiation therapy and stereotactic radiation surgery.* Radiation oncology journal, 2015. **33**(4): p. 265-275.
182. Hall, E.J., *Intensity-modulated radiation therapy, protons, and the risk of second cancers.* International Journal of Radiation Oncology*Biology*Physics, 2006. **65**(1): p. 1-7.
183. Wilson, R.R., *Radiological Use of Fast Protons.* Radiology, 1946. **47**(5): p. 487-491.
184. Boone, M.L.M., et al., *Introduction to the use of protons and heavy ions in radiation therapy: Historical perspective.* International Journal of Radiation Oncology*Biology*Physics, 1977. **3**: p. 65-69.
185. Suit, H.D., *Protons to Replace Photons in External Beam Radiation Therapy?* Clinical Oncology, 2003. **15**(1): p. S29-S31.
186. Tommasino, F. and M. Durante, *Proton radiobiology.* Cancers, 2015. **7**(1): p. 353-381.

187. Olsen, D.R., et al., *Proton therapy – A systematic review of clinical effectiveness.* Radiotherapy and Oncology, 2007. **83**(2): p. 123-132.
188. Lomax, A., *Intensity modulation methods for proton radiotherapy.* Physics in Medicine and Biology, 1999. **44**(1): p. 185-205.
189. Suit, H. and M. Urie, *Proton Beams in Radiation Therapy.* JNCI: Journal of the National Cancer Institute, 1992. **84**(3): p. 155-164.
190. Oelfke, U. and T. Bortfeld, *Intensity modulated radiotherapy with charged particle beams: Studies of inverse treatment planning for rotation therapy.* Medical Physics, 2000. **27**(6): p. 1246-1257.
191. Group, P.T.C.-O. *Particle Therapy Patient Statistics (per end of 2019)*. 2019; December 2019:[Available from: https://www.ptcog.ch/images/patientstatistics/Patientstatistics-updateDec2019.pdf.
192. Group., P.T.C.-O. *Particle therapy facilities in clinical operation*. April 2021 [cited 2021; Available from: https://www.ptcog.ch/index.php/facilities-in-operation.
193. Mohamad, O., et al., *Carbon Ion Radiotherapy: A Review of Clinical Experiences and Preclinical Research, with an Emphasis on DNA Damage/Repair.* Cancers (Basel), 2017. **9**(6).
194. Tobias, C.A., *The Future of Heavy-Ion Science in Biology and Medicine.* Radiation Research, 1985. **103**(1): p. 1-33.
195. Durante, M. and H. Paganetti, *Nuclear physics in particle therapy: a review.* Reports on Progress in Physics, 2016. **79**(9): p. 59.
196. Durante, M. and J.S. Loeffler, *Charged particles in radiation oncology.* Nature Reviews Clinical Oncology, 2010. **7**(1): p. 37-43.
197. Durante, M., *Eighth Warren K. Sinclair Keynote Address: Heavy Ions in Therapy and Space: Benefits and Risks.* Health Physics, 2012. **103**(5): p. 532-539.
198. Bird, R.P. and H.J. Burki, *Survival of synchronized Chinese hamster cells exposed to radiation of different linear-energy transfer.* Int J Radiat Biol Relat Stud Phys Chem Med, 1975. **27**(2): p. 105-20.
199. Wang, H.Y., et al., *S-PHASE CELLS ARE MORE SENSITIVE TO HIGH-LINEAR ENERGY TRANSFER RADIATION.* International Journal of Radiation Oncology Biology Physics, 2009. **74**(4): p. 1236-1241.
200. Wang, H., et al., *The Ku-dependent non-homologous end-joining but not other repair pathway is inhibited by high linear energy transfer ionizing radiation.* DNA Repair, 2008. **7**(5): p. 725-733.
201. Schardt, D., et al., *Nuclear fragmentation of high-energy heavy-ion beams in water.* Advances in Space Research, 1996. **17**(2): p. 87-94.
202. Castro, J.R., *RESULTS OF HEAVY-ION RADIOTHERAPY.* Radiation and Environmental Biophysics, 1995. **34**(1): p. 45-48.
203. Blakely, E.A., et al., *Heavy-Ion Radiobiology: Cellular Studies*, in *Advances in Radiation Biology*, J.T. Lett, Editor. 1984, Elsevier. p. 295-389.
204. Horsman, M.R., et al., *Imaging hypoxia to improve radiotherapy outcome.* Nature Reviews Clinical Oncology, 2012. **9**(12): p. 674-687.
205. Tommasino, F., E. Scifoni, and M. Durante, *New Ions for Therapy.* International Journal of Particle Therapy, 2016. **2**(3): p. 428-438.
206. Sørensen, B.S., J. Overgaard, and N. Bassler, *In vitro RBE-LET dependence for multiple particle types.* Acta Oncologica, 2011. **50**(6): p. 757-762.

207. Friedrich, T., et al., *Systematic analysis of RBE and related quantities using a database of cell survival experiments with ion beam irradiation.* Journal of Radiation Research, 2012. **54**(3): p. 494-514.
208. Durante, M., *New challenges in high-energy particle radiobiology.* The British Journal of Radiology, 2014. **87**(1035): p. 20130626.
209. Bassler, N., et al., *Dose- and LET-painting with particle therapy.* Acta Oncologica, 2010. **49**(7): p. 1170-1176.
210. Dreher, C., et al., *Optimization of carbon ion and proton treatment plans using the raster-scanning technique for patients with unresectable pancreatic cancer.* Radiation oncology (London, England), 2015. **10**: p. 237-237.
211. Akbaba, S., et al., *Carbon-ion radiotherapy in accelerated hypofractionated active raster-scanning technique for malignant lacrimal gland tumors: feasibility and safety.* Cancer Management and Research, 2019. **11**: p. 1155-1166.
212. Malouff, T.D., et al., *Carbon Ion Therapy: A Modern Review of an Emerging Technology.* Frontiers in Oncology, 2020. **10**(82).
213. Laine, A.M., et al., *The Role of Hypofractionated Radiation Therapy with Photons, Protons, and Heavy Ions for Treating Extracranial Lesions.* Frontiers in Oncology, 2016. **5**(302).
214. Story, M., A. Pompos, and R. Timmerman, *On the value of carbon-ion therapy.* Physics Today, 2016. **69**(11): p. 14-16.
215. Serber, R., *Nuclear Reactions at High Energies.* Physical Review, 1947. **72**(11): p. 1114-1115.
216. Sihver, L., D. Schardt, and T. Kanai, *Depth-Dose Distributions of High-Energy Carbon, Oxygen and Neon Beams in Water.* 放射線医学物理, 1998. **18**(1): p. 1-21.
217. Schardt, D., *Tumor therapy with high-energy carbon ion beams.* Nuclear Physics A, 2007. **787**(1): p. 633-641.
218. Haettner, E., et al., *Experimental study of nuclear fragmentation of 200 and 400 MeV/u (12)C ions in water for applications in particle therapy.* Phys Med Biol, 2013. **58**(23): p. 8265-79.
219. Golovkov, M., et al., *Fragmentation of 270 A MeV carbon ions in water*, in *Advances in Hadrontherapy*, U. Amaldi, B. Larsson, and Y. Lemoigne, Editors. 1997, Elsevier Science Bv: Amsterdam. p. 316-324.
220. Matsufuji, N., et al., *Spatial fragment distribution from a therapeutic pencil-like carbon beam in water.* Physics in Medicine and Biology, 2005. **50**(14): p. 3393-3403.
221. Schall, I., et al., *Charge-changing nuclear reactions of relativistic light-ion beams ($5 \leq Z \leq 10$) passing through thick absorbers.* Nuclear Instruments and Methods in Physics Research Section B: Beam Interactions with Materials and Atoms, 1996. **117**(3): p. 221-234.
222. Arico, G., et al., *Investigation of single carbon ion fragmentation in water and PMMA for hadron therapy.* Physics in Medicine and Biology, 2019. **64**(5): p. 15.
223. Hilgers, G., M.U. Bug, and H. Rabus, *Measurement of track structure parameters of low and medium energy helium and carbon ions in nanometric volumes.* Physics in Medicine and Biology, 2017. **62**(19): p. 7569-7597.
224. Blyth, B.J., et al., *Genetic Analysis of T Cell Lymphomas in Carbon Ion-Irradiated Mice Reveals Frequent Interstitial Chromosome Deletions: Implications for Second Cancer*

*Induction in Normal Tissues during Carbon Ion Radiotherapy.* PLOS ONE, 2015. **10**(6): p. e0130666.
225. Pignalosa, D., et al., *Chromosome inversions in lymphocytes of prostate cancer patients treated with X-rays and carbon ions.* Radiotherapy and Oncology, 2013. **109**(2): p. 256-261.
226. Schneider, U., *Modeling the Risk of Secondary Malignancies after Radiotherapy.* Genes, 2011. **2**(4): p. 1033-1049.
227. Eley, J.G., et al., *Comparative Risk Predictions of Second Cancers After Carbon-Ion Therapy Versus Proton Therapy.* International Journal of Radiation Oncology*Biology*Physics, 2016. **95**(1): p. 279-286.
228. Newhauser, W.D. and M. Durante, *Assessing the risk of second malignancies after modern radiotherapy.* Nature Reviews Cancer, 2011. **11**(6): p. 438-448.
229. Kamada, T., et al., *Carbon ion radiotherapy in Japan: an assessment of 20 years of clinical experience.* Lancet Oncol, 2015. **16**(2): p. e93-e100.
230. Kamada, T., et al., *Efficacy and Safety of Carbon Ion Radiotherapy in Bone and Soft Tissue Sarcomas.* Journal of Clinical Oncology, 2002. **20**(22): p. 4466-4471.
231. Serizawa, I., et al., *Carbon Ion Radiotherapy for Unresectable Retroperitoneal Sarcomas.* International Journal of Radiation Oncology*Biology*Physics, 2009. **75**(4): p. 1105-1110.
232. Mizoe, J.-e., et al., *Results of carbon ion radiotherapy for head and neck cancer.* Radiotherapy and Oncology, 2012. **103**(1): p. 32-37.
233. Mohr, A., et al., *Raster-scanned intensity-controlled carbon ion therapy for mucosal melanoma of the paranasal sinus.* Head & Neck, 2016. **38**(S1): p. E1445-E1451.
234. Ares, C., et al., *Effectiveness and Safety of Spot Scanning Proton Radiation Therapy for Chordomas and Chondrosarcomas of the Skull Base: First Long-Term Report.* International Journal of Radiation Oncology*Biology*Physics, 2009. **75**(4): p. 1111-1118.
235. Nomiya, T., et al., *A multi-institutional analysis of prospective studies of carbon ion radiotherapy for prostate cancer: A report from the Japan Carbon ion Radiation Oncology Study Group (J-CROS).* Radiotherapy and Oncology, 2016. **121**(2): p. 288-293.
236. Bujold, A., et al., *Sequential Phase I and II Trials of Stereotactic Body Radiotherapy for Locally Advanced Hepatocellular Carcinoma.* Journal of Clinical Oncology, 2013. **31**(13): p. 1631-1639.
237. Kato, H., et al., *Results of the first prospective study of carbon ion radiotherapy for hepatocellular carcinoma with liver cirrhosis1.* International Journal of Radiation Oncology*Biology*Physics, 2004. **59**(5): p. 1468-1476.
238. Qi, W.-X., et al., *Charged particle therapy versus photon therapy for patients with hepatocellular carcinoma: A systematic review and meta-analysis.* Radiotherapy and Oncology, 2015. **114**(3): p. 289-295.
239. Griffin, J.F., et al., *Patterns of failure after curative resection of pancreatic carcinoma.* Cancer, 1990. **66**(1): p. 56-61.
240. Shinoto, M., et al., *Carbon Ion Radiation Therapy With Concurrent Gemcitabine for Patients With Locally Advanced Pancreatic Cancer.* International Journal of Radiation Oncology*Biology*Physics, 2016. **95**(1): p. 498-504.

241. Jensen, A.D., et al., *Re-irradiation of adenoid cystic carcinoma: Analysis and evaluation of outcome in 52 consecutive patients treated with raster-scanned carbon ion therapy.* Radiotherapy and Oncology, 2015. **114**(2): p. 182-188.
242. Yamada, S., et al., *Carbon-Ion Radiation Therapy for Pelvic Recurrence of Rectal Cancer.* International Journal of Radiation Oncology*Biology*Physics, 2016. **96**(1): p. 93-101.
243. Group., P.T.C.-O. *Particle therapy facilities under construction*. April 2021 [cited 2021; Available from: https://www.ptcog.ch/index.php/facilities-under-construction.
244. Pompos, A., M. Durante, and H. Choy, *Heavy Ions in Cancer Therapy.* JAMA Oncology, 2016. **2**(12): p. 1539-1540.
245. Bortfeld, T.R. and J.S. Loeffler, *Three ways to make proton therapy affordable.* Nature, 2017. **549**(7673): p. 451-453.
246. Jäkel, O., et al., *On the cost-effectiveness of Carbon ion radiation therapy for skull base chordoma.* Radiotherapy and Oncology, 2007. **83**(2): p. 133-138.
247. Mobaraki, A., et al., *Cost-effectiveness of carbon ion radiation therapy for locally recurrent rectal cancer.* Cancer Science, 2010. **101**(8): p. 1834-1839.
248. Iwata, Y., et al., *Development of Carbon-Ion Radiotherapy Facilities at NIRS.* Ieee Transactions on Applied Superconductivity, 2018. **28**(3).
249. Ebner, D.K. and T. Kamada, *The Emerging Role of Carbon-Ion Radiotherapy.* Front Oncol, 2016. **6**: p. 140.
250. Tsujii, H., *Overview of Carbon-ion Radiotherapy*, in *Micro-Mini & Nano-Dosimetry & Innovative Technologies in Radiation Therapy*, C. Baldock, A. Rozenfeld, and P. Metcalfe, Editors. 2017.
251. Reisz, J.A., et al., *Effects of Ionizing Radiation on Biological Molecules—Mechanisms of Damage and Emerging Methods of Detection.* Antioxidants & Redox Signaling, 2014. **21**(2): p. 260-292.
252. Chiu, S.M., et al., *COPPER ION-MEDIATED SENSITIZATION OF NUCLEAR MATRIX ATTACHMENT SITES TO IONIZING-RADIATION.* Biochemistry, 1993. **32**(24): p. 6214-6219.
253. Kobayashi, K., et al., *Enhancement of radiation effect by heavy elements.* Mutation Research/Reviews in Mutation Research, 2010. **704**(1): p. 123-131.
254. Fokas, E., et al., *Targeting ATR in vivo using the novel inhibitor VE-822 results in selective sensitization of pancreatic tumors to radiation.* Cell Death & Disease, 2012. **3**(12): p. e441-e441.
255. Verhagen, C.V.M., et al., *Extent of radiosensitization by the PARP inhibitor olaparib depends on its dose, the radiation dose and the integrity of the homologous recombination pathway of tumor cells.* Radiotherapy and Oncology, 2015. **116**(3): p. 358-365.
256. Gerelchuluun, A., et al., *The Major DNA Repair Pathway after Both Proton and Carbon-Ion Radiation is NHEJ, but the HR Pathway is More Relevant in Carbon Ions.* Radiation Research, 2015. **183**(3): p. 345-356.
257. Zhou, X., et al., *DNA-PKcs Inhibition Sensitizes Cancer Cells to Carbon-Ion Irradiation via Telomere Capping Disruption.* PLOS ONE, 2013. **8**(8): p. e72641.
258. Tjio, J.H. and T.T. Puck, *Genetics of somatic mammalian cells. II. Chromosomal constitution of cells in tissue culture.* J Exp Med, 1958. **108**(2): p. 259-68.

259. Jayapal, K.R., et al., *Recombinant protein therapeutics from CHO cells - 20 years and counting.* Chemical Engineering Progress, 2007. **103**(10): p. 40-47.
260. Batista, L.F.Z., et al., *Involvement of DNA replication in ultraviolet-induced apoptosis of mammalian cells.* Apoptosis, 2006. **11**(7): p. 1139.
261. Dunkern, T.R. and B. Kaina, *Cell Proliferation and DNA Breaks Are Involved in Ultraviolet Light-induced Apoptosis in Nucleotide Excision Repair-deficient Chinese Hamster Cells.* Molecular Biology of the Cell, 2002. **13**(1): p. 348-361.
262. Whitmore, G.F., A.J. Varghese, and S. Gulyas, *Cell Cycle Responses of Two X-ray Sensitive Mutants Defective in DNA Repair.* International Journal of Radiation Biology, 1989. **56**(5): p. 657-665.
263. Hinz, J.M., et al., *Repression of mutagenesis by Rad51D-mediated homologous recombination.* Nucleic Acids Research, 2006. **34**(5): p. 1358-1368.
264. Cartwright, I.M., et al., *DNA Repair Deficient Chinese Hamster Ovary Cells Exhibiting Differential Sensitivity to Charged Particle Radiation under Aerobic and Hypoxic Conditions.* International Journal of Molecular Sciences, 2018. **19**(8): p. 2228.
265. Hall, E.J., *Radiobiology for the Radiologist: Cell survival curves*. 4th ed. 1994, Philidelphia: J.B. Lippincott Company.
266. Franken, N.A., et al., *Clonogenic assay of cells in vitro.* Nat Protoc, 2006. **1**(5): p. 2315-9.
267. Puck , T.T. and P.I. Marcus *ACTION OF X-RAYS ON MAMMALIAN CELLS.* Journal of Experimental Medicine, 1956. **103**(5): p. 653-666.
268. Salimi, M. and H. Mozdarani, *gamma-H2AX as a protein biomarker for radiation exposure response in ductal carcinoma breast tumors: Experimental evidence and literature review.* International Journal of Radiation Research, 2014. **12**(1): p. 1-11.
269. Fernandez-Capetillo, O., et al., *H2AX: the histone guardian of the genome.* DNA Repair, 2004. **3**(8): p. 959-967.
270. Kinner, A., et al., *γ-H2AX in recognition and signaling of DNA double-strand breaks in the context of chromatin.* Nucleic Acids Research, 2008. **36**(17): p. 5678-5694.
271. Fernandez-Capetillo, O., et al., *DNA damage-induced G2–M checkpoint activation by histone H2AX and 53BP1.* Nature Cell Biology, 2002. **4**(12): p. 993-997.
272. Lowndes, N.F. and G.W.L. Toh, *DNA Repair: The Importance of Phosphorylating Histone H2AX.* Current Biology, 2005. **15**(3): p. R99-R102.
273. van Attikum, H. and S.M. Gasser, *The histone code at DNA breaks: a guide to repair?* Nature Reviews Molecular Cell Biology, 2005. **6**(10): p. 757-765.
274. Bassing, C.H., et al., *Histone H2AX: A Dosage-Dependent Suppressor of Oncogenic Translocations and Tumors.* Cell, 2003. **114**(3): p. 359-370.
275. Hada, M. and A.G. Georgakilas, *Formation of clustered DNA damage after high-LET irradiation: A review.* Journal of Radiation Research, 2008. **49**(3): p. 203-210.
276. Kato, T.A., R. Okayasu, and J.S. Bedford, *Comparison of the induction and disappearance of DNA double strand breaks and gamma-H2AX foci after irradiation of chromosomes in G1-phase or in condensed metaphase cells.* Mutation Research-Fundamental and Molecular Mechanisms of Mutagenesis, 2008. **639**(1-2): p. 108-112.
277. Nazarov, I.B., et al., *Dephosphorylation of Histone γ-H2AX during Repair of DNA Double-Strand Breaks in Mammalian Cells and its Inhibition by Calyculin A.* Radiation Research, 2003. **160**(3): p. 309-317.

278. Ibañez, I.L., et al., *Induction and Rejoining of DNA Double Strand Breaks Assessed by H2AX Phosphorylation in Melanoma Cells Irradiated with Proton and Lithium Beams.* International Journal of Radiation Oncology*Biology*Physics, 2009. **74**(4): p. 1226-1235.
279. Saha, J., et al., *Biological Characterization of Low-Energy Ions with High-Energy Deposition on Human Cells.* Radiation Research, 2014. **182**(3): p. 282-291, 10.
280. Okayasu, R., *Repair of DNA damage induced by accelerated heavy ions--a mini review.* Int J Cancer, 2012. **130**(5): p. 991-1000.
281. Ristic-Fira, A.M., et al., *DNA damage assessment of human breast and lung carcinoma cells irradiated with protons and carbon ions.* Journal of Radiation Research and Applied Sciences.
282. Oonishi, K., et al., *Different effects of carbon ion beams and X-rays on clonogenic survival and DNA repair in human pancreatic cancer stem-like cells.* Radiotherapy and Oncology, 2012. **105**(2): p. 258-265.
283. Cucinotta, F.A., et al., *Radiation dosimetry and biophysical models of space radiation effects.* Gravitational and Space Biology, 2003. **16**: p. 11+.
284. Desai, N., et al., *Immunofluorescence detection of clustered gamma-H2AX foci induced by HZE-particle radiation.* Radiation Research, 2005. **164**(4): p. 518-522.
285. Jeggo, P. and M.F. Lavin, *Cellular radiosensitivity: How much better do we understand it?* International Journal of Radiation Biology, 2009. **85**(12): p. 1061-1081.
286. Kramer, M. and G. Kraft, *CALCULATIONS OF HEAVY-ION TRACK STRUCTURE.* Radiation and Environmental Biophysics, 1994. **33**(2): p. 91-109.
287. McFadden, C.H., et al., *Isolation of time-dependent DNA damage induced by energetic carbon ions and their fragments using fluorescent nuclear track detectors.* Medical Physics, 2020. **47**(1): p. 272-281.
288. Francis, Z., et al., *Carbon ion fragmentation effects on the nanometric level behind the Bragg peak depth.* Physics in Medicine and Biology, 2014. **59**(24): p. 7691-7702.
289. Liu, C.H., et al., *Reduction of Delayed Homologous Recombination by Induction of Radioadaptive Response in RaDR-GFP Mice (Yonezawa Effect): An Old Player With a New Role.* Dose-Response, 2019. **17**(1): p. 8.
290. Buglewicz, D.J., et al., *Monoenergetic 290 MeV/n carbon-ion beam biological lethal dose distribution surrounding the Bragg peak.* Scientific Reports, 2019. **9**(1): p. 6157.
291. Zhao, J., et al., *pATM and γH2AX are effective radiation biomarkers in assessing the radiosensitivity of 12C6+ in human tumor cells.* Cancer Cell International, 2017. **17**(1): p. 49.
292. Prise, K.M., et al., *EFFECT OF RADIATION QUALITY ON LESION COMPLEXITY IN CELLULAR DNA.* International Journal of Radiation Biology, 1994. **66**(5): p. 537-542.
293. Lobrich, M., et al., *gamma H2AX foci analysis for monitoring DNA double-strand break repair Strengths, limitations and optimization.* Cell Cycle, 2010. **9**(4): p. 662-669.
294. Jakob, B., M. Scholz, and G. Taucher-Scholz, *Biological imaging of heavy charged-particle tracks.* Radiation Research, 2003. **159**(5): p. 676-684.
295. Tobias, F., et al., *Spatiotemporal analysis of DNA repair using charged particle radiation.* Mutation Research-Reviews in Mutation Research, 2010. **704**(1-3): p. 54-60.
296. Whalen, M.K., et al., *Specific ATM-mediated phosphorylation dependent on radiation quality.* Radiation Research, 2008. **170**(3): p. 353-364.

297. Sridharan, D.M., et al., *Defining the Biological Effectiveness of Components of High-LET Track Structure.* Radiation Research, 2015. **184**(1): p. 105-119.
298. Chang, D.S., et al., *Oxygen Effect, Relative Biological Effectiveness and Linear Energy Transfer*, in *Basic Radiotherapy Physics and Biology*. 2014, Springer International Publishing: Cham. p. 235-240.
299. Mehnati, P., et al., *Exploration of 'over kill effect' of high-LET Ar- and Fe-ions by evaluating the fraction of non-hit cell and interphase death.* Journal of Radiation Research, 2005. **46**(3): p. 343-350.
300. Sekine, E., et al., *High LET heavy ion radiation induces lower numbers of initial chromosome breaks with minimal repair than low LET radiation in normal human cells.* Mutation Research-Genetic Toxicology and Environmental Mutagenesis, 2008. **652**(1): p. 95-101.
301. Kanai, T., et al., *Biophysical characteristics of HIMAC clinical irradiation system for heavy-ion radiation therapy.* International Journal of Radiation Oncology Biology Physics, 1999. **44**(1): p. 201-210.
302. Nickoloff, J.A., N. Sharma, and L. Taylor, *Clustered DNA Double-Strand Breaks: Biological Effects and Relevance to Cancer Radiotherapy.* Genes, 2020. **11**(1).
303. Pouget, J.P. and S.J. Mather, *General aspects of the cellular response to low- and high-LET radiation.* European Journal of Nuclear Medicine, 2001. **28**(4): p. 541-561.
304. Ward, J.F., *DNA Damage Produced by Ionizing-Radiation in Mammalian-Cells - Identities, Mechanisms of Formation, and Reparability.* Progress in Nucleic Acid Research and Molecular Biology, 1988. **35**: p. 95-125.
305. Ward, J.F., W.F. Blakely, and E.I. Joner, *Mammalian Cells Are Not Killed by DNA Single-Strand Breaks Caused by Hydroxyl Radicals from Hydrogen Peroxide.* Radiation Research, 1985. **103**(3): p. 383-392.
306. Hoffmann, M.E. and R. Meneghini, *ACTION OF HYDROGEN-PEROXIDE ON HUMAN FIBROBLAST IN CULTURE.* Photochemistry and Photobiology, 1979. **30**(1): p. 151-155.
307. Rhaese, H.J. and E. Freese, *CHEMICAL ANALYSIS OF DNA ALTERATIONS .I. BASE LIBERATION AND BACKBONE BREAKAGE OF DNA AND OLIGODEOXYADENYLIC ACID INDUCED BY HYDROGEN PEROXIDE AND HYDROXYLAMINE.* Biochimica Et Biophysica Acta, 1968. **155**(2): p. 476-&.
308. Ward, J.F., *Molecular Mechanisms of Radiation-Induced Damage to Nucleic Acids1 1The studies carried out in the author's laboratory were supported by Contract AT(04-1) GEN-12 between the U.S. Atomic Energy Commission and the University of California and by a grant from the U.S. Public Health Service*, in *Advances in Radiation Biology*, J.T. Lett and H. Adler, Editors. 1975, Elsevier. p. 181-239.
309. Regulus, P., et al., *Oxidation of the sugar radiation or bleomycin of a cluster DNA lesion moiety of DNA by ionizing could induce the formation.* Proceedings of the National Academy of Sciences of the United States of America, 2007. **104**(35): p. 14032-14037.
310. Hecht, S.M., *Bleomycin: New Perspectives on the Mechanism of Action.* Journal of Natural Products, 2000. **63**(1): p. 158-168.
311. Hecht, S.M., *THE CHEMISTRY OF ACTIVATED BLEOMYCIN.* Accounts of Chemical Research, 1986. **19**(12): p. 383-391.
312. Stubbe, J. and J.W. Kozarich, *MECHANISMS OF BLEOMYCIN-INDUCED DNA-DEGRADATION.* Chemical Reviews, 1987. **87**(5): p. 1107-1136.

313. Burger, R.M., *Cleavage of nucleic acids by bleomycin.* Chemical Reviews, 1998. **98**(3): p. 1153-1169.
314. Calafat, A.M., H. Won, and L.G. Marzilli, *A New Arrangement for the Anticancer Antibiotics Tallysomycin and Bleomycin When Bound to Zinc: An Assessment of Metal and Ligand Chirality by NMR and Molecular Dynamics.* Journal of the American Chemical Society, 1997. **119**(16): p. 3656-3664.
315. Loeb, K.E., et al., *Spectroscopic Investigation of the Metal Ligation and Reactivity of the Ferrous Active Sites of Bleomycin and Bleomycin Derivatives.* Journal of the American Chemical Society, 1998. **120**(6): p. 1249-1259.
316. Petering, D.H., R.W. Byrnes, and W.E. Antholine, *The role of redox-active metals in the mechanism of action of bleomycin.* Chemico-Biological Interactions, 1990. **73**(2): p. 133-182.
317. Lloyd, D.R. and D.H. Phillips, *Oxidative DNA damage mediated by copper(II), iron(II) and nickel(II) Fenton reactions: evidence for site-specific mechanisms in the formation of double-strand breaks, 8-hydroxydeoxyguanosine and putative intrastrand cross-links.* Mutation Research-Fundamental and Molecular Mechanisms of Mutagenesis, 1999. **424**(1-2): p. 23-36.
318. Feitelson, J., E. Hayon, and A. Treinin, *Photoionization of Phenols in Water - Effects of Light-Intensity, Oxygen, Ph, and Temperature.* Journal of the American Chemical Society, 1973. **95**(4): p. 1025-1029.
319. Ward, J.F., W.F. Blakely, and E.I. Joner, *Mammalian-Cells Are Not Killed by DNA Single-Strand Breaks Caused by Hydroxyl Radicals from Hydrogen-Peroxide.* Radiation Research, 1985. **103**(3): p. 383-392.
320. McCormick, M.L., G.R. Buettner, and B.E. Britigan, *Endogenous superoxide dismutase levels regulate iron-dependent hydroxyl radical formation in Escherichia coli exposed to hydrogen peroxide.* Journal of Bacteriology, 1998. **180**(3): p. 622-625.
321. Robison, S.H., O. Cantoni, and M. Costa, *STRAND BREAKAGE AND DECREASED MOLECULAR-WEIGHT OF DNA INDUCED BY SPECIFIC METAL-COMPOUNDS.* Carcinogenesis, 1982. **3**(6): p. 657-662.
322. Teicher, B.A., et al., *Some Complexes of Cobalt(III) and Iron(III) Are Radiosensitizers of Hypoxic EMT6 Cells.* Radiation Research, 1987. **109**(1): p. 36-46.
323. Teicher, B.A., et al., *CYTOTOXICITY, RADIOSENSITIZATION, ANTITUMOR-ACTIVITY, AND INTERACTION WITH HYPERTHERMIA OF A CO(III) MUSTARD COMPLEX.* Cancer Research, 1990. **50**(21): p. 6971-6975.
324. Jiang, Y.-W., et al., *Copper Oxide Nanoparticles Induce Enhanced Radiosensitizing Effect via Destructive Autophagy.* ACS Biomaterials Science & Engineering, 2019. **5**(3): p. 1569-1579.
325. Lloyd, D.R. and D.H. Phillips, *Oxidative DNA damage mediated by copper(II), iron(II) and nickel(II) Fenton reactions: evidence for site-specific mechanisms in the formation of double-strand breaks, 8-hydroxydeoxyguanosine and putative intrastrand cross-links.* Mutation Research/Fundamental and Molecular Mechanisms of Mutagenesis, 1999. **424**(1): p. 23-36.
326. Lloyd, D.R., D.H. Phillips, and P.L. Carmichael, *Generation of putative intrastrand cross-links and strand breaks in DNA by transition metal ion-mediated oxygen radical attack.* Chemical Research in Toxicology, 1997. **10**(4): p. 393-400.

327. Petering, D.H., R.W. Byrnes, and W.E. Antholine, *The Role of Redox-Active Metals in the Mechanism of Action of Bleomycin.* Chemico-Biological Interactions, 1990. **73**(2-3): p. 133-182.
328. Heilmann, J., et al., *Measurement of intracellular DNA double-strand break induction and rejoining along the track of carbon and neon particle beams in water.* International Journal of Radiation Oncology Biology Physics, 1996. **34**(3): p. 599-608.
329. Takata, H., et al., *Chromatin Compaction Protects Genomic DNA from Radiation Damage.* Plos One, 2013. **8**(10).
330. Lomax, M.E., L.K. Folkes, and P. O'Neill, *Biological Consequences of Radiation-induced DNA Damage: Relevance to Radiotherapy.* Clinical Oncology, 2013. **25**(10): p. 578-585.
331. Suzuki, T., J. Kuwahara, and Y. Sugiura, *COPPER-BLEOMYCIN HAS NO SIGNIFICANT DNA CLEAVAGE ACTIVITY.* Biochemistry, 1985. **24**(18): p. 4719-4721.
332. Abraham, A.T., X. Zhou, and S.M. Hecht, *Metallobleomycin-mediated cleavage of DNA not involving a threading-intercalation mechanism.* Journal of the American Chemical Society, 2001. **123**(22): p. 5167-5175.
333. Ehrenfeld, G.M., et al., *COPPER-DEPENDENT CLEAVAGE OF DNA BY BLEOMYCIN.* Biochemistry, 1987. **26**(3): p. 931-942.
334. Hecht, S.M., *Bleomycin: New perspectives on the mechanism of action.* Journal of Natural Products, 2000. **63**(1): p. 158-168.
335. Maeda, J., et al., *Hyperthermia-induced radiosensitization in CHO wild-type, NHEJ repair mutant and HR repair mutant following proton and carbon-ion exposure.* Oncology Letters, 2015. **10**(5): p. 2828-2834.
336. Haskins, A.H., et al., *Palmitoyl ascorbic acid 2-glucoside has the potential to protect mammalian cells from high-LET carbon-ion radiation.* Sci Rep, 2018. **8**(1): p. 13822.
337. Yu, H., et al., *In vitro screening of radioprotective properties in the novel glucosylated flavonoids.* International Journal of Molecular Medicine, 2016. **38**(5): p. 1525-1530.
338. Elmegerhi, S., et al., *Effect of hydroxyl group position in flavonoids on inducing singlestranded DNA damage mediated by cupric ions.* Int J Mol Med, 2018. **42**(1): p. 658-664.
339. Suzuki, M., et al., *Relative biological effectiveness for cell-killing effect on various human cell lines irradiated with heavy-ion medical accelerator in CHIBA (HIMAC) carbon-ion beams.* International Journal of Radiation Oncology Biology Physics, 2000. **48**(1): p. 241-250.
340. Takahashi, A., et al., *DNA Damage Recognition Proteins Localize along Heavy Ion Induced Tracks in the Cell Nucleus.* Journal of Radiation Research, 2008. **49**(6): p. 645-652.
341. Hirayama, R., et al., *Repair Kinetics of DNA-DSB Induced by X-rays or Carbon Ions under Oxic and Hypoxic Conditions.* Journal of Radiation Research, 2005. **46**(3): p. 325-332.
342. Hamada, N., et al., *The survival of heavy ion-irradiated Bcl-2 overexpressing radioresistant tumor cells and their progeny.* Cancer Letters, 2008. **268**(1): p. 76-81.
343. Ohnishi, T., E. Mori, and A. Takahashi, *DNA double-strand breaks: Their production, recognition, and repair in eukaryotes.* Mutation Research/Fundamental and Molecular Mechanisms of Mutagenesis, 2009. **669**(1): p. 8-12.

344. Falk, M., E. Lukasova, and S. Kozubek, *Higher-order chromatin structure in DSB induction, repair and misrepair.* Mutation Research/Reviews in Mutation Research, 2010. **704**(1): p. 88-100.
345. Chapman, J.R., Martin R.G. Taylor, and Simon J. Boulton, *Playing the End Game: DNA Double-Strand Break Repair Pathway Choice.* Molecular Cell, 2012. **47**(4): p. 497-510.
346. Takahashi, A., et al., *Nonhomologous End-Joining Repair Plays a More Important Role than Homologous Recombination Repair in Defining Radiosensitivity after Exposure to High-LET Radiation.* Radiation Research, 2014. **182**(3): p. 338-344, 7.
347. Wang, C. and S.P. Lees-Miller, *Detection and Repair of Ionizing Radiation-Induced DNA Double Strand Breaks: New Developments in Nonhomologous End Joining.* International Journal of Radiation Oncology*Biology*Physics, 2013. **86**(3): p. 440-449.
348. Jeggo, P.A., V. Geuting, and M. Löbrich, *The role of homologous recombination in radiation-induced double-strand break repair.* Radiotherapy and Oncology, 2011. **101**(1): p. 7-12.
349. Symington, L.S. and J. Gautier, *Double-Strand Break End Resection and Repair Pathway Choice.* Annual Review of Genetics, 2011. **45**(1): p. 247-271.
350. Davis, A.J. and D.J. Chen, *DNA double strand break repair via non-homologous end-joining.* Translational cancer research, 2013. **2**(3): p. 130-143.
351. Sunada, S., et al., *Investigation of the relative biological effectiveness and uniform isobiological killing effects of irradiation with a clinical carbon SOBP beam on DNA repair deficient CHO cells.* Oncol Lett, 2017. **13**(6): p. 4911-4916.
352. Hada, M. and B.M. Sutherland, *Spectrum of Complex DNA Damages Depends on the Incident Radiation.* Radiation Research, 2006. **165**(2): p. 223-230.
353. Belli, M., et al., *DNA Fragmentation in mammalian cells exposed to various light ions.* Advances in Space Research, 2001. **27**(2): p. 393-399.
354. Bee, L., et al., *The Efficiency of Homologous Recombination and Non-Homologous End Joining Systems in Repairing Double-Strand Breaks during Cell Cycle Progression.* PLOS ONE, 2013. **8**(7): p. e69061.
355. Mao, Z., et al., *Comparison of nonhomologous end joining and homologous recombination in human cells.* DNA Repair, 2008. **7**(10): p. 1765-1771.
356. Neal, J.A., et al., *Inhibition of Homologous Recombination by DNA-Dependent Protein Kinase Requires Kinase Activity, Is Titratable, and Is Modulated by Autophosphorylation.* Molecular and Cellular Biology, 2011. **31**(8): p. 1719.
357. Shrivastav, M., et al., *DNA-PKcs and ATM co-regulate DNA double-strand break repair.* DNA Repair, 2009. **8**(8): p. 920-929.
358. Connell, P.P., et al., *Pilot study examining tumor expression of RAD51 and clinical outcomes in human head cancers.* Int J Oncol, 2006. **28**(5): p. 1113-1119.
359. Takenaka, T., et al., *Combined evaluation of Rad51 and ERCC1 expressions for sensitivity to platinum agents in non-small cell lung cancer.* International Journal of Cancer, 2007. **121**(4): p. 895-900.
360. Russell, J.S., et al., *Gleevec-Mediated Inhibition of Rad51 Expression and Enhancement of Tumor Cell Radiosensitivity.* Cancer Research, 2003. **63**(21): p. 7377.
361. Ito, M., et al., *Rad51 siRNA delivered by HVJ envelope vector enhances the anti-cancer effect of cisplatin.* The Journal of Gene Medicine, 2005. **7**(8): p. 1044-1052.
362. Budke, B., et al., *RI-1: a chemical inhibitor of RAD51 that disrupts homologous recombination in human cells.* Nucleic Acids Research, 2012. **40**(15): p. 7347-7357.

363. Maeda, J., et al., *Relative biological effectiveness in canine osteosarcoma cells irradiated with accelerated charged particles.* Oncol Lett, 2016. **12**(2): p. 1597-1601.
364. Maeda, J., et al., *Natural and glucosyl flavonoids inhibit poly(ADP-ribose) polymerase activity and induce synthetic lethality in BRCA mutant cells.* Oncol Rep, 2014. **31**(2): p. 551-556.